

UC Santa Cruz

UC Santa Cruz Previously Published Works

Title

Les Houches 2011: Physics at TeV Colliders New Physics Working Group Report

Permalink

<https://escholarship.org/uc/item/645080mg>

Authors

Brooijmans, G

Gripaios, B

Moortgat, F

et al.

Publication Date

2012-03-07

Peer reviewed

LES HOUCHES 2011: PHYSICS AT TEV COLLIDERS NEW PHYSICS WORKING GROUP REPORT

G. Brooijmans¹, B. Gripaios², F. Moortgat³, J. Santiago⁴ and P. Skands⁵ (convenors)
D. Albornoz Vásquez⁶, B.C. Allanach⁷, A. Alloul⁸, A. Arbey^{5,9,10}, A. Azatov¹¹, H. Baer¹²,
C. Balázs^{13,14,15}, A. Barr¹⁶, L. Basso^{17,18,19}, M. Battaglia^{5,20,21}, P. Bechtle²², G. Bélanger²³,
A. Belyaev^{17,18}, K. Benslama²⁴, L. Bergström²⁵, A. Bharucha²⁶, C. Boehm²⁷,
M. Bondarenko¹⁷, O. Bondu⁹, E. Boos²⁸, F. Boudjema²³, T. Bringmann²⁶, M. Brown¹⁷,
V. Bunichev²⁸, S. Calvet²⁹, M. Campanelli³⁰, A. Carmona⁴, D. G. Cerdeño^{31,32}, M. Chala⁴,
R. S. Chivukula³³, D. Chowdhury³⁴, N. D. Christensen³⁵, M. Cirelli^{5,36}, S. Cox³⁷,
K. Cranmer³⁸, J. Da Silva^{23,27}, T. Delahaye³¹, A. De Roeck⁵, A. Djouadi³⁹, E. Dobson^{5,30},
M. Dolan²⁷, F. Donato⁴⁰, G. Drieu La Rochelle²³, G. Duda⁴¹, C. Duhr⁴², B. Dumont⁴³,
J. Edsjö²⁵, J. Ellis^{5,44}, C. Evoli⁴⁵, A. Falkowski³⁹, M. Felcini⁴⁵, B. Fuks⁸, E. Gabrielli⁴⁶,
D. Gaggero⁴⁷, S. Gascon-Shotkin⁹, D.K. Ghosh⁴⁸, A. Giammanco^{46,49}, R. M. Godbole³⁴,
P. Gondolo^{25,50}, T. Goto⁵¹, D. Grasso⁴⁷, P. Gris²⁹, D. Guadagnoli³⁹, J.F. Gunion⁵², U. Haisch⁵³,
L. Hartgring⁵⁴, S. Heinemeyer⁴⁵, M. Hirsch⁵⁵, J. Hewett⁵⁶, A. Ismail⁵⁶, T. Jeltema²⁰,
M. Kadastik⁴⁶, M. Kakizaki⁵⁷, K. Kannike^{46,58}, S. Khalil^{59,60}, J-L. Kneur⁶¹, M. Krämer⁶²,
S. Kraml⁴³, S. Kreiss³⁸, J. Lavallo⁶³, R. Leane^{13,15}, J. Lykken⁶⁴, L. Maccione⁶⁵,
F. Mahmoudi^{5,29}, M. Mangano⁵, S.P. Martin^{66,64,67}, D. Maurin⁴³, G. Moreau³⁹, S. Moretti^{17,18},
I. Moskalenko⁶⁸, G. Mourtaka⁶¹, M. Muhlleitner⁶⁹, I. Niessen⁷⁰, B. O’Leary⁷¹, E. Orlando⁶⁸,
P. Panci⁷², G. Polesello⁷³, W. Porod⁷¹, T. Porter⁶⁸, S. Profumo²⁰, H. Prosper⁷⁴, A. Pukhov²⁸,
A. Racioppi⁴⁶, M. Raidal⁴⁶, M. Rausch de Traubenberg⁸, A. Renaud⁷⁵, J. Reuter²²,
T. G. Rizzo⁵⁶, T. Robens⁷⁶, A. Y. Rodríguez-Marrero⁴⁵, P. Salati²³, C. Savage²⁵, P. Scott⁷⁷,
S. Sekmen^{74,5}, A. Semenov⁷⁸, C. -L. Shan⁷⁹, C. Shepherd-Themistocleous¹⁸,
E. H. Simmons³³, P. Slavich⁸⁰, C. Speckner¹⁹, F. Staub⁸¹, A. Strong⁸², R. Taillet⁷²,
F. S. Thomas⁷¹, M. C. Thomas¹⁷, I. Tomalin¹⁸, M. Tytgat⁸³, M. Ughetto^{61,84}, L. Valéry²⁹,
D. G. E. Walker⁵⁶, A. Weiler²², S. M. West^{18,85}, C. D. White⁸⁶, A. J. Williams^{18,85},
A. Wingerter⁴³, C. Wymant²⁷, J. -H. Yu⁸⁷, C. -P. Yuan⁸⁷, and D. Zerwas⁷⁵

Abstract

We present the activities of the “New Physics” working group for the “Physics at TeV Colliders” workshop (Les Houches, France, 30 May–17 June, 2011). Our report includes new agreements on formats for interfaces between computational tools, new tool developments, important signatures for searches at the LHC, recommendations for presentation of LHC search results, as well as additional phenomenological studies.

Acknowledgements

We would like to heartily thank the funding bodies, the organisers (G. Bélanger, F. Boudjema, S. Gascon, C. Grojean, J.P. Guillet, S. Kraml, G. Moreau, E. Pilon, G. Salam, P. Slavich and D. Zerwas), the staff and the other participants of the Les Houches workshop for providing a stimulating and lively environment in which to work.

- ¹ Physics Department, Columbia University, New York, NY 10027, USA
- ² Cavendish Laboratory, University of Cambridge, Cambridge CB3 0HE, UK
- ³ Institute for Particle Physics, ETH Zürich, Zürich, Switzerland
- ⁴ CAFPE and Dpto. de Física Teórica y del Cosmos, Universidad de Granada, E-18071, Granada, Spain
- ⁵ Physics Department, CERN, CH-1211 Geneva 23, Switzerland
- ⁶ Institut d'Astrophysique de Paris, UMR 7095 CNRS, Université Pierre et Marie Curie, Paris 75014, France
- ⁷ DAMTP, CMS, University of Cambridge, Cambridge, CB3 0WA, UK
- ⁸ Institut Pluridisciplinaire Hubert Curien/Département Recherches Subatomiques, Université de Strasbourg/CNRS-IN2P3, F-67037 Strasbourg, France
- ⁹ Université Claude Bernard Lyon 1, CNRS/IN2P3, Institut de Physique Nucléaire de Lyon, F-69622 Villeurbanne Cedex, France
- ¹⁰ Centre de Recherche Astrophysique de Lyon, Observatoire de Lyon, Saint-Genis Laval Cedex, F-69561, France; CNRS, UMR 5574; Ecole Normale Supérieure de Lyon, Lyon, France
- ¹¹ Dipartimento di Fisica, Università di Roma "La Sapienza", INFN Sezione, 00185 Roma, Italy
- ¹² Department of Physics and Astronomy, University of Oklahoma, Norman, OK 73019, USA
- ¹³ ARC Centre of Excellence for Particle Physics at the Tera-scale, Monash University, Melbourne, Victoria 3800 Australia
- ¹⁴ Monash Centre for Astrophysics, Monash University, Melbourne, Victoria 3800 Australia
- ¹⁵ School of Physics, Monash University, Melbourne, Victoria 3800 Australia
- ¹⁶ Department of Physics, Oxford, OX1 3RH, United Kingdom
- ¹⁷ School of Physics & Astronomy, University of Southampton, Highfield, Southampton SO17 1BJ, UK
- ¹⁸ Particle Physics Department, Rutherford Appleton Laboratory, Oxon OX11 0QX, UK
- ¹⁹ Fakultät für Mathematik und Physik, Albert-Ludwigs-Universität, D-79104 Freiburg i.Br., Germany
- ²⁰ Department of Physics and Santa Cruz Institute for Particle Physics, University of California, Santa Cruz, CA 95064, USA
- ²¹ Lawrence Berkeley National Laboratory, Berkeley, CA 94720, USA
- ²² Deutsches Elektronen-Synchrotron DESY, D-22607 Hamburg, Germany
- ²³ LAPTh, Univ. de Savoie, CNRS, B.P.110, F-74941 Annecy-le-Vieux Cedex, France
- ²⁴ Physics Department, University of Regina, 3737 Wascana Parkway, Regina-SK, Canada
- ²⁵ The Oskar Klein Centre for Cosmoparticle Physics, Department of Physics, Stockholm University, AlbaNova University Centre, SE-106 91 Stockholm, Sweden
- ²⁶ II. Institut für Theoretische Physik, Universität Hamburg, 22761 Hamburg, Germany
- ²⁷ Institute for Particle Physics Phenomenology, University of Durham, Durham DH1 3LE, UK
- ²⁸ Skobeltsyn Institute of Nuclear Physics, Lomonosov Moscow State University, 119992 Moscow, Russia
- ²⁹ Laboratoire de Physique Corpusculaire, Clermont Université, Université Blaise Pascal, CNRS/IN2P3, FR-63177 Aubière Cedex, France
- ³⁰ Department of Physics & Astronomy, University College London, WC1E 6BT London, UK
- ³¹ Instituto de Física Teórica UAM/CSIC, Universidad Autónoma de Madrid, 28049 Madrid, Spain
- ³² Departamento de Física Teórica, Universidad Autónoma de Madrid, 28049 Madrid Spain
- ³³ Michigan State University, Department of Physics and Astronomy, East Lansing, MI 48824, USA
- ³⁴ Centre for High Energy Physics, Indian Institute of Science, Bangalore 560 012, India
- ³⁵ PITTSburgh Particle physics, Astrophysics and Cosmology Center, Department of Physics and Astronomy, University of Pittsburgh, Pittsburgh, PA 15260, USA
- ³⁶ Institut de Physique Théorique, CNRS, URA 2306 & CEA/Saclay, F-91191 Gif-sur-Yvette, France
- ³⁷ Computational Engineering and Design Research group, University of Southampton, Highfield, Southampton SO17 1BJ, UK
- ³⁸ Center for Cosmology and Particle Physics, New York University, New York, NY 10003, USA
- ³⁹ Laboratoire de Physique Théorique, CNRS, Université Paris 11, 91405 Orsay Cedex, France
- ⁴⁰ Dipartimento di Fisica Teorica, Università di Torino & INFN, 10122 Torino Italy
- ⁴¹ Department of Physics, Creighton University, 2500 California Plaza, Omaha, NE 68178 USA
- ⁴² Institut für Theoretische Physik, ETH Zürich, CH-8093, Switzerland
- ⁴³ Laboratoire de Physique Subatomique et de Cosmologie, UJF Grenoble 1, CNRS/IN2P3, INPG, F-38026 Grenoble, France
- ⁴⁴ Theoretical Particle Physics and Cosmology Group, Department of Physics, King's College London, London WC2R 2LS, UK
- ⁴⁵ Instituto de Física de Cantabria (IFCA), CSIC-Universidad de Cantabria, E-39005 Santander, Spain

- ⁴⁶ NICPB, Ravala 10, 10143 Tallinn, Estonia
- ⁴⁷ INFN sezione di Pisa, Pisa, Italy
- ⁴⁸ Department of Theoretical Physics, Indian Association for the Cultivation of Science, Kolkata 700 032, India
- ⁴⁹ Université Catholique de Louvain, Louvain-la-Neuve, Belgium
- ⁵⁰ Department of Physics and Astronomy, University of Utah, Salt Lake City, UT 84112 USA
- ⁵¹ KEK Theory Center, Institute of Particle and Nuclear Studies, KEK, Tsukuba, 305-0801, Japan
- ⁵² Department of Physics, University of California at Davis, Davis CA, USA
- ⁵³ Rudolf Peierls Centre for Theoretical Physics, University of Oxford, OX1 3PN Oxford, UK
- ⁵⁴ NIKHEF, 1098 XG Amsterdam, The Netherlands
- ⁵⁵ Instituto de Fisica Corpuscular, CSIC, Universidad de Valencia, 46071 Valencia, Spain
- ⁵⁶ SLAC National Accelerator Laboratory, Menlo Park, CA 94025, USA
- ⁵⁷ Department of Physics, University of Toyama, 3190 Gofuku, Toyama 930-8555, Japan
- ⁵⁸ Scuola Normale Superiore and INFN, 56126 Pisa, Italy
- ⁵⁹ Centre for Theoretical Physics, Zewail City of Science and Technology, Sheikh Zayed, 12588, Giza, Egypt
- ⁶⁰ Department of Mathematics, Ain Shams University, Faculty of Science, Cairo 11566, Egypt
- ⁶¹ Laboratoire Charles Coulomb (L2C), Montpellier, France
- ⁶² Institute for Theoretical Particle Physics and Cosmology, RWTH Aachen University, D-52056 Aachen, Germany
- ⁶³ Laboratoire Univers & Particules de Montpellier [LUPM] CNRS-IN2P3, Université Montpellier II [UMR-5299], F-34095 Montpellier Cedex 05, France
- ⁶⁴ Fermi National Accelerator Laboratory, P.O. Box 500, Batavia, IL 60510
- ⁶⁵ Arnold Sommerfeld Center, Ludwig-Maximilians-Universität and Max-Planck-Institut fuer Physik, 80333 Munich Germany
- ⁶⁶ Department of Physics, Northern Illinois University, DeKalb IL 60115, USA
- ⁶⁷ Kavli Institute for Theoretical Physics, University of California, Santa Barbara CA 93106, USA
- ⁶⁸ Hansen Experimental Physics Laboratory and Kavli Institute for Particle Astrophysics and Cosmology, Stanford University, Stanford CA 94309 USA
- ⁶⁹ Institut für Theoretische Physik, Karlsruhe Institute of Technology, D-76128 Karlsruhe, Germany
- ⁷⁰ Theoretical High Energy Physics, IMAPP, Faculty of Science, NL-6500 GL Nijmegen, The Netherlands
- ⁷¹ Institut für Theoretische Physik und Astrophysik, Universität Würzburg, 97074 Würzburg, Germany
- ⁷² CP3-origins and the Danish Institute for Advanced Study DIAS, University of Southern Denmark, DK-5230 Odense M, Denmark
- ⁷³ INFN, Sezione di Pavia, I-27100 Pavia, Italy
- ⁷⁴ Department of Physics, Florida State University, Tallahassee, Florida 32306, USA
- ⁷⁵ LAL, Univ. Paris-Sud, IN2P3/CNRS, F-91898 Orsay Cedex, France
- ⁷⁶ IKTP, TU Dresden, 01069 Dresden, Germany
- ⁷⁷ Department of Physics, McGill University, Montreal QC H3A 2T8 Canada
- ⁷⁸ Joint Institute for Nuclear Research, 141980, Dubna, Russia
- ⁷⁹ Institute of Physics, Academia Sinica, Taipei 11529, Taiwan, R.O.C
- ⁸⁰ LPTHE, F-75252 Paris, France
- ⁸¹ Physikalisches Institut der Universität Bonn, 53115 Bonn, Germany
- ⁸² Max Planck Institut für extraterrestrische Physik, 85741 Garching, Germany
- ⁸³ Ghent University, Dept. of Physics and Astronomy, B-9000 Gent, Belgium
- ⁸⁴ Centre de Physique de Particules de Marseille (CPPM), Marseille, France
- ⁸⁵ Royal Holloway, University of London, Egham, TW20 0EX, UK
- ⁸⁶ School of Physics and Astronomy, Scottish Universities Physics Alliance, University of Glasgow, Glasgow G12 8QQ, Scotland, UK
- ⁸⁷ Department of Physics and Astronomy, Michigan State University, East Lansing 48824, USA

Contents

Introduction	7
<i>G. Brooijmans, B. Gripaios, F. Moortgat, J. Santiago, P. Skands</i>	
Tools	8
1 DLHA: Dark Matter Les Houches Agreement	9
<i>C. Balázs et al.</i>	
2 Further developments in the Flavour Les Houches Accord	45
<i>F. Mahmoudi, S. Heinemeyer, A. Arbey, A. Bharucha, T. Goto, U. Haisch, S. Kraml, M. Muhlleitner, J. Reuter, P. Slavich</i>	
3 Extension of the SUSY Les Houches Accord 2 for see-saw mechanisms	48
<i>L. Basso, A. Belyaev, D. Chowdhury, D.K. Ghosh, M. Hirsch, S. Khalil, S. Moretti, B. O'Leary, W. Porod, F. Staub</i>	
4 Automatic computation of supersymmetric renormalization group equations with FeynRules	72
<i>A. Alloul, N. Christensen, C. Duhr, B. Fuks, M. Rausch de Traubenberg</i>	
5 Implementation and automated validation of the minimal Z' model in FeynRules	78
<i>L. Basso, N. Christensen, C. Duhr, B. Fuks, C. Speckner</i>	
6 Implementation of scalar and vector resonances into FeynRules and LanHEP	85
<i>A. Belyaev, N. Christensen, C. Duhr, B. Fuks</i>	
7 SuSpect3	92
<i>A. Djouadi, J-L. Kneur, G. Moultaka, M. Ughetto, D. Zerwas</i>	
Higgs Boson and Top Quark Physics	96
8 Implications of new physics for Higgs searches at the LHC	97
<i>D. Albornoz Vásquez et al.</i>	
9 CMSSM mass spectrum at the LHC after the 125 GeV Higgs boson results	123
<i>M. Kadastik, K. Kannike, A. Racioppi, M. Raidal</i>	
10 Improved vacuum stability in scalar dark matter models	128
<i>M. Kadastik, K. Kannike, A. Racioppi, M. Raidal</i>	
11 Higgs boson production via new heavy vector-like top decays at the LHC	131
<i>A. Azatov, O. Bondu, A. Falkowski, M. Felcini, S. Gascon-Shotkin, D. K. Ghosh, G. Moreau, A. Y. Rodríguez-Marrero, S. Sekmen</i>	
12 Composite Higgs Models and the $t\bar{t}H$ Channel	143
<i>A. Carmona, M. Chala, J. Santiago</i>	
13 Top Polarisation in $H^{-}t$ and Wt production	148

	<i>R. M. Godbole, L. Hartgring, I. Niessen, C. D. White</i>	
14	Probing New Physics with Single Top + X	151
	<i>D. G. E. Walker, J.-H. Yu and C.-P. Yuan</i>	
15	Effective axial-vector coupling of the gluon and top-quark charge asymmetry at the LHC	163
	<i>E. Gabrielli, A. Giammanco, A. Racioppi, M. Raidal</i>	
16	Searching for sgluons in multitop production at the LHC	173
	<i>S. Calvet, B. Fuks, P. Gris, A. Renaud, L. Valéry, D. Zerwas</i>	
	Long-lived Particles	181
17	Metastable charginos and LHC searches	182
	<i>G. Polesello and T. Rizzo</i>	
18	Displaced vertex signatures at the LHC from B-L heavy neutrinos and MSSM FIMPs.	188
	<i>L. Basso, A. Belyaev, E. Dobson, M. C. Thomas, I. Tomalin, S. M. West, A. J. Williams</i>	
	Dark Matter	205
19	Impact of semi-annihilations on dark matter phenomenology – an example of Z_N symmetric scalar dark matter	206
	<i>G. Bélanger, K. Kannike, A. Pukhov, M. Raidal</i>	
	From Results to Interpretation	213
20	Searches for New Physics: Les Houches Recommendations for the Presentation of LHC Results	214
	<i>S. Kraml, B.C. Allanach, M. Mangano, H.B. Prosper, S. Sekmen et al.</i>	
21	High Energy Physics Model Database – HEPMDB: Towards decoding of the underlying theory at the LHC.	218
	<i>M. Bondarenko et al.</i>	

Introduction

G. Brooijmans, B. Gripaios, F. Moortgat, J. Santiago, P. Skands

This document is the report of the New Physics session of the 2011 Les Houches Workshop “Physics at TeV Colliders”. During the workshop, which brings together theorists and experimenters, a substantial number of ideas were discussed and for a number of these, in-depth studies were initiated. This report describes the results of those studies.

A first section presents progress specific to the software tools crucial in predicting new physics model signatures and interpreting experimental results. The first contribution builds on the “Les Houches Accords” tradition in proposing a “Dark Matter Les Houches Agreement,” a first step in standardizing the interface between different dark matter codes. Two other contributions propose further developments to the existing Flavor and SUSY Les Houches Accords. Additional contributions in the tools Section describe new additions to FEYNRULES and LANCHEP, and the development of SUSPECT3.

While (unfortunately) no new physics has been discovered yet, results from the 2010 and 2011 LHC runs have substantial implications for most models of new physics. In the first three contributions in the “Higgs Boson and Top Quark Physics” Section, the implications of the LHC results on Higgs searches in a variety of scenarios, the CMSSM mass spectrum, and dark matter are investigated. The next two contributions study Higgs boson production mechanisms in association with top quarks in different models. Two additional contributions use effective theory approaches to study LHC implications of the top quark charge asymmetry observed at the Tevatron and multi-top signatures of sgluon production. A two lasts contributions to this Section study some cases of new particles leading to single top-like signatures, and show the importance of polarization measurements in establishing discovery.

In a third Section, scenarios with long-lived particles are studied. These arise in a variety of new physics models and present special challenges and opportunities for LHC phenomenology. In a first case, particles with a lifetime sufficiently long that decays happen outside detectors are considered, with an MSSM point with a long-lived chargino as benchmark model. A second class of signatures studied involves particles that decay after travelling up to a meter away from the interaction point, in the context of scenarios with either heavy (and long-lived) neutrinos, or in supersymmetric models in which the observed cosmic dark matter abundance is “frozen in” by the late decay of long-lived Next-to-Lightest Supersymmetric Particles (NLSPs) to dark matter LSPs.

The fourth Section considers models in which the symmetry that stabilizes dark matter is Z_N , rather than the usual Z_2 , leading to a quite different phenomenology. One important new feature is the presence of dark matter semi-annihilations, in which a pair of dark matter particles interacts to produce a dark matter and a Standard Model particle, and the impact of these on dark matter phenomenology, including the freeze-out process and dark matter abundance, is studied.

An important issue with the experimental results involves how to present them, since the implications for models not considered as benchmarks by the experimental collaborations are generally non-trivial (if not impossible) to derive. The fifth Section of this report contains a first set of “recommendations for the presentation of LHC results” which emerged from extensive discussions between theorists and experimenters at the workshop and elsewhere. The recom-

mendations are split into those that are considered to be essential and those that are desiderata and it is hoped that they will stimulate further discussion, refinement, and implementation across the community. A second contribution in this Section presents HEPMDB, a storage environment for HEP models which can accommodate, via web interface to an HPC cluster, the validation of models, evaluation of LHC predictions and an event generation-simulation chain.

The meeting in Les Houches fostered a large number of discussions between theorists and experimenters, but, as mentioned above, in-depth studies could only be completed for a number of the generated ideas on the required timescale. Moreover, many of the discussions begun at the workshop continue to evolve in ‘real time’ as the LHC data stream in, making it difficult to document them in these proceedings in a way in which they may remain useful to the community in the longer term. Still, we expect that many future results will benefit from the discussions held at the workshop.

Tools

Contribution 1

DLHA: Dark Matter Les Houches Agreement

Coordinator: *Csaba Balázs,*

David G. Cerdeño, Rebecca Leane, Mitsuru Kakizaki, Sabine Kraml, Christopher Savage, Pat Scott, Sezen Sekmen,

AMIDAS: *Chung-Lin Shan,*

DarkSUSY: *Lars Bergström, Torsten Bringmann, Gintaras Duda, Joakim Edsjö, Paolo Gondolo,*

DMFIT and DMMW: *Stefano Profumo, Tesla Jeltema,*

DRAGON: *Carmelo Evoli, Daniele Gaggero, Dario Grasso, Luca Maccione,*

FeynRules: *Claude Duhr, Benjamin Fuks,*

GALPROP: *Igor Moskalenko, Elena Orlando, Troy Porter, Andrew Strong,*

ISAJET: *Howie Baer,*

micrOmegas: *Genevieve Bélanger, Fawzi Boudjema, Alexander Pukhov,*

PPPC4DMID: *Marco Cirelli, Mario Kadastik, Paolo Panci, Martti Raidal,*

SLHA: *Sven Kreiss, Frank S. Thomas,*

Semi-analytical propagation models: *Timur Delahaye, Fiorenza Donato, Julien Lavalle, David Maurin, Pierre Salati, Richard Taillet,*

SuperIso Relic: *Alexandre Arbey, Farvah Mahmoudi*

Abstract

This work presents a set of conventions and numerical structures that aim to provide a universal interface between computer programs calculating dark matter related observables. It specifies input and output parameters for the calculation of observables such as abundance, direct and various indirect detection rates. These parameters range from cosmological to astrophysical to nuclear observables. The present conventions lay the foundations for defining a future Les Houches Dark Matter Accord.

1 INTRODUCTION

Over the last decade a burst of activity has surrounded various dark matter related problems. As a byproduct of this activity, a number of robust numerical tools have been created by particle, astro-particle and astrophysicists. These tools predict values for observables that, when contrasted with observation, can shed light on the properties of dark matter. The dark matter related computer codes address a wide range of physical problems, of which the most important are:

1. deriving Feynman rules from Lagrangians,
2. calculating scattering amplitudes from Feynman rules,
3. building cross sections or decay rates from amplitudes,

4. computing dark matter abundance from cross sections or decay rates,
5. obtaining dark matter-nucleon scattering rates from cross sections,
6. evaluating cosmic ray yields based on annihilation cross sections or decay rates.

A certainly incomplete but representative list of such computer codes is:

[1] CalcHEP (2, 3)	[2] DarkSUSY (3, 4, 5, 6)	[3,4] DMFIT and DMMW (6)
[5] DRAGON (6)	[6] FeynRules (1)	[7] GALPROP (6)
[8] ISATools (4, 5)	[9] LanHEP (1)	[10] micrOmegas (2, 3, 4, 5, 6)
[11] PPPC4DMID (6)	[12] SuperIso Relic (4)	

where the numbers in parentheses after the names indicate what these codes do in the context of the task-list above. These two lists show that today there exists no code that covers all the dark matter related calculations (although some come very close), and there are significant overlaps between the capabilities of these codes. What these lists do not reveal is how general and sophisticated the various programs are. Not surprisingly, each of these tools has its strengths and weaknesses. Necessarily, all these codes contain hard-wired assumptions that potentially limit their capabilities.

When particle physicists found themselves in a similar situation regarding collider related calculations, they created a series of interfaces that allowed their various tools to communicate with each other [13–17]. These interfaces allow the users of the codes to easily and selectively exploit the features that each of the tools offers. The success of the Supersymmetric Les Houches Accord (SLHA) and the other accords lies in the fact that they significantly increase ease and flexibility for collider related calculations [15, 16].

Following the successful path of previous Les Houches accords, the Dark Matter Les Houches agreement (DLHA) proposes a format for storing and exchanging information relevant to dark matter calculations. In the spirit of the Les Houches accords, DLHA aims to interface various calculators to provide increased flexibility to users of these tools. Presently these calculators work semi-independently from each other and their consecutive use typically requires tedious interfacing. However careful this interfacing is, it may jeopardise the integrity of the tools and, in turn, the results of the calculation.

A related problem DLHA targets is the transparency of the dark matter calculations. Present codes input and output limited amounts of information while they may contain large amounts of implicit, hard-wired assumptions that affect their results. The more of this information is accessible, the more control a user has over the calculation. Additionally, making more assumptions explicit gives the user a chance to change them and this could lead to a more diverse and productive use of these codes. Since a DLHA file can be part of the input or the output of a numerical code calculating dark matter related observables, it aids in making implicit assumptions explicit and, potentially, it allows for changing some of those assumptions.

Here we give some examples of how such an agreement enables the user to easily interface various codes with different capabilities and thereby calculate quantities that none of these codes could calculate alone.

- Assume that code A has the capability to calculate decay rates of a dark matter candidate in an exotic particle model, but code A can only handle standard cosmology when calculating relic abundance of the dark matter. Assume that code B does not implement the exotic particle model of interest but can calculate relic abundance for non-standard

cosmologies. With the appropriate DLHA interface the decay rate can be communicated from code A to B and relic abundance of an exotic candidate can be calculated in a non-standard cosmology.

- Assume that code C has the capability to calculate the annihilation cross section of a dark matter candidate with next-to-leading order (NLO) corrections but it has no indirect detection routines built into it. Meanwhile code D can only do one thing, but it does it excellently: calculate indirect detection rates. An obvious task for DLHA is to pass the annihilation cross section from C to D , thereby making it possible to calculate a cosmic ray yield from annihilating dark matter with NLO corrections.

These examples are just a limited sample of the possibilities that DLHA offers for a resourceful user.

2 CALCULATION OF DARK MATTER RELATED OBSERVABLES

This section summarizes the relevant details of dark matter related calculations so that we can fix our notation and define the accord in the next section.

2.1 Relic abundance

Numerous microscopic models have been proposed to describe the identity of dark matter particles. Depending on the details of these models, and conditions in the early Universe, dark matter may have been produced in various different ways. For simplicity, here we only address the thermal production mechanism of weakly interacting massive particles.

2.1.1 Thermal relic abundance with standard cosmological assumptions

In this section we recapture some details of the calculation of thermally produced relic abundance of dark matter following standard cosmological assumptions. According to Big Bang cosmology the Universe cooled from temperatures substantially higher than the mass of a typical dark matter particle. At those temperatures dark matter particles were in chemical equilibrium with their environment and consequently their (co-moving) number density was unchanged. At temperatures comparable to the typical weakly interacting dark matter particle, at $T = \mathcal{O}(100 \text{ GeV}/k_B)$, the Universe was radiation dominated. (Here k_B is the Boltzmann constant.) As the Universe cooled and expanded further, dark matter particles came in thermal equilibrium with the cooling radiation and consequently their number density decreased exponentially. Later scattering between dark matter particles became rare until the scattering rate fell below the expansion rate of the Universe for the dark matter particles to stay in equilibrium. At that stage dark matter particles froze-out, that is their (co-moving) number density ceased to change.

The change of the average number density of dark matter particles, n_χ , is described by Boltzmann's equation [18–22]. This change occurs due to (co-)annihilation to Standard Model particles and to the expansion of the early Universe. Boltzmann's equation reads:

$$\frac{dn_\chi}{dt} = -\langle\sigma v\rangle (n_\chi^2 - n_{\chi,eq}^2) - 3Hn_\chi. \quad (1)$$

On the right hand side the thermally averaged product of the annihilation cross section and relative velocity of the two annihilating dark matter particles is defined by

$$\langle\sigma v\rangle = \frac{\int \sigma v dn_{1,eq} dn_{2,eq}}{\int dn_{1,eq} dn_{2,eq}} = \frac{\int \sigma v f(E_1) f(E_2) d^3 p_1 d^3 p_2}{\int f(E_1) f(E_2) d^3 p_1 d^3 p_2}. \quad (2)$$

Here p_i are the three-momenta and $E_i = \sqrt{m_i^2 + p_i^2}$ are the energies of the colliding particles with $i = 1, 2$ ¹. The total (co-)annihilation cross section σ depends on the microscopic properties of the dark matter particles and can be calculated assuming a particular dark matter model. The equilibrium number density is given by thermodynamics

$$n_{\chi,eq} = \frac{g_\chi}{(2\pi)^3} \int f(E) d^3 E, \quad (3)$$

where g_χ is the number of internal degrees of freedom of dark matter particles. Their energy distribution is the familiar

$$f(E) = \frac{1}{\exp(E/k_B T) \pm 1}. \quad (4)$$

In Eq. (1) the Hubble parameter describes the expansion rate, and in a nearly flat Friedmann-Lemaitre-Robertson-Walker (FLRW) Universe it is given by

$$H^2 = \frac{8\pi G_N}{3} \rho. \quad (5)$$

As the Universe was radiation dominated, the total energy density was the standard function of the temperature of the radiation T :

$$\rho = \rho_{rad}(T) = g_{eff}(T) \frac{\pi^2}{30} T^4, \quad (6)$$

where $g_{eff}(T)$ is the number of internal degrees of freedom of the (effectively) massless particles in the thermal bath².

The decrease in number density due to expansion of the Universe can be made implicit by rewriting Eq. (1) in terms of the co-moving number density

$$Y = \frac{n_\chi}{s}. \quad (7)$$

For the radiation dominated Universe the total entropy density is

$$s = s_{rad}(T) = h_{eff}(T) \frac{2\pi^2}{45} T^3. \quad (8)$$

The number of internal degrees of freedom of the particles contributing to the entropy is $h_{eff}(T)$ ³. Recasting Boltzmann's equation for Y as a function of $x = m_\chi/T$, where m_χ is the mass of the dark matter particle, we arrive at

$$\frac{dY}{dx} = \frac{1}{3H} \frac{ds}{dx} \langle \sigma v \rangle (Y^2 - Y_{eq}^2). \quad (9)$$

By utilising Eqs. (5), (6) and (8) this may also be written as

$$\frac{dY}{dx} = -\sqrt{\frac{\pi g_\star}{45 G_N}} \frac{m_\chi}{x^2} \langle \sigma v \rangle (Y^2 - Y_{eq}^2). \quad (10)$$

¹Throughout this section we use natural units with $c = \hbar = 1$, unless stated otherwise.

²Here we assume that the various species contributing to the total energy density are all in thermal equilibrium with each other at a common temperature T .

³For a relativistic particle with one internal degree of freedom, such as a spin zero boson, $g_{eff} = h_{eff} = 1$.

The parameter g_* incorporates the degrees of freedom arising from the energy and entropy densities

$$g_*^{1/2} = \frac{h_{eff}}{g_{eff}^{1/2}} \left(1 + \frac{1}{3} \frac{T}{h_{eff}} \frac{dh_{eff}}{dT} \right). \quad (11)$$

A value for Y_{eq} of a cold gas of dark matter is obtained for (non-)relativistic dark matter particles by taking the (low) high energy limit of the Maxwell-Boltzmann distribution. For non-relativistic dark matter particles

$$Y_{eq} = \frac{45g_{eff}}{4\pi^4} \frac{x^2 K_2(x)}{h_{eff}(m_\chi/x)}, \quad (12)$$

where $K_2(x)$ is the modified Bessel function of second order.

In various calculations it can be useful to introduce the freeze-out temperature T_f based on the condition

$$Y - Y_{eq} = \alpha Y_{eq}, \quad (13)$$

where $\alpha > 0$ is a number of order 1. Incorporating this condition into Eq. (10) a statement for freeze-out is obtained

$$\sqrt{\frac{\pi g_*}{45 G_N}} \frac{m_\chi}{x^2} \langle \sigma v \rangle \alpha (\alpha + 2) Y_{eq} = - \frac{d(\ln Y_{eq})}{dx}. \quad (14)$$

Upon substitution of Eq. (12) into Eq. (14) this allows for a numerical solution for $x = x_f$.

Equipped with the co-moving number density after freeze-out, Y_0 , the relic energy density of dark matter may be calculated. This is typically given in units of the critical energy density

$$\Omega_\chi = \frac{\rho_\chi}{\rho_c} = \frac{s_0 Y_0 m_\chi}{\rho_c}, \quad (15)$$

where ρ_c is the energy density of a flat FLRW Universe. Here s_0 is the current entropy density of the Universe. Combining Eqs. (5) and (15), the relic density may also be expressed as

$$\Omega_\chi h^2 = \frac{8\pi G_N}{3} s_0 Y_0 m_\chi \times 10^{-4} (\text{s Mpc/km})^2. \quad (16)$$

The present day normalized Hubble expansion rate h is determined via

$$H_0 = 100 h \text{ km}/(\text{s Mpc}). \quad (17)$$

2.1.2 Thermal relic abundance with non-standard cosmological assumptions

In this section, we consider the generic scenario described in Refs. [23, 24] and implemented in SuperIso Relic [12, 25] and AlterBBN [26]. In this scenario the total energy density and entropy density of the Universe are modified:

$$\rho = \rho_{rad} + \rho_D, \quad s = s_{rad} + s_D. \quad (18)$$

The temperature dependence of the additional components ρ_D and s_D can be parametrized as

$$\alpha_D(T) = \kappa_\alpha \alpha_{rad}(T_{BBN}) \left(\frac{T}{T_{BBN}} \right)^{n_\alpha}, \quad (19)$$

where $\alpha = \rho$ or s ,

$$\kappa_\alpha = \frac{\alpha_{dark}(T_{BBN})}{\alpha_{rad}(T_{BBN})}, \quad (20)$$

and T_{BBN} is the Big Bang Nucleosynthesis temperature.

The time evolution of the total entropy density is given by

$$\frac{ds}{dt} = -3Hs + \Sigma_D, \quad (21)$$

where Σ_D describes the entropy production of the additional component. Instead of parametrizing the entropy density s_D , it is sometimes better (for example for reheating models) to write Σ_D in the form of Eq. (19) with $\alpha = \Sigma$, and it is then related to the entropy density by

$$\Sigma_D = T^2 \sqrt{\frac{4\pi^3 G}{5} \left(1 + \frac{\rho_D}{\rho_{rad}}\right)} \left(s_D g_{eff}^{1/2} - \frac{1}{3} \frac{h_{eff}}{g_*^{1/2}} T \frac{ds_D}{dT} \right). \quad (22)$$

A possible generalization of the above parameterizations consists of relaxing Eq. (19) and letting ρ_D , s_D , Σ_D and/or H be general functions of the temperature.

Introducing the co-moving number density $Y = n_\chi/s$, Eq. (1) becomes

$$\frac{dY}{dx} = -\sqrt{\frac{\pi g_*}{45}} \frac{m_\chi}{x^2} \left(\frac{1 + s_D/s_{rad}}{\sqrt{1 + \rho_D/\rho_{rad}}} \right) \left(\langle \sigma v \rangle (Y^2 - Y_{eq}^2) + \frac{Y \Sigma_D}{s_{rad}^2 (1 + s_D/s_{rad})^2} \right), \quad (23)$$

where

$$Y_{eq} = \frac{45 g_{eff}}{4\pi^4} \frac{1}{1 + s_D/s_{rad}} \frac{x^2 K_2(x)}{h_{eff}(m_\chi/x)}. \quad (24)$$

The relic abundance can then be calculated based on Eq. (16).

2.2 Direct detection

If dark matter and Standard Model particles interact with strength comparable to that of the electroweak interactions, and if dark matter is massive and fast enough, then it may be detected by observing dark matter scattering on atoms. This is the aim of the direct dark matter detection experiments. To assess detection rates we calculate elastic scattering cross sections of dark matter on nuclei. These cross sections are derived from a Lagrangian describing the effective interaction of dark matter with nuclei. Nuclear form factors provide a link between the partons, the nucleons and the nucleus of the target species. For simplicity, in this first agreement, we only consider elastic dark matter-nucleus scattering. Inelastic scattering may be included in a future edition of this agreement.

The dark matter-nucleus recoil rate per unit detector mass, unit time, and unit recoil energy E is written in the form

$$\frac{dR}{dE} = \frac{\sigma_A(E)}{2m_\chi \mu_A^2} \rho_\chi \eta(E, t), \quad (25)$$

where

$$\mu_A = \frac{m_\chi m_A}{m_\chi + m_A} \quad (26)$$

is the dark matter-nucleus reduced mass with m_A the nucleus mass, $\sigma_A(E)$ is the dark matter-nucleus scattering cross section, ρ_χ is the local dark matter density, and

$$\eta(E, t) = \int_{|\mathbf{v}| > v_{\min}(E)} \frac{f(\mathbf{v}, t)}{|\mathbf{v}|} d^3v \quad (27)$$

is an average inverse dark matter speed, also called the velocity integral. Here $f(\mathbf{v}, t)$ is the dark matter velocity distribution in the reference frame of the detector, which is expected to be time dependent, and

$$v_{\min}(E) = \sqrt{\frac{m_A E}{2\mu_A^2}} \quad (28)$$

is the minimum dark matter speed that can impart a recoil energy E to the nucleus. Notice that the dark matter-nucleus differential cross section in recoil energy E for a dark matter particle of initial velocity v with respect to the nucleus has the expression

$$\frac{d\sigma_A}{dE} = \frac{\sigma_A(E)}{E_{\max}(v)} \Theta(E_{\max}(v) - E), \quad (29)$$

where

$$E_{\max}(v) = \frac{2\mu_A^2 v^2}{m_A} \quad (30)$$

is the maximum recoil energy that a particle of velocity v can impart to the nucleus.

Only the non-relativistic limit is relevant for dark matter-nucleus scattering. In this limit, only two kinds of nucleon currents survive: the spin-independent current $\psi^\dagger \psi$ and the spin-dependent current $\psi^\dagger \mathbf{S} \psi$. Here ψ is the nucleon wave function (a non-relativistic two-component Pauli spinor) and $\mathbf{S} = \frac{1}{2} \boldsymbol{\sigma}$ is the nucleon spin operator. Therefore one splits the differential dark matter-nucleus scattering cross section $\sigma_A(E)$ into its spin-independent (SI) and spin-dependent (SD) contributions,

$$\sigma_A(E) = \sigma_A^{SI}(E) + \sigma_A^{SD}(E). \quad (31)$$

Correspondingly, one often separates the spin-independent and spin-dependent contributions to the recoil rate dR/dE as

$$\frac{dR}{dE} = \left(\frac{dR}{dE} \right)^{SI} + \left(\frac{dR}{dE} \right)^{SD}. \quad (32)$$

The spin-independent part $\sigma_A^{SI}(E)$ is written as

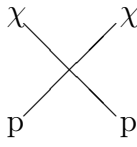
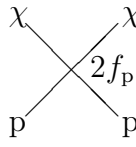
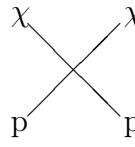
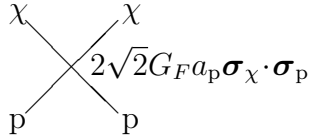
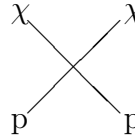
$$\sigma_A^{SI}(E) = \frac{4\mu_A^2}{\pi} \left| Z f_p F_p^{(Z,A)}(E) + (A - Z) f_n F_n^{(Z,A)}(E) \right|^2, \quad (33)$$

where Z is the number of protons in the nucleus (atomic number), A is the mass number of the nucleus, $F_p^{(Z,A)}(E)$ and $F_n^{(Z,A)}(E)$ are proton and nucleon number density form factors for the nucleus (Z, A) , normalized to $F_p^{(Z,A)}(0) = F_n^{(Z,A)}(0) = 1$, and finally $2f_p$ and $2f_n$ are the dimensionless four-particle vertices for the SI dark matter-proton and dark matter-neutron interactions, respectively.

One also introduces the pointlike dark matter-proton and dark matter-neutron cross sections, which by convention are used when reporting or interpreting experimental results,

$$\sigma_p^{SI} = \frac{4\mu_p^2}{\pi} |f_p|^2, \quad \sigma_n^{SI} = \frac{4\mu_n^2}{\pi} |f_n|^2. \quad (34)$$

Table 1: Four-particle effective vertices for dark matter-proton elastic scattering. Dark matter-neutron vertices are obtained by changing $p \rightarrow n$. s_χ is the spin of the dark matter particle.

	$s_\chi = 0$	$s_\chi = \frac{1}{2}$	$s_\chi = 1$
spin-independent			
spin-dependent	N/A		

Here μ_p and μ_n are the reduced dark matter-proton and dark matter-neutron masses.

One often assumes, and we will do so in this first agreement, that

$$F_p^{(Z,A)}(E) = F_n^{(Z,A)}(E) \equiv F_A(E). \quad (35)$$

In this case, one sometimes introduces the pointlike dark matter-nucleus cross section

$$\sigma_{A,0}^{SI} = \frac{4\mu_A^2}{\pi} \left| Z f_p + (A - Z) f_n \right|^2, \quad (36)$$

which is σ_A^{SI} with $F_p^{(Z,A)}(E) = F_n^{(Z,A)}(E) = 1$.

The spin-dependent part $\sigma_A^{SD}(E)$ is written as

$$\sigma_{(Z,A)}^{SD}(E) = \frac{32\mu_A^2 G_F^2}{(2J_A + 1)} \left[a_p^2 S_{pp}^{(Z,A)}(E) + a_n^2 S_{nn}^{(Z,A)}(E) + a_p a_n S_{pn}^{(Z,A)}(E) \right]. \quad (37)$$

Here $G_F = 1.16637 \times 10^{-5} (\hbar c)^3/\text{GeV}^2$ is the Fermi coupling constant, J_A is the nucleus total angular momentum in units of \hbar , and finally $2\sqrt{2} G_F a_p$ and $2\sqrt{2} G_F a_n$ are the effective four-particle vertices for the SD interaction of DM particles with protons and neutrons.

In Eq. (37), the dimensionless functions $S_{pp}^{(Z,A)}(E)$, $S_{nn}^{(Z,A)}(E)$, and $S_{pn}^{(Z,A)}(E)$ are the proton-proton, neutron-neutron, and proton-neutron nuclear spin structure functions. They can be written in terms of isoscalar and isovector spin structure functions $S_{00}^{(Z,A)}$, $S_{11}^{(Z,A)}$, $S_{01}^{(Z,A)}$ as

$$S_{pp}^{(Z,A)} = S_{00}^{(Z,A)} + S_{11}^{(Z,A)} + S_{01}^{(Z,A)}, \quad (38)$$

$$S_{nn}^{(Z,A)} = S_{00}^{(Z,A)} + S_{11}^{(Z,A)} - S_{01}^{(Z,A)}, \quad (39)$$

$$S_{pn}^{(Z,A)} = 2(S_{00}^{(Z,A)} - S_{11}^{(Z,A)}). \quad (40)$$

One similarly introduces

$$a_0 = a_p + a_n, \quad a_1 = a_p - a_n. \quad (41)$$

When the nuclear spin is approximated by the spin of the odd nucleon only, one finds

$$S_{pp}^{(Z,A)} = \frac{\lambda_A^2 J_A (J_A + 1) (2J_A + 1)}{\pi}, \quad S_{nn}^{(Z,A)} = 0, \quad S_{pn}^{(Z,A)} = 0, \quad (42)$$

Table 2: Even and odd operators $\mathcal{L}_{e,o}^{SI,SD}(s)$ for dark matter interactions with standard quarks q . A scalar field only interacts in a spin independent manner [27].

	s	Even operators ($i = e$)	Odd operators ($i = o$)
Spin independent (SI)	0	$2M_\chi \chi \chi^\dagger \bar{q} q$	$i(\partial_\mu \chi \chi^\dagger - \chi \partial_\mu \chi^\dagger) \bar{q} \gamma^\mu q$
	1/2	$\bar{\chi} \chi \bar{q} q$	$\bar{\chi} \gamma_\mu \chi \bar{q} \gamma^\mu q$
	1	$2M_\chi \chi_\mu \chi^\mu \bar{q} q$	$i(\chi^{\dagger\alpha} \partial_\mu \chi_\alpha - \chi^\alpha \partial_\mu \chi_\alpha^\dagger) \bar{q} \gamma_\mu q$
Spin dependent (SD)	1/2	$\bar{\chi} \gamma_5 \gamma_\mu \chi \bar{q} \gamma_5 \gamma^\mu q$	$-\frac{1}{2} \bar{\chi} \sigma_{\mu\nu} \chi \bar{q} \sigma^{\mu\nu} q$
	1	$\sqrt{6}(\partial_\mu \chi^{\dagger\beta} \chi_\beta - \chi_\beta^\dagger \partial_\mu \chi_\beta) \epsilon^{\alpha\beta\gamma\mu} \bar{q} \gamma_5 \gamma_\mu q$	$\frac{\sqrt{3}}{2} i(\chi_\mu \chi_\nu^\dagger - \chi_\mu^\dagger \chi_\nu) \bar{q} \sigma^{\mu\nu} q$

for a proton-odd nucleus, and

$$S_{pp}^{(Z,A)} = 0, \quad S_{nn}^A = \frac{\lambda_A^2 J_A(J_A + 1)(2J_A + 1)}{\pi}, \quad S_{pn}^{(Z,A)} = 0, \quad (43)$$

for a neutron-odd nucleus. Here λ_A is conventionally defined through the relation $\langle \psi_A | \mathbf{S}_A | \psi_A \rangle = \lambda_A \langle \psi_A | \mathbf{J}_A | \psi_A \rangle$, where $|\psi_A\rangle$ is the nuclear state, \mathbf{S}_A is the nucleus spin vector, and \mathbf{J}_A is its total angular momentum vector.

One sometimes introduces dark matter-nucleon pointlike cross sections. For a single proton or a single neutron, $\lambda_p = \lambda_n = 1$, $J_p = J_n = \frac{1}{2}$, and

$$\sigma_p^{SD} = \frac{36\mu_p^2 G_F^2}{\pi^2} |a_p|^2, \quad \sigma_n^{SD} = \frac{36\mu_n^2 G_F^2}{\pi^2} |a_n|^2. \quad (44)$$

We may list the expressions of the effective four-particle dark matter-nucleon couplings f_p , f_n , a_p and a_n in terms of elementary couplings to quarks and gluons for various kinds of dark matter particles, via an effective four-particle lagrangian with spin s

$$\mathcal{L}_{eff}(s) = \frac{1}{2} \left(\sum_{i=e,o} f_{N,i}(s) \mathcal{L}_{N,i}^{SI}(s) + \sum_{i=e,o} a_{N,i}(s) \mathcal{L}_{N,i}^{SD}(s) \right). \quad (45)$$

The operators $\mathcal{L}_e^{SI}(s)$ and $\mathcal{L}_o^{SI}(s)$ describe spin independent even and odd interactions, while $\mathcal{L}_e^{SD}(s)$ and $\mathcal{L}_o^{SD}(s)$ are their spin dependent counterparts.⁴ Table 2 shows the explicit forms of these operators for various values of s . The dark matter-nucleon couplings can be obtained as

$$f_N = \sum_{i=e,o} f_{N,i}(s), \quad a_N = \sum_{i=e,o} a_{N,i}(s), \quad (46)$$

Dark matter-nucleus scattering amplitudes can be calculated based on parton level amplitudes after relating nuclear couplings to dark-matter quark couplings via nucleon form factors

$$2f_{N,e} = \sum_q \frac{m_p}{m_q} f_q^N s_{q,e}, \quad 2f_{N,o} = \sum_q \frac{m_p}{m_q} f_{V_q}^N s_{q,o}, \quad (47)$$

⁴Even and odd couplings are introduced to trace symmetries under particle-antiparticle interchange. Majorana fermions, for example, have even couplings and non-Majorana fermions have odd couplings.

$$2\sqrt{2}G_F a_{N,e} = \sum_q \Delta_q^N a_{q,e}, \quad 2\sqrt{2}G_F a_{N,o} = \sum_q \delta_q^N a_{q,o}. \quad (48)$$

These form factors capture the distribution of quarks within the nucleons. The light quark flavor scalar form factors are related to the pion-nucleon sigma term and the nucleon and quark masses as

$$f_u^{p,n} = \frac{m_u}{m_d} \alpha^{+1,-1} f_d^{p,n}, \quad f_d^{p,n} = \frac{2\sigma_{\pi N}}{(1 + \frac{m_u}{m_d})m_{p,n}} \frac{\alpha^{0,1}}{1 + \alpha}, \quad f_s^{p,n} = \frac{\sigma_{\pi N} y}{(1 + \frac{m_u}{m_d})m_{p,n}} \frac{m_s}{m_d}. \quad (49)$$

Here $\alpha = B_u/B_d$, $\sigma_{\pi N} = (m_u + m_d)(B_u + B_d)/2$, $y = 2B_s/(B_u + B_d)$ and $B_q = \langle N|\bar{q}q|N\rangle$. The heavy flavor scalar form factors are typically calculated as

$$f_Q^N = \frac{2}{27} \left(1 - \sum_{q=u,d,s} f_q^N \right). \quad (50)$$

2.3 Indirect detection

Perhaps the most challenging way to discover dark matter is to detect its annihilation or decay products in the astrophysical environment. This is called indirect detection and involves the description of an initial (source) distribution of standard particles originating from dense dark matter concentrations. After the source properties are fixed, the propagation of the secondary particles has to be followed through. Here we review only the simplest cases: electron, positron, antiproton or photon production via dark matter annihilation and their subsequent propagation to us through our Galaxy using a simplified but effective treatment. We also comment on the modifications which would need to be introduced for a more detailed treatment.

Charged cosmic ray propagation through the Galaxy can be usually described by the diffusion-convection model [28]. This model assumes homogeneous propagation of charged particles within a certain diffusive region (similar to one of the simplest models of propagation called the leaky box model), but it also takes into account cooling (energy loss) effects. The diffusive region is usually assumed to have the shape of a solid flat cylinder of half-height L and radius R that sandwiches the Galactic plane: inside it, charged cosmic rays are trapped by magnetic fields; outside, they are free to stream away. The (cylindrical) coordinates of the solar system correspond to $\vec{r}_\odot = (8.33 \text{ kpc}, 0 \text{ kpc})$ [29]. The phase-space density $\psi_a(\vec{r}, p, t)$ of a particular cosmic ray species a at an instant t , at a Galactic position \vec{r} and with momentum p can be calculated by solving the cosmic ray transport equation, which has the general form [30]

$$\begin{aligned} \frac{\partial \psi_a(\vec{r}, p, t)}{\partial t} &= Q_a(\vec{r}, p, t) + \nabla \cdot (D_{xx} \nabla \psi_a - \vec{V} \psi_a) \\ &+ \frac{\partial}{\partial p} \left(p^2 D_{pp} \frac{\partial}{\partial p} \frac{1}{p^2} \psi_a \right) - \frac{\partial}{\partial p} \left(\dot{p} \psi_a - \frac{p}{3} (\nabla \cdot \vec{V}) \psi_a \right) - \frac{1}{\tau_f} \psi_a - \frac{1}{\tau_r} \psi_a \end{aligned} \quad (51)$$

Usually one assumes that steady state conditions hold, as they do if the typical time scales of the dark matter galactic collapse and of the variation of propagation conditions are much longer than the time scale of propagation itself (which is of the order of 1 Myr at 100 GeV energies). In this case, the l.h.s. can be equated to zero and the dependence on time is dropped for all quantities.

We concentrate on a version of the propagation equation which is sufficient to describe in first approximation the electron or positron and proton or antiproton flux through the Galaxy:

$$0 = Q_a(\vec{r}, E) + K(E) \nabla^2 \psi_a + \frac{\partial}{\partial E} \left(b(E) \psi_a - K_{EE}(E) \psi_a \right) - \frac{\partial}{\partial z} (\text{sign}(z) V_C \psi_a), \quad (52)$$

where now E is the energy of the secondary particle species a . Boundary conditions are imposed such that the CR density vanishes on the outer surface of the cylinder, outside of which the particles are supposed to freely propagate and escape, consistently with the physical picture described above. At $r = 0$, one imposes a symmetric condition $\partial\psi_a/\partial r(r = 0) = 0$. In momentum space one imposes null boundary conditions. The terms containing the spatial diffusion coefficient $K(E)$, the energy loss rate $b(E)$ and the diffusive reacceleration coefficient $K_{\text{EE}}(E)$ describe respectively the transport of cosmic ray species through turbulent magnetic fields, their cooling due to different phenomena (such as Inverse Compton scattering (ICS), synchrotron radiation, Coulomb scattering or bremsstrahlung) and their reacceleration due to hits on moving magnetized scattering targets in the Galaxy. The term with the convective velocity V_C describes the characteristics of the Galactic winds emanating vertically from the stars in the disk. A source term resulting from dark matter annihilation can be written as

$$Q_a(\vec{r}, E) = \frac{1}{2} \frac{dN_a}{dE} \langle \sigma_a v \rangle_0 \left(\frac{\rho_g(\vec{r})}{m_\chi} \right)^2. \quad (53)$$

Here $\langle \sigma_a v \rangle_0$ is the value of the thermally averaged annihilation cross section into the relevant species, and $\rho_g(r)$ is the dark matter energy density in the Galaxy. The energy distribution of the secondary particle a is dN_a/dE , normalized per annihilation. This formula applies to self-conjugated annihilating dark matter. In the case of non-self-conjugated dark matter, or of multicomponent dark matter, the quantities in Eq. (53) should be replaced as follows, where an index i denotes a charge state and/or particle species (indeed any particle property, collectively called "component") and $f_i = n_i/n$ is the number fraction of the i -th component:

$$\begin{aligned} m_\chi &\rightarrow \sum_i f_i m_i && \text{(mean mass),} \\ \langle \sigma_a v \rangle &\rightarrow \sum_{ij} f_i f_j \langle \sigma_{a,ij} v_{ij} \rangle && \text{(mean cross section times relative velocity),} \\ dN_a/dE &\rightarrow \frac{\sum_{ij} f_i f_j \sigma_{a,ij} v_{ij} (dN_{a,ij}/dE)}{\sum_{ij} f_i f_j \sigma_{a,ij} v_{ij}} && \text{(annihilation spectrum per annihilation).} \end{aligned} \quad (54)$$

The spatial diffusion coefficient $K(E)$ is generally taken to have the form

$$K(E) = K_0 v^\eta \left(\frac{R}{\text{GeV}} \right)^\delta, \quad (55)$$

where v is the speed (in units of c) and $R = p/eZ$ is the magnetic rigidity of the cosmic ray particles. Here Z is the effective nuclear charge of the particle and e is the absolute value of its electric charge (of course the quantities are different from 1 only in the case in which particles other than electrons, positrons, protons or antiprotons are considered). The parameter η controls the behavior of diffusion at low energy: recently, in departure from the traditional choice $\eta = 1$, other values (possibly negative) have been advocated. In more detailed treatments, the diffusion coefficient can be considered as space dependent ($K(\vec{r}, E)$) and a possible dependence on the particle direction of motion, leading to anisotropic diffusion, can be introduced.

The energy loss rate can be parametrized as

$$b(E) = b_0 E^2. \quad (56)$$

This form holds as long as one neglects the fact that energy losses are position dependent in the Galactic halo (e.g. synchrotron radiation depends on the intensity of the magnetic field, which varies in the Galaxy, and ICS depends on the density of the background light distribution, which also varies in the Galaxy), and as long as one assumes that all energy loss phenomena are proportional to E^2 (which is true only if one neglects Coulomb losses and bremsstrahlung and one considers ICS only in the Thomson scattering regime, i.e. at relatively low electron or positron energy). In a more detailed treatment, the energy loss rate can also be considered as space dependent, $b(\vec{r}, E)$, and with a more general dependence on the energy. Coulomb losses ($dE/dt \sim \text{const}$) and bremsstrahlung losses ($dE/dt \sim bE$) can also be taken into account. Some codes compute these using detailed formulae as a function of position and energy, based on the gas, interstellar radiation and magnetic field distributions [7]. The ultimate form of the energy loss rate may be a complex function which, as will be described below, can be given under FUNCTION EnerLoss.

Finally, the diffusive reacceleration coefficient $K_{\text{EE}}(E)$ is usually parameterized as

$$K_{\text{EE}}(E) = \frac{2}{9} v_A^2 \frac{v^4 E^2}{K(E)}, \quad (57)$$

where v_A is the Alfvén speed.

A propagator, or Green's function G , is used to evolve the flux which originate from the source Q at \vec{r}_S with energy E_S through the diffusive halo, to reach the Earth at point \vec{r} with energy E . This allows the general solution for Eq. (52) to be written as

$$\psi_a(\vec{r}, E) = \int_E^{m_\chi} dE_S \int d^3r_S G(\vec{r}, E; \vec{r}_S, E_S) Q_a(\vec{r}_S, E_S). \quad (58)$$

The differential flux is related to the solution in Eq. (58) via

$$\frac{d\Phi_a}{dE} = \frac{v(E)}{4\pi} \psi_a(\vec{r}, E). \quad (59)$$

For proton or antiproton propagation in the Galactic halo, additional terms in Eq. (52) should be introduced to account for spallations on the gas in the disk.

We next turn to photons. In this case, propagation is much simpler since no scattering processes take place. This leads to a straight line propagation without any energy loss, which, in the formalism above, corresponds to a trivial propagator. Thus, for photons $a = \gamma$, by utilising Eqs. (53) and (58), Eq. (59) can be approximated with

$$\frac{d\Phi_\gamma}{dE}(\phi) = \langle \sigma_\gamma v \rangle_0 \frac{dN_\gamma}{dE} \frac{1}{8\pi m_\chi^2} \int_0^\infty \rho_g^2(r(s, \phi)) ds. \quad (60)$$

Here the square of the Galactic dark matter density profile ρ_g^2 is integrated over the line of sight, parameterized by the coordinate s . The angle ϕ is the aperture between the direction of the line of sight and the axis connecting the Earth to the Galactic Center. Explicitly, the coordinate r , centered on the Galactic Center, reads

$$r(s, \phi) = (r_\odot^2 + s^2 - 2r_\odot s \cos \phi)^{1/2}. \quad (61)$$

As for Eq. (53), Eq. (60) applies to self-conjugated annihilating dark matter. If dark matter is not composed of self-conjugated particles, and n indicates the number density of particles and

\bar{n} the number density of antiparticles, the factor $n^2/2$ in the formula above has to be replaced by $n\bar{n}$.

This formula will depend very sensitively on the direction, especially near the galactic center. However, a given gamma-ray instrument will only measure an averaged value, smeared over the angular resolution. Therefore, a more useful quantity to compute is that average value in the direction given by ϕ [31],

$$\frac{d\Phi_\gamma}{dE}(\phi; \Delta\Omega) = \int d\Omega' \frac{d\Phi_\gamma}{dE}(\varphi', \theta') R_{\Delta\Omega}(\theta'), \quad (62)$$

where

$$R_{\Delta\Omega}(\theta') = \frac{1}{2\pi\theta_r^2} \exp\left(\frac{-\theta'^2}{2\theta_r^2}\right), \quad (63)$$

describes the angular resolution θ_r with $d\Omega' = d\varphi' d\cos\theta'$. Here ϕ' and θ' are polar coordinates centered on the direction ϕ , and $\Delta\Omega = \pi\theta_r^2$ (for small θ_r). For the different, slightly varying lines of sight entering the integral, $\cos\phi$ in Eq. (61) is replaced by $\cos\psi = \cos\phi\cos\theta' - \cos\varphi'\sin\phi\sin\theta'$.

2.3.1 Dark matter substructures

If dark matter particles are packed inside dense clumps, their annihilations are enhanced, and so are their indirect signatures at the Earth. The boost factor by which the yield of a smooth dark matter halo has to be multiplied depends in a simple, but not obvious, way on the spatial distribution of the clumps and on their inner structure. A population \mathcal{P} of substructures i generates at the Earth the cosmic ray density

$$\psi_a^{sub}(\vec{r}, E) = \left(\mathcal{S} \equiv \frac{1}{2} \langle \sigma_a v \rangle_0 \left(\frac{\rho_\odot}{m_\chi} \right)^2 \right) \sum_{i \in \mathcal{P}} \tilde{G}_i \xi_i, \quad (64)$$

where the effective propagator \tilde{G}_i , defined as

$$\tilde{G}_i = \int_E^{m_\chi} dE_S G(\vec{r}, E; \vec{r}_i, E_S) \frac{dN_a}{dE}, \quad (65)$$

takes into account the propagation from clump i located at \vec{r}_i , and the injection spectrum at the source. The annihilation volume ξ_i would be the volume of clump i should its density be equal to the Milky Way dark matter density ρ_\odot at the Sun. It is defined as the integral over the volume of the i -th clump

$$\xi_i = \int_{\text{clump } i} d^3r_S \left(\frac{\rho_{\text{DM}}(\vec{r}_S)}{\rho_\odot} \right)^2. \quad (66)$$

Because we have no idea of the actual population of dark matter substructures inside which we are embedded, a statistical analysis needs to be performed on the ensemble of all possible realizations of galactic clump distributions. A population of \mathcal{N}_H substructures inside the Milky Way dark matter halo yields, on average, the cosmic ray density [32–34]

$$\langle \psi_a^{sub}(\vec{r}, E) \rangle = \mathcal{N}_H \mathcal{S} \int d^3r_S \int d\xi \mathcal{D}(\vec{r}_S, \xi) \tilde{G}(\vec{r}, E; \vec{r}_S) \xi. \quad (67)$$

The probability to find a dark matter clump at location \vec{r}_S with annihilation volume ξ is denoted by $\mathcal{D}(\vec{r}_S, \xi)$. The variance associated to the average substructure signal $\langle \psi_a^{sub}(\vec{r}, E) \rangle$ can be expressed as

$$\sigma_\psi^2(\vec{r}, E) = \mathcal{N}_H \mathcal{S}^2 \int d^3 r_S \int d\xi \mathcal{D}(\vec{r}_S, \xi) \tilde{G}^2(\vec{r}, E; \vec{r}_S) \xi^2 - \frac{\langle \psi_a^{sub}(\vec{r}, E) \rangle^2}{\mathcal{N}_H}. \quad (68)$$

3 DESCRIPTION OF THE DLHA BLOCKS AND FUNCTIONS

Information in a DLHA file is organized into blocks. The general properties of the DLHA blocks follow those of the Supersymmetry Les Houches Accord (SLHA) [15]. Similarly to SLHA, the entries within the blocks are identified by the first numerical value(s) within the block. This feature allows for a flexible order of entries within a block. Most block entries are optional and can be omitted at writing. A missing entry typically signals the lack of a calculation within the program that wrote the block.

A DLHA file may contain the following blocks or statements (listed here alphabetically):

```

BLOCK ABUNDANCE
BLOCK ANNIHILATION
BLOCK ASTROPROPAG
BLOCK COSMOLOGY
BLOCK DETECTOR_NUCLEI
BLOCK DMCLUMPS
BLOCK DMSPADIST
BLOCK DMVELDIST
BLOCK DOFREEDOM
BLOCK EFFCOUPLING
BLOCK FORMFACTS
BLOCK INDIRDETSPECTRUM
BLOCK MASS
BLOCK NDMCROSSSECT
BLOCK QNUMBERS
BLOCK STRUCTFUN

```

Blocks ASTROPROPAG, COSMOLOGY, DETECTOR_NUCLEI, DMCLUMPS, DMSPADIST, DMVELDIST, DOFREEDOM, FORMFACTS and STRUCTFUN depend on the cosmological, astrophysical, standard particle and nuclear physics assumptions but are kept independent from the microscopic properties of dark matter. The rest of the blocks depend on the microscopic physics describing dark matter. A given dark matter candidate is identified in the block MASS by the PDG number and mass of the particle. If the PDG code of a particle does not exist then an arbitrary code identifying the candidate can be supplied. Further microscopic properties of the dark matter candidate are given in block QNUMBERS.

For dark matter models containing multiple dark matter candidates a separate DLHA file has to be created for each candidate. If multiple dark matter candidates contribute simultaneously to the present abundance and direct or indirect detection signals, multiple sets of blocks may appear for each candidate in separate files. For example, a DLHA file may contain

```

BLOCK MASS
# PDG code    mass                particle name

```

```

    1000022    1.29098165E+00    # 1st neutralino
    ...
BLOCK QNUMBERS
    ...
BLOCK ABUNDANCE
    ...

```

while another DLHA file might contain

```

BLOCK MASS
# PDG code    mass                particle name
    1000039    2.35019093E+00    # gravitino
BLOCK QNUMBERS
    ...
BLOCK ABUNDANCE
    ...

```

Here the ellipses denote entries irrelevant to this discussion. A user of DLHA is responsible for knowing that the two files contain information in the context of multiple dark matter candidates.

For decaying dark matter particles a standard SLHA decay file can be used to read and write the total decay width of the dark matter particle and its branching ratios into various final states.

3.1 The FUNCTION object

Departing from the tradition of previous Les Houches accords, DLHA introduces a new structure that specifies a function. A function definition is facilitated by DLHA using the following construction

```

FUNCTION <name> type=<type> args=<number of arguments>
    ...
END_FUNCTION

```

The FUNCTION heading denotes the beginning and END_FUNCTION the end of the structure. Each function is identified by a name, which follows the FUNCTION heading. In the various block descriptions below we fix the names of the possible functions and specify their content. The content of a function can be given in several different ways in DLHA. The <type> variable differentiates between these methods:

- type = P for a predefined function,
- type = C for a C function,
- type = F for a Fortran function,
- type = T for tabular information.

The number of independent variables of the function is given by the numerical value of the last argument <number of arguments> of the FUNCTION structure.

While a FUNCTION depends on one or more independent variables, it may also carry information about related parameters inside the body of the function. These parameters can be listed as follows:


```

FUNCTION <name> type=<type> args=<number of arguments>
PARAMETERS
  <parameter name 1>=<value 1>
  <parameter name 2>=<value 2>
  <parameter name 3>=<value 3>
  ...
END_PARAMETERS
<function body>
END_FUNCTION

```

Parameter names are fixed by DLHA in the block descriptions similarly to names of functions. If a parameter value is specified both outside and inside of a function, the value given inside the FUNCTION construction overrides the one appearing outside.

Predefined functions, typically the most commonly used functions for a given quantity, are specified by DLHA under the description of the various functions. A predefined function which is listed in the DLHA write-up can be referred to by the following construction following the FUNCTION heading:

```

FUNCTION <name> type=<type> args=<number of arguments>
DLHA <name> <identifier>
...
END_FUNCTION

```

Within the block descriptions DLHA fixes the function choices corresponding to various numerical values of identifiers.

As an example, the following structure specifies the use of the Einasto profile for the dark matter galactic halo profile $\rho_g(r)$:

```

FUNCTION rho_g type=P args=2
DLHA rho_g 5
END_FUNCTION

```

The Einasto profile depends on two arguments. One of them may also be fixed as:

```

FUNCTION rho_g type=P args=1
DLHA rho_g 5
PARAMETERS
  alpha=1
END_PARAMETERS
END_FUNCTION

```

In the present agreement, we only consider functions tabulated on a rectangular (but not necessary equidistant) grid. In this case the list of the independent variables and the function value is given as an n+1 column table. For tabular functions the line after the function name gives the names of the independent variables and the dimensions of the rectangular grid on which the function is specified. A schematic example of a function given in tabular format is the following:

```

FUNCTION rho_g type=T args=2
  r: 2  alpha: 3
#  r              alpha              rho_g
  0.000000E+00  1.000000E+00  2.345678E+00
  1.000000E-05  1.000000E+00  1.234567E+00
  0.000000E-05  2.000000E+00  4.567890E+00
  1.000000E-05  2.000000E+00  3.456789E+00
  0.000000E-05  3.000000E+00  6.789012E+00
  1.000000E-05  3.000000E+00  5.678901E+00
END_FUNCTION

```

A FUNCTION given in the form of a C language function could appear as:

```

FUNCTION rho_g type=C args=2
#include<math.h>
double Einasto(double r, double alpha)
{ return exp(-2*(pow(r,alpha)-1)/alpha);}
END_FUNCTION

```

The FUNCTION construction also allows passing function names that are included in a pre-compiled library:

```

FUNCTION <name> type=<type> args=<number of arguments>
  libName=<name of compiled library>
  funcName=<name of function in library>
END_FUNCTION

```

An example of this is shown in Section 3.8.

3.2 BLOCK COSMOLOGY

The COSMOLOGY block specifies the values of the cosmological parameters that enter into the calculation of dark matter related observables such as the abundance. The cosmology block may contain numerical entries such as those below. In these entries, the temperature is given in units of GeV/k , where k is the Boltzmann constant.

- 1 The value of the current entropy density of the Universe s_0 in units of $(\text{GeV}/\hbar c)^3/k$, appearing in Eq. (16).

The cosmology block also accommodates various entries that are defined as functions as described in the previous subsection. The list of these functions is given below.

Non-standard energy density $\rho_D(T)$, as described in Eq. (18), as a function of the temperature and in units of $(\text{GeV}/\hbar c)^4$.

```

FUNCTION rho_D type=<type> args=1
...
END_FUNCTION

```

Non-standard entropy density $s_D(T)$, as described in Eq. (18), as a function of the temperature and in units of $(\text{GeV}/\hbar c)^3$.

```

FUNCTION s_D type=<type> args=1
...
END_FUNCTION

```

Non-standard normalized entropy production rate $\Sigma_D(T)/\sqrt{G}$, as described in Eq. (18), as a function of the temperature and in units of $(\text{GeV}/\hbar c)^5$.

```

FUNCTION Sigma_D type=<type> args=1
...
END_FUNCTION

```

The value of the normalized Hubble expansion rate $H(T)/\sqrt{G}$, as per Eq. (17), as a function of the temperature. The normalized Hubble expansion rate is in units of $(\text{GeV}/\hbar c)^2$.

```

FUNCTION Hubble type=<type> args=1
...
END_FUNCTION

```

Note that the functions `s_D` and `Sigma_D` are not to be given simultaneously, as they refer to two different parameterizations of the entropy content of the Universe. Also, the functions `rho_D` and `Hubble` do not need to be given simultaneously.

A specific cosmology block, describing a standard cosmological scenario may appear as this:

```

BLOCK COSMOLOGY
# identifier(s)  parameter value  comment
  1              2.18421585E-03 # s_0 [GeV^3]
# -----
FUNCTION rho_D type=C args=1      # rho_D(T) [GeV^4]
...
END_FUNCTION
FUNCTION s_D type=F args=1        # s_D(T) [GeV^3]
...
END_FUNCTION

```

3.3 BLOCK DOFREEDOM

This block contains the various degrees of freedom entering into the abundance calculation.

The effective degrees of freedom $g_{eff}(T)$ in Eq. (6) as a function of the temperature are given by

```

FUNCTION g_eff type=<type> args=1
...
END_FUNCTION

```

The units of temperature are GeV/k .

As an alternative to $g_{eff}(T)$, as a function of the temperature, g_* can also be given. The latter is defined in Eq. (11).

```

FUNCTION gstar type=<type> args=1
...
END_FUNCTION

```

The effective degrees of freedom $h_{eff}(T)$ in Eq. (8) as a function of the temperature (measured in GeV/ k) are given by

```

FUNCTION h_eff type=<type> args=1
...
END_FUNCTION

```

This block containing 57 entries of g_{eff} and 48 entries for h_{eff} in tabular format might appear as follows.

```

BLOCK DOFREEDOM
FUNCTION g_eff type=T args=1
  T: 57
# T [GeV/k]          g_{eff}(T)
  1.00000000E-05    2.00000000E-00
  5.00000000E-05    2.00000000E-00
  1.00000000E-04    4.00000000E-00
...
END_FUNCTION
FUNCTION h_eff type=T args=1
  T: 48
# T [GeV/k]          h_{eff}(T)
  2.00000000E-05    1.00000000E-00
  4.00000000E-05    1.00000000E-00
  6.00000000E-05    2.00000000E-00
...
END_FUNCTION

```

3.4 BLOCK DMSPADIST

Block DMSPADIST contains information regarding the dark matter energy density distribution in various astrophysical objects, such as galaxies or nebulae. These enter the calculation of direct and indirect detection rates. Before discussing the block attributes, we list the most commonly used halo profiles and give their corresponding mathematical expressions. Each profile has a set of parameters which are dependent on the particular halo of interest. Unless otherwise stated ρ_0 sets the normalization of the profile and r_s is the scale radius.

Hernquist-Zhao density profile:

$$\rho_g(r) = \frac{\rho_0}{(r/r_s)^\gamma (1 + (r/r_s)^{(\alpha-\gamma)/\beta})^\beta}. \quad (69)$$

The Navarro-Frenk-White (NFW) distribution is a special case of this with $\alpha = 3$, $\beta = 2$, and $\gamma = 1$ [35]. The Kravtsov et al. profile can also be obtained from Eq. (69) by setting $\alpha = 3$ and $\beta = 2$ [36].

Modified isothermal profile [37]:

$$\rho_g(r) = \frac{\rho_0}{1 + (r/r_s)^2}. \quad (70)$$

Einasto profile [38]:

$$\rho_g(r) = \rho_0 \exp\left(-\frac{2}{\alpha} \left(\frac{r^\alpha}{r_s^\alpha} - 1\right)\right). \quad (71)$$

Moore et al. profile [39]:

$$\rho_g(r) = \frac{\rho_0}{(r/r_s)^{3/2} (1 + r/r_s)^{3/2}}. \quad (72)$$

Burkert profile [40]:

$$\rho_g(r) = \frac{\rho_0 r_s^3}{(r + r_s)(r^2 + r_s^2)}. \quad (73)$$

3.4.1 The structure of BLOCK DMSPADIST

Since dark matter energy density distributions can be specified for various astrophysical objects, such as external galaxies and halo substructures, more than one BLOCK DMSPADIST may appear in a DLHA file. In this case multiple BLOCK DMSPADIST blocks carry an index differentiating them from each other. For example

```
BLOCK DMSPADIST_MilkyWay
...

BLOCK DMSPADIST_NGC6388
...

BLOCK DMSPADIST_VIRGOHI21
...
```

The shape of the dark matter density distribution $\rho_g(r)$, featured in Eqs. (53) and (60), is defined by the function

```
FUNCTION rho_g type=<type> args=<number of arguments>
...
END_FUNCTION
```

The galactic halo profile is assumed to be given in units of $\text{GeV}/c^2/\text{cm}^3$, and its radial argument in units of kpc.

Identifiers for numerical parameters featured in this function for predefined density profiles are the following:

- 1 the normalization of the profile ρ_0 in units of $\text{GeV}/c^2/\text{cm}^3$,
- 2 the scale radius r_s in units of kpc,
- 3 α for the Hernquist-Zhao and Einasto profiles,

- 4 β for the Hernquist-Zhao profile,
- 5 γ for the Hernquist-Zhao profile,
- 6 the value of the dark matter mass density near Earth ρ_{\oplus} in units of $\text{GeV}/c^2/\text{cm}^3$,
- 7 our Galactocentric distance, R_0 in units of kpc.

These variables can also be used within predefined functions as PARAMETERS with the following names

```
rho_0      :  $\rho_0$  ,
r_s        :  $r_s$  ,
alpha      :  $\alpha$  ,
beta       :  $\beta$  ,
gamma      :  $\gamma$  ,
rho_oplus  :  $\rho_{\oplus}$  ,
R_0        :  $R_0$  .
```

Predefined values of the most commonly used halo distributions are

DLHA rho_g 1: Hernquist-Zhao profile, as given in Eq. (69),

DLHA rho_g 2: NFW density profile, defined by Eq. (69),

DLHA rho_g 3: Kravtsov et al. profile, defined by Eq. (69),

DLHA rho_g 4: Modified isothermal profile, as given in Eq. (70),

DLHA rho_g 5: Einasto profile, as given in Eq. (71),

DLHA rho_g 6: Moore et al. profile, as given in Eq. (72),

DLHA rho_g 7: Burkert profile, as given in Eq. (73).

For example, in a DLHA file a predefined NFW profile can be referred to as

```
# identifier(s)  parameter value      comment
1                0.385954823E+00    # rho_0 [GeV/cm^3]
2                2.000000000E+01    # scale radius r_s [kpc]
3                3.000000000E+00    # parameter  $\alpha$ 
4                2.000000000E+00    # parameter  $\beta$ 
5                1.000000000E+00    # parameter  $\gamma$ 
# -----
FUNCTION rho_g type=P args=1
  DLHA rho_g 2 # NFW profile
END_FUNCTION
```

Alternatively, the following definition can also be used:

```
FUNCTION rho_g type=P args=1
  DLHA rho_g 2 # NFW profile
  PARAMETERS
    rho_0 = 0.385954823E+00
    r_s   = 2.000000000E+01
    alpha = 3.000000000E+00
    beta  = 2.000000000E+00
```

```

    gamma = 1.000000000E+00
END_PARAMETERS
END_FUNCTION

```

A sample BLOCK DMSPADIST for a predefined Kravtsov et al. halo profile and a tabulated velocity distribution may appear as follows:

```

BLOCK DMSPADIST_MilkyWay
# identifier(s)  parameter value      comment
  1              0.385954823E+00    # rho_0 [GeV/cm^3]
  2              2.000000000E+01    # r_s [kpc]
  3              3.000000000E+00    # alpha
  4              2.000000000E+00    # beta
  6              0.385954821E+00    # rho_Earth [GeV/cm^3]
# -----
FUNCTION rho_g type=P args=1      # predefined Kravtsov
  DLHA rho_g 3
END_FUNCTION

```

3.5 BLOCK DMVELDIST

This block contains information about velocity distributions of dark matter needed in direct and indirect detection calculations. Velocities are given using the Galactic coordinate system, described below. Before discussing the block attributes, we specify common velocity distributions.

Truncated Maxwellian distribution:

$$\tilde{f}(v) = \frac{4\pi v^2}{N_{esc}(2\pi\sigma_v^2)^{3/2}} e^{-v^2/2\sigma_v^2} \theta(v_{esc} - v) \quad (74)$$

where $N_{esc} = \text{erf}(z) - 2ze^{-z^2}/\sqrt{\pi}$ with $z = v_{esc}/\sqrt{2}\sigma_v$.

Subtracted Maxwellian distribution:

$$\tilde{f}(v) = \frac{4\pi v^2}{N_{esc}(2\pi\sigma_v^2)^{3/2}} \left[e^{-v^2/2\sigma_v^2} - e^{-v_{esc}^2/2\sigma_v^2} \right] \theta(v_{esc} - v) \quad (75)$$

where $N_{esc} = \text{erf}(z) - 2z(1 + 2z^2/3)e^{-z^2}/\sqrt{\pi}$ with $z = v_{esc}/\sqrt{2}\sigma_v$.

Here N_{esc} is a normalization factor such that $\int_0^\infty \tilde{f}(v) dv = 1$, v_{esc} is the escape speed (a finite cutoff in the distribution expected due to high-speed dark matter being able to escape from the object's gravitational potential), and σ_v is a velocity dispersion parameter. In the large v_{esc} limit, the distributions in Eqs. (74) and (75) reduce to the same Maxwellian distribution with most probable speed $v_0 = \sqrt{2}\sigma_v$, 1D velocity dispersion σ_v , and 3D velocity dispersion $\sqrt{3}\sigma_v$.

For direct detection, one needs the local dark matter velocity distribution multiplied by the local dark matter density. The latter is given in the DMSPADIST block. Here we address the velocity distribution. Notice that if the local dark matter density is split into different velocity groups, each group has its own block DMVELDIST.

For direct detection (Eq. 27), one needs the dark matter velocity distribution $f(\mathbf{v}, t)$ in the rest frame of the detector. Its time dependence is expected to arise from the motion of the

Earth around the Sun and about its axis. Since these motions are known, $f(\mathbf{v}, t)$ can be obtained through a Galilean transformation from the Sun's rest frame,

$$f(\mathbf{v}, t) = f_{\odot}(\mathbf{v}_{\text{det}} + \mathbf{v}). \quad (76)$$

Here $f_{\odot}(\mathbf{u})$ is the dark matter heliocentric velocity distribution, which is a function of the dark matter velocity \mathbf{u} with respect to the Sun (heliocentric velocity), and \mathbf{v}_{det} is the detector velocity with respect to the Sun given by $\mathbf{v}_{\text{det}} = \mathbf{v}_{\oplus\text{rev}} + \mathbf{v}_{\oplus\text{rot}}$, where $\mathbf{v}_{\oplus\text{rev}}$ is the (time-varying) velocity of the Earth revolution relative to the Sun, and $\mathbf{v}_{\oplus\text{rot}}$ is the (time-varying) velocity of the Earth rotation at the location of the detector relative to the Earth's rest frame.

Enough information should be given in BLOCK DMVELDIST to reconstruct the three-dimensional heliocentric velocity distribution $f_{\odot}(\mathbf{u})$. This is achieved by giving the velocity distribution function $\tilde{f}(\mathbf{v})$ in some specified but otherwise arbitrary reference frame \tilde{S} , together with the velocity $\tilde{\mathbf{v}}$ of \tilde{S} with respect to the Sun, i.e.

$$f_{\odot}(\mathbf{u}) = \tilde{f}(\mathbf{u} - \tilde{\mathbf{v}}). \quad (77)$$

Though not required (except in a case described below), the reference frame \tilde{S} will typically be chosen such that the form for $\tilde{f}(\mathbf{v})$ becomes more simplified, as occurs in the rest frame of an isotropic velocity distribution.

3.5.1 The structure of BLOCK DMVELDIST

Similarly to the energy density, dark matter velocity distributions can be specified for various astrophysical objects: galaxies, halo substructures, or even different local velocity components. Thus, more than one BLOCK DMVELDIST may appear in a DLHA file. Multiple BLOCK DMVELDIST blocks are differentiated from each other as

```
BLOCK DMVELDIST_MilkyWay
```

```
...
```

```
BLOCK DMVELDIST_NGC6388
```

```
...
```

```
BLOCK DMVELDIST_VIRGOHI21
```

```
...
```

The function $\tilde{f}(\mathbf{v})$ is given by

```
FUNCTION fv_g type=<type> args=<number of arguments>
```

```
...
```

```
END_FUNCTION
```

The units of $\tilde{f}(\mathbf{v})$ are assumed to be $(\text{km/s})^{-n}$, where n is the number of arguments. Two different conventions apply depending on whether \tilde{f} is presented as a function of one or more than one variable, i.e., depending on whether $n = 1$ or $n > 1$. If $n > 1$, $\tilde{f}(\mathbf{v})$ must be normalized so that $\int \tilde{f}(\mathbf{v}) d^n v = 1$. If $n = 1$, i.e., if $\tilde{f}(v)$ is a function of only one variable v , it is assumed that (i) the frame \tilde{S} coincides with the frame in which the average velocity is

zero, (ii) in this frame the velocity distribution is isotropic, (iii) the variable $v = |\mathbf{v}|$ is positive and represents the speed, i.e., the magnitude of the velocity, in the frame \tilde{S} , and (iv) $\tilde{f}(v)$ is the speed distribution in \tilde{S} , normalized so that $\int_0^\infty \tilde{f}(v) dv = 1$.

Predefined values of the most commonly used velocity distributions are

DLHA fv_g 1: Truncated Maxwellian distribution, as given in Eq. (74),

DLHA fv_g 2: Subtracted Maxwellian distribution, as given in Eq. (75).

Names of numerical PARAMETERS featured in these predefined functions are the following:

sigma_v: the velocity dispersion parameter σ_v in units of km/s,

v_esc : the escape speed v_{esc} in units of km/s.

These parameters can also be given before the FUNCTION definition with the following identifiers

1 σ_v in units of km/s,

2 v_{esc} in units of km/s.

The \tilde{S} heliocentric velocity vector $\tilde{\mathbf{v}}$ is to be given by its components in the Galactic reference frame. The Galactic reference frame is a right-handed Cartesian coordinate system xyz with x axis in the direction of the Galactic Center ($l = 0, b = 0$), y axis in the direction of the Galactic rotation ($l = 90^\circ, b = 0$), and z axis in the direction of the Galaxy's axis of rotation (North Galactic Pole $b = 90^\circ$). The velocity $\tilde{\mathbf{v}}$ is thus given by the following parameters.

11 the x component \tilde{v}_x of the \tilde{S} heliocentric velocity in units of km/s,

12 the y component \tilde{v}_y of the \tilde{S} heliocentric velocity in units of km/s,

13 the z component \tilde{v}_z of the \tilde{S} heliocentric velocity in units of km/s.

A sample BLOCK DMVELDIST for a predefined truncated Maxwellian distribution may appear as follows:

```
BLOCK DMVELDIST_standard_dark_halo
# identifier(s)  parameter value      comment
  1              1.555634918E+02  # sigma_v [km/s]
  2              6.500000000E+02  # v_esc [km/s]
 11              0.000000000E+00  # vframe_x [km/s]
 12             -2.200000000E+02  # vframe_y [km/s]
 13              0.000000000E+00  # vframe_z [km/s]
# -----
FUNCTION fv_g type=P args=1 # predefined v distr.
  DLHA fv_g 1              # truncated Maxwellian
```

A sample BLOCK DMVELDIST for a tabulated velocity distribution may appear as follows:

```
BLOCK DMVELDIST_MilkyWay
  1              1.555634918E+02  # sigma_v [km/s]
  2              6.500000000E+02  # v_esc [km/s]
 11              0.000000000E+00  # vframe_x [km/s]
 12             -2.200000000E+02  # vframe_y [km/s]
 13              0.000000000E+00  # vframe_z [km/s]
FUNCTION fv_g type=T args=1      # fv_g tabulated
```

```

v: 57
# v [km/s]          f(v) [s/km]
  5.00000000E+01   1.20000000E-01
  7.50000000E+01   2.40000000E-01
  1.00000000E+02   4.90000000E-01
  ...
END_FUNCTION

```

3.6 BLOCK FORMFACTS

The nucleon form factors f^N and Δ_q^N as introduced in Eqs. (47) and (48). The corresponding identifiers are:

- 1 1 up quark scalar form factor for the proton f_u^p ,
- 1 2 down quark scalar form factor for the proton f_d^p ,
- 1 3 strange quark scalar form factor for the proton f_s^p ,
- 1 4 heavy quark scalar form factors for the proton f_Q^p ,
- 2 1 up quark scalar form factor for the neutron f_u^n ,
- 2 2 down quark scalar form factor for the neutron f_d^n ,
- 2 3 strange quark scalar form factor for the neutron f_s^n ,
- 2 4 heavy quark scalar form factors for the neutron f_Q^n ,
- 3 1 up quark vector form factor for the proton $f_{V_u}^p$,
- 3 2 down quark vector form factor for the proton $f_{V_d}^p$,
- 4 1 up quark vector form factor for the neutron $f_{V_u}^n$,
- 4 2 down quark vector form factor for the neutron $f_{V_d}^n$,
- 5 1 up quark axial-vector form factor for the proton Δ_u^p ,
- 5 2 down quark axial-vector form factor for the proton Δ_d^p ,
- 5 3 strange quark axial-vector form factor for the proton Δ_s^p ,
- 6 1 up quark axial-vector form factor for the neutron Δ_u^n ,
- 6 2 down quark axial-vector form factor for the neutron Δ_d^n ,
- 6 3 strange quark axial-vector form factor for the neutron Δ_s^n ,
- 7 1 up quark $\sigma_{\mu\nu}$ form factor for the proton δ_u^p ,
- 7 2 down quark $\sigma_{\mu\nu}$ form factor for the proton δ_d^p ,
- 7 3 strange quark $\sigma_{\mu\nu}$ form factor for the proton δ_s^p ,
- 8 1 up quark $\sigma_{\mu\nu}$ form factor for the neutron δ_u^n ,
- 8 2 down quark $\sigma_{\mu\nu}$ form factor for the neutron δ_d^n ,
- 8 3 strange quark $\sigma_{\mu\nu}$ form factor for the neutron δ_s^n .

A specific FORMFACTS block for a spin-zero dark matter candidate may look like this:

```

BLOCK FORMFACTS
# identifier(s)  value          comment
  1      1      2.30000000E-02 # f_u^p

```

1	2	3.30000000E-02	#	f_d^p
1	3	2.60000000E-01	#	f_s^p
2	1	1.80000000E-02	#	f_u^n
2	2	4.20000000E-02	#	f_d^n
2	3	2.60000000E-01	#	f_s^n

3.7 BLOCK STRUCTFUN

The nuclear structure functions $F_A(E)$ and $S_{ij}(E)$ are defined in Eqs. (33) and (35) for SI interactions, and Eqs. (37) and (38-40) for SD interactions. They may be given in the form of functions of the recoil energy E , such as

```
FUNCTION F_A type=<type> args=1
...
END_FUNCTION
```

and

```
FUNCTION S_ij type=<type> args=1
...
END_FUNCTION
```

The nuclear form factors should carry no unit, while the transferred energy E is in units of keV. For reference, the transferred energy E is related to the momentum transfer q through $E = q^2/(2m_A)$, where m_A is the nucleus mass.

The following common parametrizations of F_A are used. The exponential form factor defined as

$$F_A(qr_n) = e^{-\alpha(qr_n)^2/2} \quad \text{with} \quad r_n = a_n A^{1/3} + b_n. \quad (78)$$

The names of the corresponding parameters that appear in the PARAMETERS list are

A : A the mass number of the nucleus ,
Z : Z the atomic number of the nucleus ,
alpha: α ,
a_n : a_n in units of fm ,
b_n : b_n in units of fm .

The Helm form factor

$$F_A(qr_n) = 3 \frac{j_1(qr_n)}{qr_n} e^{-(qs)^2/2} \quad \text{with} \quad r_n^2 = c^2 + \frac{7}{3}\pi^2 a^2 - 5s^2 \quad \text{and} \quad c = c_0 A^{1/3} + c_1. \quad (79)$$

Helm specific names for PARAMETERS are

A : A the mass number of the nucleus ,
Z : Z the atomic number of the nucleus ,
c_0: c_0 in units of fm ,
c_1: c_1 in units of fm ,
a : a in units of fm ,
s : s skin thickness in units of fm .

The Fermi distribution

$$F_A(q) = \int \rho(r) e^{i\mathbf{q}\cdot\mathbf{r}} d^3r \quad \text{with} \quad \rho(r) = \rho_0(1 + e^{(r-c)/a})^{-1} \quad \text{and} \quad c = c_0 A^{1/3} + c_1. \quad (80)$$

Corresponding names of PARAMETERS are

A : A the mass number of the nucleus ,
 Z : Z the atomic number of the nucleus ,
 rho_0: ρ_0 ,
 c_0 : c_0 in units of fm ,
 c_1 : c_1 in units of fm ,
 a : a in units of fm .

Corresponding to these in DLHA the following predefined F_A form factors can be used:

DLHA F_A 1: exponential form factor,

DLHA F_A 2: Helm form factor ,

DLHA F_A 3: Fermi distribution .

Examples of specifying these form factors are:

```
# Exponential form factor:
# F(q r_n) = e^{-\alpha (q r_n)^2 / 2}
# r_n = a_n A^{1/3} + b_n
FUNCTION F_A type=P args=1
  DLHA F_A 1          # Exponential form factor
  PARAMETERS
    Z = 11
    A = 23
    alpha = 0.20000000E+00 #
    a_n   = 1.15000000E+00 # [fm]
    b_n   = 0.39000000E+00 # [fm]
  END_PARAMETERS
END_FUNCTION

# General spin-independent form factor (Helm):
# F(q r_n) = 3 \frac{j_1(q r_n)}{q r_n} e^{-(qs)^2/2}
# r_n^2 = c^2 + \frac{7}{3} \pi^2 a^2 - 5 s^2
# c = c_0 A^{1/3} + c_1
FUNCTION F_A type=P args=1
  DLHA F_A 2          # Helm form factor
  PARAMETERS
    Z = 11
    A = 23
    c_0 = 1.23000000E+00 # [fm]
    c_1 = -0.60000000E+00 # [fm]
    a   = 0.52000000E+00 # [fm]
    s   = 0.90000000E+00 # [fm] skin thickness
  END_PARAMETERS
```

```

END_FUNCTION

# Fermi distribution:
FUNCTION F_A type=P args=1
  DLHA F_A 3          # Fermi distribution
  PARAMETERS
    Z = 11
    A = 23
    c_0 = 1.23000000E+00 # [fm]
    c_1 = -0.60000000E+00 # [fm]
    a   = 0.52000000E+00 # [fm]
  END_PARAMETERS
END_FUNCTION

# Sodium (spin-dependent, tabulated)
FUNCTION S_00 type=T args=1
  PARAMETERS
    Z = 11
    A = 23
  END PARAMETERS
  E: 101
#   E           S_00
    0.000000E+00 1.000000E+00
    1.000000E+00 0.997000E+00
    2.000000E+00 0.994000E+00
    ...
END FUNCTION

```

3.8 BLOCK DETECTOR_NUCLEI

An alternative way to specify nuclear structure functions S_{ij} is the following.

```

BLOCK DETECTOR_NUCLEI # DAMA
# Num Fraction A Z J FSD S00 S01 S11
  1 0.153 23 11 1.5 STD S00Na23 S00Na23 S11Na23
  2 0.847 127 53 2.5 STD S00I127 S00I127 S11I127

FUNCTION S00Na23 type=C args=1
  libName=libmicromegas.so
  funcName=S00Na23
END_FUNCTION

```

3.9 BLOCK MASS

Block MASS is part of SLHA. It is used by DLHA to identify the dark matter particle and to specify its mass. Specific examples of BLOCK MASS appear in the introduction of this section.

3.10 BLOCK QNUMBERS

This block is part of the Les Houches BSM Generator Accord and defined in Ref. [41]. The block contains information on the spin, self-conjugate nature, the standard ($SU(3)_C$, $SU(2)_W$, $U(1)_Y$) and exotic charges of the particle. It may be extended to also contain information about quantum numbers corresponding to discrete symmetries such as R-parity, KK-parity, T-parity, Z-parities.

3.11 BLOCK ABUNDANCE

Abundances of any species of dark matter particles receive their own block, detailing their properties. The elements of the abundance block are the following.

- 1 The freeze-out temperature T_f in units of GeV/ k as defined by the condition in Eq. (13).
- 2 The chosen value of α for Eq. (13).
- 3 The thermal average of the total (co-)annihilation cross section times velocity at freeze-out $\langle\sigma v\rangle(T_f)$ in units of cm^3/s as defined in Eq. (2).
- 4 The average energy density of the dark matter particle $\Omega_\chi h^2$ due to thermal production, in units of the critical density as given in Eq. (16).
- 5 Same as above but for non-thermal production.
- 6 Percentage contribution to the total cross section by (co-)annihilation channels. This line will appear multiple times for a cross section with multiple (co-)annihilation channels. Each line lists the PDG codes of the two final state particles along with the percent at which it contributes to the total (co-)annihilation cross section.

An example of BLOCK ABUNDANCE for a thermally produced dark matter candidate with an abundance of $\Omega_\chi h^2 = 0.11018437$ is the following:

```
BLOCK ABUNDANCE
# identifier(s)  parameter value      comment
1               5.16392660E+00 # T_f [GeV/k]
2               1.50000000E+00 # alpha
3               3.18452057E-26 # <sigma v>(T_f) [cm^3/s]
4               0.11018437E+00 # Omega h^2 thermal
# annihilation channel contribution to <sigma v>(T_f) [%]
# identifier(s) PGD code 1  PGD code 2    %
6               ...         ...         ...
```

3.12 BLOCK EFFCOUPLING

The entries of this block are the effective dark matter-nucleon couplings as defined in Eqs. (47) and (48).

- 1 Spin-independent scalar coupling f_p for $s_\chi = 1/2$ and the proton,
- 2 spin-independent scalar coupling f_n for $s_\chi = 1/2$ and the neutron,
- 3 spin-dependent axial-vector coupling a_p for $s_\chi = 1/2$ and the proton,
- 4 spin-dependent axial-vector coupling a_n for $s_\chi = 1/2$ and the neutron.

An example for an EFFCOUPLING block is the following

BLOCK EFFCOUPLING

```
# identifier(s)  parameter value  comment
1                0.10000000E+00 # f_p
2                0.10000000E+00 # f_n
3                0.00000000E+00 # a_p
4                0.00000000E+00 # a_n
```

3.13 BLOCK NDMCROSSECT

This block contains the spin-independent and spin-dependent nucleon-dark matter elastic scattering cross sections $\sigma_N^{SI,SD}$ found using Eqs. (34) and (44).

- 1 The spin-independent proton-dark matter elastic scattering cross section σ_p^{SI} in units of cm^2 ,
- 2 The spin-independent neutron-dark matter elastic scattering cross section σ_n^{SI} in units of cm^2 ,
- 3 The spin-dependent proton-dark matter elastic scattering cross section σ_p^{SD} in units of cm^2 ,
- 4 The spin-dependent neutron-dark matter elastic scattering cross section σ_n^{SD} in units of cm^2 .

An example for a NDMCROSSECT block is the following

BLOCK NDMCROSSECT

```
# identifier(s)  parameter value  comment
1                0.12345678E-41 # \sigma^{SI}_p [cm^2]
2                0.23456789E-41 # \sigma^{SI}_n [cm^2]
3                0.34567890E-41 # \sigma^{SD}_p [cm^2]
4                0.45678901E-41 # \sigma^{SD}_n [cm^2]
```

3.14 BLOCK ASTROPROPAG

This and the following blocks describe aspects of the calculations relevant to indirect detection experiments. BLOCK ASTROPROPAG contains parameters and functions of the propagation model for charged cosmic rays. The parameters in this block are the following:

- 1 normalization of the spatial diffusion coefficient K_0 , in Eq. (55),
- 2 coefficient η , controlling the dependence on v of the spatial diffusion coefficient in Eq. (55),
- 3 coefficient δ parameterizing the steepness of the spatial diffusion coefficient in energy, in Eq. (55),
- 4 normalization of the energy loss coefficient b_0 , in Eq. (56),
- 5 half-height L of the diffusion box in units of kpc,
- 6 radius R of the diffusion box in units of kpc,
- 7 re-acceleration parameter v_A in units of km/s, in Eq. (57),
- 8 Galactic wind parameter V_C in units of km/s, in Eq. (52).

A spatial diffusion coefficient with generic energy or rigidity dependence can be defined by the function

```

FUNCTION SpatDiff type=<type> args=1
...
END_FUNCTION

```

A predefined spatial diffusion coefficient dependence is given by Eq. (55) and can be indicated by

```

FUNCTION SpatDiff type=P args=1
DLHA SpatDiff 1
END_FUNCTION

```

The energy loss coefficient for charged cosmic rays, $b(E)$, can also be defined by

```

FUNCTION EnerLoss type=<type> args=1
...
END_FUNCTION

```

Its predefined form, given by Eq. (56), is indicated as

```

FUNCTION EnerLoss type=P args=1
DLHA EnerLoss 1
END_FUNCTION

```

3.15 BLOCK DMCLUMPS

This is a recommended block and it is only sketched in this version of DLHA. It should store information regarding dark matter substructures. It stores the relevant information on the distribution of dark matter substructures inside the Milky Way halo.

The inner structures of clumps are similar to the dark matter distributions inside galactic halos. Whatever the favourite density profile, code builders need to compute the annihilation volume ξ as a function of the substructure mass M_{cl} . For this, they need to compute the virial radius R_{vir} of a given clump. This radius encompasses an average density

$$\bar{\rho}(R_{\text{vir}}) = \frac{M_{\text{cl}}}{(4\pi/3)R_{\text{vir}}^3} = \Delta_{\text{vir}} \Omega_{\text{M}} \rho_{\text{C}}^0, \quad (81)$$

which is Δ_{vir} times larger than the average cosmological matter density $\Omega_{\text{M}}\rho_{\text{C}}^0$. The concentration of the clump is defined as the ratio

$$c_{\text{vir}} = \frac{R_{\text{vir}}}{r_{-2}}, \quad (82)$$

where the clump density profile has slope -2 at radius $r = r_{-2}$. The mass-to-concentration relation can be parameterized as [34]

$$\ln(c_{\text{vir}}) = \sum_{i=0}^4 C_i \left\{ \ln \left(\frac{M_{\text{cl}}}{M_{\odot}} \right) \right\}^i. \quad (83)$$

The output is the annihilation volume ξ as a function of the clump mass M_{cl} .

The substructure probability distribution $\mathcal{D}(\vec{r}_S, \xi)$ and the total number of clumps \mathcal{N}_H inside the Milky Way halo can be inferred from the space and mass distribution function $d^4\mathcal{N}_{\text{cl}}/dM_{\text{cl}}d^3r_S$. As an illustration, we can assume the space distribution of clumps to be isotropic and independent of the mass spectrum, so that

$$\frac{d^2\mathcal{N}_{\text{cl}}}{4\pi r_S^2 dr_S dM_{\text{cl}}} = \frac{d\mathcal{N}_{\text{cl}}}{dM_{\text{cl}}} \times \mathcal{P}(r_S). \quad (84)$$

The mass distribution is taken in general to be the power law

$$\frac{d\mathcal{N}_{\text{cl}}}{dM_{\text{cl}}} = \frac{C}{M_{\text{cl}}^\alpha}, \quad (85)$$

where the normalization constant C is calculated by requiring that the Milky Way halo contains a certain number of substructures with mass in the range M_1 to M_2 . In Ref. [34] for instance, there are 100 clumps between 10^8 and $10^{10}M_\odot$. The mass spectrum of the clumps extends from M_{inf} to M_{sup} which are inputs of the code.

The last input is the space distribution function $\mathcal{P}(r_S)$. Substructures do not follow the smooth dark matter distribution. In particular, they are tidally disrupted near the Galactic center, hence a deficit with respect to the smooth component. As an illustration, a possible clump distribution is given by the isothermal profile with core radius a

$$\mathcal{P}(r_S) = \frac{\kappa}{a(a^2 + r_S^2)}. \quad (86)$$

Assuming that the integral of $\mathcal{P}(r_S)$ from $r = r_{\text{min}}$ to $r = r_{\text{max}}$ is normalized to unity leads to the constant

$$\kappa = \frac{1/4\pi}{(u_2 - u_1) - \{\arctan(u_2) - \arctan(u_1)\}}, \quad (87)$$

where $u_1 = r_{\text{min}}/a$ and $u_2 = r_{\text{max}}/a$. This is just an example. What is actually needed is the input function $\mathcal{P}(r_S)$.

3.16 BLOCK ANNIHILATION

Input block (from various particle physics model codes) that can be used by other codes to calculate the source spectra from annihilation. This block contains the total annihilation cross section and partial cross sections into different Standard Model final states.

1 Annihilation cross section times velocity, σv in the $v \rightarrow 0$ limit and in units of cm^3/s , followed by a table of annihilation channels with branching fractions with the following columns:

column 1 branching fraction (BR),

column 2 number of annihilation products (NDA),

column 3 PDG code of annihilation product 1,

column 4 PDG code of annihilation product 2.

An example entry could look like

```
BLOCK ANNIHILATION
      1          3.000000E-26      # sigma v (v->0) [cm^3/s]
```

#	BR	NDA	ID1	ID2	comment
	9.50000000E-01	2	24	-24	# X X -> W+ W-
	4.00000000E-02	2	5	-5	# X X -> b b-bar
	1.00000000E-02	2	25	36	# X X -> H ₁ ⁰ H ₃ ⁰

3.17 BLOCK INDIRDETSPECTRUM $i n$

The spectra of end products (such as positrons, gamma rays, antiprotons, etc.) in the halo (or vacuum) or in an environment (like the Sun) can be calculated from the information given in the blocks above. These spectra can then be used as input for programs that solve the cosmic ray propagation equations, or calculate the fluxes from particular sources in the sky in case of neutral particles. If for example the block ANNIHILATION is given at the same time as any of the spectrum blocks given below, the blocks below should take precedence, i.e. the codes should *not* recalculate the spectra if a spectrum is already given in the DLHA file.

The block definition is

```
BLOCK INDIRDETSPECTRUM  $i n$ 
```

where i is the dark matter particle and n is the spectrum type:

- $n = 1$: positron spectrum in vacuum (or the halo),
- $n = 2$: antiproton spectrum in vacuum (or the halo),
- $n = 3$: antideuteron spectrum in vacuum (or the halo),
- $n = 4$: gamma-ray spectrum in vacuum (or the halo),
- $n = 5$: electron neutrino spectrum in vacuum (or the halo),
- $n = 6$: muon neutrino spectrum in vacuum (or the halo),
- $n = 7$: tau neutrino spectrum in vacuum (or the halo),
- $n = 101$: electron neutrino spectrum at the Earth from annihilations in the Sun,
- $n = 102$: electron anti-neutrino spectrum at the Earth from annihilations in the Sun,
- $n = 103$: muon neutrino spectrum at the Earth from annihilations in the Sun,
- $n = 104$: muon anti-neutrino spectrum at the Earth from annihilations in the Sun,
- $n = 105$: tau neutrino spectrum at the Earth from annihilations in the Sun,
- $n = 106$: tau anti-neutrino spectrum at the Earth from annihilations in the Sun,
- $n = 113$: μ^- spectrum at the Earth (coming from muon neutrino nucleon interactions) from annihilations in the Sun,
- $n = 114$: μ^+ spectrum at the Earth (coming from muon neutrino nucleon interactions) from annihilations in the Sun,
- $n = 201$: electron neutrino spectrum at the Earth from annihilations in the Earth,
- $n = 202$: electron anti-neutrino spectrum at the Earth from annihilations in the Earth,
- $n = 203$: muon neutrino spectrum at the Earth from annihilations in the Earth,
- $n = 204$: muon anti-neutrino spectrum at the Earth from annihilations in the Earth,
- $n = 205$: tau neutrino spectrum at the Earth from annihilations in the Earth,
- $n = 206$: tau anti-neutrino spectrum at the Earth from annihilations in the Earth,

$n = 213$: μ^- spectrum at the Earth (coming from muon neutrino nucleon interactions) from annihilations in the Earth,

$n = 214$: μ^+ spectrum at the Earth (coming from muon neutrino nucleon interactions) from annihilations in the Earth.

The content of the block is the energy distribution dN/dE as the function of the energy E :

```
E          dN/dE
```

The spectrum dN/dE is the yield per annihilation or decay at that energy (for $n < 100$). For spectra from the Sun/Earth ($n > 100$), the units of dN/dE are per annihilation per m^2 .

A typical spectrum block could then look like

```
BLOCK INDIRDETSPECTRUM 1 4 # gamma-ray spectrum
#      E          dN/dE
  1.000000E-02  1.000000E-4
  2.000000E-02  1.200000E-4
  :
```

3.18 DECAY files

For decaying dark matter particles a standard SLHA decay file can be used to read and write the total decay width of the dark matter particle and its branching ratios into various final states. In SLHA DECAY entries are possible for decay channels of various particles, including the dark matter particle. They look similar to the ANNIHILATION block above. To be able to calculate the complete spectrum from annihilation and decay of a dark matter particle, we also need the partial decay widths (or branching ratios) for other new physics particles, e.g. new Higgs bosons. These DECAY structures should follow the same format as in SLHA2. For example, the decay of a Higgs boson might look like

```
#      PDG          Width
DECAY  1000039      3.287443E+35
#      BR          NDD   ID1   ID2   channel
  9.50000000E-01    2     24   -24   # W+ W-
  5.00000000E-02    2     5    -5    # b b-bar
# -----
#      PDG          Width
DECAY  35           3.287443E+00
#      BR          NDA   ID1   ID2
  9.000000E-01     2     5    -5    # b b-bar
  6.000000E-02     2     24   -24   # W- W+
  4.000000E-02     2     23   -23   # Z0 Z0
```

4 OPEN ISSUES

A partial list of open issues is addressed in various degrees of detail.

4.1 Cosmology related open issues

- Other generalizations of the standard cosmological equations would be useful.
- The standard inflation scenario should be discussed as well.
- What about a decaying inflaton scenario? Can be presented as an example.

4.2 Astrophysics related related open issues

- The notation in BLOCK DMSPADIST is confusing. ρ_0 is not the density at R_0 . The local density could be called ρ_\odot and the Galactocentric distance R_\odot . It should be clearly stated that either the density is defined with respect to the change of slope (or the interior mass) and then parameters (1, 2, 3, 4, and 5) are needed, or with respect to the local density, which requires parameters (2, 3, 4, 5, 6, and 7). Giving all the parameters is also possible but one needs to check consistency.
- Ideally, DLHA should be able to accommodate innately anisotropic distributions.
- A capability for non-spherical and/or clumped halo distributions is also desirable.

4.3 Direct detection related open issues

- For non-self conjugate dark matter particles there is a need to present nuclear cross sections for antiparticles. This is not possible within the present setup.

4.4 Indirect detection related open issues

- Photon energy losses need to be improved.
- Solar modulation needs a unified treatment.
- The quantities that enter the transport equation (for example, the diffusion coefficient, the re-acceleration term, ...) should be standardized, in such a way that free parameters are identified.

4.5 Other open issues

- Kinetic decoupling of DM particles should be discussed. This sets the small-scale cutoff in the spectrum of density perturbations, viz. the mass of smallest dark matter halos, and can have impact on, e.g., the anisotropy spectrum and the 'boost factor' for indirect searches.
- Concerning the calculation of the relic density, the importance of the QCD phase transition should be stressed. This may impact strongly the calculation if the dark matter candidate is light (10 GeV/c² or so). The QCD phase transition temperature should be a parameter to put in BLOCK DOFREEDOM.
- BLOCK DMPDGCODE: suggestion for a new block more explicitly identifying the DM candidate(s).

```

1  0  1000022 # neutralino
1  1  1000012 # sneutrino
...
2  0  9999999 # axion

```

- With large tables in large parameter scans, I/O may take a long time.
- In scenarios/models with Z_3 , Z_4 etc., different interactions and processes appear.
- What about semi-annihilations?

ACKNOWLEDGEMENTS

The authors thank Xerxes Tata for useful comments. C.B. and R.L. were funded in part by the Australian Research Council under Project ID DP0877916 and in part by the ARC Centre of Excellence for Particle Physics at the Terascale. C.B. was partially funded by Project of Knowledge Innovation Program (PKIP) of the Chinese Academy of Sciences, Grant No. KJCX2.YW.W10. G.B., F.B. and A.P. were supported in part by the GDRI-ACPP of CNRS. T.B. acknowledges support from the German Research Foundation (DFG) through Emmy Noether grant BR 3954/1-1. D.G.C. is supported by the Ramón y Cajal program of the Spanish MICINN. T.D. was supported by the Spanish MICINN's Consolider-Ingenio 2010 Programme under grant CPAN CSD2007-00042. D.G.C. and T.D. also thank the support of the Spanish MICINN's Consolider-Ingenio 2010 Programme under grant MultiDark CSD2009-00064, the Spanish MICINN under grant FPA2009-08958, the Community of Madrid under grant HEPHACOS S2009/ESP-1473, and the European Union under the Marie Curie-ITN program PITN-GA-2009-237920. The work of M.C. is supported in part by the French national research agency ANR under contract ANR 2010 BLANC 041301 and by the EU ITN network UNILHC. J.E. and C.S. are grateful to the Swedish Research Council (VR) for financial support. P.G. was supported by NSF award PHY-1068111 and acknowledges support by the Oskar Klein Centre during his sabbatical visit. S.K. was supported by the US National Science Foundation grants PHY-0854724 and PHY-0955626. A.P. was supported by the Russian foundation for Basic Research, grant RFBR-10-02-01443-a. S.P. is partly supported by the US Department of Energy, Contract DE-FG02-04ER41268, and by NSF Grant PHY-0757911. P.S. is supported by the Lorne Trottier Chair in Astrophysics and an Institute for Particle Physics Theory Fellowship. The development of GALPROP is partially supported by NASA grants NNX09AC15G and NNX10AE78G, and by the Max-Planck Society.

Contribution 2

Further developments in the Flavour Les Houches Accord

F. Mahmoudi, S. Heinemeyer, A. Arbey, A. Bharucha, T. Goto, U. Haisch, S. Kraml, M. Muhlleitner, J. Reuter, P. Slavich

Abstract

The Flavour Les Houches Accord (FLHA) specifies a standard set of conventions for flavour-related parameters and observables such as Wilson coefficients, form factors, decay tables, etc, using the generic SUSY Les Houches Accord (SLHA) file structure. The accord provides a model-independent interface between codes evaluating and/or using flavour-related observables.

We present here a few clarifications and improvements to the accord. In addition, we provide instructions for a new block concerning the electric and magnetic dipole moments.

1 INTRODUCTION

The FLHA [17] exploits the existing organisational structure of SLHA [15, 16] and defines an accord for the exchange of flavour related quantities. In brief, the purpose of this accord is to present a set of generic definitions for an input/output file structure which provides a universal framework for interfacing flavour-related programs. Furthermore, the standardised format provides the users with clear and well-structured results.

The FLHA project has started in Les Houches 2009 where a first proposal was prepared [42]. This proposal was further completed in the form of an official and published write-up in [17]. FLHA is fully compatible with SLHA and can contain the SLHA blocks relevant for flavour physics such as SMINPUTS, VCKMIN, UPMNSIN, VCKM, IMVCKM, UPMNS, IMUPMNS and MODSEL. The FLHA specific block names start with “F” in order to emphasise their belonging to FLHA. The blocks which are already defined include: FCINFO, FMODESEL, FMASS, FLIFE, FCONST, FCONSTRATIO, FBAG, FWCOEF, IMFWCOEF, FOBS, FOBSERR, FOBSSM and FPARAM.

In the following, we provide more details about the definition of the meson mixings in BLOCK FOBS and introduce BLOCK FDIPOLE for the electric and magnetic dipole moments.

2 MESON MIXINGS

Meson mixing is assigned observable type 7 in BLOCK FOBS. In the FLHA, we assume the standard definition for the meson mixings. The oscillation frequency of Q_q^0 and \bar{Q}_q^0 mixing is characterised by the mass difference of the heavy and light mass eigenstates [43]:

$$\Delta M_q \equiv M_H^q - M_L^q = 2\text{Re} \sqrt{(M_{12}^q - \frac{i}{2}\Gamma_{12}^q)(M_{12}^{q*} - \frac{i}{2}\Gamma_{12}^{q*})}, \quad (1)$$

where M_{12} and Γ_{12} are the transition matrix elements from virtual and physical intermediate states respectively. For the kaon systems this gives:

$$\Delta M_K = 2\text{Re } M_{12}. \quad (2)$$

In the case of $\Delta B = 2$ transitions since $|\Gamma_{12}| \ll |M_{12}|$, one can write:

$$\langle B_q^0 | \mathcal{H}_{\text{eff}}^{\Delta B=2} | \bar{B}_q^0 \rangle = 2M_{B_q} M_{12}^q, \quad (3)$$

where M_{B_q} is the mass of B_q meson and

$$\Delta M_q = 2|M_{12}^q|. \quad (4)$$

The quantity given in the block is ΔM_q and the unit is fixed to 1/ps. We use the PDG number of the oscillating mesons for the parent and the flipped sign for the daughter.¹ The number of daughters is fixed to 1. For example, the $B_s - \bar{B}_s$ oscillation frequency is given as:

```
Block FOBS # Flavour observables
# ParentPDG type value q NDA ID1 ID2 ID3 ... comment
531 7 1.9e01 0 1 -531 # Delta M_s
```

Similarly, the corresponding SM values and the errors can be given in BLOCK FOBSSM and BLOCK FOBSERR, respectively. Note that the matrix elements (which are not physical observables) cannot be given in this block. Such quantities can be expressed in terms of Wilson coefficients, decay constants, bag parameters, etc. which are defined in the FLHA, or they can be given in a user defined block.

3 DIPOLE MOMENTS

We define BLOCK FDIPOLE which contains the electric and magnetic dipole moments. The standard for each line in the block should correspond to the FORTRAN format

```
(1x,I10,3x,I1,3x,I1,3x,1P,E16.8,0P,3x,'#',1x,A),
```

where the first ten-digit integer should be the PDG code of a particle, the second integer the type (electric or magnetic), the next integer the model (SM, NP or SM+NP, as in FWCOEF) and finally the last double precision number the value of the moment. The electric dipole moments must be given in e.cm unit.

The PDG codes for the nuclei follows the PDG particle numbering scheme [44]: “Nuclear codes are given as 10-digit numbers $\pm 10LZZZAAAI$. For a (hyper)nucleus consisting of n_p protons, n_n neutrons and n_Λ Λ 's, $A = n_p + n_n + n_\Lambda$ gives the total baryon number, $Z = n_p$ the total charge and $L = n_\Lambda$ the total number of strange quarks. I gives the isomer level, with $I = 0$ corresponding to the ground state ... To avoid ambiguities, nuclear codes should not be applied to a single hadron, like p , n or Λ^0 , where quark-contents-based codes already exist.” As an example, the PDG code of the deuteron is 1000010020.

The types of the moments are defined as follows:

¹Exceptions to this rule are possible, for instance, in the case of $K-\bar{K}$ mixing, where the states K_{long} and K_{short} with their PDG numbers 130 and 310, respectively, can be used.

- 1 : electric
- 2 : magnetic

The electric and magnetic moments can be given for the SM only, the New Physics (NP) only or the total contributions of both SM and NP, using the following definitions:

- 0 : SM
- 1 : NP
- 2 : SM+NP

For example the muon anomalous magnetic moment can be given as:

```
Block FDIPOLE # Electric and Magnetic dipole moments
# PDG_code type M value comment
13 2 1 3.02e-09 # 1/2 (g-2)_mu
```

CONCLUSIONS

The Flavour Les Houches Accord is a helpful tool for interfacing flavour physics and high p_T physics codes in order to exploit maximal information from both collider and flavour data. We presented here a few clarifications and improvements viz. the published write-up [17]. The FLHA will continue to improve as the number of codes and interfaces grows in order to accommodate the specific needs of the relevant programs.

Contribution 3

Extension of the SUSY Les Houches Accord 2 for see-saw mechanisms

L. Basso, A. Belyaev, D. Chowdhury, D.K. Ghosh, M. Hirsch, S. Khalil, S. Moretti, B. O'Leary, W. Porod, F. Staub

Abstract

The SUSY Les Houches Accord (SLHA) 2 extended the first SLHA to include various generalisations of the Minimal Supersymmetric Standard Model (MSSM) as well as its simplest next-to-minimal version. Here, we propose further extensions to it, to include the most general and well-established see-saw descriptions (types I/II/III, inverse, and linear) in both an effective and a simple gauged extension of the MSSM framework.

1 INTRODUCTION

If neutrinos are *Majorana* particles, their mass at low energy is described by a unique dimension-5 operator [45]

$$m_\nu = \frac{f}{\Lambda}(HL)(HL). \quad (1)$$

Using only renormalizable interactions, there are exactly three tree-level models leading to this operator [46]. The first one is the exchange of a heavy fermionic singlet, called the right-handed neutrino. This is the celebrated see-saw mechanism [47–51], nowadays called see-saw type I. The second possibility is the exchange of a scalar $SU(2)_L$ triplet [52, 53]. This is commonly known as see-saw type II. And lastly, one could also add one (or more) fermionic triplets to the field content of the SM [54]. This is known as see-saw type III. The see-saw mechanism provides a rationale for the observed smallness of neutrino masses, by the introduction of the inverse of some large scale Λ . In see-saw type I, for example, Λ is equal to the mass(es) of the right-handed neutrinos. Since these are $SU(2)_L$ singlets, their masses can take any value, and with neutrino masses as indicated by the results from oscillation experiments $m_\nu \sim \sqrt{\Delta m_A^2} \sim 0.05$ eV, where Δm_A^2 is the atmospheric neutrino mass splitting, and couplings of order $\mathcal{O}(1)$, the scale of the see-saw is estimated to be very roughly $m_{SS} \sim 10^{15}$ GeV. This value is close to, but slightly lower than, the scale of grand unification. In addition there exist see-saw models with large couplings at the electroweak scale, such as the linear [55] and inverse [56] see-saw models.

In the MSSM the gauge couplings unify nearly perfectly at an energy scale close to $m_G \simeq 2 \times 10^{16}$ GeV. Adding new particles which are charged under the SM group at a scale below m_G tends to destroy this attractive feature of the MSSM, unless the new superfields come in complete $SU(5)$ multiplets. For this reason, within supersymmetric see-saw models, one usually realizes the type II see-saw by adding 15-plets [46, 57] and the type III see-saw by the addition of 24-plets.

Just like with any other extensions of the SM based on supersymmetry (SUSY), those implementing see-saw realisations have seen several different conventions used over the years, many of which have become widespread. Such a proliferation of conventions has some drawbacks though from a calculational point of view: results obtained by different authors or computing tools are not always directly comparable. Indeed, to enable this comparison, a consistency check of all the relevant conventions and the implementation of any necessary translations thereof must first be made. Needless to say, this is a time-consuming and rather error-prone task.

To remedy this problem, the original SUSY Les Houches Accord (SLHA1) was proposed [15]. The SLHA1 uniquely defined a set of conventions for SUSY models together with a common interface between codes. The latter can be broadly categorised in terms of four different kinds of tools: *(i)* spectrum calculators (which calculate the SUSY mass and coupling spectrum, assuming some SUSY-breaking terms and a matching of SM parameters to known data); *(ii)* observables calculators (packages which calculate one or more of the following: inclusive cross sections, decay partial widths, relic dark matter densities and indirect/precision observables); *(iii)* Monte Carlo (MC) event generators (which calculate exclusive cross sections through explicit simulation of high-energy particle collisions, by including resonance decays, parton showering, hadronisation and underlying-event effects); *(iv)* SUSY fitting programs (which fit SUSY model parameters to data). (See <http://www.ipp.dur.ac.uk/montecarlo/BSM/> for an up-to-date collection and description of such tools.) Further, SLHA1 provided users with input and output in a common format, which is more readily comparable and transferable. In short, the basic philosophy was to specify a unique set of conventions for SUSY extensions of the SM together with generic file structures to be communicated across the four types of codes above, *(i) – (iv)*, based on the transfer of three different ASCII files: one for model input, one for spectrum calculator output and one for decay calculator output.

The original protocol, SLHA1, was strictly limited to the MSSM with real parameters and R-parity conservation neglecting generation mixing. An expanded version was proposed in [16] (see also [58] in Ref. [59]), known as SLHA2, whereby various MSSM generalisations were included: *i.e.*, those involving CP, R-parity and flavour violation as well as the simplest extension of the MSSM, the so-called next-to-MSSM (NMSSM). Herein, we further develop this protocol, by including the most general and well-established see-saw descriptions in both an effective and a simple gauged extension of the MSSM. The new conventions and control switches described here comply with those of SLHA2 (and, retrospectively, also SLHA1) unless explicitly mentioned in the text. Our effort here is paralleled by other generalisations of the previous accords documented elsewhere in these proceedings, altogether eventually contributing to the definition of a future release of the original protocol.

2 THE SEE-SAW MECHANISM

In this section, we discuss different implementations of the see-saw mechanism. As already stated in the introduction, the aim of the see-saw mechanism is to explain the neutrino masses and mixing angles. This is done by linking the tiny masses to other parameters which are of the naturally expected order. The general idea can be summarized by writing down the most general mass matrix combining left-handed neutrino (L), right-handed neutrino (R) and additional singlet fields carrying lepton number (S):

$$\begin{pmatrix} m_{LL} & m_{LR} & m_{LS} \\ m_{LR}^T & m_{RR} & m_{RS} \\ m_{LS}^T & m_{RS}^T & m_{SS} \end{pmatrix} \quad (2)$$

Looking at specific limits of this matrix, we can recover the different see-saw realizations: $m_{LL} = m_{LS} = m_{RS} = 0$ leads to type I, type III is obtained in the same limit but with m_{RR} stemming from $SU(2)_L$ triplets. $m_{LL} = m_{RR} = m_{LS} = 0$ is the characteristic matrix for inverse see-saw, while $m_{LL} = m_{RR} = m_{SS} = 0$ is the standard parametrization of the linear see-saw. What all these different see-saw models have in common is the way the tiny neutrino masses are recovered, just by suppressing them with very high scales for the new fields. This is strictly true for the type I/II/III models. The linear and inverse see-saw versions work slightly differently: the heaviness of the new fields is reduced at the price of introducing a relatively small dimensionless parameter, usually connected to an explicit violation of the lepton number.

In the following subsection we discuss models which can explain the origin of the distinct neutrino mass matrices.

2.1 Type I/II/III

The simplest see-saw models describe neutrino masses with an effective operator arising after integrating out heavy superfields. While one generation of 15-plets is sufficient to explain the entire neutrino data, this is not the case with just one 24-plet if $SU(5)$ -invariant boundary conditions are assumed on the new parameters and more generations have to be included. We will therefore treat the number of generations of singlets, 15- and 24-plets as free parameter. Bearing this in mind, the models will be described with minimal addition of superfields, in the basis after $SU(5)$ symmetry breaking (see table 1¹). All these fields are integrated out during the RGE evaluation, such that, at the SUSY scale, only the particle content of the MSSM remains.

We give in the following the unified equations which would lead to a mixed scenario of see-saw types I, II, and III. The Eqs (3), (6), and (9) are specific to type I, Eqs (4), (7), and (10) refer to type II and Eqs (5), (8), and (11) refer to type III.

The combined superpotential of all three types can be written as

$$W - W_{\text{MSSM}} = W_I + W_{II} + W_{III}$$

where

$$W_I = Y_\nu \hat{\nu}^c \hat{L} \hat{H}_u + \frac{1}{2} M_{\nu^c} \hat{\nu}^c \hat{\nu}^c \quad (3)$$

$$W_{II} = \frac{1}{\sqrt{2}} Y_T \hat{L} \hat{T} \hat{L} + \frac{1}{\sqrt{2}} Y_S \hat{d}^c \hat{S} \hat{d}^c + Y_Z \hat{d}^c \hat{Z} \hat{L} \\ + \frac{1}{\sqrt{2}} \lambda_1 \hat{H}_d \hat{T} \hat{H}_d + \frac{1}{\sqrt{2}} \lambda_2 \hat{H}_u \hat{T} \hat{H}_u + M_T \hat{T} \hat{T} + M_Z \hat{Z} \hat{Z} + M_S \hat{S} \hat{S} \quad (4)$$

$$W_{III} = \sqrt{\frac{3}{10}} Y_B \hat{H}_u \hat{B}_M \hat{L} + Y_W \hat{H}_u \hat{W}_M \hat{L} + Y_X \hat{H}_u \hat{X}_M \hat{d}^c \\ + M_X \hat{X}_M \hat{X}_M + \frac{1}{2} M_W \hat{W}_M \hat{W}_M + \frac{1}{2} M_G \hat{G}_M \hat{G}_M + \frac{1}{2} M_B \hat{B}_M \hat{B}_M \quad (5)$$

The soft-breaking terms can be split into three categories: terms stemming from the superpotential couplings when replacing the fermions with their scalar superpartners ($L_{SB,W}$), the scalar soft-breaking masses for each chiral superfield ($L_{SB,\phi}$) and the soft-breaking masses for

¹We use always the convention that all given $U(1)$ charges are those appearing in the covariant derivative, i.e. $\partial_\mu - igQA_\mu$.

Type I					
SF	Spin 0	Spin $\frac{1}{2}$	Generations	$U(1) \otimes SU(2) \otimes SU(3)$	R -parity of fermion
$\hat{\nu}^c$	$\tilde{\nu}^c$	ν^c	n_1	$(0, \mathbf{1}, \mathbf{1})$	+
Type II					
SF	Spin 0	Spin $\frac{1}{2}$	Generations	$U(1) \otimes SU(2) \otimes SU(3)$	R -parity of fermion
\hat{T}	\tilde{T}	T	n_{15}	$(1, \mathbf{3}, \mathbf{1})$	−
$\hat{\bar{T}}$	$\tilde{\bar{T}}$	\bar{T}	n_{15}	$(-1, \mathbf{3}, \mathbf{1})$	−
\hat{S}	\tilde{S}	S	n_{15}	$(-\frac{2}{3}, \mathbf{1}, \mathbf{6})$	−
$\hat{\bar{S}}$	$\tilde{\bar{S}}^*$	\bar{S}^*	n_{15}	$(\frac{2}{3}, \mathbf{1}, \bar{\mathbf{6}})$	−
\hat{Z}	\tilde{Z}	Z	n_{15}	$(\frac{1}{6}, \mathbf{2}, \mathbf{3})$	−
$\hat{\bar{Z}}$	$\tilde{\bar{Z}}$	\bar{Z}	n_{15}	$(-\frac{1}{6}, \mathbf{2}, \bar{\mathbf{3}})$	−
Type III					
SF	Spin 0	Spin $\frac{1}{2}$	Generations	$U(1) \otimes SU(2) \otimes SU(3)$	R -parity of fermion
\hat{W}_M	\tilde{W}_M	W_M	n_{24}	$(0, \mathbf{3}, \mathbf{1})$	+
\hat{G}_M	\tilde{G}_M	G_M	n_{24}	$(0, \mathbf{1}, \mathbf{8})$	+
\hat{B}_M	\tilde{B}_M	B_M	n_{24}	$(0, \mathbf{1}, \mathbf{1})$	+
\hat{X}_M	\tilde{X}_M	X_M	n_{24}	$(\frac{5}{6}, \mathbf{2}, \bar{\mathbf{3}})$	+
$\hat{\bar{X}}_M$	$\tilde{\bar{X}}_M$	\bar{X}_M	n_{24}	$(-\frac{5}{6}, \mathbf{2}, \mathbf{3})$	+

Table 1: New chiral superfields appearing in the effective type I/II/III see-saw models. While $n_{15} = 1$ is sufficient to explain neutrino data, n_1 and n_{24} must be at least 2.

the gauginos ($L_{SB,\lambda}$). Since the gauge sector is not modified, $L_{SB,\lambda}$ reads as in the MSSM. The soft-breaking terms stemming from the superpotential are

$$L_{SB,W} - L_{SB,W,MSSM} = L_{SB,W}^I + L_{SB,W}^{II} + L_{SB,W}^{III}$$

where

$$L_{SB,W}^I = T_\nu \tilde{\nu}^c \tilde{L} H_u + \frac{1}{2} B_{\nu^c} \tilde{\nu}^c \tilde{\nu}^c + \text{H.c.} \quad (6)$$

$$L_{SB,W}^{II} = \frac{1}{\sqrt{2}} T_T \tilde{L} \tilde{T} \tilde{L} + \frac{1}{\sqrt{2}} T_S \tilde{d}^c \tilde{S} \tilde{d}^c + T_Z \tilde{d}^c \tilde{Z} \tilde{L} + \frac{1}{\sqrt{2}} T_1 H_d \tilde{T} H_d \\ + \frac{1}{\sqrt{2}} T_2 H_u \tilde{T} H_u + B_T \tilde{T} \tilde{T} + B_Z \tilde{Z} \tilde{Z} + B_S \tilde{S} \tilde{S} + \text{h.c.} \quad (7)$$

$$L_{SB,W}^{III} = \sqrt{\frac{3}{10}} T_B H_u \tilde{B}_M \tilde{L} + T_W H_u \tilde{W}_M \tilde{L} + T_X H_u \tilde{X}_M \tilde{d}^c + B_X \tilde{X}_M \tilde{\bar{X}}_M \\ + \frac{1}{2} B_W \tilde{W}_M \tilde{W}_M + \frac{1}{2} B_G \tilde{G}_M \tilde{G}_M + \frac{1}{2} B_B \tilde{B}_M \tilde{B}_M + \text{H.c.} \quad (8)$$

while the soft-breaking scalar masses read

$$L_{SB,\phi} - L_{SB,\phi,MSSM} = L_{SB,\phi}^I + L_{SB,\phi}^{II} + L_{SB,\phi}^{III}$$

where

$$L_{SB,\phi}^I = -(\tilde{\nu}^c)^\dagger m_{\nu^c}^2 \tilde{\nu}^c \quad (9)$$

$$L_{\text{SB},\phi}^{II} = -m_S^2 \tilde{S}^* \tilde{S} - m_{\tilde{S}}^2 \tilde{S}^* \tilde{S} - m_T^2 \tilde{T}^* \tilde{T} - m_{\tilde{T}}^2 \tilde{T}^* \tilde{T} - m_Z^2 \tilde{Z}^* \tilde{Z} - m_{\tilde{Z}}^2 \tilde{Z}^* \tilde{Z} \quad (10)$$

$$L_{\text{SB},\phi}^{III} = -\tilde{B}_M^\dagger m_B^2 \tilde{B}_M - \tilde{W}_M^\dagger m_W^2 \tilde{W}_M - \tilde{G}_M^\dagger m_G^2 \tilde{G}_M \\ - \tilde{X}_M^\dagger m_X^2 \tilde{X}_M - \tilde{\tilde{X}}_M^\dagger m_{\tilde{X}}^2 \tilde{\tilde{X}}_M \quad (11)$$

2.1.0.1 GUT conditions and free parameters

Since the new interactions in Eq.s (4) to (5) are the result of $SU(5)$ -invariant terms, it is natural to assume a unification of the different couplings at the GUT scale.

$$M_T = M_Z = M_S \equiv M_{15}, \quad Y_S = Y_T = Y_Z \equiv Y_{15} \quad (12)$$

$$Y_B = Y_W = Y_X \equiv Y_{24}, \quad M_X = M_W = M_G = M_B \equiv M_{24} \quad (13)$$

In the same way the bi- and trilinear soft-breaking terms unify and they are connected to the superpotential parameters by

$$B_{\nu^c} \equiv B_0 M_{\nu^c}, \quad T_\nu \equiv A_0 Y_\nu \quad (14)$$

$$B_{15} \equiv B_0 M_{15}, \quad T_{15} \equiv A_0 Y_{15} \quad (15)$$

$$B_{24} \equiv B_0 M_{24}, \quad T_{24} \equiv A_0 Y_{24} \quad (16)$$

In case of CMSSM-like boundary conditions, this leads to the following free parameters

$$B_0, M_{\nu^c}, Y_\nu, M_{15}, \lambda_1, \lambda_2, Y_{15}, M_{24}, Y_{24} \quad (17)$$

in addition to the well-known MSSM parameters

$$m_0, M_{1/2}, A_0, \tan \beta, \text{sign}(\mu) \quad (18)$$

In principle, this B_0 is not the same as the B for the Higgs, though in a minimal case they may be defined to be equal at the GUT scale. Furthermore, $T_i = A_0 Y_i$ holds at the GUT scale.

2.1.0.2 Effective neutrino masses.

The effective neutrino mass matrices appearing in type I/II/III at SUSY scale are

$$m_\nu^I = -\frac{v_u^2}{2} Y_\nu^T M_R^{-1} Y_\nu \quad (19)$$

$$m_\nu^{II} = \frac{v_u^2}{2} \frac{\lambda_2}{M_T} Y_T. \quad (20)$$

$$m_\nu^{III} = -\frac{v_u^2}{2} \left(\frac{3}{10} Y_B^T M_B^{-1} Y_B + \frac{1}{2} Y_W^T M_W^{-1} Y_W \right). \quad (21)$$

2.2 Inverse and linear see-saw

The inverse and linear see-saw realisations are obtained in models that provide three generations of a further gauge singlet carrying lepton number in addition to three generations of the well-known right-handed neutrino superfields, here $\hat{\nu}^c$ (see table 2).

The only additional terms in the superpotential which are allowed by conservation of gauge quantum numbers are

$$W - W_{\text{MSSM}} = Y_\nu \hat{\nu}^c \hat{L} \hat{H}_u + M_R \hat{\nu}^c \hat{N}_S + \begin{cases} \frac{1}{2} \mu_N \hat{N}_S \hat{N}_S & \text{inverse see-saw} \\ Y_{LN} \hat{N}_S \hat{L} \hat{H}_u & \text{linear see-saw} \end{cases}. \quad (22)$$

SF	Spin 0	Spin $\frac{1}{2}$	Generations	$U(1) \otimes SU(2) \otimes SU(3)$	lepton number	R -parity of fermion
$\hat{\nu}^c$	$\tilde{\nu}^c$	ν^c	n_{ν^c}	$(0, \mathbf{1}, \mathbf{1})$	+1	+
\hat{N}_S	\tilde{N}_S	N_S	n_{N_S}	$(0, \mathbf{1}, \mathbf{1})$	-1	+

Table 2: New chiral superfields appearing in models with inverse and linear see-saw.

It is important to note that the last term in each model breaks lepton number explicitly, but is expected for different reasons.

The soft-breaking terms read

$$L_{\text{SB},W} = L_{\text{SB},W,\text{MSSM}} + T_\nu \tilde{\nu}^c \tilde{L} H_u + B_R \tilde{\nu}^c \tilde{N}_S + \left\{ \begin{array}{ll} \frac{1}{2} B_N \tilde{N}_S \tilde{N}_S & \text{inverse see-saw} \\ T_{LN} \tilde{N}_S \tilde{L} H_u & \text{linear see-saw} \end{array} \right\} + \text{H.c.} \quad (23)$$

$$L_{\text{SB},\phi} = L_{\text{SB},\phi,\text{MSSM}} - (\tilde{\nu}^c)^\dagger m_{\nu^c}^2 \tilde{\nu}^c - \tilde{N}_S m_N^2 \tilde{N}_S^*. \quad (24)$$

while $L_{\text{SB},\lambda}$ is again the same as for the MSSM. It is necessary to split the sneutrinos and the singlets into their scalar and pseudoscalar components:

$$\tilde{\nu}_L = \frac{1}{\sqrt{2}} (\sigma_L + i\phi_L), \quad \tilde{\nu}^c = \frac{1}{\sqrt{2}} (\sigma_R + i\phi_R), \quad \tilde{N}_S = \frac{1}{\sqrt{2}} (\sigma_S + i\phi_S). \quad (25)$$

In comparison to the MSSM, additional mixings between fields take place: the left- and right-handed scalar components mix with the scalar component of the singlet fields. The same holds for the pseudoscalar components. Furthermore, the neutrinos mix with the fermionic singlet fields to build up 9 Majorana fermions. All three appearing 9×9 mass matrices can be diagonalised by unitary matrices. We define the basis for the mass matrices as

- Scalar sneutrinos: $(\sigma_L, \sigma_R, \sigma_S)^T$
- Pseudoscalar sneutrinos: $(\phi_L, \phi_R, \phi_S)^T$
- Neutrinos: $(\nu_L, \nu^c, N_S)^T$

The neutrino mass matrix then reads

$$\left(\begin{array}{ccc} 0 & \frac{v_u}{\sqrt{2}} Y_\nu & 0 \\ \frac{v_u}{\sqrt{2}} Y_\nu^T & 0 & M_R \\ 0 & M_R^T & \mu_N \end{array} \right) \text{ (inverse) or } \left(\begin{array}{ccc} 0 & \frac{v_u}{\sqrt{2}} Y_\nu & \frac{v_u}{\sqrt{2}} Y_{LN} \\ \frac{v_u}{\sqrt{2}} Y_\nu^T & 0 & M_R \\ \frac{v_u}{\sqrt{2}} Y_{LN}^T & M_R^T & 0 \end{array} \right) \text{ (linear),} \quad (26)$$

Note, the presence of v_u in all terms of the first column and row is just coincidence caused by the given, minimal particle content. For more general models different VEVs can appear.

2.2.0.3 Free parameters

If CMSSM-like boundary conditions are assumed, the following new free parameters arise:

$$M_R, Y_{LN}, \mu_N, B_0 \quad (27)$$

in addition to those given in Eq. (18).

Calculating the eigenvalues of the above mass matrices, it can be seen that the light neutrino masses are linear functions of Y_{LN} in the linear see-saw models, while the neutrino masses

are linearly proportional to μ_N , as in the inverse see-saw models. The neutrino masses in the two models read

$$m_\nu^{LS} \simeq \frac{v_u^2}{2} (Y_\nu (Y_{LN} M_R^{-1})^T + (Y_{LN} M_R^{-1}) Y_\nu^T) , \quad (28)$$

$$m_\nu^{IS} \simeq \frac{v_u^2}{2} Y_\nu (M_R^T)^{-1} \mu_N M^{-1} Y_\nu^T . \quad (29)$$

Hence we propose that both models, and any combination of the two, be specified by extending Y_ν to a $3 \times (n_{\nu^c} + n_{N_S})$ Yukawa matrix, incorporating Y_{LN} as Y_ν^{ij} with i running from $n_{\nu^c} + 1$ to $n_{\nu^c} + n_{N_S}$. Implementation of each model consists of zeros being specified in the appropriate entries in the relevant matrices (*e.g.* specifying that the elements of Y_ν corresponding to Y_{LN} are zero recovers the inverse see-saw model, while specifying that μ_N is zero recovers the linear see-saw model).

2.3 See-saw in models with $U(1)_R \times U(1)_{B-L}$ gauge sector

Models based on a $SO(10)$ GUT theory can lead to a gauge sector containing the product group $U(1)_R \times U(1)_{B-L}$, through the breaking pattern

$$SO(10) \rightarrow SU(3)_C \times SU(2)_L \times SU(2)_R \times U(1)_{B-L} \rightarrow SU(3)_C \times SU(2)_L \times U(1)_R \times U(1)_{B-L} . \quad (30)$$

The $U(1)_R \times U(1)_{B-L}$ factors will be subsequently broken to the hypercharge $U(1)_Y$ of the SM. However, it is possible that this final breaking scale is just around the TeV scale without spoiling gauge unification [60]. This can therefore lead to interesting phenomenology and can have an important impact on the Higgs sector [61]. The first version of these models included a linear see-saw mechanism, but it has been shown that also the inverse see-saw can be included [62]. Since the realization of the linear model is rather involved, we describe here only the version with inverse see-saw.

Notice that, in general, these models contain not only gauge couplings per each Abelian gauge group, but also so-called ‘off-diagonal couplings’, as discussed in appendix A. The minimal particle content for such model extending the MSSM, leading to the spontaneous breaking of $U(1)_R \times U(1)_{B-L}$ and to neutrino masses, is given in table 3. This particle content consists of 3 generations of 16-plets of $SO(10)$, 2 additional Higgs fields and 3 generations of a singlet field. The vector superfields are given in table 4.

2.3.0.4 Superpotential

We assume for the following discussion that the superpotential can contain the following terms:

$$W - W_{MSSM} = Y_\nu \hat{\nu}^c \hat{L} \hat{H}_u - \mu_\xi \hat{\xi}_R \hat{\xi}_R + Y_{N\nu^c} \hat{N}_S \hat{\nu}^c \hat{\xi}_R + \mu_N \hat{N}_S \hat{N}_S . \quad (31)$$

Notice that, again, the \hat{N}_S superfield carries lepton number and that therefore the term μ_N provides its explicit violation.

2.3.0.5 Soft-breaking terms

$$L_{SB,W} - L_{SB,W,MSSM} = T_\nu \tilde{L} H_u \tilde{\nu}^c - B_\xi \bar{\xi}_R \xi_R + T_{N\nu^c} \tilde{N}_S \tilde{\nu}^c \xi_R + B_N \tilde{N}_S \tilde{N}_S + \text{H.c.} \quad (32)$$

SF	Spin 0	Spin $\frac{1}{2}$	Generations	$U(1)_{B-L} \otimes SU(2) \otimes U(1)_R \otimes SU(3)$
Matter fields (fermionic components have positive R -parity)				
\hat{Q}	$\tilde{Q} = \begin{pmatrix} \tilde{u}_L \\ \tilde{d}_L \end{pmatrix}$	$Q = \begin{pmatrix} u_L \\ d_L \end{pmatrix}$	3	$(\frac{1}{6}, \mathbf{2}, 0, \mathbf{3})$
\hat{L}	$\tilde{L} = \begin{pmatrix} \tilde{\nu}_L \\ \tilde{e}_L \end{pmatrix}$	$L = \begin{pmatrix} \nu_L \\ e_L \end{pmatrix}$	3	$(-\frac{1}{2}, \mathbf{2}, 0, \mathbf{1})$
\hat{u}^c	\tilde{u}^c	u^c	3	$(-\frac{1}{6}, \mathbf{1}, -\frac{1}{2}, \overline{\mathbf{3}})$
\hat{d}^c	\tilde{d}^c	d^c	3	$(-\frac{1}{6}, \mathbf{1}, \frac{1}{2}, \overline{\mathbf{3}})$
$\hat{\nu}^c$	$\tilde{\nu}^c$	ν^c	3	$(\frac{1}{2}, \mathbf{1}, -\frac{1}{2}, \mathbf{1})$
\hat{e}^c	\tilde{e}^c	e^c	3	$(\frac{1}{2}, \mathbf{1}, \frac{1}{2}, \mathbf{1})$
\hat{N}_S	\tilde{N}_S	N_S	n_{N_S}	$(0, \mathbf{1}, 0, \mathbf{1})$
Higgs fields (scalar components have positive R -parity)				
\hat{H}_d	$H_d = \begin{pmatrix} H_d^0 \\ H_d^- \end{pmatrix}$	$\tilde{H}_d = \begin{pmatrix} \tilde{H}_d^0 \\ \tilde{H}_d^- \end{pmatrix}$	1	$(0, \mathbf{2}, -\frac{1}{2}, \mathbf{1})$
\hat{H}_u	$H_u = \begin{pmatrix} H_u^+ \\ H_u^0 \end{pmatrix}$	$\tilde{H}_u = \begin{pmatrix} \tilde{H}_u^+ \\ \tilde{H}_u^0 \end{pmatrix}$	1	$(0, \mathbf{2}, \frac{1}{2}, \mathbf{1})$
$\hat{\xi}_R$	ξ_R^0	$\tilde{\xi}_R^0$	1	$(-\frac{1}{2}, \mathbf{1}, \frac{1}{2}, \mathbf{1})$
$\hat{\bar{\xi}}_R$	$\bar{\xi}_R^0$	$\tilde{\bar{\xi}}_R^0$	1	$(\frac{1}{2}, \mathbf{1}, -\frac{1}{2}, \mathbf{1})$

Table 3: Chiral Superfields appearing in models with $U(1)_R \times U(1)_{B-L}$ gauge sector which incorporate linear and inverse see-saw mechanisms.

SF	Spin $\frac{1}{2}$	Spin 1	$SU(N)$	Coupling	Name
\hat{B}'	$\lambda_{\tilde{B}'}$	B'	$U(1)$	g_{BL}	B-L
\hat{W}_L	λ_L	W_L	$SU(2)$	g_L	left
\hat{B}_R	$\lambda_{\tilde{B}_R}$	B_R	$U(1)$	g_R	right
\hat{g}	$\lambda_{\tilde{g}}$	g	$SU(3)$	g_s	color

Table 4: Vector superfields appearing in models with $U(1)_R \times U(1)_{B-L}$ gauge sector.

$$L_{SB,\phi} - L_{SB,\phi,\text{MSSM}} = -\tilde{N}_S^\dagger m_N^2 \hat{S} - m_\xi^2 |\xi_R|^2 - m_{\bar{\xi}}^2 |\bar{\xi}_R|^2 - (\tilde{\nu}^c)^\dagger m_{\nu^c}^2 \tilde{\nu}^c \quad (33)$$

$$L_{SB,\lambda} = \frac{1}{2} \left(-\lambda_{\tilde{B}'}^2 M_{B-L} - 2\lambda_{\tilde{B}'} \lambda_{\tilde{B}_R} M_{RB} - M_2 \lambda_{\tilde{W},i}^2 - M_3 \lambda_{\tilde{g},\alpha}^2 - \lambda_{\tilde{B}_R}^2 M_R + \text{H.c.} \right) \quad (34)$$

The term $\lambda_{\tilde{B}'} \lambda_{\tilde{B}_R} M_{RB}$ is a consequence of the presence of two Abelian gauge groups, see section A.

2.3.0.6 Symmetry breaking

Since it is assumed that in these models the scale of spontaneous symmetry breaking to the SM gauge group is near the TeV scale, it is possible to restrict ourselves to a direct one-step breaking pattern (*i.e.*, $SU(2)_L \times U(1)_R \times U(1)_{B-L} \rightarrow U(1)_{EM}$). This breaking pattern takes place when the Higgs fields in the left and right sectors receive VEVs. We can parametrise the

scalar fields as follows:

$$H_d^0 = \frac{1}{\sqrt{2}} (v_d + \sigma_d + i\phi_d), \quad H_u^0 = \frac{1}{\sqrt{2}} (v_u + \sigma_u + i\phi_u) \quad (35)$$

$$\xi_R = \frac{1}{\sqrt{2}} (v_{\xi_R} + \sigma_R + i\phi_R), \quad \bar{\xi}_R = \frac{1}{\sqrt{2}} (v_{\bar{\xi}_R} + \sigma_{\bar{R}} + i\phi_{\bar{R}}). \quad (36)$$

It is useful to define the quantities $v_R = v_{\xi_R}^2 + v_{\bar{\xi}_R}^2$ and $\tan \beta_R = \frac{v_{\bar{\xi}_R}}{v_{\xi_R}}$, in analogy to $v^2 = v_d^2 + v_u^2$ and to $\tan \beta = \frac{v_u}{v_d}$.

2.3.0.7 Particle mixing

Additional mixing effects take place in the gauge and Higgs sectors due to the additional gauge fields considered, besides the neutrino and sneutrino cases. The three neutral gauge bosons B' , B_R and W^3 mix to form three mass eigenstates: the massless photon, the well-known Z boson, and a Z' boson. This mixing can be parameterised by a unitary 3×3 matrix which diagonalises the mass matrix of the gauge bosons, such as

$$(\gamma, Z, Z')^T = U^{\gamma ZZ'} (B', B_R, W^3)^T. \quad (37)$$

Similarly, this model contains 7 neutralinos which are an admixture of the three neutral gauginos, of the two neutral components of the Higgsino doublets and of the two additional fermions coming from the right sector. The mass matrix, written in the basis $(\lambda_{\tilde{B}'}, \tilde{W}^0, \tilde{H}_d^0, \tilde{H}_u^0, \lambda_{\tilde{B}_R}, \tilde{\xi}_R, \tilde{\bar{\xi}}_R)$, can be diagonalised by a unitary matrix, here denoted with Z^N . In the Higgs sector we choose the mixing basis and rotation matrices to be, respectively,

- Scalar Higgs fields: $(\sigma_d, \sigma_u, \sigma_R, \sigma_{\bar{R}})^T$ and Z^H
- Pseudoscalar Higgs fields: $(\phi_d, \phi_u, \phi_R, \phi_{\bar{R}})^T$ and Z^A .

The neutrino and sneutrino sectors are similar to the case discussed in section 2.2: the scalar fields are decomposed into their CP -even and odd components according to eq. (25). The mass matrices are defined in the same basis. If all terms of Eq. (31) are present, the resulting masses of the light neutrinos are a result of an inverse see-saw. The mass matrix is analog to the left matrix given in Eq. (26) with M_R replaced by $\frac{1}{\sqrt{2}} Y_{N\nu^c} v_{\xi_R}$.

2.3.0.8 Free parameters

If CMSSM-like boundary conditions are assumed, the following new free parameters arise:

$$Y_{N\nu^c}, \mu_N, B_0, \tan \beta_R, \text{sign}(\mu_\xi) M_{Z'} \quad (38)$$

in addition to those given in Eq. (18). Here we have assumed that the parameters μ_ξ and B_ξ are fixed by the tadpole equations. The relationships of the soft trilinear terms to the Yukawa couplings are as before, and $B_N = B_0 \mu_N$.

2.4 See-saw in models with $U(1)_Y \times U(1)_{B-L}$ gauge sector

The final category of models considered here includes an additional $B-L$ gauge group tensored to the SM gauge groups, *i.e.* $SU(3)_C \times SU(2)_L \times U(1)_Y \times U(1)_{B-L}$. The corresponding vector superfields are given in table 5. The minimal version of these models [63–65] extends

the MSSM particle content with three generations of right-handed superfields. Two additional scalars, singlets with respect to SM gauge interactions but carrying $B - L$ charge, are added to break $U(1)_{B-L}$, as well as allowing for a Majorana mass term for the right-handed neutrino superfields. Furthermore, two new lepton fields per generation can be included to specifically implement the inverse see-saw mechanism [66]. All particles and their quantum numbers are given in table 6. This table contains also the charge assignment under a Z_2 symmetry which is just present in case of the inverse see-saw model².

SF	Spin $\frac{1}{2}$	Spin 1	$SU(N)$	Coupling	Name
\hat{B}	$\lambda_{\hat{B}}$	B	$U(1)$	g_1	hypercharge
\hat{W}	$\lambda_{\hat{W}}$	W^-	$SU(2)$	g_2	left
\hat{g}	$\lambda_{\hat{g}}$	g	$SU(3)$	g_3	color
\hat{B}'	$\lambda_{\hat{B}'}$	B'	$U(1)$	g_B	B-L

Table 5: Vector superfields appearing in models with $U(1)_Y \times U(1)_{B-L}$ gauge sector.

SF	Spin 0	Spin $\frac{1}{2}$	Generations	$(U(1)_Y \otimes SU(2) \otimes SU(3) \otimes U(1)_{B-L})$	Z_2 inverse SS
Matter fields (fermionic components have positive R -parity)					
\hat{Q}	$\tilde{Q} = \begin{pmatrix} \tilde{u}_L \\ \tilde{d}_L \end{pmatrix}$	$Q = \begin{pmatrix} u_L \\ d_L \end{pmatrix}$	3	$(\frac{1}{6}, \mathbf{2}, \mathbf{3}, \frac{1}{6})$	+
\hat{L}	$\tilde{L} = \begin{pmatrix} \tilde{\nu}_L \\ \tilde{e}_L \end{pmatrix}$	$L = \begin{pmatrix} \nu_L \\ e_L \end{pmatrix}$	3	$(-\frac{1}{2}, \mathbf{2}, \mathbf{1}, -\frac{1}{2})$	+
\hat{d}^c	\tilde{d}^c	d^c	3	$(\frac{1}{3}, \mathbf{1}, \bar{\mathbf{3}}, -\frac{1}{6})$	+
\hat{u}^c	\tilde{u}^c	u^c	3	$(-\frac{2}{3}, \mathbf{1}, \bar{\mathbf{3}}, -\frac{1}{6})$	+
\hat{e}^c	\tilde{e}^c	e^c	3	$(1, \mathbf{1}, \mathbf{1}, \frac{1}{2})$	+
$\hat{\nu}^c$	$\tilde{\nu}^c$	ν^c	3	$(0, \mathbf{1}, \mathbf{1}, \frac{1}{2})$	+
Higgs fields (scalar components have positive R -parity)					
$\hat{\eta}$	η	$\tilde{\eta}$	1	$(0, \mathbf{1}, \mathbf{1}, -1)$	-
$\hat{\tilde{\eta}}$	$\tilde{\eta}$	$\tilde{\tilde{\eta}}$	1	$(0, \mathbf{1}, \mathbf{1}, +1)$	-
\hat{H}_d	H_d	\tilde{H}_d	1	$(-\frac{1}{2}, \mathbf{2}, \mathbf{1}, 0)$	+
\hat{H}_u	H_u	\tilde{H}_u	1	$(\frac{1}{2}, \mathbf{2}, \mathbf{1}, 0)$	+
Additional field for inverse see-saw (fermionic components have positive R -parity)					
\hat{N}_S	\tilde{N}_S	N_S	n_{N_S}	$(0, \mathbf{1}, \mathbf{1}, -\frac{1}{2})$	-
\hat{N}'_S	\tilde{N}'_S	N'_S	$n_{N'_S}$	$(0, \mathbf{1}, \mathbf{1}, \frac{1}{2})$	+

Table 6: Chiral Superfields appearing in models with $U(1)_Y \times U(1)_{B-L}$ gauge sector. The minimal particle content is needed for see-saw type I, the additional fields can be used to incorporate an inverse see-saw. The $SU(2)_L$ doublets are named as in table 3. The Z_2 in the last column is not present in the minimal model but just in the model with inverse see-saw. The number of generations of \hat{N}'_S must match those of \hat{N}_S for anomaly cancellation.

²Notice that in comparison to Ref. [66], the charge assignments of the new particles in the inverse see-saw model, as well as the Z_2 symmetry, have been redefined for consistency with the similar minimal model of Ref. [63].

The additional terms for the superpotential in comparison to the MSSM read

$$W - W_{\text{MSSM}} = Y_\nu \hat{l} \hat{H}_u \hat{\nu}^c + \begin{cases} Y_{\eta\nu^c} \hat{\nu}^c \hat{\eta} \hat{\nu}^c - \mu_\eta \hat{\eta} \hat{\eta} & \text{minimal see-saw} \\ Y_{IS} \hat{\nu}^c \hat{\eta} \hat{N}'_S + \mu_N \hat{N}'_S \hat{N}'_S & \text{inverse see-saw} \end{cases}.$$

The extra parity is not applicable to the minimal case, thus the see-saw term $Y_{\eta\nu^c} \hat{\nu}^c \hat{\eta} \hat{\nu}^c$ is allowed, whereas it is forbidden in the inverse see-saw model. Instead, in the inverse see-saw model the $\mu_N \hat{N}'_S \hat{N}'_S$ term plays an important role, even though since \hat{N}'_S carries $B - L$ charge, this term violates $B - L$ charge conservation similarly to the terms in Eq. (22) and Eq. (31) which break lepton number. This term is assumed to come from higher-order effects. (A similar term for the \hat{N}'_S field is possible but not relevant, since the N'_S does not take part in the mixing with the neutrinos.) A possible bilinear term $\hat{N}'_S \hat{N}'_S$ is forbidden by the Z_2 symmetry given in the last column of Table 6. This discrete symmetry also forbids terms like $\hat{N}'_S \hat{N}'_S \eta$ or $\hat{N}'_S \hat{N}'_S \bar{\eta}$ as well as the μ_η -term that is necessary to obtain a pure inverse see-saw scenario. The additional soft-breaking terms are written as follows:

$$L_{\text{SB},W} - L_{\text{SB},W,\text{MSSM}} = T_\nu \tilde{l} H_u \tilde{\nu}^c + \begin{cases} T_{\eta\nu^c} \tilde{\nu}^c \eta \tilde{\nu}^c - B_\eta \eta \bar{\eta} & \text{minimal see-saw} \\ T_{IS} \tilde{\nu}^c \eta \tilde{N}'_S + B_N \tilde{N}'_S \tilde{N}'_S & \text{inverse see-saw} \end{cases} + \text{H.c.} \quad (39)$$

$$L_{\text{SB},\phi} - L_{\text{SB},\phi,\text{MSSM}} = -m_\eta^2 |\eta|^2 - m_{\bar{\eta}}^2 |\bar{\eta}|^2 - (\tilde{N}'_S m_N^2 \tilde{N}'_S + \tilde{N}'_{S'} m_{N'}^2 \tilde{N}'_S \text{ in inverse see-saw}) \quad (40)$$

$$L_{\text{SB},\lambda} = \frac{1}{2} \left(-\lambda_B^2 M_1 - \lambda_{\tilde{B}} \lambda_{\tilde{B}'} M_{BB'} - M_2 \lambda_{\tilde{W},i}^2 - M_3 \lambda_{\tilde{g},\alpha}^2 - \lambda_{\tilde{B}'}^2 M_{BL} + \text{H.c.} \right) \quad (41)$$

To break $SU(2)_L \times U(1)_Y \times U(1)_{B-L}$ to $U(1)_{em}$, the neutral MSSM Higgs fields and the new SM scalar singlets acquire VEVs:

$$H_d^0 = \frac{1}{\sqrt{2}} (v_d + \sigma_d + i\phi_d), \quad H_u^0 = \frac{1}{\sqrt{2}} (v_u + \sigma_u + i\phi_u) \quad (42)$$

$$\eta = \frac{1}{\sqrt{2}} (\sigma_\eta + v_\eta + i\phi_\eta), \quad \bar{\eta} = \frac{1}{\sqrt{2}} (\sigma_{\bar{\eta}} + v_{\bar{\eta}} + i\phi_{\bar{\eta}}) \quad (43)$$

We also define here

$$v^2 = v_d^2 + v_u^2, \quad \tan \beta = \frac{v_u}{v_d} \quad (44)$$

as well as

$$v_x = v_{\eta_R}^2 + v_{\bar{\eta}_R}^2, \quad \tan \beta' = \frac{v_{\bar{\eta}}}{v_\eta} \quad (45)$$

The left- and right-handed sneutrinos are decomposed into their scalar and pseudoscalar components according to Eq. (25). Similarly, in the inverse see-saw model, the scalar component of \hat{N}'_S reads

$$\tilde{N}'_S = \frac{1}{\sqrt{2}} (\sigma_S + i\phi_S) \quad (46)$$

The additional mixing effects which take place in this model are similar to the case of $U(1)_R \times U(1)_{B-L}$ discussed in section 2.3. In the gauge sector three neutral gauge bosons appear which mix to give rise to the massless photon, the Z boson, and a Z' boson:

$$(\gamma, Z, Z')^T = U^{\gamma Z} (B, W^3, B')^T. \quad (47)$$

Notice that when the kinetic mixing is neglected, the B' field decouples and the mass matrix of the gauge bosons becomes block diagonal, where the upper 2×2 block reads as in the SM. In the matter sector we choose the basis and the mixing matrices which diagonalise the mass matrices respectively as follows:

- Neutralinos: $(\lambda_{\tilde{B}}, \tilde{W}^0, \tilde{H}_d^0, \tilde{H}_u^0, \lambda_{\tilde{B}'}, \tilde{\eta}, \tilde{\bar{\eta}})^T$ and Z^N
- Scalar Higgs fields: $(\sigma_d, \sigma_u, \sigma_\eta, \sigma_{\bar{\eta}})^T$ and Z^H
- Pseudoscalar Higgs fields: $(\phi_d, \phi_u, \phi_\eta, \phi_{\bar{\eta}})^T$ and Z^A
- Scalar sneutrinos: $(\sigma_L, \sigma_R, \sigma_S)^T$ and $Z^{\sigma\nu}$
- Pseudoscalar sneutrinos: $(\phi_L, \phi_R, \phi_S)^T$ and $Z^{\phi\nu}$
- Neutrinos: $(\nu_L, \nu^c, N_S)^T$ and U^V

where the σ_S, ϕ_S , and N_S are only present in the inverse see-saw case. The neutrino mass matrices for the minimal and inverse see-saw cases can be written as

$$\left(\begin{array}{cc} 0 & \frac{v_u}{\sqrt{2}} Y_\nu \\ \frac{v_u}{\sqrt{2}} Y_\nu^T & \frac{v_\eta}{\sqrt{2}} Y_{\eta\nu^c} \end{array} \right) \text{ or } \left(\begin{array}{ccc} 0 & \frac{v_u}{\sqrt{2}} Y_\nu & 0 \\ \frac{v_u}{\sqrt{2}} Y_\nu^T & 0 & \frac{v_\eta}{\sqrt{2}} Y_{IS} \\ 0 & \frac{v_\eta}{\sqrt{2}} Y_{IS}^T & \mu_N \end{array} \right) \quad (48)$$

respectively. In the minimal case, the see-saw of type I is recovered. The light neutrino mass matrix can be approximated in this case by

$$m_\nu \simeq -\frac{v_u^2}{\sqrt{2}v_\eta} Y_\nu Y_{\eta\nu^c}^{-1} Y_\nu. \quad (49)$$

In the inverse see-saw case, the light neutrino masses can be written as

$$m_\nu \simeq -\frac{v_u^2}{2} Y_\nu^T (Y_{IS}^T)^{-1} \mu_N Y_{IS} Y_\nu \quad (50)$$

2.4.0.9 Free parameters

If the minimum conditions for the vacuum are solved with respect to μ, B_μ, μ_η and B_η , the following parameters can be treated as free in addition of those given in Eq. (18):

$$Y_{\eta\nu^c}, Y_{IS}, \mu_N, B_0, \tan\beta', \text{sign}(\mu_\eta), M_{Z'} \quad (51)$$

where we have used again $B_N = B_0 \mu_N$.

3 TOWARDS SLHA_{v3}

The purpose of this paper is to define the extensions of the SUSY Les Houches Accords required to incorporate the models described above. In this context and with respect to the implementation of further models in future, it is helpful to propose some general rules for the naming of blocks and the allocation of PDG particle codes, which we present below.

We would like to point out that the SLHA conventions allow for redundant information to be contained in additional blocks. Hence, in the interests of backward compatibility, we propose that if the following names for the blocks are used, but in cases where the old SLHA1/2 blocks would also suffice, they should also be written in addition, *e.g.* if there are only four neutralinos, NMIX should be written as well as NEUTRALINORM, both containing the same information.

3.0.0.10 *Block names for input and output*

Blocks used to give parameters as input end with “IN”, while the corresponding values as output are written in blocks without the ending “IN”. For example, the gauge couplings at the output scale are given in the GAUGE block, while one could define them as input at the input scale with the GAUGEIN block.

3.0.0.11 *Block names for mixing matrices*

In SLHA 2 the neutralino and Higgs mixing matrices of the MSSM and NMSSM were named differently. However, the information about the current model is already given in the block MODSEL and the renaming is thus redundant. Therefore, in order to prevent a confusing amount of names for mixing matrices in different models we propose to use always the same names for the following mixing matrices regardless of their dimension:

- Scalar Higgs mixing matrix: SCALARRM
- Pseudoscalar Higgs mixing matrix: PSEUDOSCALARRM
- Charged Higgs mixing matrix: CHARGEDSCALARRM
- Neutralino mixing matrix: NEUTRALINORM (corresponds to NMIX in SLHA1/2)
- Chargino mixing matrices: CHARGINOPLUSRM and CHARGINOMINUSRM (corresponds to VMIX and UVMIX respectively in SLHA1/2)
- Up-squark mixing matrix: UPSQUARKRM (corresponds to USQMIX in SLHA1/2)
- Down-squark mixing matrix: DOWNSQUARKRM (corresponds to DSQMIX in SLHA1/2)
- Charged slepton mixing matrix: CHARGEDSLEPTONRM (corresponds to SELMIX in SLHA1/2)
- Sneutrino mixing matrix: SNEUTRINORM (corresponds to SNUMIX in the MSSM). In the case of splitting the sneutrinos into real and imaginary parts, SNEUTRINOEVENRM for the CP-even and SNEUTRINOODDRM for the CP-odd states should be used (corresponding to SNSMIX and SNMIX in SLHA1/2)

To distinguish these names from the SLHA1/2-specific names we have always used the suffix RM for Rotation Matrix.

3.0.0.12 *Block names for couplings*

For the naming of blocks which correspond to couplings and soft-breaking terms we propose to use names which already give information about the meaning of the parameter: the new names contain abbreviations for the involved fields and start with a prefix to assign the meaning of the parameters. The different prefixes should be

- Y: trilinear superpotential coupling
- T: trilinear softbreaking coupling
- M: bilinear superpotential coupling
- B: bilinear softbreaking coupling
- L: linear superpotential coupling
- S: linear softbreaking coupling
- M2: soft breaking scalar mass-squared

Because of the prefixes which already give information about the spin of the involved particles, it is not necessary to distinguish between fermions and scalars when naming the blocks.

However, this requires the convention that all Majorana mass terms for fermions from chiral superfields appear in the superpotential, leaving only bilinear mass terms for the scalars in the soft SUSY-breaking Lagrangian. We propose the following names:

- MSSM: H_u : HU, H_d : HD, d^c : D, u^c : U, q : Q, e^c : E, l : L
- See-saw types I-III: ν^c : NUR, S : 15S, \bar{S} : 15SB, Z : 15Z, \bar{Z} : 15ZB, T : 15T, \bar{T} : 15TB, G : 24G, W : 24W, X : 24X, \bar{X} : 24XB, B : 24B
- inverse and linear see-saw: S : SL
- $U(1)_R \times U(1)_{B-L}$ models: ξ_R : CR, $\bar{\xi}_R$: CRB
- $U(1)_Y \times U(1)_{B-L}$ models: η : BIL, $\bar{\eta}$: BILB, N_S : NS, N'_S : NSP

Using these conventions, the block YU for the up-type Yukawa coupling in the MSSM would be replaced by YHUQU and the block name for the μ -term would be MHUHD.

3.0.0.13 EXTPAR and MSOFT

In the MSSM the input parameters for the gaugino masses and the Higgs soft-breaking masses are given in EXTPAR. However, their output is given in MSOFT. Similarly, the singlet couplings in the NMSSM are defined by EXTPAR but their output is in NMSSMRUN. This is in some conflict with the general rule to use always the the input name plus IN as output. Therefore, we propose that all new one-dimensional soft-breaking parameters and couplings involved in the see-saw models presented here are not given in EXTPAR as input, but rather in the given output with the prefix IN.

3.0.0.14 PDG particle numbering scheme

We would like to introduce a consistent numbering scheme for the additional elementary particles introduced by such models, such that further particles may be added without worrying about accidentally using a pre-existing code, which also allows one to gather some information about the particle. While the proposed scheme would give new numbers to particles which already have codes, we restrict ourselves just to giving our new particles unique codes, while hoping that codes compliant with the new standard would be able to read either the old code or the new code for particles. The proposal is a signed nine digit integer for each mass eigenstate, which should easily fit in a 32-bit integer.

We note that the existing scheme is already mildly inconsistent, insofar as adding a fourth generation already has a PDG numbering scheme (17 for the extra neutrino and 18 for the τ'), yet SLHA2 uses 100017 and 100018 for CP-odd sneutrinos which are degrees of freedom from the first three generations. We note also that the Flavor Les Houches Accord [17] uses 17 and 18 for summing over the three Standard Model generations.

Since the particle code is a signed integer, pairs of conjugate particles are assigned the same code with different signs. We propose a convention for which particle gets the positive sign:

- If the particle is self-conjugate, there is only the positive sign. If the fermion is Majorana, it only has positive sign. If the scalar part of the superfield can be written in terms of self-conjugate CP eigenstates, it should be. If it cannot, the scalar field should be assigned a sign according to the rules below.

- If the particle has non-zero electric charge, the state with positive electric charge is taken as the particle (hence the positron is taken as the particle).
- If the particle is electrically neutral, but has baryon number B or lepton number L , the state with positive $B - L$ is taken as the particle (hence antineutrinos are taken as the particle).
- If the particle has $B - L = 0$ according to traditional assignment, but is still baryon- or lepton-like, a “temporary” $B - L$ is assigned. If the particle has color charge a temporary B is first assigned by finding the combination of triplets and antitriplets which could combine to form the particle’s representation: adding $+1/3$ for each triplet and $-1/3$ for each antitriplet, the combination which has the *lowest magnitude* of temporary B is assigned; *e.g.* an octet may be formed by a triplet with an antitriplet, giving $B = 0$, or by three triplets, giving $B = 1$, or three antitriplets, giving $B = -1$: in this case, $B = 0$ as the lowest $|B|$ is assigned. This temporary $B - L$ is only for the purposes of determining which state is taken to be the particle with positive code.
- If the neutral, colorless particle has no natural assignment by (temporary) $B - L$, there are still a few cases:
 - the fermion is massless: the left-handed fermion is given the positive code, thus in supersymmetric models, the scalars left-chiral superfields also are given positive codes if their fermions are massless.
 - the fermion has a Dirac mass: this does not occur in the MSSM, NMSSM, or any of the extended models described here. However it is conceivable. We propose that the model builder is responsible for deciding to assign a temporary lepton number to one of the fields and thus fix the convention.

Under this scheme, quarks and squarks would have the same signs as they already have in the PDG conventions, leptons would have the opposite sign (*e.g.* the muon would have a negative code), and charginos and W bosons would have the same signs.

Once the sign is fixed, the digits are as follows:

1st digit: 1 if it is a mass eigenstate which has an admixture of a Standard Model gauge eigenstate (including the Higgs doublet), 2 if it does not mix with the Standard Model particles.

2nd digit: twice the spin of the particle.

3rd digit: the CP nature: complex bosons (spin 0, 1, or 2) and Dirac fermions have 0, while (massless or massive) scalar bosons, massless vector bosons, massless tensor bosons, and Majorana fermions have 1. Pseudoscalar bosons (massless or massive) and massive vector and tensor bosons have 2.

4th and 5th digits: a 2-digit number for the $SU(3)$ representation; $SU(3)$ singlets have 00; representations up to dimension 64 have either the Dynkin labels for an unbarred representation, or 99 minus the Dynkin labels for the barred representation. These representations are enumerated in [67]. Any particles with $SU(3)$ representation that does not fit into this scheme are assigned 99 (for instance those of dimension 65 or greater).

6th and 7th digits: a 2-digit number for the electric charge; six times the absolute value of the electric charge, relative to the electron, up to a maximum of $98/6$. Any particle with a charge that does not fit into this scheme is assigned 99. For example, an electron would have 06, while a down quark would have 02, and a doubly-charged scalar would have 12.

8th and 9th digits: a generation number; 01 should be given to the lightest particle of any group which share the same first seven digits, 02 to the 2nd-lightest, and so on.

Consequently what might be considered to be the same model with or without R -parity will have different codes for some of its mass eigenstates. In the MSSM, with R -parity there would be three charged antileptons 110000601, 110000602, and 110000603, and two charginos 210000601 and 210000602, while without R -parity there would be five charged antileptons 110000601, 110000602, 110000603, 110000604 and 110000605, and no 210000601 or 210000602.

Additionally, the codes for the neutrinos will depend on whether they are Dirac or Majorana in the considered model.

4 EXTENSIONS TO SLHA

In this section we describe the implementation of the models presented in section 2 using the conventions defined in the previous section. Note that all parameters can be implemented in complex forms and the corresponding information can be passed by using the corresponding blocks starting with “IM” [16].

4.1 Block format

In the following, all blocks with a single index are to be written in the FORTRAN format (1x,I5,3x,1P,E16.8,0P,3x,'#',1x,A) (the same format as the SLHA1 blocks HMIX, GAUGE, *etc.*). These blocks will be denoted as “rank one”. All blocks with two indices are to be written in the FORTRAN format (1x,I2,1x,I2,3x,1P,E16.8,0P,3x,'#',1x,A) (the same format as the SLHA1 blocks NMIX, UMIX, *etc.*). These blocks will be denoted as “rank two”. All blocks with two indices are to be written in the FORTRAN format (1x,I2,1x,I2,1x,I2,3x,1P,E16.8,0P,3x,'#',1x,A) (the same format as the SLHA2 blocks RVLAMLLE, RVLAMLQD, *etc.*). These blocks will be denoted as “rank three”.

4.2 Blocks required for each model

Each model requires the presence of certain blocks. Some blocks are common to several models. We summarize the blocks needed for each of the models described in section 2 under the entry for selecting this model in the MODSEL block 4.3.1.

4.3 Extra Flags In Existing Blocks

4.3.1 Block MODSEL

Flag 3 (particle content) has further switches, arranged in groups: 11X is for effective realizations, 12X non-effective models, 13X for $U(1)_R \times U(1)_{B-L}$ models, and 14X is for $U(1)_Y \times U(1)_{B-L}$ models, the initial digit 1 indicating see-saw. 2XY might be used for fourth-generation models, 3XY for another set of models, and so on. In addition to the sets of required blocks listed for each model below, the SEESAWGENERATIONS block must also be given, and the appropriate flags set.

– Effective models

110: Most general $SU(5)$ -invariant effective see-saw (combination of types I-III); all the blocks required for types I-III below are required.

- 111: type I see-saw; the following blocks are required: MNURNURIN, BNURNURIN, M2NURNURIN, YNURLHUIN, TNURLHUIN.
- 112: type II see-saw ($SU(5)$ version); the following blocks are required: M15S15SBIN, B15S15SBIN, M215SIN, M215SBIN, M15T15TBIN, B15T15TBIN, M215TIN, M215TBIN, M15Z15ZBIN, B15Z15ZBIN, M215ZIN, M215ZBIN, YD15SDIN, TD15SDIN, YL15TLIN, TL15TLIN, YD15ZLIN, TD15ZLIN, YHD15THDIN, THD15THDIN, YHU15TBHUIN, THU15TBHUIN. Any or all of the blocks M15S15SBIN, M15T15TBIN, M15Z15ZBIN may be left absent if the block M15IN is present, and the missing terms are taken as copies of M15IN. Similarly for YD15SDIN, YL15TLIN, YD15ZLIN and Y15IN, and TD15SDIN, TL15TLIN, TD15ZLIN and Y15IN times A_0 .
- 113: type III see-saw ($SU(5)$ version); the following blocks are required: M24W24WIN, B24W24WIN, M224WIN, M24G24GIN, B24G24GIN, M224GIN, M24B24BIN, B24B24BIN, M224BIN, M24X24XBIN, B24X24XBIN, M224XIN, M224XBIN, YHU24BLIN, THU24BLN, YHU24WLN, THU24WLN, YHU24BLIN, THU24BLN, YHU24XBDIN, THU24XBDIN. Any or all of the blocks M24W24WIN, M24G24GIN, M24B24BIN, M24X24XBIN may be left absent if the block M24IN is present, and the missing terms are taken as copies of M24IN. Similarly for B24W24WIN, B24G24GIN, B24B24BIN, B24X24XBIN and B24IN; YHU24BLIN, YHU24WLN, YHU24XBDIN and Y24IN; and THU24BLIN, THU24WLN, THU24XBDIN and Y24IN times A_0 .
- 114: type II see-saw (minimal version, only triplets); the following blocks are required: M15T15TBIN, B15T15TBIN, M215TIN, M215TBIN, YL15TLIN, TL15TLIN, YHD15THDIN, THD15THDIN, YHU15TBHUIN, THU15TBHUIN. If TL15TLIN is absent, YL15TLIN times A_0 is used in its place.
- 115: type III see-saw (minimal version, only triplets); the following blocks are required: M24W24WIN, B24W24WIN, M224WIN, YHU24WLN, THU24WLN. If THU24WLN is absent, YHU24WLN times A_0 is used in its place.
- Linear and inverse see-saw:
- 120 : combined inverse and linear see-saw; the following blocks are required: MNURSIN, BNURSIN, MNSNSIN, BNSNSIN, M2NSIN, M2NURIN, YNURLHUIN, TNURLHUIN. Purely inverse or linear see-saw is specified by appropriate zeroes in the block entries.
- $U(1)_R \times U(1)_{B-L}$:
- 131 : reserved for minimal see-saw
- 132 : inverse see-saw; the following blocks are required in addition to those required by the $U(1)_R \times U(1)_{B-L}$ minimal see-saw: MNSNSIN, BNSNSIN, M2NSIN, YNSNURCRIN, TNSNURCRIN.
- 133 : reserved for linear see-saw
- $U(1)_Y \times U(1)_{B-L}$:
- 141 : minimal see-saw; the following blocks are required: MBILBILBIN, BBILBILBIN, M2NURIN, M2BILIN, M2BILBIN, YNURLHUIN, TNURLHUIN, YNURBILNURIN, TNURBILNURIN.
- 142 : inverse see-saw; the following blocks are required in addition to those required by the $U(1)_Y \times U(1)_{B-L}$ minimal see-saw: MNSNSIN, BNSNSIN, M2NSIN, YNSNURBILIN, TNSNURBILIN.

In addition, the $U(1)_R \times U(1)_{B-L}$ and $U(1)_Y \times U(1)_{B-L}$ models require that the appropriate entries in GAUGEIN, MSOFTIN, MINPAR, and EXTPAR are set correctly.

4.3.2 *Block MINPAR*

We extend the MINPAR block to include the input parameters necessary for the addition of an extra Abelian gauge group. We do not reproduce the existing entries here since there are quite a few. We only show those that are new and those that have new interpretations.

- 2: The common soft mass term for all the the gauginos.
- 6: The cosine of the phase of the μ' parameter.
- 7: The ratio of the two vacuum expectation values that either break $U(1)_R \times U(1)_{B-L}$ to $U(1)_Y$ or break $U(1)_{B-L}$ leaving $U(1)_Y$ intact.
- 8: The mass of the Z' boson.
- 9: The common bilinear mass parameter B_0 .

4.3.3 *Block GAUGE*

We extend the GAUGE block to include the couplings necessary for the addition of an extra Abelian gauge group. We reproduce the existing entries here for completeness.

- 1: The coupling $g_1(Q)$ (also known as $g'(Q)$ in some conventions) of the $U(1)_Y$ gauge in models which have it, or the coupling $g_R(Q)$ of the $U(1)_R$ gauge in such models where the $U(1)_R$ in combination with another $U(1)$ gauge breaks down to $U(1)_Y$.
- 2: The coupling $g_2(Q)$ (also known as $g(Q)$ in some conventions) of the $SU(2)_L$ gauge.
- 3: The coupling $g_3(Q)$ of the $SU(3)_c$ gauge.
- 4: The coupling $g_{BL}(Q)$ of the $U(1)_{B-L}$ gauge.
- 14: The off-diagonal coupling $g_T(Q)$ of the two $U(1)$ gauges in the triangle basis.

4.3.4 *Block MSOFT*

We extend the MSOFT block to include the soft mass terms necessary for the addition of an extra Abelian gauge group. We do not reproduce the existing entries here since there are quite a few. We only show those that are new and those that have new interpretations.

- 1: The soft mass term for the gaugino of the $U(1)_Y$ gauge in models which have it, or the gaugino of the $U(1)_R$ gauge in such models where the $U(1)_R$ in combination with another $U(1)$ gauge breaks down to $U(1)_Y$.
- 4: The soft mass term for the gaugino of the $U(1)_{B-L}$ gauge.
- 5: The soft mass term mixing the gauginos of the two $U(1)$ gauges.

4.3.5 *Block EXTPAR*

We extend the EXTPAR block to include the parameters necessary for the addition of an extra Abelian gauge group. We do not reproduce the existing entries here since there are quite a few. We only show those that are new and those that have new interpretations. Bear in mind that just as in the MSSM, contradictory inputs should not be given.

- 124: The tree-level mass-squared $m_{\phi_R}^2$ of the pseudoscalar formed by the doublets breaking $SU(2)_R$.
- 126: The pole mass m_{ϕ_R} of the pseudoscalar formed by the doublets breaking $SU(2)_R$.

4.4 Extended blocks superseding existing blocks

4.4.1 Block *XPMNSRM* (rank two), superseding *UPMNS* (rank one)

In the super-PMNS basis the mass matrices of the charged leptons and the three light neutrinos are diagonal and the relevant generation mixing information is given in the PMNS matrix. In the SLHA2 the input block *UPMNSIN* was defined in terms of three mixing angles and three phases [16] whereas for the output the complete 3×3 mixing has to be given in the block *UPMNS*. In general more than 3 neutrinos contribute and thus we propose that similarly the generalized PMNS matrix, which is rectangular, shall be given for both input and output. In the basis where, as above, the charged lepton and the extended neutrino mass matrices are diagonal, this matrix corresponds to the coupling between the left-handed charged leptons with the W boson and the neutrinos divided by $g/\sqrt{2}$.

4.5 New blocks

Blocks used to give parameters as input end with “IN”, while the corresponding values as output are written in blocks without the ending “IN”.

4.5.1 Block *SEESAWGENERATIONS* (rank one)

This block specifies the number of generations of the extra fields of the see-saw models.

- 1: The number n_{ν^c} of right-handed neutrino generations in the type I, inverse, linear, and $U(1)_Y \times U(1)_{B-L}$ see-saw models.
- 2: The number n_{N_s} of neutrino-like singlet generations in the inverse, linear, and $U(1)_Y \times U(1)_{B-L}$ see-saw models, and also the number of parity-odd neutrino-like singlet generations in $U(1)_Y \times U(1)_{B-L}$ inverse see-saw models.
- 15: The number n_{15} of 15-plet generations in the type II model.
- 24: The number n_{24} of 24-plet generations in the type III model.

4.5.2 Block *SCALARRM* (rank two)

This block specifies the mixing matrix of the neutral scalar Higgs bosons. The gauge eigenstates that are rotated into the mass-ordered mass eigenstates are ordered as H_d^0, H_u^0 , then a model-dependent ordering. For see-saw types II and III, there are no further entries, because these fields are assumed to be integrated out. For $U(1)_R \times U(1)_{B-L}$, they are $\xi_R^0, \bar{\xi}_R^0$. For $U(1)_Y \times U(1)_{B-L}$, they are $\eta, \bar{\eta}$.

4.5.3 Block *PSEUDOSCALARRM* (rank two)

This block specifies the mixing matrix of the neutral pseudoscalar Higgs bosons. They are ordered analogously to how *SCALARRM* is ordered.

4.5.4 Block *GAUGEIN* (rank one)

This block specifies the gauge couplings at the input scale. The entries are analogous to those of the *GAUGE* block.

4.5.5 Block *MSOFTIN* (rank one)

This block specifies the soft mass terms at the input scale. The entries are analogous to those of the *MSOFT* block.

4.5.6 Superpotential mass matrix blocks (rank two)

The superpotential mass matrix blocks are *MNURNUR*(IN) for M_{ν^c} , *M15S15SB*(IN) for M_S , *M15T15TB*(IN) for M_T , *M15Z15ZB*(IN) for M_Z , *M24W24W*(IN) for M_W , *M24G24G*(IN) for M_G , *M24B24B*(IN) for M_B , *M24X24XB*(IN) for M_X , *MNURS*(IN) for M_R , *MNSNS*(IN) for μ_N , *MCRCRB*(IN) for μ_ξ , and *MBILBILB*(IN) for μ_η . *M15*(IN) for M_{15} is used when M_S , M_T , and M_Z are set to a common value. *M24*(IN) for M_{24} is used when M_W , M_B , M_G , and M_X are set to a common value. Though some of the models are described with only a single generation of some types of field, we allow for extra generations, and thus define all the mass matrix blocks as being rank two, even though the minimal case would use only the (1, 1) entry of some of them.

4.5.7 Soft SUSY-breaking mass matrix blocks (rank two)

The soft SUSY-breaking mass matrix blocks are *M2NUR*(IN) for $m_{\nu^c}^2$, *M215S*(IN) for m_S^2 , *M215SB*(IN) for m_S^2 , *M215T*(IN) for m_T^2 , *M215TB*(IN) for m_T^2 , *M215Z*(IN) for m_Z^2 , *M215ZB*(IN) for m_Z^2 , *M224W*(IN) for m_W^2 , *M224G*(IN) for m_G^2 , *M224B*(IN) for m_B^2 , *M224X*(IN) for m_X^2 , *M224XB*(IN) for m_X^2 , *M2NS*(IN) for m_N^2 , *M2CR*(IN) for m_ξ^2 , *M2CRB*(IN) for m_ξ^2 , *M2BIL*(IN) for m_η^2 , *M2BILB*(IN) for m_η^2 , and *M2NSP*(IN) for $m_{N'}^2$. Though some of the models are described with only a single generation of some types of field, we allow for extra generations, and thus define all the mass matrix blocks as being rank two, even though the minimal case would use only the (1, 1) entry of some of them.

4.5.8 Soft SUSY-breaking bilinear matrix blocks (rank two)

The soft SUSY-breaking bilinear matrix blocks are *BNURNUR*(IN) for B_{ν^c} , *B15S15SB*(IN) for B_S , *B15T15TB*(IN) for B_T , *B15Z15ZB*(IN) for B_Z , *B24W24W*(IN) for B_W , *B24G24G*(IN) for B_G , *B24B24B*(IN) for B_B , *B24X24XB*(IN) for B_X , *BNURS*(IN) for B_R , *BNSNS*(IN) for B_N , *BCRCRB*(IN) for B_ξ , and *BBILBILB*(IN) for B_η . *B15*(IN) for B_{15} is used when B_S , B_T , and B_Z are set to a common value. *B24*(IN) for B_{24} is used when B_W , B_B , B_G , and B_X are set to a common value.

4.5.9 Yukawa coupling matrix blocks (rank three)

The first digit is the generation index of the 15-plet or 24-plet field in type II and III models respectively, and is 1 for the other models. The 2nd pair of indices correspond to the usual indices of the minimal cases. The Yukawa coupling matrix blocks are *YNURLHU*(IN) for Y_ν , *YL15TL*(IN) for Y_T , *YD15SD*(IN) for Y_S , *YD15ZL*(IN) for Y_Z , *YHD15THD*(IN) for λ_1 , *YHU15TBHU*(IN) for λ_2 , *YHU24BL*(IN) for Y_B , *YHU24WL*(IN) for Y_W , *YHU24XBD*(IN) for Y_X , *YNSLHU*(IN) for Y_{LN} , *YNSNURCR*(IN) for $Y_{N\nu^c}$, *YNURBILNUR*(IN) for $Y_{\eta\nu^c}$, and *YNSNURBIL*(IN) for Y_{IS} . *Y15*(IN) for Y_{15} is used when Y_S , Y_T , and Y_Z are set to a common value. *Y24*(IN) for Y_{24} is used when Y_B , Y_W , and Y_X are set to a common value.

4.5.10 Soft SUSY-breaking trilinear matrix blocks (rank three)

There is a soft SUSY-breaking trilinear matrix block for each Yukawa coupling matrix block, with the same name but with the initial “Y” replaced by “T”, corresponding to the “ T_{blah} ” associated with the “ Y_{blah} ” matrices. However, there is no T15(IN) for T_{15} or T24(IN) for T_{24} ; instead, in such constrained parameter sets, $A_0 \times Y_{15/24}$ is used.

4.5.11 Block GAMZZPRM (rank two)

This is the gauge boson rotation matrix $U^{\gamma ZZ'}$ given at the SUSY scale.

CONCLUSIONS AND OUTLOOK

In this contribution we propose an extension of the existing SLHA accords to include several see-saw models. Firstly, this requires new blocks to be defined for the additional couplings and masses needed within the various models. In this connection, we do not restrict ourselves to individual versions of the latter but also allow for combinations of such models in order to be as general as possible. Secondly, several new particles have to be postulated. For these, we propose a 9-digit scheme for the corresponding PDG-codes, which could in fact be of more general use than for see-saw models only, yet it needs to be tested extensively against the properties of existing and possibly new SUSY models before widespread adoption. One issue that has to be addressed as next step is the proper definition of the additional parameters in the so-called super-PMNS basis. Moreover, also $SU(2)_R$ models are not yet covered in this proposal.

Appendix

A Kinetic mixing

It is well known that in models with several $U(1)$ gauge groups, kinetic mixing terms

$$-\chi_{ab} \hat{F}^{a,\mu\nu} \hat{F}_{\mu\nu}^b, \quad a \neq b \quad (\text{A.1})$$

between the field-strength tensors are allowed by gauge and Lorentz invariance [68], as $\hat{F}^{a,\mu\nu}$ and $\hat{F}^{b,\mu\nu}$ are gauge invariant quantities by themselves, see *e.g.* [69]. Even if these terms are absent at tree level at a particular scale, they might be generated by RGE effects [70, 71]. This happens usually if the two Abelian gauge groups cannot be embedded in a larger gauge group simultaneously or if incomplete gauge multiplets of the fundamental theory are integrated out. It is easier to work with non-canonical covariant derivatives instead of off-diagonal field-strength tensors such as in eq. (A.1). The equivalence of both approaches has been shown in [70, 72]. We show here the special case of two Abelian gauge groups $U(1)_A \times U(1)_B$. The covariant derivatives has the form

$$D_\mu = \partial_\mu - iQ_\phi^T G A \quad (\text{A.2})$$

where Q_ϕ is a vector containing the charges of the field ϕ with respect to the two Abelian gauge groups, G is the gauge coupling matrix

$$G = \begin{pmatrix} g_{AA} & g_{AB} \\ g_{BA} & g_{BB} \end{pmatrix} \quad (\text{A.3})$$

and A contains the gauge bosons $A = (A_\mu^A, A_\mu^B)^T$. As long as the two Abelian gauge groups are unbroken there is freedom to rotate the gauge bosons. It is convenient to choose a basis in

which G gets a triangle form

$$G' = \begin{pmatrix} g & \tilde{g} \\ 0 & g' \end{pmatrix} \quad (\text{A.4})$$

Mixing effects of Abelian gauge groups appear not only in the gauge sector but also for the gauginos because also terms of the form

$$M_{AB}\lambda_A\lambda_B \quad (\text{A.5})$$

are allowed by gauge and Lorentz invariance [72, 73].

B PDG CODES AND EXTENSIONS

We summarise here our codes for existing and for the extra particle content of the see-saw models. In the first column of Tables B.1 to B.3, the conventional PDG number is shown.

Colored Fermions		
PDG	Particle	PDG.IX
2	u	110100401
4	c	110100402
6	t	110100403
-1	\bar{d}	110890201
-3	\bar{s}	110890202
-5	\bar{b}	110890203
1000021	\tilde{g}	211110001

(a)

Colorless, Charged Fermions		
PDG	Particle	PDG.IX
-11	e^+	110000601
-13	μ^+	110000602
-15	τ^+	110000603
1000024	$\tilde{\chi}_1^+$	210000601
1000037	$\tilde{\chi}_2^+$	210000602

(b)

Neutral Fermions		
PDG	Particle	PDG.IX
-12/12	$\bar{\nu}_1^D / \nu_1^M$	110000001 / 111000001
-14/14	$\bar{\nu}_2^D / \nu_2^M$	110000002 / 111000002
-16/16	$\bar{\nu}_3^D / \nu_3^M$	110000003 / 111000003
	$\bar{\nu}_4^D / \nu_4^M$	110000004 / 111000004
	$\bar{\nu}_5^D / \nu_5^M$	110000005 / 111000005
	$\bar{\nu}_6^D / \nu_6^M$	110000006 / 111000006
	$\bar{\nu}_7^D / \nu_7^M$	110000007 / 111000007
	$\bar{\nu}_8^D / \nu_8^M$	110000008 / 111000008
	$\bar{\nu}_9^D / \nu_9^M$	110000009 / 111000009
1000022	$\tilde{\chi}_1^0$	211000001
1000023	$\tilde{\chi}_2^0$	211000002
1000025	$\tilde{\chi}_3^0$	211000003
1000035	$\tilde{\chi}_4^0$	211000004
1000045	$\tilde{\chi}_5^0$	211000005
	$\tilde{\chi}_6^0$	211000006
	$\tilde{\chi}_7^0$	211000007

(c)

Table B.1: (a) The down-type quarks are considered antiparticles due to having negative electric charge, hence the anti-downs are the defining states, and since they are color antitriplets, their color digits are 89 (99 – 10). (b) In the case of R -parity violation, these fields mix to eigenstates with codes 1100006XY. (c) ν^D are dirac neutrinos while ν^M are Majorana neutrinos. In the case of R -parity violation, the fields mix forming (Majorana) mass eigenstates with PDG.IX codes 1110000XY.

ACKNOWLEDGEMENTS

We want to congratulate the Les Houches organisers for a great and fruitful workshop atmosphere, good food, and the amazing scenery of the French alps. We also want to thank Nazila

Colored Scalars		
PDG	Particle	PDG.IX
1000002	\tilde{u}_1	200100401
1000004	\tilde{u}_2	200100402
1000006	\tilde{u}_3	200100403
2000002	\tilde{u}_4	200100404
2000004	\tilde{u}_5	200100405
2000006	\tilde{u}_6	200100406
-1000001	\tilde{d}_1^*	200890201
-1000003	\tilde{d}_2^*	200890202
-1000005	\tilde{d}_3^*	200890203
-2000001	\tilde{d}_4^*	200890204
-2000003	\tilde{d}_5^*	200890205
-2000005	\tilde{d}_6^*	200890206

(a)

Vector Bosons		
PDG	Particle	PDG.IX
21	g	121110001
22	γ	121000001
23	Z	122000001
32	Z'	122000002
33	Z''	122000003
24	W^+	120000601
34	W'^+	120000602

(b)

Table B.2: (a) New PDG code for colored scalars. (b) The W^+ is considered to be the particle (and hence the W^- the antiparticle) since it has positive electric charge.

Mahmoudi for the enlighting comments about FLHA. LB, AB and SM thank the NExT Institute and Royal Society for partial financial support. LB has also been partially supported by the Deutsche Forschungsgemeinschaft through the Research Training Group GRK 1102 *Physics of Hadron Accelerators*. D.K.G. acknowledges partial support from the Department of Science and Technology, India under the grant SR/S2/HEP-12/2006. BOL and WP are supported by the by the German Ministry of Education and Research (BMBF) under contract no. 05H09WWEF.

Colorless, Charged Scalars		
PDG	Particle	PDG.IX
25	h_1	101000001
35	h_2	101000002
45	h_3	101000003
	h_4	101000004
36	A_1^0	102000001
46	A_2^0	102000002
-1000012/1000012	$\tilde{\nu}_1^* / \text{Re}(\tilde{\nu}_1)$	200000001 / 201000001
-1000014/1000014	$\tilde{\nu}_2^* / \text{Re}(\tilde{\nu}_2)$	200000002 / 201000002
-1000016/1000016	$\tilde{\nu}_3^* / \text{Re}(\tilde{\nu}_3)$	200000003 / 201000003
1000017	$\text{Im}(\tilde{\nu}_1)$	202000001
1000018	$\text{Im}(\tilde{\nu}_2)$	202000002
1000019	$\text{Im}(\tilde{\nu}_3)$	202000003
	$\tilde{\nu}_4^* / \text{Re}(\tilde{\nu}_4) / \text{Im}(\tilde{\nu}_4)$	200000004 / 201000004 / 202000004
	$\tilde{\nu}_5^* / \text{Re}(\tilde{\nu}_5) / \text{Im}(\tilde{\nu}_5)$	200000005 / 201000005 / 202000005
	$\tilde{\nu}_6^* / \text{Re}(\tilde{\nu}_6) / \text{Im}(\tilde{\nu}_6)$	200000006 / 201000006 / 202000006
	$\tilde{\nu}_7^* / \text{Re}(\tilde{\nu}_7) / \text{Im}(\tilde{\nu}_7)$	200000007 / 201000007 / 202000007
	$\tilde{\nu}_8^* / \text{Re}(\tilde{\nu}_8) / \text{Im}(\tilde{\nu}_8)$	200000008 / 201000008 / 202000008
	$\tilde{\nu}_9^* / \text{Re}(\tilde{\nu}_9) / \text{Im}(\tilde{\nu}_9)$	200000009 / 201000009 / 202000009

Table B.3: In the case of R -parity violation but CP conservation, the CP-even and CP-odd components mix separately to form eigenstates with PDG.IX codes 1010000XY and 1020000XY, respectively. If CP violation is present, the numbers are 1000000XY and 2000000XY respectively (no R -parity violation) or just 1000000XY (with R -parity violation).

Contribution 4

Automatic computation of supersymmetric renormalization group equations with FeynRules

Adam Alloul, Neil Christensen, Claude Duhr, Benjamin Fuks, Michel Rausch de Traubenberg

Abstract

We discuss the progress on the automatic computation of renormalization group equations with FEYNRULES. We also present a new interface to the SUSPECT 3 package in order to automatically calculate supersymmetric spectra .

1 INTRODUCTION

Supersymmetry, and in particular its minimal version dubbed the Minimal Supersymmetric Standard Model (MSSM) [74, 75], is among the most popular extensions of the Standard Model (SM) of particle physics. Linking fields with opposite statistics, it matches bosonic (fermionic) partners to the SM fermions (bosons). The MSSM addresses a set of conceptual problems of the SM, such as stabilizing the large hierarchy between the electroweak scale and the Planck scale, unifying the gauge couplings at high energy or proposing a candidate for the dark matter in the universe. However, if supersymmetry were an exact symmetry, both the SM particles and their superpartners would have the same mass. As this is not observed experimentally, supersymmetry must be broken at low energies. In order to remain a viable solution to the hierarchy problem, this breaking must be soft, resulting in superpartners with masses around the TeV scale. Therefore, the quest for supersymmetric particles is one of the main experimental topics at the Large Hadron Collider (LHC) at CERN. The latest results of the general purpose LHC experiments ATLAS and CMS are currently pushing the limits on the masses of the superpartners to a higher and higher range [76, 77], thereby severely constraining the supersymmetric parameter space. However, most limits only hold in the context of the so-called constrained MSSM framework, where the 105 free parameters of the MSSM are reduced to a set of four parameters and a sign, assuming some organizing principle based on unification at high energy. In contrast, there is a much broader class of supersymmetric theories which may be valuable to be investigated from a phenomenological point of view.

Even if all of these non-minimal models contain many free parameters, an organizing principle governing the bulk of the parameters is strongly favored. Indeed, such a principle allows to reduce the number of degrees of freedom (of the parameter space) and renders the model accessible to phenomenological studies. Furthermore, it is also motivated by the current experimental data, coming from *e.g.* flavor physics. In their most general version, supersymmetric theories predict large rates for flavor violating processes, which must however, in order to be in agreement with the observations, be suppressed within the framework of the SM. An organizing principle would then either forbid or suppress the relevant terms in the supersymmetric Lagrangian, restoring agreement with the data. Inspired by scenarios such as supergravity scenarios with a minimal Kähler potential, where *e.g.* all the scalar particles get a common mass

at the Planck scale, this organizing principle may however only be valid at some high energy scale. Therefore, in order to study the phenomenology of supersymmetric models at collider experiment scales, all the parameters must be run down from the high input scale (where, *e.g.*, they are supposed to unify) to low energies using renormalization group equations.

In the following, we describe an extension of the superspace module of FEYNRULES [6, 78] which allows to automatically derive the renormalization group equations related to the parameters of any supersymmetric theory from the superfield content of the theory and the implementation of the model dependent pieces of the Lagrangian, *i.e.*, the superpotential and the soft supersymmetry breaking Lagrangian. Furthermore, we also show how these equations can be automatically exported to the supersymmetric spectrum generator SUSPECT 3 for a numerical extraction of the model spectrum, the C++ version of the SUSPECT 2 package [79].

The outline of this contribution is as follows: in Section 2 we present a review on how to obtain renormalization group equations for generic supersymmetric theories. In Section 3 we show how to extract these equations at the one-loop level automatically with FEYNRULES, and in Section 4 we describe the new interface to the SUSPECT 3 program. Our conclusions are drawn in Section 5.

2 RENORMALISATION GROUP EQUATIONS FOR A GENERIC SOFTLY BROKEN SUPERSYMMETRIC MODEL

A generic supersymmetric theory can be described by fixing the superfield content and the (gauge) symmetries leaving the corresponding Lagrangian invariant. We introduce a gauge group G and representations \mathcal{R} of the corresponding algebra spanned by the hermitian matrices T^a and we denote the gauge coupling constant by g . The chiral sector of the theory consists in a set of left-handed chiral superfields Φ^i lying in the representation \mathcal{R}^i of G . The gauge sector contains a vector superfield V of the gauge group. The supersymmetric and gauge invariant Lagrangian, together with the associated soft supersymmetry breaking Lagrangian, is given by

$$\mathcal{L} = \mathcal{L}_{\text{chiral}} + \mathcal{L}_{\text{Yang-Mills}} + \mathcal{L}_{\text{superpotential}} + \mathcal{L}_{\text{soft}} , \quad (1)$$

where $\mathcal{L}_{\text{chiral}}$ and $\mathcal{L}_{\text{Yang-Mills}}$ contain the kinetic terms as well as the gauge interactions of the different particles, which are entirely fixed by supersymmetry and gauge invariance. Their explicit form in terms of component fields can be found, *e.g.*, in Refs. [78, 80, 81]. In contrast, $\mathcal{L}_{\text{superpotential}}$ is model-dependent (but gauge-invariant) and is derived from the superpotential describing the interactions among the different chiral supermultiplets. Assuming renormalizability in addition, the most general superpotential takes the form

$$W(\Phi) = \frac{1}{6} y_{ijk} \Phi^i \Phi^j \Phi^k + \frac{1}{2} \mu_{ij} \Phi^i \Phi^j + \alpha_i \Phi^i , \quad (2)$$

where y , μ and α are the coupling strengths dictating the supersymmetric (non-gauge) interactions of the theory. Finally, the last part of the Lagrangian of Eq. (1), $\mathcal{L}_{\text{soft}}$, is also model-dependent (and gauge-invariant as well) and contains the soft supersymmetry breaking terms *i.e.* terms of dimension two and three breaking supersymmetry. The latter can be generically written as

$$\mathcal{L}_{\text{soft}} = -\frac{1}{6} h_{ijk} \phi^i \phi^j \phi^k - \frac{1}{2} b_{ij} \phi^i \phi^j - a_i \phi^i - \frac{1}{2} M \lambda \cdot \lambda - \frac{1}{2} \phi_i^\dagger (m^2)^i_j \phi^j + \text{h.c.} , \quad (3)$$

where ϕ^i denotes the scalar component of the chiral superfield Φ^i and λ the (two-component fermionic) gaugino field embedded within the vector superfield V . This Lagrangian contains hence mass terms for gauginos and scalar fields M and m^2 as well as linear, bilinear and trilinear scalar interactions derived from the form of the superpotential. The coupling strengths of the interactions are given by the h , b and a parameters. In the rest of this section, all the supersymmetry-breaking and superpotential parameters are assumed to be generic non-zero complex numbers.

We now turn to the renormalization group equations linking the values of the parameters at two different energy scales. Even if the results have been known at the one-loop [82, 83] and two-loop levels for a long time [84–88], and could even be derived by other means (*e.g.*, supergraph techniques), we only focus here on the one-loop contributions. An extension to the two-loop level is foreseen in a near future. A generic renormalization group equation for a parameter x takes the form

$$\frac{d}{dt}x = \beta_x. \quad (4)$$

where we have introduced the β -function of the parameter x . As previously mentioned, this quantity can be expanded perturbatively,

$$\beta_x = \frac{1}{16\pi^2}\beta_x^{(1)} + \frac{1}{(16\pi^2)^2}\beta_x^{(2)} + \dots, \quad (5)$$

where $\beta_x^{(1)}$ and $\beta_x^{(2)}$ are the one-loop and two-loop contributions, respectively. In the following, we then provide the first coefficient of the β -functions of all the parameters introduced above.

Starting with the gauge sector, the first coefficients of the β -functions of the gauge coupling constant g and of the gaugino mass parameter M read

$$\begin{aligned} \beta_g^{(1)} &= g^3 \left[S(\mathcal{R}) - 3C(G) \right], \\ \beta_M^{(1)} &= 2g^2 M \left[S(\mathcal{R}) - 3C(G) \right]. \end{aligned} \quad (6)$$

In the expressions above, we have introduced the quadratic Casimir invariant $C(G)$ of the adjoint representation and $S(\mathcal{R})$, the total Dynkin index for the representation \mathcal{R} . Let us note that this last quantity must be summed over all the chiral superfields lying in this representation, accounting in addition for their multiplicity. In the case of an abelian group, we define $S(\mathcal{R})$ as the sum of the squared charges of the whole chiral content of the theory, accounting again for the multiplicity of each superfield. Turning to the superpotential parameters, the first coefficient of the β -functions of the linear, bilinear and trilinear interaction parameters are given by,

$$\begin{aligned} \beta_{\alpha_i}^{(1)} &= \alpha_p (\gamma^{(1)})^p{}_i, \\ \beta_{\mu_{ij}}^{(1)} &= \mu_{ip} (\gamma^{(1)})^p{}_j + \mu_{pj} (\gamma^{(1)})^p{}_i, \\ \beta_{y_{ijk}}^{(1)} &= y_{ijp} (\gamma^{(1)})^p{}_k + y_{ipk} (\gamma^{(1)})^p{}_j + y_{pjk} (\gamma^{(1)})^p{}_i, \end{aligned} \quad (7)$$

respectively. In the expression above, the first coefficient of the anomalous dimensions γ are defined as

$$(\gamma^{(1)})^j{}_i = \frac{1}{2}y_{ipq}y^{*jpa} - 2\delta^j{}_i g^2 C(i), \quad (8)$$

where $C(i)$ refers to the quadratic Casimir invariant of the representation of G in which the chiral superfield Φ^i lies. The first coefficients of the beta functions of the soft supersymmetry

breaking parameters, *i.e.*, of the linear, bilinear and trilinear scalar interactions, are given by

$$\begin{aligned}
\beta_{a_i}^{(1)} &= \frac{1}{2} y_{ipq} y^{*rpq} a_r + y^{*rpq} h_{ipq} \alpha_r + \mu_{ir} y^{*rpq} b_{pq} + 2 y_{ipq} (m^2)^q_r \mu^{*pr} + h_{ipq} b^{*pq} , \\
\beta_{b_{ij}}^{(1)} &= \frac{1}{2} b_{ip} y^{*pqr} y_{qrj} + \frac{1}{2} y_{ijr} y^{*rpq} b_{pq} + \mu_{ip} y^{*pqr} h_{qrj} - 2 [b_{ij} - 2M\mu_{ij}] g^2 C(i) + (i \leftrightarrow j) , \\
\beta_{h_{ijk}}^{(1)} &= \frac{1}{2} h_{ijr} y^{*rpq} y_{pqk} + y_{ijr} y^{*rpq} h_{pqk} - 2 [h_{ijk} - 2M y_{ijk}] g^2 C(k) + (i \leftrightarrow k) + (k \leftrightarrow j) .
\end{aligned} \tag{9}$$

Finally, the first term in the beta function for the scalar mass terms reads

$$\begin{aligned}
\beta_{(m^2)^i_j}^{(1)} &= \frac{1}{2} y^{*ipq} y_{pqr} (m^2)^r_j + \frac{1}{2} y_{jpq} y^{*pqr} (m^2)^i_r + 2 y^{*ipq} y_{jpr} (m^2)^r_q + h_{jpp} h^{*ipq} \\
&\quad - 8 \delta^i_j M M^\dagger g^2 C(i) + 2 g^2 (T_a)^i_j \text{Tr} [T^a m^2] .
\end{aligned} \tag{10}$$

We note that the terms in this equation depending explicitly on the representation matrices of the gauge group vanish identically for non-abelian gauge groups. In the abelian case, these matrices must be read as the squared abelian charge of the considered superfield.

3 EXTRACTING RENORMALIZATION GROUP EQUATIONS WITH FEYNRULES

In order to be able to extract the renormalization group equations of a given supersymmetric theory in an automated way with FEYNRULES, the latter must be implemented using the superspace module [78]. However, as discussed in the previous section, the derivation of the coefficients of the beta-functions requires the computation of the multiplicity of each superfield. In order to allow FEYNRULES to perform this task efficiently, both the superpotential and the soft supersymmetry breaking Lagrangian must be implemented using the function SUDot for $SU(N)$ -invariant products of N superfields. Hence, taking the example of the MSSM, the μ -term of the superpotential would be implemented as

```
MUH SUDot [HU [aa] , HD [aa] , aa]
```

where the SUDot function receives as arguments the sequence of the contracted superfields with all indices explicit. The contracted $SU(N)$ indices are set to a single given value for all superfields, the latter being repeated as the last argument of the SUDot function. In our example, it is labeled aa. As another example, the up-type squark trilinear soft supersymmetry breaking interaction terms would be implemented as

```
-tu [ff1, ff2] URs [ff1, cc1] SUDot [QLs [aa, ff2, cc1] , hus [aa] , aa]
```

We refer to Ref. [78] for the definition of the superfields, fields and parameters. After the model file has been loaded, the renormalization group equations can be extracted via the command

```
RGE [LSoft, SuperW]
```

where LSoft and SuperW denote the variables in which the soft supersymmetry breaking Lagrangian have been stored. The RGE command computes the renormalization group equations according to Eq. (4), using the beta-functions provided in Eqs. (6), (7), (9) and (10).

We have validated our implementation against the well-known results from the literature both in the context of the MSSM [84] and the Next-to-Minimal Supersymmetric Standard Model [89]. We give, as examples, two renormalization group equations given by FEYNRULES in the framework of the general MSSM. For notations, we refer to Ref. [78]. The evolution of the μ -parameter of the superpotential and the one of the corresponding b -parameter in the soft supersymmetry breaking Lagrangian are driven by

$$\begin{aligned} \frac{d\mu}{dt} &= \mu \left[-\frac{3g'^2}{80\pi^2} - \frac{3g_w^2}{16\pi^2} + \frac{3}{16\pi^2} \text{Tr}[\mathbf{y}^{\text{d}\dagger} \mathbf{y}^{\text{d}}] + \frac{3}{16\pi^2} \text{Tr}[\mathbf{y}^{\text{u}\dagger} \mathbf{y}^{\text{u}}] + \frac{1}{16\pi^2} \text{Tr}[\mathbf{y}^{\text{e}\dagger} \mathbf{y}^{\text{e}}] \right], \\ \frac{db}{dt} &= b \left[-\frac{3g'^2}{80\pi^2} - \frac{3g_w^2}{16\pi^2} + \frac{3}{16\pi^2} \text{Tr}[\mathbf{y}^{\text{d}\dagger} \mathbf{y}^{\text{d}}] + \frac{3}{16\pi^2} \text{Tr}[\mathbf{y}^{\text{u}\dagger} \mathbf{y}^{\text{u}}] + \frac{1}{16\pi^2} \text{Tr}[\mathbf{y}^{\text{e}\dagger} \mathbf{y}^{\text{e}}] \right] \\ &\quad + \mu \left[\frac{3g'^2 M_1}{40\pi^2} + \frac{3g_w^2 M_2}{8\pi^2} + \frac{3}{8\pi^2} \text{Tr}[\mathbf{y}^{\text{d}\dagger} \mathbf{T}^{\text{d}}] + \frac{3}{8\pi^2} \text{Tr}[\mathbf{y}^{\text{u}\dagger} \mathbf{T}^{\text{u}}] + \frac{1}{8\pi^2} \text{Tr}[\mathbf{y}^{\text{e}\dagger} \mathbf{T}^{\text{e}}] \right]. \end{aligned} \quad (11)$$

4 AN INTERFACE TO THE SUSPECT 3 SUPERSYMMETRIC SPECTRUM GENERATOR

In collaboration with the SUSPECT 3 team, A. Djouadi, J.L. Kneur, G. Moutaka, M. Ughetto and D. Zerwas, we have designed an interface exporting the renormalization group equations derived by FEYNRULES into a format which can be used by the spectrum calculator SUSPECT 3 presented in Section 7. Within MATHEMATICA, this interface is called as any other FEYNRULES interface,

```
WriteSuSpectOutput[LSoft, SuperW]
```

where again, the variables LSoft and SuperW contain the soft supersymmetry breaking Lagrangian and the superpotential, respectively. When this command is issued, FEYNRULES internally calls the function RGE and exports the results in a header and source file `DerivativeExternal.h` and `DerivativeExternal.cxx`, respectively. The header file contains the class definitions of SUSPECT 3 and the source file contains the renormalization group equations themselves. The two files have to be copied into the SUSPECT 3 directories (`inc` and `src`). Once SUSPECT 3 has been recompiled, the renormalization group equations provided by FEYNRULES can be used either if the counter 0 of the block `SUSPECT_CONFIG` of the input SLHA file is set to 99 (external renormalization group equations) or directly in memory as described in Section 7.

5 CONCLUSION

In this contribution we have presented a new module in the FEYNRULES package that allows to compute one-loop renormalization group equations for supersymmetric theories in an automated way. FEYNRULES extracts all the one-loop β functions of the model directly from the superfield spectrum and the superpotential and soft-supersymmetry breaking terms of the Lagrangian, which allows to obtain the renormalization group equations for any supersymmetric model. The renormalization group equations obtained in this way can then be written to file in a format that can be linked against the SUSPECT 3 program, thus allowing to perform the renormalization group running numerically and to obtain the spectrum for arbitrary non-minimal supersymmetric theories.

ACKNOWLEDGEMENTS

AA, BF and MRT are particularly grateful to D. Zerwas for enlightening discussions on SUSPECT 3. CD and BF would like to thank CERN and LAPTH for their hospitality during the workshop during which some of the work contained herein was performed. AA, BF and MRT are supported by the Theory-LHC France-initiative of the CNRS/IN2P3. This work was supported by the Research Executive Agency (REA) of the European Union under the Grant Agreement number PITN-GA-2010-264564 (LHCPhenoNet).

Contribution 5

Implementation and automated validation of the minimal Z' model in FeynRules

Lorenzo Basso, Neil D. Christensen, Claude Duhr, Benjamin Fuks, Christian Speckner

Abstract

We describe the implementation of a well-known class of $U(1)$ gauge models, the “minimal” Z' models, in FeynRules. We also describe a new automatized validation tool for FeynRules models which is controlled by a web interface and allows the user to run a complete set of $2 \rightarrow 2$ processes on different matrix element generators, different gauges, and compare between them all. If existing, the comparison with independent implementations is also possible. This tool has been used to validate our implementation of the “minimal” Z' models.

1 INTRODUCTION

The Large Hadron Collider (LHC) has begun exploring the TeV scale of physics. To determine the full set of properties of the new physics expected to appear, we will have to implement new theoretical models for TeV scale physics into LHC simulation software such as CalcHEP [1, 90, 91], MadGraph [92–96] and Whizard [97, 98].

Among the various possible extensions of the Standard Model (SM), those containing an extra $U(1)$ gauge group play a special role (see [99–101] and references therein). The associated Z' boson(s) may be among the first objects to be probed at the LHC, due to the simplicity of their signals at colliders. The phenomenology of Z' bosons has been intensively studied (for some reviews, see [102–106]). Despite the important role of Z' physics, we note the absence of commonly accessible code for its analysis with the existing Monte Carlo tools. In the past, each analysis has started with a new, private implementation of a particular Z' model, a process which is inefficient and error prone.

For this reason, we have implemented a class of $U(1)$ models in FeynRules [6, 107, 108] which covers the complete set of “minimal” Z' models [104, 105, 109, 110]. In this implementation, the various “minimal” models are chosen by setting a parameter which continuously varies among the many possibilities. By implementing this model in FeynRules, we allow its implementation to be used in CalcHEP, MadGraph and Whizard without any modification of those codes. Furthermore, we have made this model implementation public on the FeynRules website so that anyone can use it.

Although this approach of automatically generating the different model implementations from a single “master” implementation greatly reduces the risk of creating faulty model implementation, possible issues can still arise from either faulty FeynRules input or software bugs. While it is virtually impossible to prove the correctness of a model implementation, confidence can be gained from comparing the model between different codes supported by FeynRules,

between different gauges and, if available, by comparing to existing, independent implementations. Still, doing such a comparison by hand is very cumbersome as it requires expertise in each simulation package, setting up each package, matching the respective setups (in particular the cuts and model input) and then running and comparing a set of processes as large as possible. This procedure shows a lot of potential for automatization. In order to facilitate this, we have developed an easy-to-use validation framework driven by a web application. The framework allows registered users to upload a model which is automatically run through FeynRules in order to check for syntactical correctness and generate model implementations for the different Monte Carlo tools supported by the framework (at the moment MadGraph, CalcHEP and Whizard). After this sanity check, a list of all possible $2 \rightarrow 2$ processes in the model (restrictions can be applied to the process list) is generated. For each process on the list and each different generator, the cross section is automatically evaluated and compared between the different tools.

Using this web validation tool, we have validated our class of “minimal” Z' models by comparing over a thousand $2 \rightarrow 2$ processes between CalcHEP and Whizard and by comparing between Feynman and unitary gauge. This allowed us to find the remaining bugs in this model implementation and fix them. The model we have made public shows agreement between CalcHEP and Whizard and between Feynman and unitary gauges.

2 THE MINIMAL Z' MODELS IN FEYNRULES

In this section we discuss the implementation of the Minimal Z' Model [110, 111]. This model is based on a $SU(3)_C \times SU(2)_L \times U(1)_Y \times U(1)_{B-L}$ gauge symmetry, i.e., the Standard Model (SM) gauge group is augmented by a $U(1)$ factor related to the gauged Baryon minus Lepton ($B - L$) number. The model is “minimal” as it extends the SM with a minimum amount of modifications in all the sectors. In addition to the new $U(1)_{B-L}$ gauge sector, the model includes three right-handed neutrinos (designed to cancel anomalies) and an additional complex Higgs boson (χ) which is a singlet under the SM gauge groups but is charged under $U(1)_{B-L}$ and is responsible for giving mass to the additional Z' gauge boson. The classical, gauge invariant Lagrangian can be decomposed as $\mathcal{L} = \mathcal{L}_{YM} + \mathcal{L}_S + \mathcal{L}_f + \mathcal{L}_Y + \mathcal{L}_{ghost}$.

The non-Abelian field strengths in \mathcal{L}_{YM} are the same as in the SM whereas the Abelian ones can be written as $\mathcal{L}_{YM}^{\text{Abel}} = -\frac{1}{4}F^{\mu\nu}F_{\mu\nu} - \frac{1}{4}F'^{\mu\nu}F'_{\mu\nu}$ (where $F_{\mu\nu} = \partial_\mu B_\nu - \partial_\nu B_\mu$ and $F'_{\mu\nu} = \partial_\mu B'_\nu - \partial_\nu B'_\mu$). In this field basis, the covariant derivative reads:

$$D_\mu \equiv \partial_\mu + ig_S T^\alpha G_\mu^\alpha + ig T^a W_\mu^a + ig_1 Y B_\mu + i(\tilde{g}Y + g'_1 Y_{B-L})B'_\mu. \quad (1)$$

Since \tilde{g} is a free parameter of the theory (assuming a fixed g'_1), this model describes a one-dimensional class of Z' theories. A discrete set of popular Z' models (see, e.g. [104, 105, 109]) can be recovered by a suitable definition of both \tilde{g} and g'_1 . A few of them are summarised in Table 1.

We now describe a few important aspects of our FeynRules implementation of this model. First of all, we note that the model files are set to Feynman gauge by default. If unitary gauge is desired, the variable `$FeynmanGauge` must be set to `False` inside the Mathematica session after loading the model, but before calculating Feynman rules.

Unless stated otherwise, all particles and parameters that exist in the SM are the same as in the default FeynRules SM implementation. We have renamed the tauon to `1` and its antiparticle to `L` in order to match the CalcHEP conventions. Since we have added new gauge bosons, scalar

Model	Parameterization
$U(1)_{B-L}$	$\tilde{g} = 0$
$U(1)_\chi$	$\tilde{g} = -4/5g'_1$
$U(1)_R$	$\tilde{g} = -2g'_1$

Table 1: Specific parametrisations of the Minimal Z' Models: $U(1)_{B-L}$, $U(1)_\chi$ and $U(1)_R$.

fields and neutrinos which mix with the SM fields, their mixing partners have been mostly renamed. The new names are given in Table 2 together with the new parameters. For an overall description of their meaning and some useful relations, see Refs. [110, 111]. The columns marked FR give the names that are used in the matrix element generators.

	Particles			Parameters			
	Symbol	PDG code		Independent	Dependent		
	\mathcal{L}	FR		\mathcal{L}	FR	\mathcal{L}	FR
Light Neutrino 1	ν_{l_1}	n1	12	g'_1	g1p	M_Z	MZ
Light Neutrino 2	ν_{l_2}	n2	14	\tilde{g}	gt	$\sin \theta'$	Sp
Light Neutrino 3	ν_{l_3}	n3	16	$M_{Z'}$	MZp	x	x
Heavy Neutrino 1	ν_{h_1}	~n1	9910012	m_{h_1}	MH1	λ_1	lam1
Heavy Neutrino 2	ν_{h_2}	~n2	9910014	m_{h_2}	MH2	λ_2	lam2
Heavy Neutrino 3	ν_{h_3}	~n3	9910016	$\sin \alpha$	Sa	λ_3	lam3
Light Higgs	h_1	H1	9900025	m_{ν_l}	MnL	y_i^D	yndi
Heavy Higgs	h_2	H2	9900026	m_{ν_h}	MnH	y_i^M	ynmi
Z' boson	Z'	Zp	9900032	M_W	MW	$\sin \alpha_i$	Sani

Table 2: New particles and parameters and the related ASCII symbols exported by FeynRules to the matrix element generators.

In order to use the resulting matrix element generator code, it is important to know which parameters are independent and can be adjusted by the user. In the neutral gauge boson sector, the choice we made is to keep the new gauge couplings (g'_1 and \tilde{g}) as independent parameters, thus allowing to easily identify the various benchmark models, and to express the remaining quantities in terms of the Z' mass, using the following relation, independent of the Z mass:

$$x = \frac{M_{Z'}}{2g'_1} \sqrt{1 - \frac{\tilde{g}^2 v^2}{4M_{Z'}^2 - v^2(g_w^2 + g_1^2)}}, \quad (2)$$

which generalises a similar formula for the pure $B - L$ model (where $\tilde{g} = 0$). This choice implies that the Z boson mass is now treated as an internal parameter, function of $M_{Z'}$, despite the usual conventions. It is left to the user to choose a Z' mass that satisfies existing experimental limits. On the other hand, we have defined the W boson mass as an independent parameter. Finally, in the scalar sector, the scalar masses and mixing angle α are kept as input parameters instead of the λ_i parameters appearing in the potential. (See Ref. [111] for details.)

3 WEB VALIDATION

Although FeynRules greatly simplifies the process of implementing new models and reduces the probability of errors during implementation considerably, there is still the possibility of mistakes. We have taken great pains to validate the FeynRules package [107] and we plan to continually extend and improve these tests in order to make the FeynRules package ever more dependable. On the other hand, when a new model is implemented, it has been up to the author of that new model to validate it. We have proposed guidelines for this validation [42], but, in practice, the level of model validation has been irregular. The problem is that, as a result of there being thousands of Feynman rules, testing a handful of them (which is achievable by a human) is not sufficient to fully validate a model. It would be far better if all the vertices could be tested. This requires automation. Some tests that can be automated are the following:

- comparison of all $1 \rightarrow 2$ and $1 \rightarrow 3$ partial widths between matrix element generators,
- comparison of all $2 \rightarrow 2$ and $2 \rightarrow 3$ cross sections between matrix element generators,
- comparison between gauges in these processes,
- comparison of these processes with an independent implementation of the model.

Even though these tests cannot guarantee a model implementation is error-free, our experience shows that they can help to discover remaining bugs in many cases.

We have begun a project to create an automated validation tool which implements the tests described in the previous paragraph for FeynRules models. Although not yet finalized, it has achieved sufficient maturity to be useful for model validation and has, in fact, been used for the validation of the “minimal” Z' model here described, of which we will say more in the next section. This validation tool is implemented as a web (HTML / Javascript) application and should, therefore, work on any web enabled device. A user who wishes to validate a model using this package, would point his or her browser to the url of the web validation website and would control the validation of his or her model via the web interface. Approved, authenticated users can upload FeynRules model files for testing. They can also upload implementations of their models done by independent parties for comparison. Once the model files have passed some basic sanity tests, the user is able to run the full suite of validation tests on his or her model. The model and the results of the validation will remain private until explicitly made public by the author, when ready. In the future, we plan to add the ability to export the results of the validations to other useful formats, such as \LaTeX .

After uploading the model files and passing the sanity tests, the user can generate a list of processes for comparison. We currently support $2 \rightarrow 2$ processes, but plan to add support for others in the future. By default, the web interface generates all $2 \rightarrow 2$ processes allowed by the symmetries of the model, up to permutations of the external particles. The user can reduce the number of generated processes by entering further restrictions. The restrictions that are currently supported are the following:

- restricting the number of particles of each spin,
- limiting the number of particles of each gauge group index defined in the model,
- restricting the number of particles of each charge type defined in the model.

In a future version, the user will be able to fine tune this list by manually adding or removing processes.

After generating a list of processes to study, the user can choose which matrix element generators to use and in which gauges. Currently available choices are CalcHEP in Feynman and unitary gauge, MadGraph in unitary gauge and Whizard in Feynman and unitary gauge. Support for other matrix element generators is planned for the future. The user can also choose whether to include an independently implemented model in the validation. Typically, multiple tests are performed:

- in one test, multiple matrix element generators are run, all in unitary gauge;
- in another test, gauge invariance is tested by running CalcHEP in both gauges;
- in yet another test, gauge invariance is again tested by running Whizard in both gauges¹.

Once the process list, the matrix element generators and the gauges are chosen, the calculations can be performed. The web validation organizes the calculations and submits them to a Condor [112] scheduler for running them on a computer cluster. For each process, it collides the incoming particles at an energy which is greater than threshold and far from any resonance in order to not be sensitive to particle widths (each matrix element generator deals with the widths differently). In addition, a p_T cut is applied in order to remove T-channel singularities. The web validation only submits a small number of jobs to the cluster at a time for each test. When those jobs are finished, it submits more. In this way, if multiple users are running tests, the jobs are mixed together on the Condor cluster and each sees progress at roughly the same rate. Once a job finishes, the web validation software stores the resulting cross section and Monte-Carlo uncertainty in a MySQL database for later analysis. Comparisons of the differential cross section at an individual phase space point is planned for a later version.

After the jobs are done, the validation software analyzes χ^2 for each process which is given by:

$$\chi^2 = \sum_i \left(\frac{\sigma_i - \sigma_{best}}{\Delta\sigma_i} \right)^2, \quad (3)$$

where σ_i is the cross section obtained from matrix element generator and gauge i , σ_{best} is the best value for the cross section and $\Delta\sigma_i$ is the Monte Carlo uncertainty for the cross section obtained from matrix element generator and gauge i . The value of σ_{best} is obtained by minimizing χ^2 . The resulting values for χ^2 are then histogrammed and a χ^2 distribution is plotted and presented on the web page for the test (see examples in the next section) along with the theoretical χ^2 distribution theoretically expected from Poisson statistics.

Typically, a correctly implemented model will give a χ^2 distribution as good as or better than the theoretical χ^2 curve². Furthermore, the results of the processes are listed in order of χ^2 starting with the highest value. When the histogrammed χ^2 values are worse than the theoretical χ^2 curve, it is likely that there is something wrong with the model. In this case, there are typically one or more processes with very large values of χ^2 listed at the top of the process list. By analyzing the details of these discrepant processes, the user can often find the mistake in his or her implementation.

¹We note that testing gauge invariance in CalcHEP is slightly different than testing gauge invariance in Whizard. In CalcHEP, both Goldstone bosons and Faddeev-Popov ghosts are included in the external states to cancel unphysical polarizations of gauge bosons in the analytic polarization sum. Whizard on the other hand calculates helicity amplitudes and sums over physical helicities only. As a result, they test slightly different aspects of gauge invariance which can be useful for finding bugs.

²We find that if the model is implemented correctly, then the χ^2 distribution is often shifted towards smaller χ^2 than would be expected from pure Poisson statistics.

Validating simulation software is extremely important in order to avoid wrong physics results coming from faulty software. We, again, emphasize that this automated validation software should complement other tests. The user should still check that the Feynman rules given by FeynRules, as well as various physical distributions, are correct and agree with published vertices/distributions where possible. This automated validation software should be used as an additional test that increases the confidence in a model implementation.

4 VALIDATION OF THE MINIMAL Z' MODEL

Before running it through the automated validation suite described in the previous section, the minimal Z' model had already been checked in the following ways:

- the limit cases of the SM and the minimal $B - L$ model [113] are correctly obtained,
- the Z' width and all its partial decay widths have been compared to calculations by hand and agree,
- we have compared our production cross section for the Z'_χ with the similar $SO(10)$ inspired model in the literature [106] and found agreement to within the uncertainties of the PDF's and matrix element generators used to do the calculations,
- we have checked that certain vanishing vertices are not spuriously produced by our implementation (e.g., no interactions between a photon ghost and other neutral gauge bosons or neutral ghosts are allowed).

After completing these initial tests, the model was uploaded to the validation server and a series of tests was run. We used the validation software to generate all $2 \rightarrow 2$ processes allowed by the symmetries of our model, which gave 1424 processes on which we ran the following tests:

- Test 1: For each process, we compared the Feynman and unitary gauges in CalcHEP,
- Test 2: For each process, we compared the Feynman and unitary gauges in Whizard,
- Test 3: For each process, we compared CalcHEP and Whizard in unitary gauge.

Plots of the resulting χ^2 distribution (c.f. Eq. 3) are shown in Fig. 1. The curves show that

- No large discrepancy was found.
- The binned results from our tests did better than expected from a theoretical χ^2 distribution.

5 CONCLUSIONS

We have implemented a class of $U(1)$ gauge models that spans the space of “minimal” Z' models with a continuous parameter interpolating among them. The FeynRules implementation of the model has been made publicly available through the FeynRules website.

We have also implemented a new automatized validation package. This package is accessible on the internet and allows a registered user to upload their models and run a series of tests on them. The tests which are currently supported are a comparison of all $2 \rightarrow 2$ processes

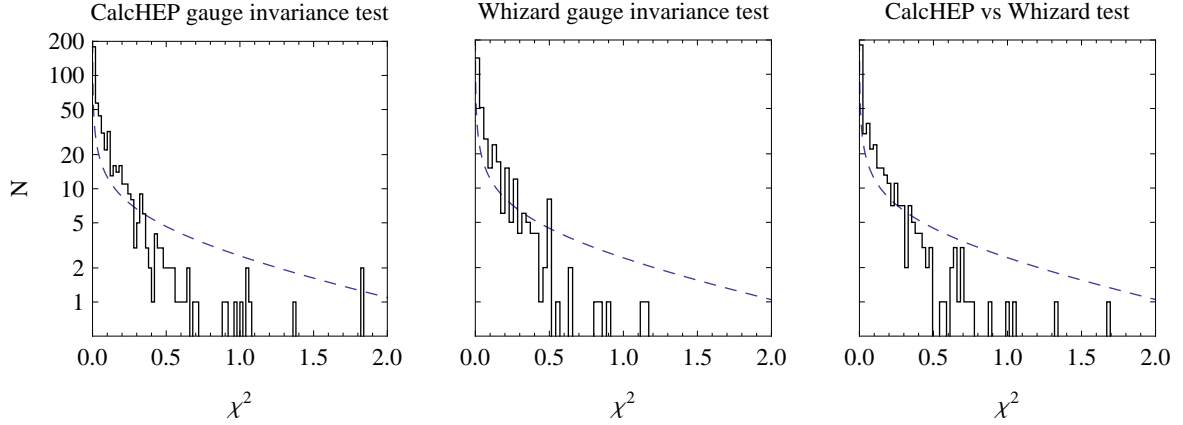


Figure 1: Plots of the binned (solid) and theoretical (dashed) χ^2 . The results of the CalcHEP gauge invariance test, Whizard gauge invariance test and CalcHEP versus Whizard (in unitary gauge) test are shown on the left, middle and right respectively. Actual data is solid, while the theoretical χ^2 distribution is given by the dashed line.

between different matrix element generators and between Feynman and unitary gauges. After calculation of each cross section, the validation package calculates χ^2 for each process and presents the resulting χ^2 distribution to the user together with the test results.

Using this web validation package we have validated the implementation of the “minimal” Z' models and found full consistency.

ACKNOWLEDGEMENTS

We would like to congratulate the Les Houches organisers for a great and fruitful workshop atmosphere, good food, and the amazing scenery of the French alps. LB thanks the NExT Institute for partial financial support. LB and CS have been supported by the Deutsche Forschungsgemeinschaft through the Research Training Group GRK 1102 *Physics of Hadron Accelerators*. NC was partially supported by the United States National Science Foundation under grant NSF-PHY-0705682 and partially by the PITTsburgh Particle Physics, Astrophysics and Cosmology Center (PITT PACC). The server that ran the web validation software was bought with funds from IISN 4.4517.08. We would like to thank Vincent Boucher and the Center for Cosmology, Particle Physics and Phenomenology (CP3) at the Université catholique de Louvain / Louvain-la-Neuve for administering the server.

Contribution 6

Implementation of scalar and vector resonances into FeynRules and LanHEP

Abstract

In this summary report we discuss the implementation of a set of operators in FEYNRULES and LANHEP that can be used to study in a bottom-up approach new scalar and vector resonances coupling to quarks.

1 INTRODUCTION

Monte Carlo event generators play an important role in making reliable predictions for events to be observed in collider experiments, both to describe the backgrounds and possible candidate signals. In particular, the simulation of a hadronic collision requires not only an accurate description of the underlying hard scattering process, but also of the parton showering and hadronization as efficiently provided by programs such as HERWIG [114, 115], PYTHIA [116, 117] and SHERPA [118, 119]. As regards the generation of the hard matrix element itself, a lot of effort has gone into the development of several multipurpose matrix element generators, such as COMPHEP/CALCHEP [1, 90, 91], MADGRAPH/MADEVENT [92–96], SHERPA and WHIZARD [97, 98]. Even though these programs are in principle able to generate the (tree-level) matrix element for any process in a renormalizable quantum field theory built on scalar, vector and fermion fields, the implementation of a full Beyond the Standard Model (BSM) theory can be a tedious and error-prone task, often requiring the implementation of one vertex at the time following the conventions specific to each code. Recently, this task has been alleviated by the introduction of new tools that allow to obtain the Feynman rules directly from a Lagrangian and to export them to various matrix element generators in an automated way.

The aim of this contribution is to present the summary report on the implementation of a certain class of operators that allow to study possible BSM contributions such as the forward-backward asymmetry measured by the CDF and DØ collaborations at the Fermilab Tevatron collider [120, 121] into various matrix element generators. The goal is to provide a framework in which the anomaly observed at the Tevatron can be studied in a bottom-up approach. More precisely, we have implemented all the operators classified in Refs. [122, 123] into both FEYNRULES [6, 78, 107] and LANHEP [9, 124–126].

FEYNRULES is a MATHEMATICA®¹ package that allows computation of Feynman rules from a Lagrangian and can export them to various matrix element generators in an automated way, thus allowing implementation of the model into these tools. For the moment, interfaces to COMPHEP/CALCHEP, FEYNARTS/FORMCALC [127–132], GoSAM [133], MADGRAPH/MADEVENT [134, 135], SHERPA and WHIZARD [108] are available.

The LANHEP package is also designed to automatically generate Feynman rules for a given Lagrangian. LANHEP is written in the C programming language and can be easily compiled and installed on any platform. Its first version was released in 1996 and was effectively

¹MATHEMATICA is a registered trademark of Wolfram Research, Inc.

used to derive Feynman rules for the Minimal Supersymmetric Standard Model for the COMPHEP package. LANHEP reads the Lagrangian written as a text file in a compact form, close to the one used in publications. Lagrangian terms can be written with summation over indices of broken symmetries and using special symbols for complicated expressions, such as covariant derivatives and strength tensors for gauge fields. LANHEP creates an output file with Feynman rules in the format of COMPHEP, CALCHEP and FEYNARTS model files as well as has an option to generate the output file in the form of a L^AT_EX table. Also, LANHEP can generate one-loop counterterms in the FEYNARTS format. One should also add that the latest LanHEP v.3.15 has an option (under test) for outputting the model in UFO format which provides a way to interface it with MADGRAPH/MADEVENT.

The outline of this contribution is as follows: In Section 2 we review the operators and the spectrum of the resonances we implemented. In Sections 3 and 4 we discuss the implementation of all these operators into the FEYNRULES and LANHEP packages. We compare the two implementations in Section 5 by computing a selection of decay rates and 2-to-2 cross section with MADGRAPH 5 and CALCHEP. Our conclusions are drawn in Section 6.

2 SCALAR AND VECTOR RESONANCES COUPLING TO QUARK PAIRS

In this section we briefly discuss the various renormalizable operators of scalar or vector resonances coupling to quark pairs we have implemented into FEYNRULES and LANHEP. These operators are particularly interesting to study possible BSM origins of the anomaly in the forward-backward asymmetry in top-quark pair production measured at the Tevatron. In Refs. [122, 123] a classification was made of possible operators describing scalar and vector resonances carrying charges under the SM gauge group and contributing to the processes $u\bar{u}, d\bar{d} \rightarrow t\bar{t}$. These resonances thus provide a (non-exhaustive) list of operators that can be used to study potential BSM corrections to the asymmetry in a bottom-up approach.

The Lagrangian of the “model” containing all these new scalar and vector resonances can be written as a sum of three terms

$$\mathcal{L} = \mathcal{L}_{SM} + \mathcal{L}_{BSM,kin} + \mathcal{L}_{BSM,int} . \quad (1)$$

While \mathcal{L}_{SM} denotes the SM Lagrangian, $\mathcal{L}_{BSM,kin}$ and $\mathcal{L}_{BSM,int}$ describe the resonances’ kinetic terms and couplings to quarks. The kinetic terms for the new resonances can schematically be written in the form

$$\begin{aligned} \mathcal{L}_{BSM,kin} = & \frac{1}{2} D_\mu \varphi_i D^\mu \varphi_i - \frac{1}{2} m_{\varphi_i}^2 \varphi_i^2 + D_\mu \Phi_i^\dagger D^\mu \Phi_i - m_{\Phi_i}^2 \Phi_i^\dagger \Phi_i \\ & - \frac{1}{4} (D_\mu v_{i\nu} - D_\nu v_{i\mu}) (D^\mu v_i^\nu - D^\nu v_i^\mu) - \frac{1}{2} m_{v_i}^2 v_{i\mu} v_i^\mu \\ & - \frac{1}{2} (D_\mu V_{i\nu}^\dagger - D_\nu V_{i\mu}^\dagger) (D^\mu V_i^\nu - D^\nu V_i^\mu) - m_{V_i}^2 V_{i\mu}^\dagger V_i^\mu , \end{aligned} \quad (2)$$

where φ_i (Φ_i) and $v_{i\mu}$ ($V_{i\mu}$) denote generic real (complex) scalar and vector fields transforming in some irreducible representation of the SM gauge group, and D_μ denotes the $SU(3)_c \times SU(2)_L \times U(1)_Y$ covariant derivative. The explicit list of all scalar and vector fields considered in Refs. [122, 123] is given in Tables 1 and 2. We note that, while all gauge interactions of the new resonances are taken into account via the covariant derivative, we do not include possible

Field	Charges	Operator	Coupling
ϕ	$(1, 2)_{-1/2}$	$-\bar{Q}_L g^u u_R \phi - \bar{Q}_L g^d d_R \tilde{\phi} + \text{h.c.}$	–
Φ	$(8, 2)_{-1/2}$	$-\bar{Q}_L g^u T^a u_R \Phi^a - \bar{Q}_L g^d T^a d_R \tilde{\Phi}^a + \text{h.c.}$	–
ω^1	$(3, 1)_{-1/3}$	$-\epsilon_{ijk} \bar{d}_{Rj} g u_{Rk}^c \omega_i^{1\dagger} + \text{h.c.}$	–
Ω^1	$(\bar{6}, 1)_{-1/3}$	$-\frac{1}{2} \bar{K}_{ij}^\alpha [\bar{d}_{Ri} g u_{Rj}^c + \bar{d}_{Rj} g u_{Ri}^c] \Omega_\alpha^{1\dagger} + \text{h.c.}$	–
ω^4	$(3, 1)_{-4/3}$	$-\epsilon_{ijk} \bar{u}_{Rj} g u_{Rk}^c \omega_i^{4\dagger} + \text{h.c.}$	$g^T = -g$
Ω^4	$(\bar{6}, 1)_{-4/3}$	$-\frac{1}{2} \bar{K}_{ij}^\alpha [\bar{u}_{Ri} g u_{Rj}^c + \bar{u}_{Rj} g u_{Ri}^c] \Omega_\alpha^{4\dagger} + \text{h.c.}$	$g^T = g$
σ	$(3, 3)_{-1/3}$	$-\epsilon_{ijk} \bar{Q}_{Li} g \tau^I \epsilon_{Q_{Lj}^c} \sigma_{kI}^\dagger + \text{h.c.}$	$g^T = -g$
Σ	$(\bar{6}, 3)_{-1/3}$	$-\frac{1}{2} \bar{K}_{ij}^\alpha [\bar{Q}_{Li} g \tau^I \epsilon_{Q_{Lj}^c} + \bar{Q}_{Lj} g \tau^I \epsilon_{Q_{Li}^c}] \Sigma_{\alpha I}^\dagger + \text{h.c.}$	$g^T = g$

Table 1: Operators describing the couplings of the scalar resonances to quarks [122, 123]. g, g^u and g^d are coupling matrices in flavor space, τ^I are the Pauli matrices and \bar{K}_{ij}^α is the Clebsch-Gordan coefficient linking two triplet representations to a sextet representation. The last column gives the symmetries of the coupling matrices g (if any).

Field	Charges	Operator	Coupling
\mathcal{B}_μ	$(1, 1)_0$	$-(\bar{Q}_L g^Q \gamma^\mu Q_L + \bar{u}_R g^u \gamma^\mu u_R + \bar{d}_R g^d \gamma^\mu d_R) \mathcal{B}_\mu$	$g^\dagger = g$
\mathcal{W}_μ	$(1, 3)_0$	$-\bar{Q}_L g \gamma^\mu \tau^I Q_L \mathcal{W}_\mu^I$	$g^\dagger = g$
\mathcal{B}_μ^1	$(1, 1)_1$	$-\bar{d}_R g \gamma^\mu u_R \mathcal{B}_\mu^{1\dagger} + \text{h.c.}$	–
\mathcal{G}_μ	$(8, 1)_0$	$-(\bar{Q}_L g^Q \gamma^\mu T^a Q_L + \bar{u}_R g^u \gamma^\mu T^a u_R + \bar{d}_R g^d \gamma^\mu T^a d_R) \mathcal{G}_\mu^a$	$g^\dagger = g$
\mathcal{H}_μ	$(8, 3)_0$	$-\bar{Q}_L g \gamma^\mu \tau^I T^a Q_L \mathcal{H}_\mu^{aI}$	$g^\dagger = g$
\mathcal{G}_μ^1	$(8, 1)_1$	$-\bar{d}_R g \gamma^\mu T^a u_R \mathcal{G}_\mu^{1a\dagger} + \text{h.c.}$	–
\mathcal{Q}_μ^1	$(3, 2)_{1/6}$	$-\epsilon_{ijk} \bar{d}_{Rj} g \gamma^\mu \epsilon_{Q_{Lk}^c} \mathcal{Q}_\mu^{1i\dagger} + \text{h.c.}$	–
\mathcal{Q}_μ^5	$(3, 2)_{-5/6}$	$-\epsilon_{ijk} \bar{u}_{Rj} g \gamma^\mu \epsilon_{Q_{Lk}^c} \mathcal{Q}_\mu^{5i\dagger} + \text{h.c.}$	–
\mathcal{Y}_μ^1	$(\bar{6}, 2)_{1/6}$	$-\frac{1}{2} \bar{K}_{ij}^\alpha [\bar{d}_{Ri} g \gamma^\mu \epsilon_{Q_{Lj}^c} + \bar{d}_{Rj} g \gamma^\mu \epsilon_{Q_{Li}^c}] \mathcal{Y}_\mu^{1\alpha\dagger} + \text{h.c.}$	–
\mathcal{Y}_μ^5	$(\bar{6}, 2)_{-5/6}$	$-\frac{1}{2} \bar{K}_{ij}^\alpha [\bar{u}_{Ri} g \gamma^\mu \epsilon_{Q_{Lj}^c} + \bar{u}_{Rj} g \gamma^\mu \epsilon_{Q_{Li}^c}] \mathcal{Y}_\mu^{5\alpha\dagger} + \text{h.c.}$	–

Table 2: Operators describing the couplings of the vector resonances to quarks [122, 123]. g, g^Q, g^u and g^d are coupling matrices in flavor space, τ^I are the Pauli matrices and \bar{K}_{ij}^α is the Clebsch-Gordan coefficient linking two triplet representations to a sextet representation. The last column gives the symmetries of the coupling matrices g (if any).

mixing effects among the new resonances or with SM particles². Besides interacting with the SM gauge bosons, the new resonances also couple to quark pairs via three-point interactions described by $\mathcal{L}_{BSM,int}$ and summarized in Tables 1 and 2.

3 IMPLEMENTATION INTO FEYNRULES

The Lagrangian implemented into FeynRules follows exactly the classification of operators given in Refs. [122, 123]. The implementation is completely generic, and allows to choose freely the numerical values for the new masses and couplings, including all possible flavor and/or CP -violating effects in the coupling constants. In this way the implementation allows

²It would in principle be possible to consider for example kinetic mixing between the SM gauge bosons and the new vector fields. We do not however include these terms into the Lagrangian.

for a maximum of flexibility when studying the resonances. We have implemented all the operators described in the previous section into FEYNRULES. The implementation is based on the implementation of the Standard Model (SM) in FEYNRULES shipped together with the package. The additional files needed for the new interactions can be downloaded from the FEYNRULES website [136]. In the rest of this section we give a very brief account on the implementation and how to use the model files. For a full documentation we refer to the corresponding website.

In order to allow for the study of only a subset of the new resonances, we have implemented each of the entries in Tables 1 and 2 into a separate model file. A given subset of files corresponding to a given set of resonances of interest can then be loaded at run time into FeynRules. More precisely, the implementation consists of the following files,

- `Representation.fr`: The SM implementation in FEYNRULES does not contain any definitions regarding the sextet representation of the QCD gauge group. The file `Representation.fr` extends the definition of the SM gauge group in FEYNRULES by adding the corresponding representation.
- `SCxy.fr`, x, y being integers: These files contain all the declarations and interactions of a new scalar particle transforming in the representation (x, y) of $SU(3)_c \times SU(2)_L$ (e.g., `SC12.fr` contains the definitions of the resonance ϕ transforming in the representation $(1, 2)_{-1/2}$ defined in Table 1).
- `Vxy.fr`, x, y being integers: Similar to `SCxy.fr`, but for the vector resonances.

The files can then be loaded into FEYNRULES and combined at leisure at run time. As an example, the SM extended by the scalar resonances ϕ and σ defined in Table 1 can be loaded into FEYNRULES via the command

```
LoadModel[ "SM.fr", "Representation.fr", "SC12.fr", "SC33.fr" ].
```

We emphasize that the file `SM.fr` should be loaded first, in order to set up correctly the SM part of the model. Furthermore, in order to allow for a maximum of flexibility, all the new numerical input parameters (masses and coupling matrices) are kept completely generic. In particular the masses of all new resonances are given a default value of 1 TeV, and all the coupling matrices are implemented as generic complex matrices (subject to the symmetry constraints given in the last column in Tables 1 and 2), initialized to the identity matrix in the model files. Note that, as the widths of the resonances are functions of the masses and the couplings, it is important to recompute the widths of the particles every time the numerical input parameters are changed.

After the model has been loaded into FEYNRULES, the Feynman rules can be obtained and exported to matrix element generators in the usual way. However, some of the interactions appearing in these operators have rather unusual color structures (color sextets, ϵ_{ijk}), which are in general not supported by all the matrix element generators. As a consequence not all the interactions can be implemented into all the matrix element generators for which a FEYNRULES interface exists. To our knowledge, the only matrix element generator currently able to deal with all the color structures involved is MADGRAPH 5.

4 IMPLEMENTATION INTO LANHEP

The Lagrangian implemented into LANHEP also corresponds exactly to the classification of operators given in Refs. [122, 123]. One should note that LANHEP as well as CALCHEP need

to be extended to deal with colour sextet representations as well as with interactions involving the epsilon colour tensor ϵ_{ijk} connecting three colour-triplet particles. So, the respective interactions are not implemented at the moment into LANHEP. The request to extend LANHEP to include these interactions has been sent to its author.

The implementation of the rest interactions from Tables 1 and 2 is done in the form of a separate model which includes also SM interactions. All models are available for download at the High Energy Model Database website [137].

As in the case of FEYNRULES, the LANHEP implementation of these models is generic and written in the form of module files with a naming scheme similar to FEYNRULES. For example the term with $\mathcal{H}_\mu(8, 3)_0$ interactions is implemented in the `v830.mdl` file which is included in the `sm+v830.mdl` model. Similarly, one can add several new interactions to the SM in the LANHEP format.

5 COMPARISON OF THE TWO IMPLEMENTATIONS

To verify the FEYNRULES and LANHEP implementations, we have confronted the two implementations by computing a selection of decay rates and 2-to-2 cross sections with MADGRAPH 5 and CALCHEP. The input files for MADGRAPH 5 were generated with FEYNRULES, whereas the input files for CALCHEP were generated with LANHEP. In the rest of this section we present a brief summary of the comparison. For all the processes presented in this section, the masses of all the resonances are set to 1 TeV and the coupling matrices are assumed to be the identity matrix (including the CKM matrix).

As a first check, we computed the decay rates of a resonance into light quarks. It is easy to show that, in the scenario where all the resonances have the same mass, and all the coupling matrices are proportional to the identity matrix³, the decay rates into light quarks are linked and only one of them is independent, which we choose to be

$$\gamma \equiv \Gamma(\phi^0 \rightarrow u \bar{u}) = \frac{|g|^2 N_c M}{16\pi}, \quad (3)$$

where ϕ^0 denotes the weak isospin (+1/2) component of the scalar field ϕ , $\phi^T = (\phi^0, \phi^-)$, M is the mass of the decaying particle and N_c is the number of colors. The decay rates of all other scalar resonances are related to γ via the relations

$$\begin{aligned} \Gamma(\phi^- \rightarrow d \bar{u}) &= 2\gamma, \\ \Gamma(\Phi^0 \rightarrow u \bar{u}) &= \frac{1}{6}\gamma, \\ \Gamma(\Phi^- \rightarrow d \bar{u}) &= \Gamma(\Omega^1 \rightarrow \bar{u} \bar{d}) = \Gamma(\Sigma_{2/3} \rightarrow \bar{d} \bar{d}) = \Gamma(\Sigma_{-1/3} \rightarrow \bar{u} \bar{d}) = \\ &= \Gamma(\Sigma_{-4/3} \rightarrow \bar{u} \bar{u}) = \frac{1}{3}\gamma, \\ \Gamma(\omega^1 \rightarrow \bar{u} \bar{d}) &= \Gamma(\Omega^4 \rightarrow \bar{u} \bar{u}) = \Gamma(\sigma_{-1/3} \rightarrow \bar{u} \bar{s}) = \frac{2}{3}\gamma, \\ \Gamma(\sigma_{2/3} \rightarrow \bar{d} \bar{s}) &= \Gamma(\sigma_{-4/3} \rightarrow \bar{u} \bar{c}) = \frac{4}{3}\gamma, \\ \Gamma(\omega^4 \rightarrow \bar{u} \bar{c}) &= \frac{8}{3}\gamma. \end{aligned} \quad (4)$$

³Note that some of the coupling matrices in Table 1 are antisymmetric. In this case we assume that the entries in the upper triangular half are equal to unity.

	FR + MG5	LH + CH		FR + MG5	LH + CH
$\phi^0 \rightarrow u \bar{u}$	59.683	59.683	$\mathcal{B} \rightarrow u \bar{u}$	79.577	79.577
$\phi^- \rightarrow d \bar{u}$	119.37	119.37	$\mathcal{W}^3 \rightarrow u \bar{u}$	39.789	39.789
$\Phi^0 \rightarrow u \bar{u}$	9.9472	9.9472	$\mathcal{W}^+ \rightarrow u \bar{d}$	79.577	79.577
$\Phi^- \rightarrow d \bar{u}$	19.894	19.894	$\mathcal{B}^1 \rightarrow u \bar{d}$	39.789	39.789
$\omega^1 \rightarrow \bar{u} \bar{d}$	39.789	–	$\mathcal{G} \rightarrow u \bar{u}$	13.263	13.263
$\Omega^1 \rightarrow \bar{u} \bar{d}$	19.894	–	$\mathcal{H}^3 \rightarrow u \bar{u}$	6.632	6.632
$\omega^4 \rightarrow \bar{u} \bar{c}$	159.15	–	$\mathcal{H}^+ \rightarrow u \bar{d}$	13.263	13.263
$\Omega^4 \rightarrow \bar{u} \bar{u}$	39.789	–	$\mathcal{G}^1 \rightarrow u \bar{d}$	6.632	6.632
$\sigma_{-1/3} \rightarrow \bar{u} \bar{s}$	39.789	–	$\mathcal{Q}_{2/3}^1 \rightarrow \bar{d} \bar{d}$	26.526	–
$\sigma_{2/3} \rightarrow \bar{d} \bar{s}$	79.578	–	$\mathcal{Q}_{-1/3}^1 \rightarrow \bar{u} \bar{d}$	26.526	–
$\sigma_{-4/3} \rightarrow \bar{u} \bar{c}$	79.578	–	$\mathcal{Q}_{-1/3}^5 \rightarrow \bar{u} \bar{d}$	26.526	–
$\Sigma_{-1/3} \rightarrow \bar{u} \bar{d}$	19.894	–	$\mathcal{Q}_{-4/3}^5 \rightarrow \bar{u} \bar{u}$	26.526	–
$\Sigma_{-4/3} \rightarrow \bar{u} \bar{u}$	19.894	–	$\mathcal{Y}_{-1/3}^1 \rightarrow \bar{u} \bar{d}$	13.263	–
$\Sigma_{2/3} \rightarrow \bar{d} \bar{d}$	19.894	–	$\mathcal{Y}_{2/3}^1 \rightarrow \bar{d} \bar{d}$	13.263	–
			$\mathcal{Y}_{-4/3}^5 \rightarrow \bar{u} \bar{u}$	13.263	–
			$\mathcal{Y}_{-1/3}^5 \rightarrow \bar{u} \bar{d}$	13.263	–

Table 3: Decay widths (in GeV) for the scalar (left) and vector (right) resonances computed with FEYNRULES and MADGRAPH 5 (FR+MG5), and LANHEP and CALCHEP (LH+CH). The LANHEP implementation currently does not include ϵ_{ijk} or sextet color structures.

Similarly, the decay rates of the vector resonances are related to γ as well:

$$\begin{aligned}
\Gamma(\mathcal{B} \rightarrow u \bar{u}) &= \Gamma(\mathcal{W}^+ \rightarrow u \bar{d}) = \frac{4}{3} \gamma, \\
\Gamma(\mathcal{W}^3 \rightarrow u \bar{u}) &= \Gamma(\mathcal{B}^1 \rightarrow u \bar{d}) = \frac{2}{3} \gamma, \\
\Gamma(\mathcal{G} \rightarrow u \bar{u}) &= \Gamma(\mathcal{H}^+ \rightarrow u \bar{d}) = \Gamma(\mathcal{Y}_{-1/3}^1 \rightarrow \bar{u} \bar{d}) = \Gamma(\mathcal{Y}_{2/3}^1 \rightarrow \bar{d} \bar{d}) = \\
&= \Gamma(\mathcal{Y}_{4/3}^5 \rightarrow \bar{u} \bar{u}) = \Gamma(\mathcal{Y}_{-1/3}^5 \rightarrow \bar{u} \bar{d}) = \frac{2}{9} \gamma, \\
\Gamma(\mathcal{G}^1 \rightarrow u \bar{d}) &= \Gamma(\mathcal{H}^3 \rightarrow u \bar{u}) = \frac{1}{9} \gamma, \\
\Gamma(\mathcal{Q}_{2/3}^1 \rightarrow \bar{d} \bar{d}) &= \Gamma(\mathcal{Q}_{-1/3}^1 \rightarrow \bar{u} \bar{d}) = \Gamma_{\mathcal{Q}_{-1/3}^5 \rightarrow \bar{u} \bar{d}} = \Gamma_{\mathcal{Q}_{-4/3}^5 \rightarrow \bar{u} \bar{u}} = \frac{4}{9} \gamma.
\end{aligned} \tag{5}$$

We have computed all the decay rates into light quarks numerically via MADGRAPH 5 and CALCHEP, and we have checked that all the above relations are verified. The results are summarized in Table 3. Note that the LANHEP implementation currently does not include ϵ_{ijk} or sextet color structures.

As the main purpose of our implementation is to study possible BSM contributions to the $t\bar{t}$ asymmetry measured at the Tevatron, we have also compared a selection of cross sections for $u\bar{u}, d\bar{d} \rightarrow t\bar{t}$. We generated the signal diagrams with MADGRAPH 5 and CALCHEP for a (partonic) center-of-mass energy $\sqrt{s} = 2$ TeV, and we neglected widths in the propagators. We found perfect agreement between the FEYNRULES and LANHEP implementations. The results are summarized in Table 4. In particular, the results satisfy the following relations (which follow

	FR+MG5	LH+CH
$u\bar{u} \rightarrow \phi^0, (\phi^0)^\dagger \rightarrow t\bar{t}$	1.6633	1.6707
$d\bar{d} \rightarrow \phi^0, (\phi^0)^\dagger \rightarrow t\bar{t}$	1.6633	1.6707
$u\bar{u} \rightarrow \Phi^0, (\Phi^0)^\dagger \rightarrow t\bar{t}$	0.3696	0.3713
$d\bar{d} \rightarrow \Phi^0, (\Phi^0)^\dagger \rightarrow t\bar{t}$	0.3696	0.3713
$u\bar{u} \rightarrow \mathcal{B} \rightarrow t\bar{t}$	4.5618	4.5890
$d\bar{d} \rightarrow \mathcal{B} \rightarrow t\bar{t}$	4.5618	4.5890
$u\bar{u} \rightarrow \mathcal{W}^3 \rightarrow t\bar{t}$	1.1173	1.1122
$d\bar{d} \rightarrow \mathcal{W}^3 \rightarrow t\bar{t}$	1.1173	1.1122
$u\bar{u} \rightarrow \mathcal{G} \rightarrow t\bar{t}$	1.0137	1.0198
$d\bar{d} \rightarrow \mathcal{G} \rightarrow t\bar{t}$	1.0137	1.0198
$u\bar{u} \rightarrow \mathcal{H}^3 \rightarrow t\bar{t}$	0.2483	0.2494
$d\bar{d} \rightarrow \mathcal{H}^3 \rightarrow t\bar{t}$	0.2483	0.2494

Table 4: Cross sections (in pb) computed with FEYNRULES and MADGRAPH 5 (FR+MG5), and LANEHEP and CALCHEP (LH+CH). No cuts are applied to the final state.

simply from color algebra considerations):

$$\begin{aligned}
\sigma(u\bar{u} \rightarrow \Phi^0 \rightarrow t\bar{t}) &= \frac{N_c^2 - 1}{4N_c^2} \sigma(u\bar{u} \rightarrow \phi^0 \rightarrow t\bar{t}) = \frac{2}{9} \sigma(u\bar{u} \rightarrow \phi^0 \rightarrow t\bar{t}), \\
\sigma(u\bar{u} \rightarrow \mathcal{G} \rightarrow t\bar{t}) &= \frac{N_c^2 - 1}{4N_c^2} \sigma(u\bar{u} \rightarrow \mathcal{B} \rightarrow t\bar{t}) = \frac{2}{9} \sigma(u\bar{u} \rightarrow \mathcal{B} \rightarrow t\bar{t}), \\
\sigma(u\bar{u} \rightarrow \mathcal{H}^3 \rightarrow t\bar{t}) &= \frac{N_c^2 - 1}{4N_c^2} \sigma(u\bar{u} \rightarrow \mathcal{W}^3 \rightarrow t\bar{t}) = \frac{2}{9} \sigma(u\bar{u} \rightarrow \mathcal{W}^3 \rightarrow t\bar{t}).
\end{aligned} \tag{6}$$

6 CONCLUSION

In this contribution we have discussed the implementation into FEYNRULES and LANEHEP of all the scalar and vector resonances with SM quantum numbers coupled to quark pairs presented in Refs. [122, 123]. These operators are relevant to study in a bottom-up approach the possible BSM contributions to the anomaly in the forward-backward asymmetry in top pair production measured by the CDF and DØ experiments. The implementation was done in a modular way, allowing the user to decide which resonances to consider, and gives the possibility to include all possible flavor and or CP -violating effects. The FEYNRULES model files are publicly available and can be downloaded from the FEYNRULES website [136]. The LANEHEP model files will be publicly available soon for download at the HEPMDB website [137].

ACKNOWLEDGEMENTS

CD and BF would like to thank CERN and LAPTH for their hospitality during the workshop during which some of the work contained herein was performed. BF is supported by the Theory-LHC France-initiative of the CNRS/IN2P3. This work was supported by the Research Executive Agency (REA) of the European Union under the Grant Agreement number PITN-GA-2010-264564 (LHCPhenoNet). A.B. thanks the NEXt Institute and Royal Society for partial financial support.

Contribution 7

SuSpect3

A.Djouadi, J-L. Kneur, G. Moultaka, M. Ughetto, D. Zerwas

Abstract

We present here an overview of the SuSpect3 project, ultimately aimed to be a major upgrade of the present SuSpect2 code for calculation of spectra in various supersymmetric models.

1 INTRODUCTION

The public Fortran code **SuSpect** [79] calculates the supersymmetric and Higgs particle spectrum in the Minimal Supersymmetric Standard Model (MSSM). In its present version (latest 2.41), it can deal with specific supersymmetry-breaking models with universal boundary conditions at high scales, such as the gravity (mSUGRA), anomaly (AMSB) or gauge (GMSB) mediated supersymmetry breaking models, as well as non-universal MSSM (restricted however to R -parity and CP conservation). Input and Output can be driven from the standard SLHA format files [15]. The algorithm includes the main mandatory ingredients such as the renormalization group evolution (RGE) of parameters between low and high energy scales, the consistent implementation of radiative electroweak symmetry breaking, and the calculation of the physical masses of the Higgs bosons and supersymmetric particles including the full one-loop and dominant two-loop radiative corrections. In addition a control of important theoretical and experimental features is available, such as the absence of non-physical minima, the amount of fine-tuning in the electroweak symmetry breaking condition, or the agreement with some precision observables. Although SuSpect2 is still considered essentially up-to-date and will continue to be maintained in the future, a major upgrade is timely for several reasons.

Given the experimental prospects for supersymmetry, the available tools for the interpretation of the data to come at the LHC should allow high flexibility in implementing new models and/or new theoretical improvements and variants of the existing ones. It is obviously necessary to keep up with the state of the art regarding any eventual new and more precise theoretical calculation that can affect the predictions. It is also desirable to be able to encode in the same tool a large variety of supersymmetric models, non-minimal extensions, more general flavor structure in the (s)quark and (s)lepton sectors, R -parity violation, CP -violating phases, new energy thresholds related to low or high scale extended gauge groups, modified GUT or universality conditions, etc. The task becomes less formidable than it may seem if one recognizes properly the generic features of the various extensions. An object oriented programming approach is particularly suitable in this context. SuSpect3, which we describe below, is the first step in this project. It is a C++ version of the latest SuSpect2 version, fully rewritten with an object-oriented architecture but containing the same algorithms as SuSpect2 (though details of the implementation have changed). In the following the structure and the implementation will be described first. Then a comparison between SuSpect2 and SuSpect3 for an mSUGRA benchmark point as well as a scan will be described.

2 STRUCTURE AND IMPLEMENTATION

C++ was chosen for the implementation of SuSpect3. The use of this language is widespread in the experimental high energy physics community, where ATLAS and CMS rely on it for a major part of their software, as well as in the theoretical community, where the event generators PYTHIA8 [117] and Herwig++ [138] have moved from FORTRAN to this language.

In writing SuSpect3 care was taken not to resort to a line-by-line technical conversion of SuSpect2 as this would have been a change of syntax with no added benefit. The rewrite limits the inheritance structure to essentially three layers. Additionally the possibility of using other codes for parts of the calculations usually performed by SuSpect2 is also foreseen. An example is the use of the renormalization group equations provided by tools such as SARAH [139] or Feynrules [140].

As a first test of the flexibility and the robustness of the new implementation, the first and second generation of sfermions were separated. In SuSpect2 these were hard-coded to be equal. The change took less than a day (testing included), giving a first indication of the robustness of the new structure.

The internal communication between different objects is assured by an implementation of the SLHA structure in memory. The SLHA object contains all SLHA1 standard blocks as well as supplementary blocks used internally.

The top object `suspect` has three methods: `Initialize`, `Execute` and `Finalize`. For the initialization polymorphism is used: one can either use the default settings of SuSpect (SPS1a), read an SLHA file by passing the name of the file as argument or create and initialize an SLHA object in memory and pass it as argument to the object `suspect`. After the calculation, the output is given either on screen or written to a file.

The requested model is configured in the `suspect` object: the MSSM (defined at either a high scale or at the EWSB scale), mSUGRA, AMSB, mGMSB and CompressedSUSY have been implemented so far. In these objects only the initialization of the model as well as the definition of the boundary conditions have to be implemented. The next layer consists of `Model4Scales`, `Model3Scales` or `Model2Scales`. These classes implement the logic of the sequence of the calculation of the spectrum. The separation is driven by the number of scales involved in the definition of the model. All `Model2/3/4Scales` are objects which inherit from a common baseclass `ModelBase`. This class holds the data members common to all classes: an RGE solver, determination of the \overline{DR} parameters, the calculators of the particle masses, the implementation of electroweak symmetry breaking (`EWSBBase`) etc. As an example: the object `ModelmSUGRA` (created in the object `suspect`) inherits from `Model3Scales` as its parameters are defined at the GUT scale, RGE-evolved to the EWSB scale and corrections to the Standard Model particles are calculated at the scale of the Z boson mass. `ModelAMSB` is derived from `Model3Scales`. As GMSB has an additional intermediate scale, it is derived from the `Model4Scales`, whereas `ModelLowScaleMSSM` is derived from `Model2Scales`.

The RGE evolution from one scale to another is steered by the object `Model2/3/4Scales`. The `RgeEvolution` object can be called multiple times in a calculation. The object fetches the information in the SLHA object, solves the RGE equations and writes the final result back into the SLHA object.

Each particle to be calculated is implemented as an object which can be configured to include radiative corrections or not. All particle objects inherit from a common baseclass. The calculation of the particle masses from the parameters is steered by the object `ModelBase`. The

result of the calculations is stored in the SLHA object.

If the environment variable ROOTSYS is defined, ROOT will be linked automatically. If the variable is not defined, the compilation will be performed without in a transparent way. The ROOT output file contains a tree suspect3 with the content of the SLHA blocks.

3 Results

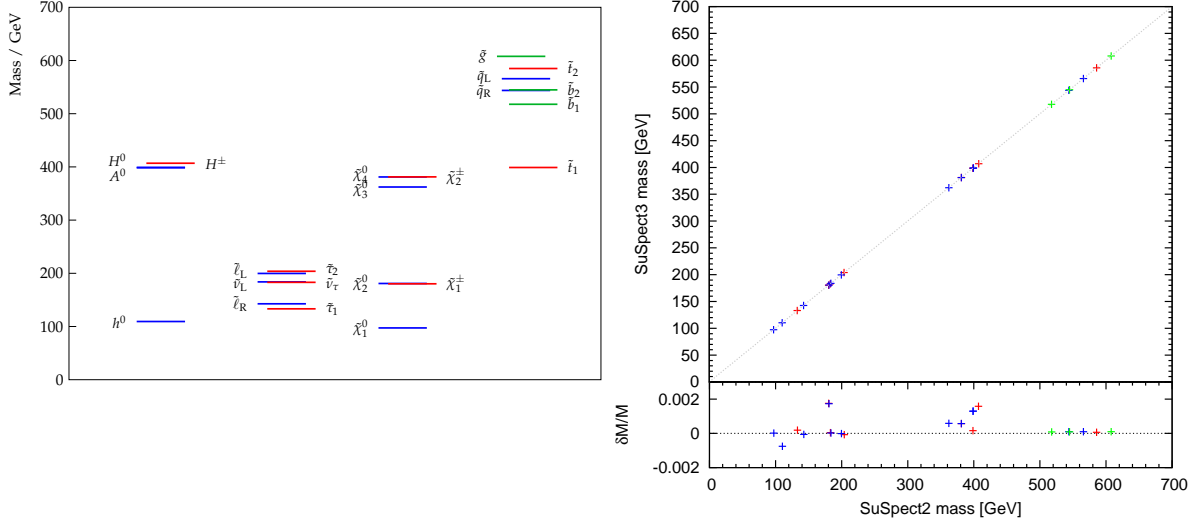


Figure 1: On the left, the SPS1a spectrum is shown as computed by SuSpect3. On the right, the comparison of the masses calculated by SuSpect2 and SuSpect3 is shown.

As a benchmark point the well known mSUGRA point SPS1a [141] has been used to compare SuSpect3 and SuSpect2. SPS1a has the GUT scale boundary conditions: $A_0 = -100$ GeV, $\tan \beta = 10$, $m_0 = 100$ GeV and $m_{1/2} = 250$ GeV. The Higgs mass parameter μ was chosen to be positive. The electroweak symmetry breaking scale (EWSB) is set to 1 TeV as suggested in Ref. [142]. At each step of the algorithm, comparisons were performed to make sure that all details agree. As an example, the spectrum predicted by SuSpect3 as well as the comparison of the mass of the particles with respect to SuSpect2 are shown in Figure 1. The two predictions are in good agreement at the per mil level.

As a further illustration a scan was performed in mSUGRA. Three parameters ($A_0 = -100$ GeV, $\tan \beta = 10$, $\mu > 0$) were fixed. The common scalar and sfermion masses were scanned from 100 GeV to 1 TeV in steps of 9 GeV. In Figure 2 the relative deviation of SuSpect2 and SuSpect3 is shown. As an illustration the mass of the lightest Higgs boson and the mass of the lightest stop quark are used. The first is sensitive to the radiative corrections and the second is sensitive to the mixing effects. Thus both are good sensitive indicators whether all ingredients of the calculation agree. With the exception of 3 points each for the stop and the Higgs mass the agreement is at the per mil level for the 10201 points analyzed. For the stop quark mass the RMS of the relative difference is one tenth of a per mil.

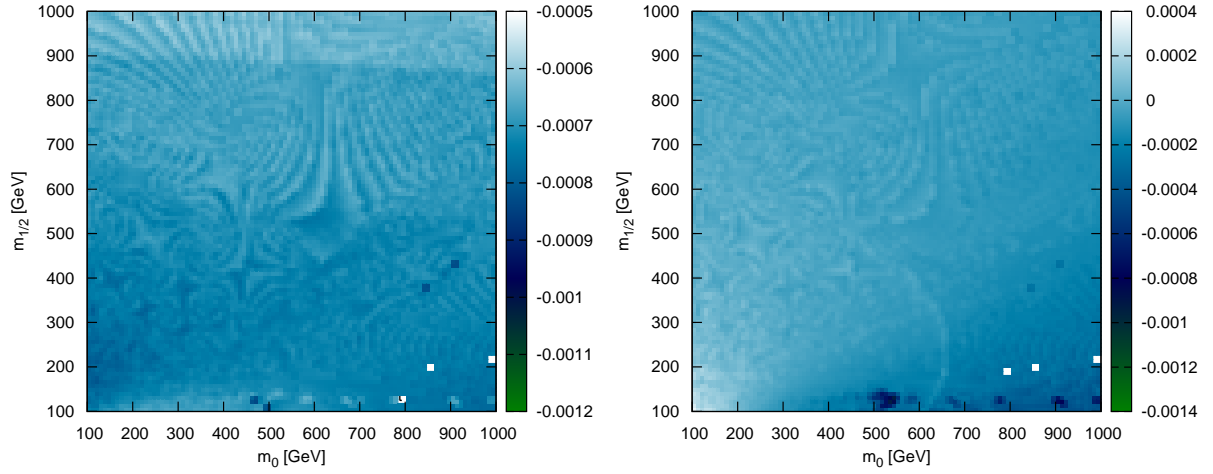


Figure 2: The two plots show relative differences between SuSpect2 and SuSpect3 with respect to SuSpect3. The left one is for M_h , and the right one for $M_{\tilde{t}_1}$. Scan on m_0 and $m_{1/2}$ has been performed for mSUGRA with $A_0 = -100$, $\tan \beta = 10$ and $\mu > 0$.

4 OUTLOOK

The rewriting of SuSpect3 in C++ with added features and a more flexible design to accommodate the use of calculations by other tools is on its way. All models currently implemented in SuSpect2 have been implemented in SuSpect3. All major options allowed by SuSpect2 have also been implemented in SuSpect3. The first comparisons for SPS1a show very good agreement. In the next months SuSpect3 will be tested intensely before making it available to a selected public for tests and later on releasing it publicly as an addition to SuSpect2.

ACKNOWLEDGEMENTS

D.Z. would like to thank the Aspen Center for Physics for its hospitality. Part of this work was developed in the GDR Terascale (CNRS).

Higgs Boson and Top Quark Physics

Contribution 8

Implications of new physics for Higgs searches at the LHC

Daniel Albornoz Vásquez, Alexandre Arbey, Marco Battaglia, Geneviève Bélanger, Alexander Belyaev, Céline Boehm, Fawzi Boudjema, Matthew Brown, Jonathan Da Silva, Abdelhak Djouadi, Guillaume Drieu La Rochelle, Béranger Dumont, Rohini Godbole, Mitsuru Kakizaki, Sabine Kraml, Farvah Mahmoudi, Alexander Pukhov, Sezen Sekmen, Akin Wingarter, Chris Wymant

Abstract

We examine to what extent the Higgs sectors of extensions of the Standard Model (SM) are constrained on the one hand by the LHC searches for the SM Higgs boson, on the other hand by LHC searches for new particles beyond the SM. The models considered include the MSSM and some of its extensions, as well as a minimal UED model and the SM with a sequential 4th generation. Among other issues, we discuss expectations for the signal strength of a light Higgs in the $\gamma\gamma$ channel in these models. Where relevant we discuss also the WW/ZZ channels. Moreover, we assess the implications of the recent hints of a Higgs signal at the LHC corresponding to a Higgs mass near 125 GeV.

1 Introduction

The search for the Higgs boson is one of the primary goals of the Large Hadron Collider (LHC). At present, combined ATLAS analyses with integrated luminosity of up to 4.9 fb^{-1} exclude, at 95% CL, a SM Higgs in the mass ranges $112.7 \text{ GeV} < M_H < 115.5 \text{ GeV}$ and $131 \text{ GeV} < M_H < 453 \text{ GeV}$ [143]. CMS excludes at 95% CL the SM Higgs in the range $127 \text{ GeV} < M_H < 600 \text{ GeV}$ with integrated luminosity of $4.6\text{--}4.7 \text{ fb}^{-1}$ [144]. This leaves a window of $m_h = 115.5 - 127 \text{ GeV}$, in good agreement with expectations from electroweak fits.

Furthermore, ATLAS reported an excess of 2.8σ in $H \rightarrow \gamma\gamma$, consistent with $M_H \approx 126 \text{ GeV}$ [143]. This excess is larger than expected from a SM Higgs by $(\sigma \times BR)/(\sigma \times BR)_{\text{SM}} = 2 \pm 0.8$. CMS also reported an excess in the same channel but for a slightly lower mass of $M_H \approx 124 \text{ GeV}$ —this excess is consistent with a SM Higgs [144]. New limits in the channels $H \rightarrow \tau\tau$, bb as well as in $H \rightarrow WW$, ZZ with the gauge bosons decaying leptonically were also reported. For a Higgs lighter than about 140 GeV, limits on $(\sigma \times BR)/(\sigma \times BR)_{\text{SM}}$ range from 3–5 [144] in the $\tau\tau$ channel and from 3–8 in the $b\bar{b}$ channel from vector boson fusion.

These results, however, cannot be applied directly to the Higgs boson(s) in extensions of the SM. Indeed for both production and decay, the predictions for non-standard Higgses [145] can differ significantly from the SM ones. First, the Higgs couplings to vector bosons or to fermions can differ from the values in the SM. In supersymmetry (SUSY), for instance, these couplings (in particular the ones to b-quarks) are modified in the limit of low pseudoscalar Higgs mass, M_A [146–148]. Furthermore, the loop-induced couplings hgg and $h\gamma\gamma$ can receive

important contributions from new fermions and scalars. Finally, there can be new decay modes of the Higgs either into stable particles (e.g., light dark matter candidates [149–155], leading to invisible Higgs decays), or into new particles whose decay modes are not searched for, e.g., the singlet Higgs of the NMSSM [156–158] or of models with light scalar singlets [159]. Enhanced invisible decays of the light Higgs of course lead to reduced rates for all visible modes. Dedicated searches for the invisible Higgs were advocated at the LHC in either vector boson fusion [160, 161] or in associated vector boson production [161, 162].

The implications of supersymmetry and other extensions of the SM on Higgs searches have been extensively studied over the years. In SUSY, the effect of top squarks on loop-induced Higgs processes was found to be large especially for light stops [163–168], while the effect of charginos on the $h \rightarrow \gamma\gamma$ width was shown to be more modest [149, 169]. Changes in the $h \rightarrow b\bar{b}$ partial width due to supersymmetric corrections can enhance or suppress the branching ratio into photons [146, 165]. The modification of the $H \rightarrow b\bar{b}$ partial width by introducing an extra singlet that mixes with the doublet Higgs can also enhance the $\gamma\gamma$ branching ratio in the NMSSM [170] or in models with a hidden Higgs sector [171]. More generally, in the MSSM with new degrees of freedom (BMSSM), modifications of the Higgs couplings can potentially lead to largely suppressed or enhanced signals in all channels [172–174]. In universal extra-dimension models, little Higgs models and in models with a fourth generation, the new top-like quark in the loop is known to increase the Higgs production from gluons, while the decay into photons is only moderately affected. On the contrary in extra-dimensional models based on RS (or their composite Higgs 4-d duals), the Higgs production is generally reduced [175, 176].

Last but not least, the above-mentioned excess of events reported by the LHC collaborations hinting at a more or less SM-like Higgs with mass near 125 GeV motivated many interpretations in the contexts of extensions of the SM, including e.g. [177–189].

In this contribution, we reexamine the case of Higgs production and decays in several extensions of the SM: the constrained Minimal Supersymmetric Standard Model (CMSSM) and the Minimal Supersymmetric Standard Model (MSSM) with parameters defined at the electroweak scale, including the so-called phenomenological MSSM (pMSSM) with 19 free parameters as well as a similar model with 11 free parameters; the BMSSM with the same field content as the MSSM but allowing for higher-dimensional operators; the next-to-minimal MSSM (NMSSM); the MSSM with L–R mixed sneutrinos; the MSSM with an extended gauge symmetry (UMSSM); the minimal UED model; and the SM with a fourth generation (SM4). For each case, we describe the constraints on the parameter space used in the different analyses and examine the consequences for the Higgs sector, both for the mass range and/or for the signal strength in the most relevant channels, generally $gg \rightarrow H \rightarrow \gamma\gamma$. When relevant, other modes, including invisible Higgs decays, are discussed. We also highlight in some cases the implications of the excess corresponding to $M_H \approx 125$ GeV observed at the LHC.

2 The MSSM

The expectations for the Higgs in the MSSM were explored in a variety of models defined at the GUT scale, such as the CMSSM, AMSB, GMSB, or at the electroweak scale, such as the pMSSM. In all these models, the light Higgs mass is expected to be less than about 135 GeV (see [146] and references therein) and above the LEP bound of 114 GeV, thus in the region where the main search channel at the LHC is $gg \rightarrow h \rightarrow \gamma\gamma$. To raise the Higgs mass much above the Z scale requires large contributions from 3rd generation squarks; in particular a large

mixing in the stop sector is needed to reach the high end of the M_H range possible in the MSSM. Note, however, that a Higgs with mass near 125 GeV, as favored by recent LHC results, requires some fine-tuning [179]. The parameter space of a given model is subject to various constraints from precision data, searches for new particles at colliders, flavor physics as well as astroparticle and cosmology constraints. Taking into account all these constraints, the allowed range for the Higgs mass can be much restricted.

The LHC Higgs searches are sensitive not only to the value of the light Higgs mass but also to the strength of the Higgs signal in each search channel. In the following, we will examine the predictions for the expected light Higgs mass in the MSSM with parameters defined at the weak scale, taking into account LHC constraints on SUSY and/or Higgs particles, and/or dark matter constraints. Moreover, we consider the signal strength for the main search channel, defined as

$$R_{gg\gamma\gamma} \equiv \frac{\sigma(gg \rightarrow h)_{\text{BSM}} \text{BR}(h \rightarrow \gamma\gamma)_{\text{BSM}}}{\sigma(gg \rightarrow h)_{\text{SM}} \text{BR}(h \rightarrow \gamma\gamma)_{\text{SM}}}. \quad (1)$$

Before showing these results, let us summarize the expectations for the (effective) Higgs couplings to SM particles in the MSSM. The ggh coupling is dominated by the top-quark loop, while the $h\gamma\gamma$ coupling is dominated by the contribution from W bosons with a subdominant contribution from top quarks of opposite sign. Both couplings can receive a large contribution from third generation sfermions, in particular from stops [163]. The light stop interferes constructively with the top when there is no mixing in the stop sector, while the interference is destructive in the case of large mixing. In the first case hgg will increase, while in the latter it will decrease. The contrary is true for the $h\gamma\gamma$ couplings. Weakly interacting particles such as charginos and sleptons will contribute only to the $h\gamma\gamma$ coupling. In particular, light staus that are heavily mixed can enhance the $h \rightarrow \gamma\gamma$ rate [184].

Apart from the contribution of light superpartners in the loops, other particles that can induce large modifications of some of the light Higgs couplings and branching ratios are light pseudoscalars and light LSP's (lightest SUSY particle). The latter lead to new invisible decay modes of the Higgs, and thus to reduced rates for all visible modes. The light pseudoscalar case is now strongly constrained by LHC searches for a Higgs produced through b-quarks and decaying into $\tau\tau$. Nevertheless values of M_A for which the tree-level couplings of the Higgs to SM particles can show large deviations as compared to the SM case are still possible. For example the ratios of the Higgs couplings to SM particles, $R_{WWh} = \sin(\alpha - \beta)$ and $R_{tth} = \cos\alpha / \sin\beta$ where α is the Higgs mixing angle, are considerably smaller than one only for low values of M_A , while $R_{bbh} = R_{\tau\tau h} = \sin\alpha / \cos\beta$ is enhanced especially at large values of $\tan\beta$ [146, 164]. Furthermore, corrections to the $hb\bar{b}$ vertex arise from higher-order effects, in particular the ΔM_b correction, which can lead to a much enhanced $hb\bar{b}$ coupling at large values of $\tan\beta$ [146]. Because the $b\bar{b}$ mode is the dominant decay channel of the light Higgs, in this case the total width of the Higgs becomes much larger in the MSSM than in the SM. This means that the branching ratios into other modes, such as $\text{BR}(h \rightarrow \gamma\gamma)$, can be suppressed even if the $h\gamma\gamma$ coupling is itself SM-like. Supersymmetric contributions can thus lead to modifications in both production and decays as compared to the SM.

2.1 Constrained MSSM

A. Arbey, M. Battaglia, A. Djouadi, F. Mahmoudi

In constrained MSSM scenarios the various soft SUSY-breaking parameters obey a number of universal boundary conditions at a high energy scale such as the GUT scale, thus reducing

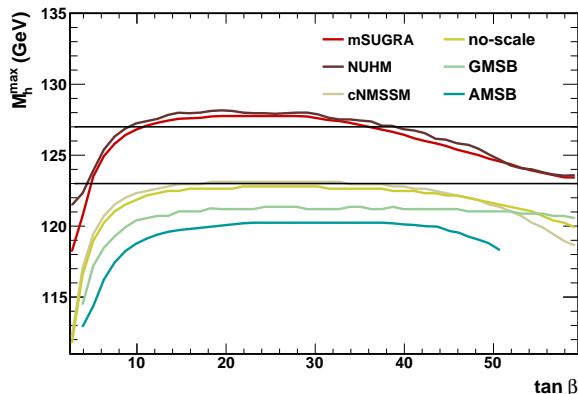


Figure 1: The maximal value of the h mass defined as the value for which 99% of the scan points have a mass smaller than it, shown as a function of $\tan \beta$ for the various constrained MSSM models.

the number of basic input parameters. Since the various parameters which enter the radiative corrections to the MSSM Higgs sector are not all independent, it is not possible to freely tune the relevant weak-scale parameters to obtain a given value of M_h . In particular, a Higgs mass of around 125 GeV can have drastical consequences on the constrained MSSM scenarios [177] as can be seen from Fig. 1. The upper bound on M_h in these scenarios can be qualitatively understood by considering in each model the allowed values of the trilinear coupling A_t , which essentially determines the stop mixing parameter X_t and thus the value of M_h for a given scale M_S . In GMSB, one has $A_t \approx 0$ at relatively low scales and its magnitude does not significantly increase in the evolution down to the scale M_S . This implies that we are almost in the no-mixing scenario which gives a low value of M_h . In AMSB, one has a non-zero A_t that is fully predicted at any renormalisation scale in terms of the Yukawa and gauge couplings; however, the ratio A_t/M_S with M_S determined from the overall SUSY breaking scale $m_{3/2}$ turns out to be rather small, implying again that we are close to the no-mixing scenario. Finally, in the mSUGRA model, since we have allowed A_t to vary in a wide range as $|A_0| \leq 9$ TeV, one can get a large A_t/M_S ratio which leads to a heavier Higgs particle. However, one cannot easily reach A_t values such that $X_t/M_S \approx \sqrt{6}$ so that we are not in the maximal-mixing scenario. In turn, in two particular cases of mSUGRA, namely the “no-scale” and the “approximate cNMSSM” scenarios, the upper bound on M_h is much lower than in the more general mSUGRA case and, in fact, barely reaches the value $M_h \approx 123$ GeV. The main reason is that these scenarios involve small values of A_0 at the GUT scale, $A_0 \approx 0$ for no-scale and $A_0 \approx -\frac{1}{4}m_{1/2}$ for the cNMSSM. One then obtains A_t values at the weak scale that are too low to generate a significant stop mixing and, hence, one is again close to the no-mixing scenario. Thus, only a very small fraction of the parameter space of these two sub-classes of the mSUGRA model survive (in fact, the ones leading to the M_h^{\max} value) if one indeed has $M_h = 125 \pm 2$ GeV. These models hence should have a very heavy spectrum as a value $M_S \gtrsim 3$ TeV is required to increase M_h^{\max} . In the VCMSSM, values $M_h \simeq 124.5$ GeV can be reached as A_0 can be large for large m_0 , $A_0 \approx -m_0$, allowing at least for typical mixing. Finally, since the NUHM is more general than mSUGRA as we have two more free parameters, the $[\tan \beta, M_h]$ area shown in Fig. 1 is larger than in the mSUGRA case. However, since we are in the decoupling regime and the value of M_A does not matter much (as long as it is larger than a few hundred GeV) and the key weak-scale parameters entering the determination of M_h , i.e. $\tan \beta$, M_S and A_t are

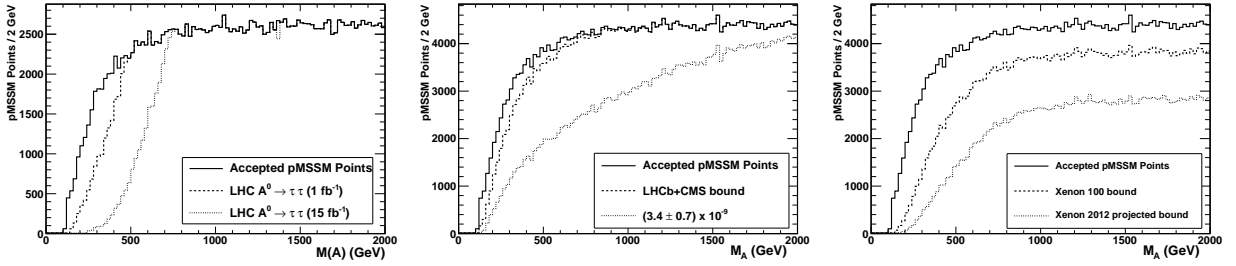


Figure 2: Distribution of pMSSM points after the $A^0 \rightarrow \tau^+\tau^-$ search (left), after the $B_s \rightarrow \mu^+\mu^-$ constraint (middle) and after the dark matter direct detection constraint (right) projected on the M_A for all accepted pMSSM points, and after applying projected limits.

approximately the same in both models, one obtains a bound M_h^{\max} that is only slightly higher in NUHM compared to mSUGRA. Thus, the same discussion above on the mSUGRA scenario, holds also true in the NUHM case.

2.2 pMSSM

A. Arbey, M. Battaglia, A. Djouadi, F. Mahmoudi

Studies considering general MSSM scenarios without implicit correlations between the masses of the supersymmetric particle partners, such as the 19-parameter phenomenological MSSM (pMSSM), have demonstrated that a wide phase space of solutions, compatible with flavour physics, low energy data and dark matter constraints and beyond the current sensitivity of the LHC experiments, exists [190–192]. Even at the end of next year LHC run, with an anticipated integrated luminosity of order of 15 fb^{-1} per experiment, many of these solutions, in particular those with gluino masses above 800 GeV will not be tested. These solutions are compatible with all present bounds and a good fraction of them has acceptable values of the fine tuning parameter. This will not make possible to falsify the MSSM as the model of new physics beyond the SM and the source of relic dark matter in the universe, if no missing E_T signal will be observed at the LHC by the end of 2012. On the other hand, searches for the Higgs bosons can be used as an alternative path to tightly constrain and test the MSSM at the LHC.

We consider four sets of constraints on SUSY parameters [193]. The result of the direct search for the A^0 boson at the LHC is the single most constraining piece of information on the $(M_A, \tan\beta)$ plane. We compute the product of production cross section and decay branching fraction into τ pairs for the A^0 for each accepted pMSSM point. Fig. 2 shows the points surviving this selection in function of M_A . The 2012 data should severely constrain the low M_A scenario by removing all solutions with $M_A < 220$ GeV and restricting the region with $M_A < 400$ GeV to $\tan\beta$ values below 10.

The second important constraint comes from the decay $B_s \rightarrow \mu^+\mu^-$. At large $\tan\beta$, the SUSY contribution to this process is dominated by the exchange of neutral Higgs bosons, and very restrictive constraints can be obtained on the supersymmetric parameters [194]. Indeed, the couplings of the neutral Higgs bosons to b quark and muons are proportional to $\tan\beta$, which can lead to enhancement of orders of magnitude as compared to the SM prediction which is helicity suppressed. We compare our accepted pMSSM points to the combined limit from LHCb and CMS at 95% C.L. of $\text{BR}(B_s \rightarrow \mu^+\mu^-) < 1.1 \times 10^{-8}$ [195] as well as to the projected

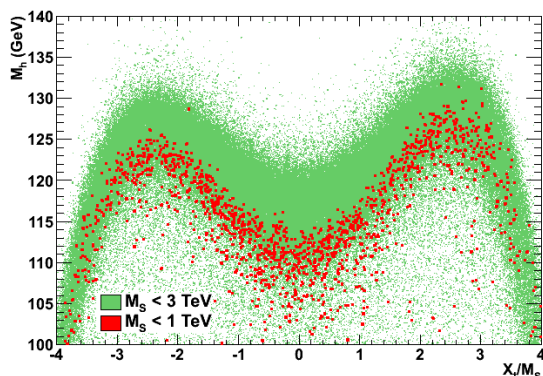


Figure 3: The mass of the h boson as a function of X_t/M_S in the pMSSM when all other soft SUSY-breaking parameters and $\tan\beta$ are scanned.

constraint in the case of observation of the decay with a SM-like rate of $\text{BR}(B_s \rightarrow \mu^+\mu^-) = (3.4 \pm 0.7) \times 10^{-9}$, to which we have attached a 20% total relative uncertainty, by the end of the 7 TeV run. The results are presented in Fig. 2 in function of M_A . The current limit affects the low M_A values up to 700 GeV, excluding large $\tan\beta$ values, below $M_A=200$ GeV. The projected constraint has a stronger impact, with more than half of the spectrum being excluded for $M_A \lesssim 700$ GeV.

A third important sector is that of dark matter direct detection experiments. In particular, the recent XENON 100 result [196], places a 90% C.L. upper bound on the spin-independent $\tilde{\chi}p$ cross section around 10^{-8} pb for $M_{\text{WIMP}} = 100$ GeV and excludes $\simeq 20\%$ of the accepted pMSSM points in our scan. By the end of 2012, this bound should be improved by a factor of 7, if no signal is observed. The $\tilde{\chi}p$ spin-independent scattering process has contributions from scalar quark exchange and t-channel Higgs exchange [197]. The latter dominates over vast region of the parameter space with the Higgs coupling to the proton depending on its coupling to gluons, through a heavy quark loop and to non-valence quarks. The scattering cross section retains a strong sensitivity on the CP-odd boson mass as highlighted in Fig. 2 which shows the pMSSM points retained after the XENON 100 and the projected 2012 sensitivity. The 2012 data should exclude virtually all solutions with $M_A < 200$ GeV independent on the value of $\tan\beta$, if no signal is detected.

These constraints, originating from different sectors of the theory, are all sensitive to the SUSY parameters most relevant for setting the couplings and decay branching fractions of the light h^0 bosons. Their combination provides the boundary conditions for the parameter space where we test the possible suppression of the yields in the LHC Higgs searches.

Finally, the determination of the mass of the lightest Higgs boson with an accuracy of order of 1 GeV places some significant constraints on the SUSY parameters, in particular when its central value corresponds to a mass close to the edge of the range predicted in the MSSM. In Fig. 3 the obtained M_h in the pMSSM is displayed as a function of the ratio of parameters X_t/M_S .

In order to evaluate the constraints from M_h determination, we select the accepted pMSSM points from our scan, which have $123 < M_h < 127$ GeV. Fig. 4 shows the points fulfilling these conditions, which are also allowed by the other 2011 data constraints and by the 2012 projec-

tion. We observe that imposing the value of M_h selects a wedge in the $(M_A - \tan \beta)$ plane, at

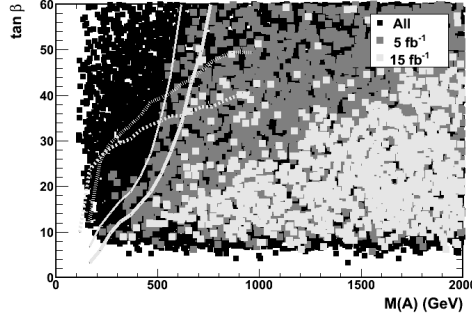


Figure 4: pMSSM points in the $(M_A, \tan \beta)$ parameter space, giving $123 < M_h < 127$ GeV. The different shades of grey show the points in the pMSSM without cuts and those allowed by the 2011 data and by the projected 2012 data, assuming no signal beyond the lightest Higgs boson is observed. The lines in the top plot show the regions which include 90% of the scan points for the $A \rightarrow \tau^+\tau^-$ and $B_s \rightarrow \mu^+\mu^-$ decays at the LHC and the dark matter direct detection at the XENON experiment.

rather heavy A^0 masses and moderate to large values of $\tan \beta$ and extending beyond the projected sensitivity of the searches in the $A^0 \rightarrow \tau^+\tau^-$ but also that of direct DM detection and would be compatible with a SM-like value for the rate of the $B_s^0 \rightarrow \mu^+\mu^-$ decay.

2.3 Bayesian analysis of the pMSSM

S. Kraml and S. Sekmen

In [191], we performed a global Bayesian analysis of the pMSSM in light of the results of SUSY searches published by the CMS collaboration based on the first $\sim 1 \text{ fb}^{-1}$ of data taken during the 2011 LHC run at 7 TeV. Concretely, we used the results from three independent CMS analyses, the α_T hadronic [198], the same-sign dilepton [199] and the opposite-sign dilepton [200] analyses, and analyzed whether and how they impact the probability density distributions of masses and parameters. To this end, we compared for each mass and parameter, the ‘‘CMS’’ posterior densities after inclusion of the above mentioned results to the ‘‘preLHC’’ posterior density based on the constraints from $BR(b \rightarrow s\gamma)$, $BR(B_s \rightarrow \mu\mu)$, $R(B_u \rightarrow \tau\nu)$ and Δa_μ , together with Higgs and SUSY mass limits from LEP as detailed in Table 1 of [191].

Our analysis is easily applied to the Higgs sector. In the 1D distributions of Fig. 5, the light blue histograms represent the preLHC probability densities; the blue, green and red lines show, respectively, the effects of the OS di-lepton, SS di-lepton and α_T hadronic CMS analyses; and the dashed black lines show the final posterior densities after inclusion of the results of all three analyses. We see that the probability density of m_h peaks at about 120 GeV and is basically unaffected by the SUSY search results. When imposing no constraint on Ωh^2 , the $m_h = 123 - 127$ GeV window has 27.4% probability. This decreases only marginally to 26.4% when requiring $\Omega h^2 \leq 0.136$.

The $R_{gg\gamma\gamma}$ ratio peaks around 0.9, and does not extend much above 1. Requiring $\Omega h^2 \leq 0.136$ slightly narrows the distribution but does not change it qualitatively. The probability of finding $R_{gg\gamma\gamma} > 1$ is 8.88% in the general case, and 6.32% when requiring $\Omega h^2 \leq 0.136$. Here note that we actually approximated $\sigma(gg \rightarrow h) \times BR(h \rightarrow \gamma\gamma) \approx \Gamma_{\text{tot}} \times BR(h \rightarrow gg) \times BR(h \rightarrow \gamma\gamma)$, computing both the MSSM and the SM widths and branching ratios

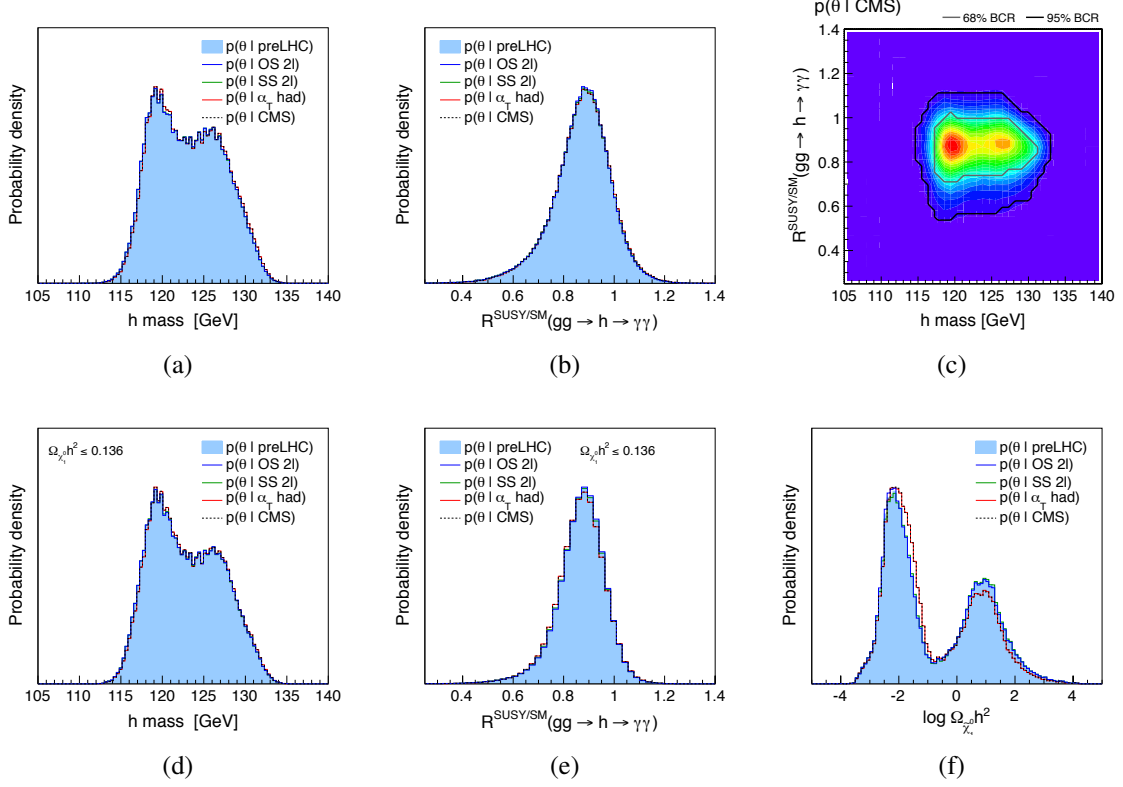


Figure 5: Marginalized 1D posterior densities for m_h (left) and $R_{gg\gamma\gamma}$ (middle), and the 2D posterior in the $R_{gg\gamma\gamma}$ versus m_h plane (top right). Also shown is the 1D posterior density of Ωh^2 (bottom right). In the top row, no constraint is imposed on Ωh^2 , while in the bottom left and bottom-middle plots $\Omega h^2 \leq 0.136$.

with HDECAY 3.4 [201], which is the version implemented in SUSY-HIT [202]. While radiative corrections are somewhat different for $gg \rightarrow h$ and $h \rightarrow gg$, one can reasonably assume that these differences largely cancel out when taking the MSSM/SM ratio.

It is also interesting to ask what is the effect of requiring a Higgs mass near 125 GeV. This is illustrated in Fig. 6, where show posterior density distributions for some quantities that are relevant for the Higgs sector, namely $\tan \beta$, $m_{\tilde{t}_1}$, A_t and $r_t = A_t^2 / (m_{\tilde{t}_1}^2 + m_{\tilde{t}_2}^2)$. The light green filled histograms and the dark green lines compare the probability densities after CMS analyses, $p(\theta|\text{CMS})$, without and with requiring the Higgs mass to fall within the $m_h = 123 - 127$ GeV window. As can be seen, a Higgs mass near 125 GeV somewhat favors intermediate values of $\tan \beta$, and strongly favors large A_t with $r_t \approx 1$. However, there is basically no effect on the $m_{\tilde{t}_1}$ distribution. We also checked the m_A distribution and found it does not change when requiring $m_h = 123 - 127$ GeV.

2.4 MSSM and light neutralinos

D. Albornoz Vasquez, G. Bélanger, R. Godbole, A. Pukhov

We consider a constrained version of the pMSSM with only eleven free parameters defined at the electroweak scale, as in [203, 204]:

$$M_1, M_2, M_3, \mu, \tan \beta, M_A, M_{\tilde{L}}, M_{\tilde{R}}, M_{\tilde{q}_{1,2}}, M_{\tilde{q}_3}, A_t.$$

To explore the parameter space we use a Markov Chain Monte-Carlo (MCMC) first presented

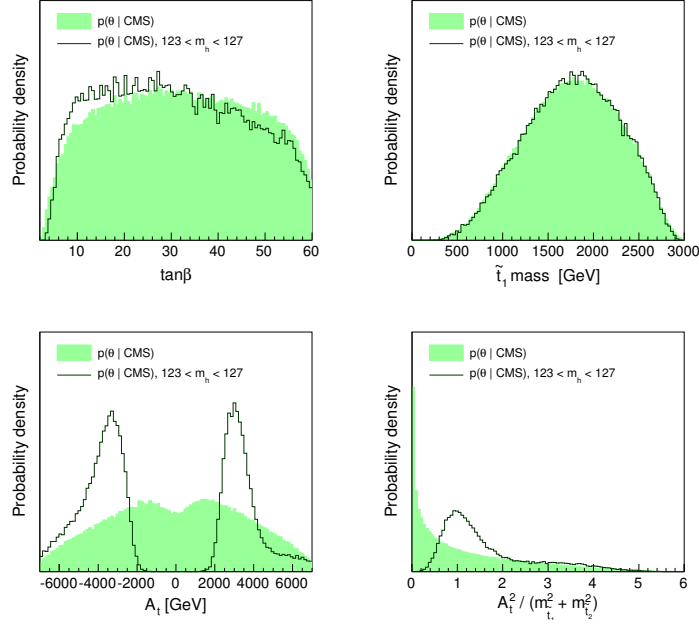


Figure 6: Marginalized 1D posterior densities for $\tan\beta$, $m_{\tilde{t}_1}$, A_t and $A_t^2/(m_{\tilde{t}_1}^2 + m_{\tilde{t}_2}^2)$ after OS, SS and α_T hadronic CMS analyses. The effect of imposing $m_h = 123 - 127$ GeV is apparent from comparing the dark green lines to the light green filled histograms, which show the probability densities after CMS analyses without additional requirements on m_h .

in [205] that relies on micrOMEGAs2.4 [206–208] for the computation of all observables and on SuSpect for the calculation of the supersymmetric spectrum [79]. We include limits on B physics observables, on the anomalous magnetic moment of the muon $(g - 2)_\mu$ and on the sparticles masses obtained from LEP. Limits on the Higgs mass are obtained from HiggsBounds(3.1.3) which includes LEP and Tevatron results as well as first LHC results [209, 210]. More recent results from CMS presented in [211, 212] are added a posteriori. We also require that the dark matter relic density be within 10 – 100% of the WMAP measured value thus allowing for the LSP to be only a fraction of the dark matter component. Furthermore astroparticle constraints from dark matter direct detection (XENON100) and the photon flux from dwarf spheroidal galaxies (Fermi-LAT) are added a posteriori. In this analysis we explore carefully the parameter space which allows for light neutralinos, thus we expect to have some large suppressions of the Higgs signal.

As for the SM Higgs, searches for the light Higgs in the MSSM rely mainly on $gg \rightarrow h \rightarrow \gamma\gamma$. By computing the signal strength as compared to the SM we find that the MSSM Higgs signal can be at most as large as that of the SM Higgs and is suppressed when $M_A < 400$ GeV due to shifts in the Higgs couplings as mentioned above. The predictions for $R_{gg\gamma\gamma}$ as a function of the pseudoscalar mass are displayed in Fig. 7, left panel. Note that many of the points with a light pseudoscalar are constrained by either Fermi-LAT, XENON100 (points in red), latest Higgs searches at the LHC and/or the new upper limit on $BR(B_s \rightarrow \mu^+\mu^-)$ (points in yellow), nevertheless there are still allowed points where the Higgs signal is less than 10% of its SM value. Since these are associated with a light M_A , they can be probed further in searches for the neutral and charged component of the heavy Higgs doublet in CMS and ATLAS and/or a more precise measurement of $BR(B_s \rightarrow \mu^+\mu^-)$. When $M_A > 400$ GeV and one is in the decoupling

limit the suppression in $R_{gg\gamma\gamma}$ is usually more modest. Nevertheless it is still possible to have $R_{gg\gamma\gamma}$ as low as 0.2 even when M_A is at the TeV scale. This occurs when the LSP is lighter than $M_h/2$ and the invisible width of the Higgs is large. Note that there are a few points at large values of M_A where $R_{gg\gamma\gamma} \approx 0.01$, these all correspond to points where the LH soft mass for sleptons is below 100 GeV, the charged sleptons are just above the LEP exclusion and the sneutrino is light enough that the dominant decay of the Higgs is into sneutrinos. Other suppression of $R_{gg\gamma\gamma}$ arises from the stop sector. The effect is usually below 30%, although for stop masses below 500 GeV we found points where $R_{gg\gamma\gamma}$ can drop as low as 0.4.

The predictions for $R_{gg\gamma\gamma}$ as a function of the light Higgs mass show that $R_{gg\gamma\gamma}$ has little dependence on the scalar mass provided it lies in the 110 – 130 GeV range. However it is important to note that for a Higgs of 126 GeV we find $R_{gg\gamma\gamma} > 0.4$, which means that the signal strength would be compatible with the excess of events reported by ATLAS. Also note that for a Higgs in the narrow mass range 110 – 114 GeV, we always find $R_{gg\gamma\gamma} < 0.8$, because these values of M_h are found only in the non-decoupling limit.

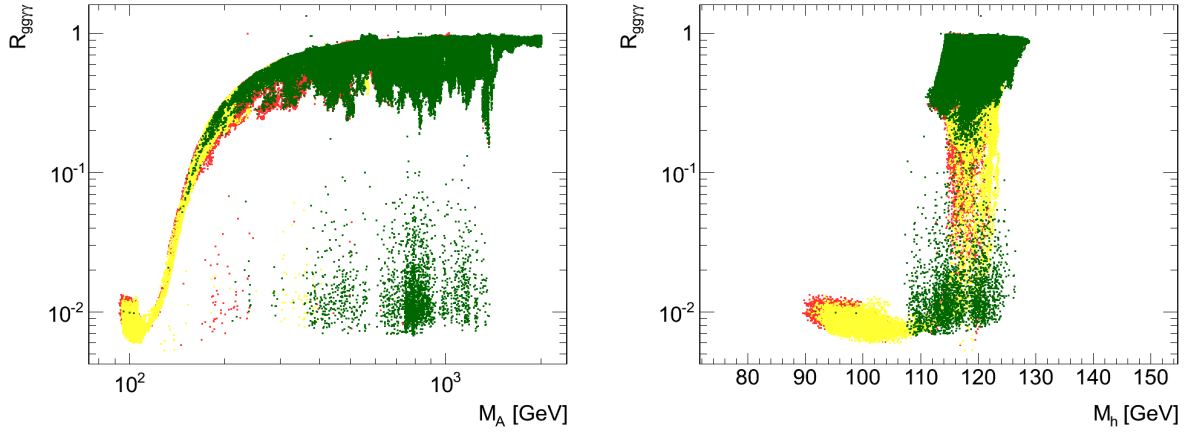


Figure 7: $R_{gg\gamma\gamma}$ as a function of the pseudoscalar mass (left) and light scalar mass (right) for allowed points (green). In yellow, points excluded by collider constraints (Higgs and $BR(B_s \rightarrow \mu^+ \mu^-)$), in red those excluded by astrophysical constraints (XENON100 and Fermi-LAT).

The Higgs signal can be more strongly suppressed than found in other studies [191, 192]. This is due to the large fraction of light neutralinos in our sample allowing for a large branching fraction of the Higgs into invisible particles, see Fig. 8. A large invisible partial width involves special conditions on the parameter space and can therefore be probed by SUSY searches at the LHC. Indeed invisible decays of the Higgs requires not only a light LSP but also a significant coupling of the LSP to the Higgs. This means that the light neutralino which is predominantly bino must have also a higgsino component. Thus μ cannot be large. This also means that the mass of the lightest chargino, which is driven by μ is strongly correlated with the Higgs invisible width. We find that when the invisible width of the Higgs is larger than 20%, then the chargino is lighter than 200GeV [204].

3 Beyond the MSSM

3.1 BMSSM

F. Boudjema, G. Drieu La Rochelle

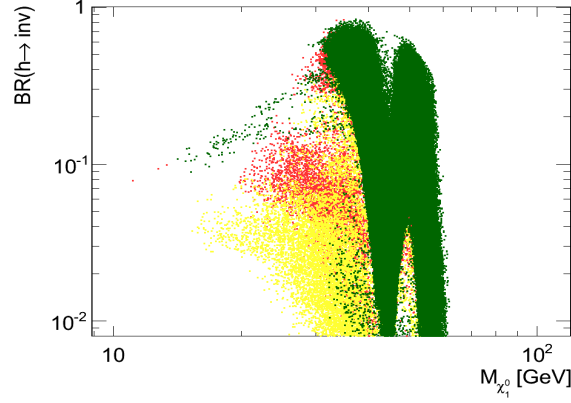


Figure 8: $\text{BR}(h \rightarrow \text{inv})$ as a function of the LSP mass, same color code as Fig. 7.

The BMSSM model is the extension of the MSSM obtained by adding to the Higgs sector of the Kähler potential and superpotential new higher dimensional operators that are suppressed by a heavy scale M :

$$K_{\text{eff}} = K^{(0)} + \frac{1}{M}K^{(1)} + \frac{1}{M^2}K^{(2)} + O\left(\frac{1}{M^3}\right) \quad (2)$$

$$W_{\text{eff}} = W^{(0)} + \frac{1}{M}W^{(1)} + \frac{1}{M^2}W^{(2)} + O\left(\frac{1}{M^3}\right) \quad (3)$$

Those new operators only involve the MSSM Higgs superfields, so the particle content of the BMSSM is the same as the one of the MSSM. The resulting theory can then be described in the effective field theory approach. This model has been studied in different contexts including Higgs phenomenology (see [172–174, 213–219]), vacuum stability [220], fine tuning [221, 222], dark matter [223–226], cosmology [227], baryogenesis [228, 229] and flavour physics [230, 231]. Regarding the Higgs, its first motivation was to increase the lightest Higgs mass to a large value ($m_h \in [150 - 250]$ GeV). Here we will not dwell upon the model itself, but show some of the predictions in the channels searched for at the LHC.

To obtain these predictions we have used the MSSM scenario $m_{h \text{ max}}$ ([165]), with only two free parameters, M_{A_0} and $\tan \beta$. In the following we have scanned these parameters within the range

$$M_{A_0} \in [50, 450] \text{ GeV}, \quad \tan \beta \in [2, 40]. \quad (4)$$

We recall that in the $m_{h \text{ max}}$ scenario, the superpartner masses are set to 1 TeV, the gaugino masses are set to $M_2 = 300$ GeV, $M_1 = \frac{5}{3} \tan^2 \theta_W M_2$ and $M_3 = 800$ GeV. All trilinear couplings are set to 0 except for $A_b = A_t = 2 \frac{\mu}{\tan \beta} + 2$ TeV. The additional parameters brought by the higher-dimensional operators are the new physics scale M (and the supersymmetry breaking mass m_s), and the effective coefficients that we name ζ_{1i} ($i = 0, 1$) and a_{ij} ($i = 1..6, j = 0..2$). The scales have been fixed to

$$M = 1.5 \text{ TeV} \quad m_s = \mu = 300 \text{ GeV}, \quad (5)$$

and the effective coefficients have been left free. A scan has been performed within

$$\zeta_{1i}, a_{ij} \in [-1, 1]. \quad (6)$$

The phenomenology of this model shows many features different from those of the MSSM, indeed the Higgs scalar sector is dramatically affected so most of the relations between the couplings of the Higgses to the SM particles that held in the MSSM case are no longer true. A detailed analysis can be found in ref. [216,218] but we will now focus on the application of the LHC constraints that were obtained in [174].

In all the plots below, the following data sets, corresponding to the December 2011 release, are used to constrain the model.

- $Vh \rightarrow V\bar{b}b$: CMS 4.7 fb^{-1} .
- $h \rightarrow \bar{\tau}\tau$: CMS 4.6 fb^{-1} and ATLAS 1.06 fb^{-1} .
- $h \rightarrow \gamma\gamma$: CMS 4.8 fb^{-1} and ATLAS 4.9 fb^{-1} .
- $h \rightarrow ZZ \rightarrow 4l$: CMS 4.71 fb^{-1} and ATLAS 4.8 fb^{-1} .
- $h \rightarrow WW \rightarrow l\nu l\nu$: CMS 4.6 fb^{-1} and ATLAS 2.05 fb^{-1} .

We have used the 95% CL value for $\sigma_{\text{exclusion}}$ as given by the collaborations. We have combined all channels by a quadrature sum and we show only points that pass the combined exclusion. Note that the exclusion is done separately on each of the three neutral Higgses (unless they are degenerate in mass, in which case the signals are added) and the test is successful only if each individual test is successful. The search for the charged Higgs $H^+ \rightarrow \tau^+\nu_\tau$ has also been included.

As compared to the MSSM, the light Higgs of the BMSSM can be much heavier, that is to say $m_h \in [150, 250] \text{ GeV}$, but only at the price of being SM-like, which means that this case is now ruled out by the LHC. We will then focus on the case of a light Higgs, say $m_h < 150 \text{ GeV}$. The relevant channels are thus $\gamma\gamma$, ZZ and WW , but there is also a constraint coming from other Higgses (that may be much heavier) in the $\tau\tau$ channel. Indeed this last one is $\tan\beta$ enhanced, so in some cases it is more constraining than direct searches on the lightest Higgs. We show in figure 9 the ratio $R_{\gamma\gamma\phi} = \frac{\sigma_{pp \rightarrow \phi \rightarrow \gamma\gamma}}{\sigma_{pp \rightarrow h \rightarrow \gamma\gamma}^{SM}}$ which tells how much we can lower the prediction of the Standard Model. This ratio is computed by evaluating first which Higgs (h or H) has the highest signal given the current sensitivity (that is to say the highest value for $\frac{\sigma}{\sigma_{\text{exclusion}}}$), and then take its mass and its signal strength normalised to the Standard Model. This means that some of the points correspond to the lightest Higgs and others to the heaviest one.

One notices that, as expected, the allowed region is bounded from above by the combination of LHC searches, mainly the $h \rightarrow \gamma\gamma$ with $\sim 5\text{fb}^{-1}$ from ATLAS and CMS, but also the WW and ZZ channels (since we combine all channels in quadrature). Actually there is only a small range $120 - 130 \text{ GeV}$, corresponding to the excesses seen in the $\gamma\gamma$ channels, that allows for points with $R_{\gamma\gamma h} > 1$. Note that since we are in the no-signal hypothesis we cannot use this graph to discuss on the interpretation of the excess, to this aim, one would have to switch off the constraints from the 95% exclusion limit on this mass range. This is done in the corner of the plot in fig 9, which shows $R_{\gamma\gamma\phi}$ when the constraints from $\gamma\gamma$, ZZ and WW channels are not taken into account.

The conclusion from this figure is two-fold: first the signal strength can be much lowered relatively to the SM, which yields a possibly very elusive model, and secondly there are points with signal strength higher than the SM. On the WW side, the signal strength can also be much reduced. Regarding the $R_{\gamma\gamma}$ plot, one notices that the higher part of our range, that is $m_h \in [130 - 150] \text{ GeV}$, is more sensitive to the searches (indeed the upper bound is much lower in this part), so that the model is more constrained on this mass range. This comes from the

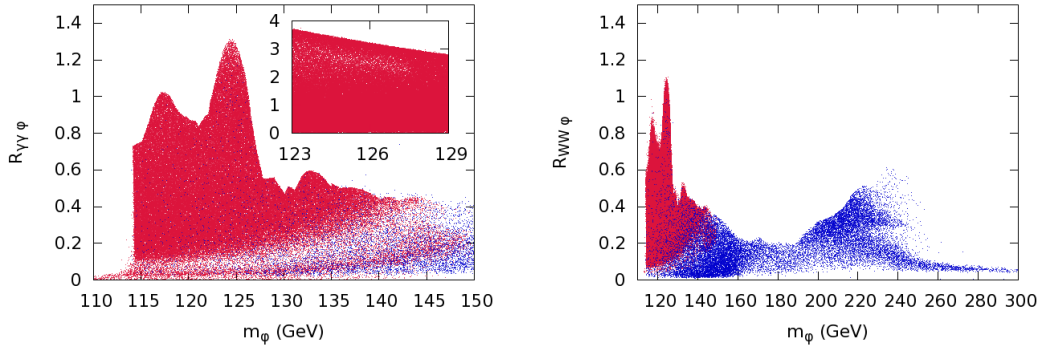


Figure 9: $R_{\gamma\gamma\phi}$ (left) and $R_{WW\phi}$ (right) as a function of the lightest Higgs mass. Red points correspond to signal coming from the lightest Higgs, and blue from the heaviest. We only show points that pass the combination of all LHC searches. On the right corner of the left plot $R_{\gamma\gamma h}$ is shown in the case that the 95% exclusion constraints are switched off.

WW and ZZ channels, that lose sensitivity when the mass decreases.

3.1.1 Invisible Higgs decays

Our choice of the MSSM benchmark (the $m_{h\max}$ scenario) has the advantage of leaving the issue of superpartners aside, since the SUSY scale is at 1 TeV, but it also precludes the possibility of rather light neutralinos. If one allows for the lightest neutralino to be as light as 50 GeV, it will modify directly the Higgs signals since a new decay channel opens in this case. In order to have a non-negligible branching ratio, one must ensure that the lightest neutralino has both a bino and a higgsino component: in our case putting $\mu = 200$ GeV and $M_1 = 50$ GeV was enough to see some changes. We have plotted in Fig. 10 the branching ratio of the lightest Higgs. While one could hope that it would enhance the robustness of the model towards LHC searches with masses higher than 150 GeV, it turns out that this branching ratio is quickly overturned by the decays to vector bosons, so that for $m_h > 150$ GeV, the branching is lower than 10% and thus cannot avoid that all points with $m_h > 150$ GeV be excluded by the LHC. On the light range however, the branching can go as high as 70%, which will directly reduce the sensitivity in all channels by the same amount.

We have seen that the BMSSM accounts for a light Higgs that could be quite difficult to find at the LHC: indeed the signal of the lightest Higgs can be reduced significantly with respect to the SM or the MSSM. Though this study has been done in the no-signal hypothesis, the reader would have noticed that the predicted signal can be higher than the SM value, which would be of particular importance in interpreting a possible signal from the latest excesses around $m_h \sim 125$ GeV reported by the ATLAS and CMS collaborations.

3.2 NMSSM

D. Alborno Vázquez, G. Bélanger, C. Boehm, J. Da Silva, C. Wymant

The NMSSM is a simple extension of the MSSM that contains an additional gauge singlet superfield. The VEV of this singlet induces an effective μ term that is naturally of the order of the electroweak scale, thus providing a solution to the naturalness problem [158]. The model contains three CP-even (H_1, H_2, H_3) and two CP-odd (A_1, A_2) Higgs bosons, the former result

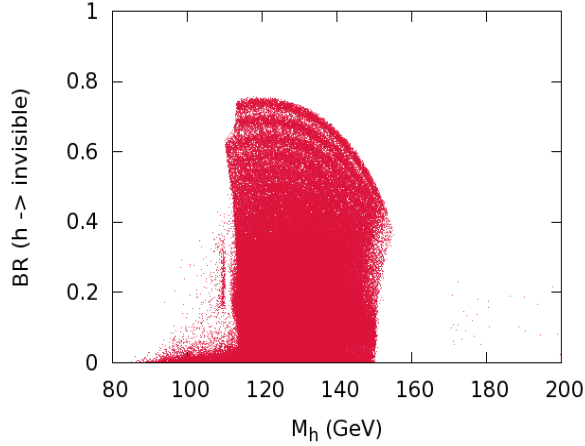


Figure 10: Branching ratio of the light Higgs to invisible in the case where the lightest neutralino is as light as 50 GeV. Only points that pass the combination of all LHC searches are shown.

from a mixing of the singlet with the two neutral CP-even doublets of the MSSM. The coupling $\lambda S H_u H_d$ in the superpotential leads to a positive contribution to the mass of the SM-like Higgs boson for small values of $\tan \beta$. Furthermore singlet/doublet mixing can lead to an additional increase in the mass of the SM-like Higgs while the lighter eigenstate, H_1 , can evade all collider bounds even if its mass is much below the electroweak scale provided its singlet component is large enough to have much reduced couplings to the SM fields [158]. A Higgs mass in the range 122-128 GeV is thus obtained naturally in the NMSSM and can correspond either to H_1 or H_2 . In the following we discuss the expectations for the main search channel, $gg \rightarrow H_i \rightarrow \gamma\gamma$, for both scalars.

The model that we consider has input parameters which are defined at the weak scale. The free parameters are taken to be the gaugino masses $M_1, M_2 = M_3/3$, the Higgs sector parameters $\mu, \tan \beta, \lambda, \kappa, A_\lambda, A_\kappa$, two common soft masses for the sleptons $M_{\tilde{L}}, M_{\tilde{R}}$ and soft masses for the squarks of the first and second generation $M_{\tilde{q}_{1,2}}$ and of the third generation, $M_{\tilde{q}_3}$ as well as only one non-zero trilinear coupling, A_t (see [205] for more details). Note that the model contains an additional neutralino, the singlino. We make two separate analyses. In the first one we take only one common soft mass for sleptons as well as one for squarks and only consider scenarios with a neutralino LSP lighter than 15 GeV, in the second one we relax these conditions. For both analyses we perform an MCMC exploration of the parameter space of the model imposing constraints from Higgs and SUSY searches at colliders, flavour physics, $(g-2)_\mu$ as well as from dark matter observables such as the relic density, the spin-independent direct detection limit from XENON and the photon flux from dwarf spheroidal galaxies [205]. The latter are obtained with micrOMEGAs2.4 [208] interfaced to NMSSMTools [232] for the computation of the spectrum and particle physics constraints. For all the allowed points we then impose LHC limits from SUSY searches as well as more recent constraints on the Higgs sector from an interface to HiggsBounds 3.5.0beta [209, 210]. For SUSY searches we implement the ATLAS jets and missing energy search at 1.04 fb^{-1} [233]. For each SUSY point, signal events were generated with Herwig++ 2.5.1 [115, 138]. Using RIVET 1.5.2 [234] the experimental cuts of each search channel can be applied; for the ATLAS jets and missing E_T search these are included [235] in the RIVET package. For the case with only light neutralinos

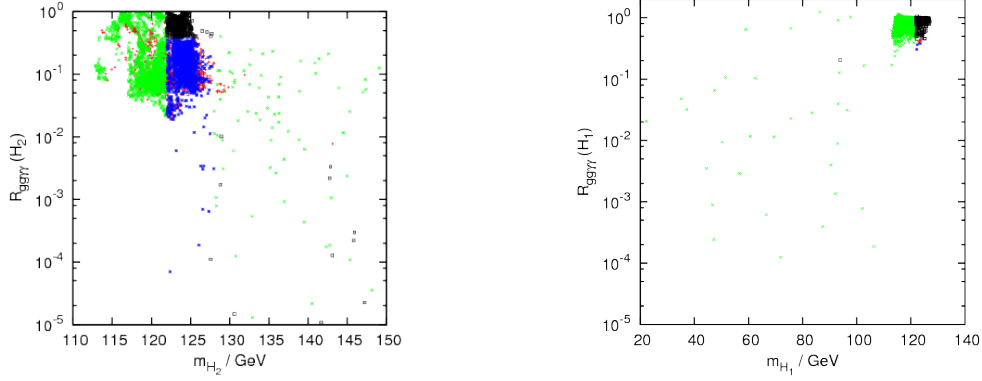


Figure 11: $R_{gg\gamma\gamma}$ as a function of M_{H_2} in the light neutralino LSP model (left panel) and $R_{gg\gamma\gamma}$ as a function of M_{H_1} for arbitrary neutralino masses (right panel). Blue points have $122 \text{ GeV} < M_{H_i} < 128 \text{ GeV}$ and black squares have in addition $R_{gg\gamma\gamma} > 0.4$. Red points are ruled out by HiggsBounds constraints or SUSY searches.

this SUSY search had hardly any impact on the sample. Firstly the majority of points had a heavy coloured spectrum, giving low production cross-sections. Secondly, allowed points with light squark masses, $300 - 600 \text{ GeV}$, had a singlino LSP and rather light sleptons so that leptons were produced in the squark decay chains. The jets and missing E_T SUSY searches that do not veto on leptons, which would show some sensitivity to these configurations, are not included in this analysis at present. For the sample generated allowing for heavier neutralinos, the more familiar result of $m_{\text{squark}} \gtrsim 0.6 - 1 \text{ TeV}$ (depending on m_{gluino}) was enforced by the search. In this sample the LSP is generally not the singlino thus allowing for the standard $q \rightarrow q\chi_1^0$ decay.

We first present the results for the Higgs sector for the scenario with light neutralinos. Imposing this condition means that the model must contain either a light scalar or pseudoscalar Higgs which is mostly singlet. This field is required for efficient annihilation of the neutralino LSP in the early Universe. Typically we found H_1 to be below the electroweak scale with a large singlet component while H_2 was SM-like. In some cases the light singlet Higgs field is a pseudoscalar and H_1 is SM-like, its mass barely reaches 122 GeV while M_{H_2} can take any value up to the TeV scale. It is also possible for both scalars to be heavily mixed and have a mass around $100\text{-}130 \text{ GeV}$. The predictions for $R_{gg\gamma\gamma}$ as a function of the H_2 mass are displayed in Fig. 11 (left panel). Here we only display the region where this channel is relevant, that is for a Higgs mass below 150 GeV . We find that $R_{gg\gamma\gamma} < 1$ and that the maximum rate occurs mostly for a Higgs below 127 GeV . The couplings of H_2 are usually SM-like, nevertheless large suppressions in $R_{gg\gamma\gamma}$ are found. This occurs because the width of the Higgs is enhanced by many new non-standard decay channels such as $\chi_1\chi_1, \chi_2\chi_1$ or channels involving light Higgses, thus reducing the branching fraction into photons. We have also computed $R_{gg\gamma\gamma}$ for the lightest Higgs and found that it is usually much below 1 because H_1 has a large singlet component. Only a few points with a SM-like H_1 with a mass near 122 GeV have $R_{gg\gamma\gamma} \approx 1$.

Many points predict a Higgs in the range compatible with the excess reported by ATLAS, $122 \text{ GeV} < m_{H_i} < 128 \text{ GeV}$, as mentioned above it is usually H_2 . These points are highlighted in blue in Fig. 11. For a fraction of these points the strength of the signal in $\gamma\gamma$ is also compatible with the 2σ range reported by ATLAS ($R_{gg\gamma\gamma} > 0.4$), these points are denoted by black squares in Fig. 11. Furthermore we found that in the few cases where H_1 was heavy enough to be in the preferred range, the corresponding value $R_{gg\gamma\gamma}$ was also in the desired range.

We then relaxed the upper limit on the neutralino mass and repeated the analysis. In this case we considered only the subset of points with a relic density in agreement with the 3σ value extracted by WMAP and we did not implement the LHC limits from SUSY searches. As opposed to the previous case, we found that in general H_1 was SM-like with a mass near 120 GeV while H_2 was heavy. Indeed, there is no need to fine-tune the Higgs sector to have a light singlet for efficient neutralino annihilation as other mechanisms are available. The value of $R_{gg\gamma\gamma}$ for the lightest Higgs, H_1 , is displayed in Fig. 11 (right panel). The points where one Higgs is in the range favored by ATLAS mostly have $R_{gg\gamma\gamma} > 0.4$, thus they appear as black squares in Fig. 11, the invisible decays of the Higgs being much less important than in the previous case as they are often not kinematically accessible. Note that in this figure we apply the color-coding for either H_1 or H_2 so black squares at low values of M_{H_1} correspond to points where H_2 is in the ATLAS preferred range with $R_{gg\gamma\gamma}$ that is not strongly suppressed. An analysis of the constrained MSSM [187] also found that after imposing collider, B-physics, dark matter and $(g-2)_\mu$ constraints, only H_1 could be in the range preferred by ATLAS and that this Higgs was SM-like.

3.3 MSSM+RH (s)neutrino

B. Dumont and S. Kraml

A supersymmetric alternative to the see-saw mechanism proposed in [150, 236] can lead to naturally light Dirac neutrinos and generate weak-scale sneutrino A-terms that are not proportional to the small neutrino Yukawa couplings. These large $A_{\tilde{\nu}}$ terms induce a non-negligible mixing between left and right-handed (RH) sneutrinos. The lighter sneutrino mass eigenstate, $\tilde{\nu}_1$, can thus become the LSP and a viable cold dark matter candidate. A particularly interesting case, on which we concentrate here, is a mainly RH light mixed sneutrino LSP with mass below 10 GeV [237]. Such a light mixed sneutrino LSP has a dramatic effect on SUSY signatures at the LHC [238] (see also [239]). Moreover, since the sneutrino coupling to the Higgs is proportional to $A_{\tilde{\nu}}$, the presence of the mixed sneutrino significantly impacts mass and decay modes of the lightest Higgs. First, it is important to notice that m_h is *decreased* through loop diagrams involving sneutrinos that induce corrections $\propto |A_{\tilde{\nu}}|^4$. Another important consequence of the light sneutrino dark matter scenario is a dramatic change of the decay branching fractions of h . Indeed, the lightest Higgs decays dominantly invisibly into sneutrinos ($BR(h \rightarrow \text{invisible}) \gtrsim 90\%$). In addition, if the decay into neutralinos is kinematically allowed, it adds a small contribution to the invisible width of the lightest Higgs because $BR(\tilde{\chi}_1^0 \rightarrow \tilde{\nu}\nu) \approx 100\%$.

To assess the consequences for Higgs phenomenology in a global way, we perform an MCMC analysis of the MSSM+RH neutrino parameter space, including all relevant constraints from Higgs and dark matter searches. (Regarding the latter, we carefully take into account nuclear and astrophysical uncertainties.) The calculations are done using `micrOMEGAs` linked to appropriately modified versions of `SuSpect` and `HDECAY`. Higgs mass limits are computed with `HiggsBounds3.5.0beta`. We assume GUT relations for the gaugino masses, $M_1 \simeq M_2/2 \simeq M_3/6$, a common soft mass of 2 TeV for squarks of the first and second generation ($m_{\tilde{q}_{L,R}} \approx 2$ TeV), and of 1 TeV for squarks of the third generation, $m_{\tilde{Q}_3} = m_{\tilde{U}_3} = m_{\tilde{D}_3} = 1$ TeV. The pseudoscalar Higgs mass m_A is also fixed to 1 TeV. We scan over all remaining free parameters, including the sneutrino and charged slepton soft terms of the 1st/2nd (assumed to be degenerate) and the 3rd generation. We set a loose 95% upper bound on the relic density, $\Omega_{\text{DM}} h^2 < 0.135$, using a smooth step-like function and we compute the χ^2 for the direct detection limits from

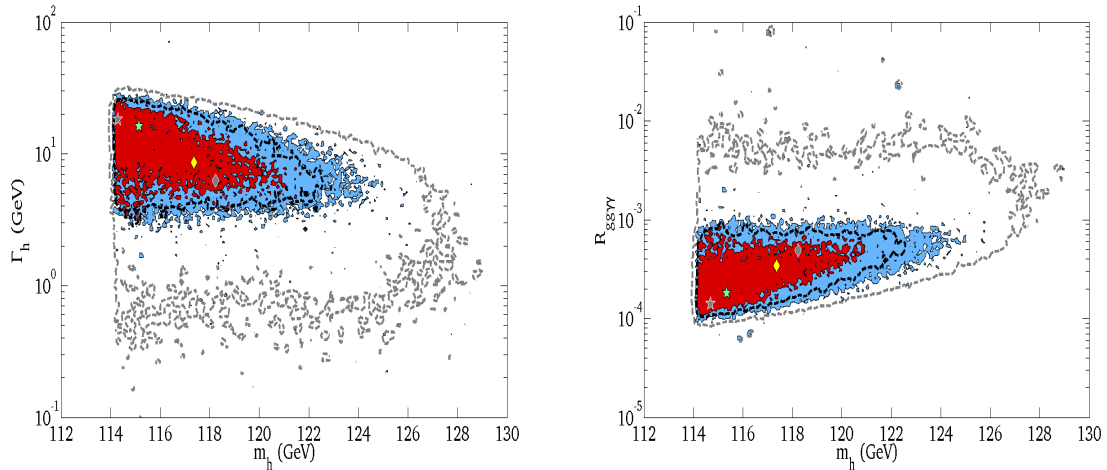


Figure 12: Scan results concerning the lightest Higgs. On the left Γ_h versus m_h , on the right $R_{gg\gamma\gamma}$ versus m_h . In both cases, the red and blue surfaces are the 68% and 95% Bayesian credible regions (BCR), respectively, requiring $m_{\tilde{g}} > 750$ GeV. The green star indicates our best fit point, the yellow rhombus locates the weighted average of the distribution. The black and the grey dotted lines identify the 68% and 95% BCR, respectively, in which instead of $m_{\tilde{g}} > 750$ GeV we set $m_{\tilde{g}} > 500$ GeV. In this latter case, the best fit point and the weighted average are shown in grey.

XENON100, CDMS and CoGeNT (we thank Thomas Schwetz for providing his private code to this end [240, 241]). We combine these constraints, and others (e.g. the value of $(g-2)_\mu$), in a global likelihood function. Regarding SUSY mass limits from the LHC, the CMSSM limit for the case of heavy squarks [233, 242] applies to our case. To take this into account we require a posteriori $m_{\tilde{g}} > 750$ GeV. We present our main results on the properties of the lightest Higgs in this model in Fig. 12 and Table 1.

The mass of our Higgs is constrained by the invisible searches at LEP [243, 244] and we find the usual lower bound $m_h > 114$ GeV. We see in Fig. 12 that Γ_h tends to decrease with increasing m_h . Conversely, $R_{gg\gamma\gamma}$ tends to increase with increasing m_h . This is because higher masses tend to have a smaller $A_{\tilde{\nu}}$ due to the negative corrections to m_h involving sneutrinos, and then the lightest Higgs-sneutrino-sneutrino coupling, $g_{h\tilde{\nu}\tilde{\nu}} \propto A_{\tilde{\nu}}$, is smaller. For the same reason, going from $m_{\tilde{g}} > 500$ GeV to $m_{\tilde{g}} > 750$ GeV has a large effect on the predicted Higgs mass range: with $M_2 \simeq M_3/3$, increasing the gluino mass suppresses the neutralino t-channel exchange contribution to the $\tilde{\nu}_1$ annihilation (i.e. the $\tilde{\nu}_1\tilde{\nu}_1 \rightarrow \nu\nu$ and $\tilde{\nu}_1^*\tilde{\nu}_1^* \rightarrow \bar{\nu}\bar{\nu}$ channels), which has to be compensated by a larger Higgs-exchange contribution, and hence a larger $A_{\tilde{\nu}}$ term, to still achieve $\Omega_{\text{DM}}h^2 < 0.135$. Thus the 95% upper bound on the BCI of m_h changes from 124.6 GeV to 124.2 GeV to 122.2 GeV, when going from no limit on $m_{\tilde{g}}$ to $m_{\tilde{g}} > 500$ GeV to $m_{\tilde{g}} > 750$ GeV. (These numbers will of course somewhat vary if we take the stop soft masses as free parameters in the fit.)

The left panel of Fig. 12 shows that $\Gamma_h \approx 3 - 30$ GeV $\approx 10^{3-4} \Gamma_{h,\text{SM}}$, due to the predominant decay into two sneutrinos. In the right panel, we see that $R_{gg\gamma\gamma}$ is always < 0.1 and more likely of the order of a few $\times 10^{-4}$. Therefore, if the 125 GeV excess in the $\gamma\gamma$ channel is to be confirmed, this model would be ruled out in its present form. If not, this Higgs boson is a very good candidate for the invisible searches at the LHC in the WW fusion channel.

Observables	68% BCI		95% BCI	
	lower	upper	lower	upper
m_h (GeV)	114.2	118.2	114.1	122.2
Γ_h (GeV)	5.2	14.7	3.5	22.6
$1 - BR(h \rightarrow \text{invisible})$	2.6×10^{-4}	9.8×10^{-4}	1.5×10^{-4}	2.4×10^{-3}
$R_{gg\gamma\gamma} \times 10^4$	1.9	5.9	1.2	9.0

Table 1: 68% and 95% Bayesian credible intervals (BCI) of some Higgs-related observables.

3.4 UMSSM

G. Bélanger J. Da Silva

The UMSSM is an extension of the MSSM with a gauge group that contains an extra $U(1)'$ symmetry. Here we will assume that this model is derived from an E_6 model and in the numerical example we will choose the $U(1)'$ to correspond to $U(1)_\psi$, one of the two abelian subgroups of E_6 . In addition to the MSSM superfields, the model contains a new vector superfield, B' , and a new singlet scalar superfield, S , thus leading to a new gauge boson, Z' . The Higgs sector consists of 3 CP-even scalars, one CP-odd Higgs and a charged Higgs. The μ parameter, is generated from the VEV of the singlet field responsible for the breaking of the $U(1)'$ symmetry and is thus naturally at the weak scale. In this model the light Higgs mass receives new contributions from the superpotential term as in the NMSSM as well from $U(1)'$ D-terms [245]. This means that it is more natural than in the MSSM to obtain a light Higgs with a mass of 125 GeV. In fact the light Higgs can easily exceed the value already excluded by LHC searches for a Higgs with SM couplings. Typically the Higgs spectrum will consist of an SM-like light Higgs, a heavy mostly doublet scalar which is almost degenerate with the pseudoscalar and the charged Higgs, and a predominantly singlet scalar. The singlet state is rather heavy as its mass is close to that of the Z' , which is constrained by the LHC to be above the TeV scale. This also implies that the singlet component of the light state is usually not large enough to significantly relax the bound on the lightest Higgs contrary to what occurs in the NMSSM. Thus the couplings of the light Higgs are SM-like.

Apart from the shift in the mass of the light Higgs, the main impact on the Higgs phenomenology in this model arises from the possible contribution of invisible Higgs decays. In the UMSSM the dark matter candidate can be either the right-handed sneutrino or the neutralino. Both can be light and contribute to invisible modes of the Higgs. In [246] we have investigated the parameter space of the UMSSM that was consistent with precision measurements, LHC limits on the Z' mass, the upper bound on the relic density, $\Omega h^2 < 0.1228$, limits from DM direct detection experiments (XENON100 [196]) as well as with the limit from $\Delta M_{d,s}$ in the B-meson [247] in the case of a sneutrino LSP. Here we allow either dark matter candidate and specifically investigate the invisible branching ratio of the light Higgs. We also vary the common soft squark mass in the range 500-2000 GeV. The results are displayed in Fig. 13 for a light Higgs mass in the range 100-160 GeV considering only the cases when $M_{LSP} < M_h/2$. We find that even though the invisible branching ratio can reach one, in general and even under the condition of a light LSP, the visible decay modes are not significantly suppressed. Thus the model can accommodate a Higgs in the mass range compatible with the excess of events observed at the LHC with a signal strength comparable to the SM Higgs.

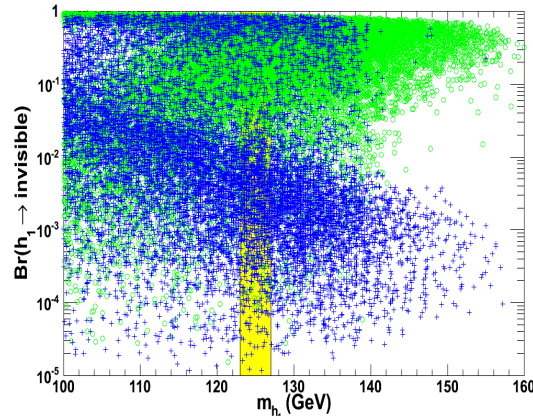


Figure 13: The invisible branching ratio of the light Higgs as a function of its mass distinguishing the cases where the sneutrino (circle) or neutralino (cross) is the LSP. The region with $123 \text{ GeV} < M_h < 127 \text{ GeV}$ is highlighted in yellow.

4 Non supersymmetric models

4.1 UED

A. Belyaev, G. Bélanger, M. Brown, M. Kakizaki, A. Pukhov

Theories with Universal Extra Dimensions (UED) are very promising. In the UED framework *all* SM particles propagate in the bulk, which results in the conservation of Kaluza-Klein (KK) number¹ at tree level and conservation of KK parity at any loop level. This KK parity conservation is the consequence of the orbifold symmetry (e.g. S_1/Z_2 orbifold and Z_2 symmetry in case of one universal extra dimension) which insures the conservation of the “evenness” or “oddness” of KK number in an interaction. As a result of this symmetry, UEDs predict a stable lightest Kaluza-Klein particle (LKP) which would be a candidate for dark matter (DM).

The simplest UED theory is the 5D theory known as minimal Universal Extra Dimensions (mUED). The phenomenology of mUED has been studied very intensively in many publications, but so far none of the experimental papers has set LHC limits on mUED. This is not surprising – the search for mUED is much more difficult than the search of SUSY within the experimentally well-explored mSUGRA scenario the LHC.

The main reason is that mUED provides much smaller missing transverse momentum due to a small mass splitting between KK-partners of SM particles of the same KK level. Though DM sets an upper limit on the scale of mUED below about 1.6 TeV [248], this scale will be very difficult to test even with the 14 TeV LHC. However, the Higgs sector provides a very powerful constraint on mUED. First of all, the Higgs mass is limited to be below 230 GeV by the simple requirement that the dark matter candidate should be neutral. Second, as we will demonstrate, the signals from the Higgs boson from mUED are *always* enhanced as compared to those of the SM. Therefore, the excellent LHC sensitivity to the SM Higgs boson would lead to even better sensitivity to the Higgs boson within the mUED scenario. For example, by the end of 2012 the LHC will be able to completely exclude the SM Higgs boson below 230 GeV, or observe it at least at the 3σ level. If the hints of a Higgs signal are not confirmed, and a SM Higgs boson is excluded, this would mean that mUED is excluded completely for all scales!

¹Boundary conditions induce momentum quantization along the extra dimension(s) and the corresponding quantum numbers(s) are called KK number(s).

Here we evaluate and present the effect of KK-particles in the loop for $gg \rightarrow h$ production and Higgs decay to $\gamma\gamma$ and W^+W^- . This effect is different for different Higgs signatures and this non-universality should be taken into account when establishing limits on the mUED parameter space. As far as we know, this is the first time the above mentioned non-universality is taken into account in the context of UED models.

The matrix elements \mathcal{M} for the $gg \rightarrow h$ and $h \rightarrow \gamma\gamma$ processes both take the form $\mathcal{M} = \tilde{\mathcal{M}}(m_h^2 g^{\mu\nu}/2 - p^\nu q^\mu) \sum \epsilon_\mu \epsilon_\nu$, where p and q are the momenta of the external photons or gluons (approximated as on-shell), m_h is the Higgs boson mass, and the sum is over gluon or photon polarisations. For $gg \rightarrow h$ we have

$$\tilde{\mathcal{M}}_{ggh} = -\frac{\alpha_s}{4\pi v} \sum_q F_{ggh,q}$$

with

$$F_{ggh,q} = f_F(m_q, m_h) + \sum_{n=1}^N m_q \sin(2a_q^{(n)}) \left(\frac{1}{m_{q,1}^{(n)}} f_F(m_{q,1}^{(n)}, m_h) + \frac{1}{m_{q,2}^{(n)}} f_F(m_{q,2}^{(n)}, m_h) \right)$$

and

$$f_F(m, m_h) = \frac{8m^2}{m_h^2} - \frac{4m^2}{m_h^2} (m_h^2 - 4m^2) C_0(m, m_h),$$

where C_0 is the scalar three-point Passarino-Veltman function

$$C_0(m, m_h) = \begin{cases} -\frac{2}{m_h^2} \left[\arcsin\left(\frac{m_h}{2m}\right) \right]^2 & m^2 \geq m_h^2/4 \\ \frac{1}{2m_h^2} \left[\ln\left(\frac{1+\sqrt{1-4m^2/m_h^2}}{1-\sqrt{1-4m^2/m_h^2}}\right) - i\pi \right]^2 & m^2 < m_h^2/4. \end{cases}$$

Note that for each SM quark there are *two* KK partners at each KK level n with masses $m_{q,1}^{(n)}$ and $m_{q,2}^{(n)}$. At tree level these are equal:

$$m_{q,\text{tree}}^{(n)} = \sqrt{m_q^2 + \frac{n^2}{R^2}},$$

where R is the compactification radius of the extra dimension (and the same goes for W boson and scalar masses used below); but if radiative corrections are included (see e.g. Ref. [249]) the masses split. Similarly, the mixing angles $a_q^{(n)}$ required to diagonalise the KK quark mass matrices differ from the tree-level form

$$a_{q,\text{tree}}^{(n)} = \frac{1}{2} \arctan\left(\frac{m_q R}{n}\right)$$

once radiative corrections are included, but the mixings for type 1 and 2 quarks remain equal to each other, in contrast to the masses. In our analysis we used one-loop corrected expressions for all masses and mixings as detailed in Ref. [249]). One should also note that the higher-order corrections to $gg \rightarrow H$ presented here can be substantial, of the order of 50% or even larger. However, these corrections largely cancel out when taking the ratio of mUED to SM rates.

The sum over KK modes n is taken up to a cutoff N , corresponding to a momentum cutoff in the extra dimension of NR^{-1} . Mild cutoff-dependence is expected in perturbatively

non-renormalisable theories such as mUED. In our quantitative analysis we chose $N = 20$ and included only t and b in the sum over quark flavours q , which is an excellent approximation due to the size of their Yukawa couplings compared to those of the other quarks. One should note that for large N the rest of the sum is proportional to $1/N$. Therefore, setting $N = 20$ yields about 5% accuracy as compared to the full sum.

The $h \rightarrow \gamma\gamma$ matrix element is given by

$$\tilde{\mathcal{M}}_{h\gamma\gamma} = -\frac{e^2 g}{16\pi^2 m_W} F_{h\gamma\gamma},$$

where

$$F_{h\gamma\gamma} = F_{h\gamma\gamma}^{\text{SM}} + \sum_{n=1}^{Nt} F_{h\gamma\gamma}^{(n)}$$

and

$$F_{h\gamma\gamma}^{\text{SM}} = f_V(m_W, m_h) + \sum_f n_c Q_f^2 f_F(m_f, m_h).$$

The Fermion loop function f_F was given earlier and the vector function introduced above is

$$f_V(m, m_h) = -2 - 12 \frac{m^2}{m_h^2} + 12 \frac{m^2}{m_h^2} (m_h^2 - 2m^2) C_0(m, m_h).$$

The sum could be taken over all SM fermions f , each with charge $Q_f e$, setting n_c to 3 for quarks and 1 for leptons. In our treatment, however, we again only included t and b quarks. The contribution from the n th level KK fermions is

$$F_{h\gamma\gamma}^{(n)} = \frac{m_W^2}{m_{W,n}^2} f_V(m_{W,n}, m_h) + f_S^{(n)}(m_{a,n}, m_{W,n}, m_h) + \sum_f n_c Q_f^2 \left(\frac{m_f}{m_{f,1}^{(n)}} \sin 2a_f^{(n)} f_F(m_{f,1}^{(n)}, m_h) + \frac{m_f}{m_{f,2}^{(n)}} \sin 2a_f^{(n)} f_F(m_{f,2}^{(n)}, m_h) \right).$$

Here we have a new scalar loop function for the charged scalars $a_{\pm}^{(n)}$ that appear in the loop,

$$f_S(m_{a,n}, m_{W,n}, m_h) = \left[\frac{2m_W^2}{m_{W,n}^2} \left(1 - \frac{2m_{a,n}^2}{m_h^2} \right) - 2 \right] [1 - 2C_0(m_{a,n}, m_h)].$$

The dependence of the two matrix elements on m_h and the inverse compactification radius R^{-1} (these are the two free parameters of mUED, other than the very weak cutoff dependence) is shown in Figure 14, and clearly indicates that for a light Higgs boson the hgg coupling is enhanced while $h\gamma\gamma$ is suppressed. The R^{-1} dependence enters through the KK masses and mixing angles.

Using our model's predictions for Higgs boson production enhancement for different values of m_h and R^{-1} together with the latest CMS [144] and ATLAS [143] limits on Higgs boson production, we can exclude regions of the (m_h, R^{-1}) plane. We statistically combined data from Fig. 6 (top) of the CMS paper and Fig. 3 of the ATLAS paper in each of the $\gamma\gamma$ and W^+W^- channels; the resulting limits on mUED are shown in Fig 15 (left). These constraints are combined with other constraints from DM relic density [248] as well as EW precision tests [250] in Fig. 15 (right).

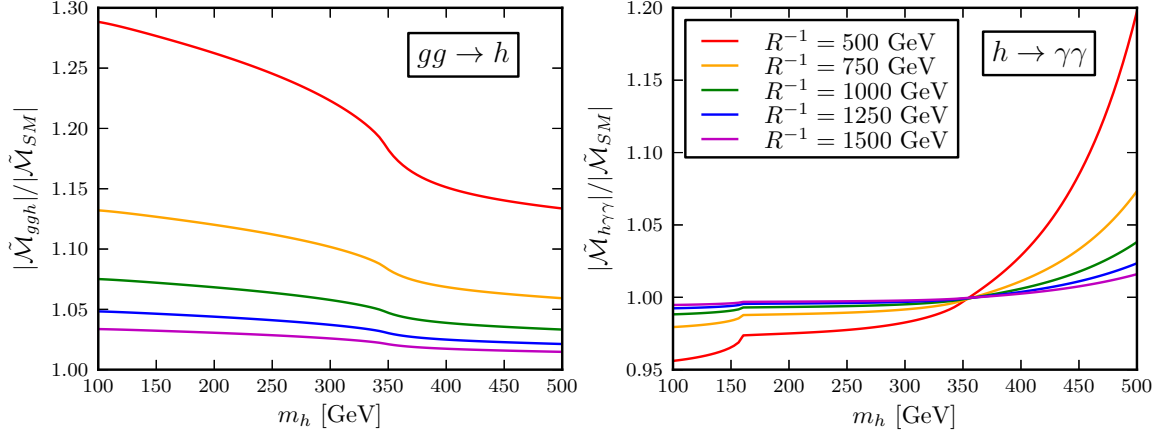


Figure 14: Ratio of mUED and SM matrix elements for $gg \rightarrow h$ (left) and $h \rightarrow \gamma\gamma$ (right) processes for the following values of R^{-1} from top to bottom in each plot: 500, 750, 1000, 1250 and 1500 GeV. The number of KK modes is $N = 20$.

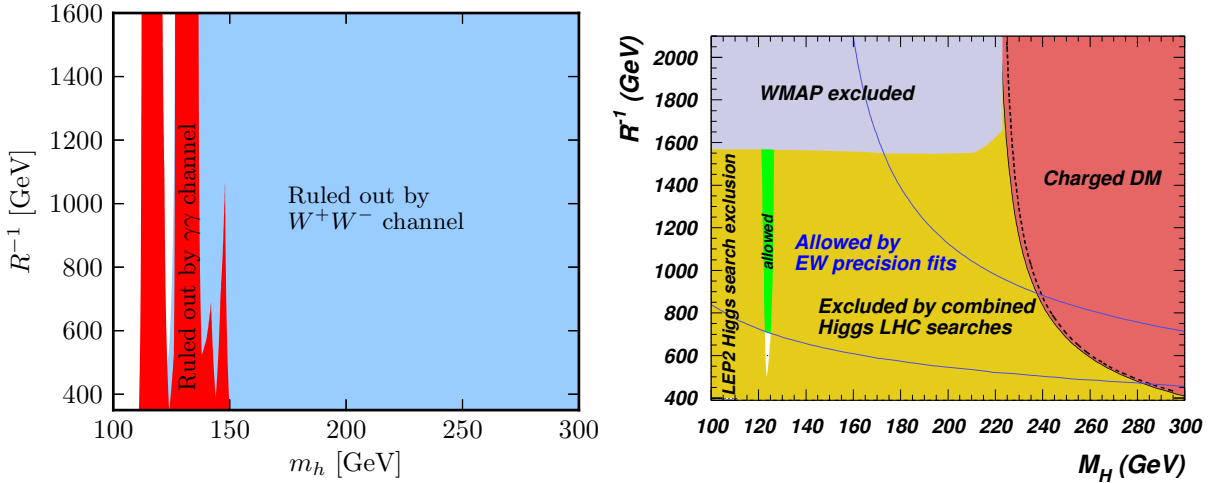


Figure 15: Left: exclusion of mUED (m_h, R^{-1}) parameter space at 95% CL from the Higgs boson search using combined ATLAS and CMS limits in the $\gamma\gamma$ and W^+W^- channels. Right: combination of Higgs constraints (from the left frame), EW precision and DM relic density limits on the mUED parameter space.

We can see that the Higgs search provides a powerful constraint on the mUED model since Higgs boson production is enhanced. Compared to previous studies [251], we have included mass corrections for the particles in the loop, providing more realistic predictions of mUED cross sections, and have accurately combined non-universal enhancement in $\gamma\gamma$ and W^+W^- matrix elements, which has not been done previously. This allowed us to find accurate limits on the mUED (m_h, R^{-1}) parameter space. After combination of ATLAS and CMS limits for each individual channel ($\gamma\gamma$ and W^+W^-), we found that $R^{-1} < 500$ GeV is excluded at 95%CL, while for larger R^{-1} only a very narrow ($\pm 1 - 3$ GeV) mass window around $m_h = 125$ GeV is left. This is the region where the excess of the events in the Higgs search channels is reported by the ATLAS and CMS collaborations and where the exclusion limit is weaker.

4.2 SM4

A. Wingerter

4.2.1 Motivation for a Fourth Chiral Generation

Introducing a fourth chiral generation is one of the simplest and most straightforward extensions of the SM. There are 9 additional parameters, namely the masses of the fourth generation fermions $m_{t'}$, $m_{b'}$, $m_{\tau'}$, $m_{\nu'}$, the mixing angles θ_{14} , θ_{24} , θ_{34} , and 2 new CP phases. The relatively small number of new parameters makes the Standard Model with four generations (SM4) highly predictable and testable.

Before observing the slight excess around 126 GeV [143, 144] that may indicate the presence of a Higgs boson, some physicists were getting increasingly worried about the tension between the lower Higgs boson mass bound of 114.4 GeV set by LEP [252] and the best-fit value of $m_H = 80_{-23}^{+30}$ GeV [44] as obtained from electroweak precision measurements (EWPMs). In the presence of a fourth generation, the EWPMs may be consistent with much larger values for the Higgs mass, if the mass splittings $|m_{t'} - m_{b'}|$ and $|m_{\tau'} - m_{\nu'}|$ are chosen accordingly (see Fig. (13) in Ref. [253]). Also, the SM does not predict the number of generations, and the constraints from flavor physics are weaker than previously assumed [254] and allow for sizable mixing of order the Cabibbo angle between the third and the fourth generation, even after taking the EWPMs into account [255]. The *direct*² measurement of $|V_{tb}| = 1.02_{-0.11}^{+0.10}$ from single-top production [256] is consistent with $|V_{tb}| = 1$, but leaves enough room for a fourth generation replica t' of the top quark to couple to the b quark. Basically, this is all in support of a “Why not?” type of argument.

Some of the other reasons usually given in favor of the existence of a fourth generation are less convincing. Following Ref. [257] many recent publications have maintained that in the presence of a fourth generation the gauge couplings may unify without supersymmetry (SUSY). However, a closer inspection shows that the fourth generation quark and Higgs boson masses required in this scenario are excluded by experiment [212, 258–260]. Also, it has been discussed in the literature whether the extra CP violation introduced by the 2 additional phases in the 4-by-4 CKM matrix may be sufficient to render electroweak baryogenesis in the SM viable [261]. According to Refs. [262, 263], the first order phase transition in the SM is not strong enough to preserve the generated baryon asymmetry from being washed out, but the presence of extra scalars in the MSSM may change the picture.

4.2.2 Impact of a 126 GeV Higgs Boson on the SM4

At 1-loop, the running quartic coupling $\lambda(\mu)$ develops a Landau pole for some $\mu = \mu_0$, and this tells us that the SM stops making sense at the scale μ_0 for the corresponding Higgs mass $m_H^2 = \lambda v^2$. This fact can be interpreted in either of two ways: If we assume that the theory is valid beyond μ_0 , the Higgs mass must be less than m_H . On the other hand, if we assume (or know) that the Higgs mass is m_H , the triviality bound gives us the maximal scale μ_0 up to which the SM can be *perturbatively* valid. At 2-loop, the quartic coupling does not develop a Landau pole, but approaches an ultraviolet fixed point λ_{FP} (see Fig. 16 (a)). The SM ceases to be perturbative long before λ reaches the fixed point [264], and usually one adopts either $\lambda < \lambda_{\text{FP}}/2$ (loose) or $\lambda < \lambda_{\text{FP}}/4$ (tight) as a condition for perturbativity.

²Previous determinations of $|V_{tb}|$ assumed unitarity of the 3-by-3 CKM matrix.

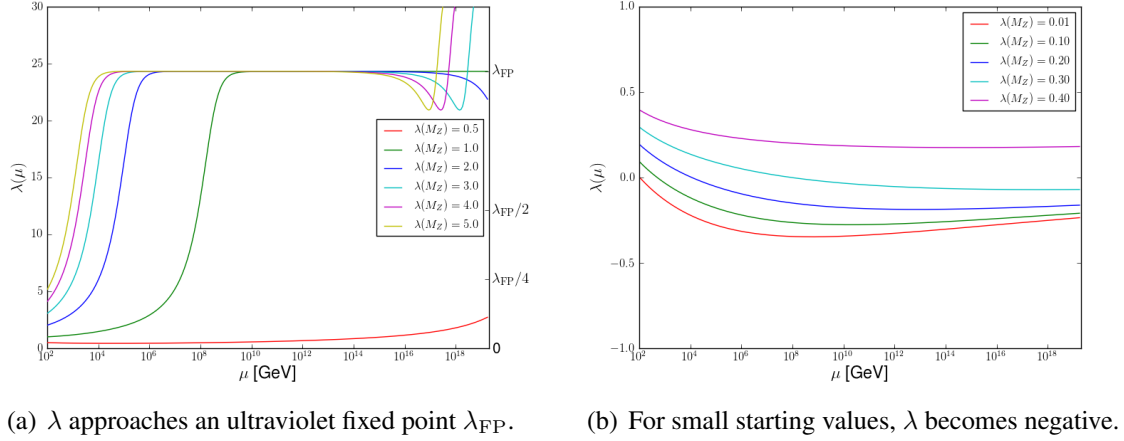


Figure 16: The 2-loop running of the quartic Higgs coupling $\lambda(\mu)$ in the SM.

A lower bound on the Higgs mass can be derived from the requirement of vacuum stability [265]. For too small starting values, $\lambda(\mu)$ is driven negative (see Fig. 16 (b)), and to a good approximation [266,267] that is tantamount to the effective Higgs potential becoming unbounded from below. As before, the scale where this happens indicates where the SM breaks down. Alternatively, one obtains a lower limit on the Higgs mass. It is important to note that in this 2-loop analysis (both for the triviality and the stability bound), the radiative corrections to the tree-level relations between the Higgs boson mass m_H and the quartic coupling λ on the one hand, and the top quark mass m_t and the Yukawa coupling y_t on the other, cannot be neglected [268]. The generalization of these so-called Higgs and top matching corrections to the case of the SM4 are given in Ref. [269].

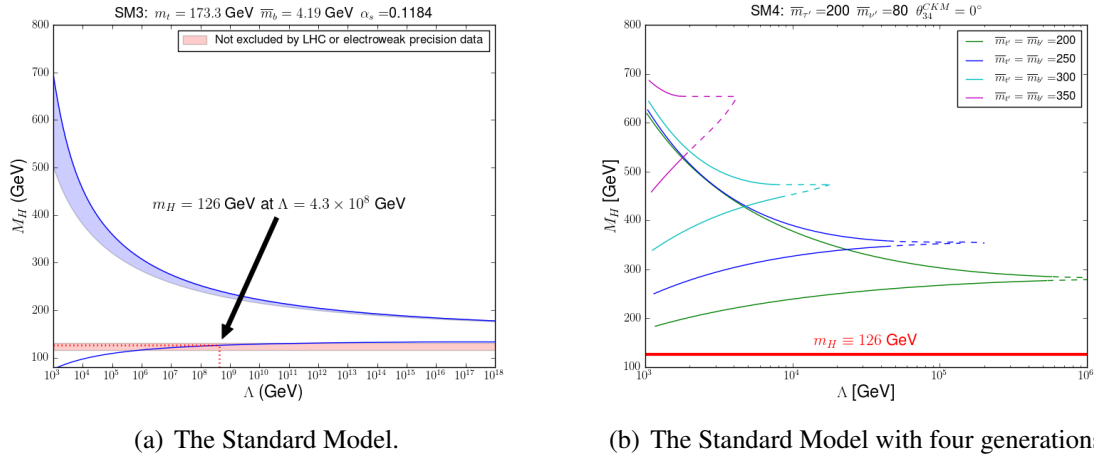


Figure 17: The triviality and stability bounds in the Standard Model with three and four generations, respectively [269]. The blue shaded area below the triviality bound in the left panel corresponds to the uncertainty introduced by choosing $\lambda < \lambda_{\text{FP}}/2$ or $\lambda < \lambda_{\text{FP}}/4$, respectively, as the condition for perturbativity of the quartic coupling. The dashed lines in the right panel indicate that at least one of the Yukawa couplings has become non-perturbative, i.e. $y_f \geq \sqrt{4\pi}$ for $f = t, t', b', \tau', \nu'$.

In Fig. 17 (a) we show the triviality and stability bounds for the SM. The recent LHC results [143, 144] together with LEP data [252] exclude the mass range $m_H < 115.5$ GeV and $127 \text{ GeV} < m_H < 600$ GeV at 95% C.L. Electroweak precision measurements set 95% C.L. upper bounds for the Higgs mass of 185 GeV and 158 GeV, respectively, depending on whether one includes the LEP direct search results or not [270]. This basically leaves a small window of $115.5 \text{ GeV} < m_H < 127$ GeV that is not yet excluded (red band in Fig. 17 (a)). One immediate consequence is that the SM cannot be perturbatively valid up to some grand unification scale³ M_{GUT} : The stability bound crosses 127 GeV at $\Lambda = 1.3 \times 10^9$ GeV. If the slight excess that points to a Higgs boson with mass $m_H = 126$ GeV can be substantiated with more data, this would correspond to a cut-off scale for the SM around $\Lambda_c = 4.3 \times 10^8$ GeV (red dotted line in Fig. 17 (a)). Albeit beyond the reach of the LHC, this is one of the lowest scales so far for which we have hints for physics beyond the Standard Model (BSM). Of course, this does not mean that there is no new physics before Λ_c , but rather this sets an upper bound. One easy way to evade that conclusion is e.g. to assume that the vacuum is metastable or to introduce a second Higgs doublet.

In Fig. 17 (b) we show the triviality and stability bounds for the SM4. Perhaps the most striking feature (as compared to the case of the SM) is that the curves now intersect and bound a finite region. As such, there is a priori a highest scale Λ_c beyond which the theory does not make sense. Generally, the Yukawa couplings become non-perturbative before reaching Λ_c (indicated by the dashed line style in Fig. 17 (b)) so that the real cut-off scale is lower. Note that the stability bound is much more sensitive to the new particles than the triviality bound and sets the stronger constraints.

We have indicated in Fig. 17 (b) the slight excess around 126 GeV and see that it is clearly excluded by the stability bound for all values of the fourth generation fermion masses. More plots where $m_{t'}$, $m_{b'}$, $m_{\tau'}$, $m_{\nu'}$ and θ_{34} are varied within sensible limits can be found in Ref. [269] and lead to the same conclusion. The other two mixing angles θ_{14} and θ_{24} are small [254], and their effect on the stability and triviality bounds is negligible. Even without taking this excess into account, the Higgs exclusion limits in the context of the SM4 [212, 260] cannot be reconciled with the stability and triviality bounds and therefore forbid a fourth chiral generation of fermions for any choice of masses and mixing angles. Of course, this statement is subject to the assumptions we used to calculate the stability and triviality bounds such as absolute stability of the vacuum, no more than one Higgs doublet, etc. For the sake of completeness, though, it should be noted that the Higgs searches do not cover the region $m_H > 600$ GeV, and there exists a small window $600 \text{ GeV} < m_H < 700$ GeV that is allowed by the stability and triviality bounds, and by the EWPMs. However, as Fig. 17 and Fig. 2 in Ref. [269] show, the cut-off scale in this case is at most 2 TeV.

Also, the experimental limits on the fourth generation quark [258, 259] and lepton [44] masses are now closing in on the unitarity bounds $m_{t'}, m_{b'} \lesssim 500$ GeV and $m_{\tau'}, m_{\nu'} \lesssim 1000$ GeV [271] and leave very little room for a fourth generation. The bounds we obtained from theory by considering the stability and triviality bounds are complementary in the sense that they also apply in situations where the direct search limits do not hold, and at the same time set stronger constraints on the lepton masses than currently available from direct search experiments. For a critical discussion of the direct search limits, especially the assumption $m_{t'} - m_{b'} < M_W$, see Ref. [269].

³Since the stability bound is asymptotically flat, choosing $M_{\text{GUT}} \sim 10^{15}$ GeV or 10^{16} GeV does not change the conclusions.

5 Conclusions

The properties of non-standard Higgs bosons can differ significantly from those of the SM one for each production and decay process at the LHC. While for most of the MSSM parameter space the most relevant search channel is a Higgs produced in gluon fusion decaying into two photons, in extensions of the MSSM or in UED the Higgs decay into vector boson pairs is also an important channel. Interpreting LHC results therefore requires careful combination of the limits from each production times decay channel independently. An exclusion of the SM Higgs by the end of this year at 95% C.L. would rule out the whole parameter space of mUED while SUSY models have enough flexibility to avoid this limit. We have also shown that the excess of events corresponding to a Higgs with a mass of 125 GeV reported by ATLAS and CMS could be compatible with any of the extensions to the Standard Model considered, provided the invisible Higgs decay mode is not too large.

6 Acknowledgements

The work of GB, FB, AP was supported in part by the GDRI-ACPP of CNRS. AB and MB thank the Royal Society for partial financial support. AB also thanks the NExT Institute and SEPnet for financial support. JD acknowledges the CMIRA 2011 EXPLO'RA DOC program of the French region Rhône-Alpes for financial support. RMG wishes to acknowledge the Department of Science and Technology of India, for financial support under the J.C. Bose Fellowship scheme under grant no. SR/S2/JCB-64/2007. The work of AP was supported by the Russian foundation for Basic Research, grant RFBR-10-02-01443-a.

Contribution 9

CMSSM mass spectrum at the LHC after the 125 GeV Higgs boson results

M. Kadastik, K. Kannike, A. Racioppi, M. Raidal

Abstract

We show that if the Higgs boson mass is 125 ± 1 GeV, the CMSSM sparticle spectrum that is testable at the LHC is restricted only to two distinct possibilities – either of the lightest slepton or stop are degenerate in mass with the lightest supersymmetric particle that is the dark matter. This implies that the CMSSM spectrum is now known. However, the two possible options both represent very difficult spectra for the LHC because very soft particles are produced in sparticle decays. We encourage the LHC experiments to perform detailed studies of the two possible CMSSM sparticle spectra.

1 INTRODUCTION

The consistent ATLAS [143] and CMS [144] hints for the existence of a $M_H \approx 125$ GeV Higgs boson have profound implications [177–179, 181, 182, 184, 272] for the sparticle mass spectrum in the context of the minimal supersymmetric standard model (MSSM). In particular, the versions of the MSSM with unification constraints on supersymmetry (SUSY) breaking parameters, such as the CMSSM or mSUGRA, becomes severely fine-tuned [272–276]. The reason is that such a high value of the Higgs boson mass requires unusually large scalar masses to generate the indicated Higgs mass at loop level.

At the same time, a $M_H \approx 125$ GeV Higgs boson mass implies that the possible LHC phenomenology of new CMSSM particles becomes highly predictive. This is because the global fits of the CMSSM parameter space are dominated by two phenomena [277]. The first one is the production of the correct dark matter (DM) relic density via very finely tuned freeze-out processes. The second is explaining the measured value of the muon anomalous magnetic moment $(g - 2)_\mu$ with extra contributions from sparticles. All other phenomenological constraints, summarized in Table 1, are less constraining and, at present, play a role only in some particular corner of the CMSSM parameter space. As a result, the DM freeze-out processes alone determine the sparticle spectrum that is potentially observable at the LHC.

In this work we point out that the 125 GeV Higgs implies only two possible options for the CMSSM phenomenology at the LHC – the lightest stable SUSY particle, the DM, is (almost) degenerate with either the lightest slepton or stop. This is because for $M_H \approx 125$ GeV only the slepton and stop coannihilation processes can produce the correct DM density and have light sparticles. All other DM freeze-out processes imply unobservable sparticle spectra at the LHC. If, in addition, one also requires generation of the measured $(g - 2)_\mu$, at 3σ level only the slepton coannihilation region of the CMSSM parameter space survives (with a poor fit). This may be testable at the LHC.

quantity	experiment	Standard Model
$\alpha_3(M_Z)$ [282]	0.1184 ± 0.0007	parameter
m_t [283]	173.2 ± 0.9	parameter
m_b [44]	4.19 ± 0.12	parameter
$\Omega_{\text{DM}} h^2$ [284]	0.112 ± 0.0056	0
δa_μ [285]	$(2.8 \pm 0.8) \times 10^{-9}$	0
$\text{BR}(B_d \rightarrow X_s \gamma)$ [286]	$(3.50 \pm 0.17) \times 10^{-4}$	$(3.15 \pm 0.23) 10^{-4}$
$\text{BR}(B_s \rightarrow \mu^+ \mu^-)$ [287]	$< 1.1 \times 10^{-8}$ at 95%C.L.	$(0.33 \pm 0.03) 10^{-8}$
$\text{BR}(B_u \rightarrow \tau \bar{\nu})/\text{SM}$ [288]	1.25 ± 0.40	1

Table 1: Constraints used for the CMSSM analyses.

The implications of those results for the LHC are twofold. On the one hand, the CMSSM spectra testable at the LHC are now known and the experiments can concentrate on detailed studies of those spectra. On the other hand, those spectra are really difficult because the transverse momenta of the particles produced in sparticle decays are predicted to be very small due to the sparticle degeneracies. The aim of this work is to encourage the LHC experiments to analyze the slepton and stop degenerate spectra in detail.

2 THE DIFFICULT CMSSM SPECTRA

The CMSSM is one of the most thoroughly studied SUSY models and the CMSSM parameter space was rather fine-tuned already before the 125 GeV Higgs hint [277–281]. Naturally, if the Higgs boson is discovered with mass $M_H = 125 \pm 1$ GeV, one would like to know what the implication of this discovery is for the LHC phenomenology of this model. At the GUT scale the parameter space of the CMSSM is described by five parameters,

$$m_0, M_{1/2}, A_0, \tan \beta, \text{sign}(\mu), \quad (1)$$

the common scalar mass, the common gaugino mass, the common trilinear coupling, the ratio of the two Higgs vacuum expectation values (vevs) and the sign of the higgsino mass parameter. To scan over the CMSSM parameter space we randomly generate parameters in the following ranges: $300 < m_0$, $M_{1/2} < 10000$ GeV, $|A_0| < 5m_0$, $3 < \tan \beta < 60$, $\text{sign}(\mu) = \pm$. We use the MicrOMEGAs package [206, 208] to compute the electroweak scale sparticle mass spectrum, the Higgs boson masses, the DM relic abundance Ω_{DM} , the spin-independent DM-nucleon direct detection cross section σ_{SI} and the other observables in Table 1. In addition, we require $M_H = 125 \pm 1$ GeV. There is a few GeV theoretical uncertainty in the computation of SUSY Higgs masses in the available codes. Therefore, to select the phenomenologically acceptable parameter space we impose 3σ hard cuts for the observables in Table 1. Our approach should be regarded as an example study of the CMSSM parameter space for a heavy Higgs boson; qualitatively similar results should hold if the real Higgs boson mass deviates from 125 GeV by a few GeV. We first study the parameter space that induces correct M_H and Ω_{DM} . We discuss the implications of the $(g - 2)_\mu$ constraint later.

In Fig. 1 we present our results in scatter plots without the $(g - 2)_\mu$ constraint. In the left panel the results are presented in the $(m_0, M_{1/2})$ plane and in the right panel in the $(M_{\text{DM}}, \sigma_{\text{SI}})$ plane, where the first 100 days XENON100 constraint [196] is also shown. One can identify five

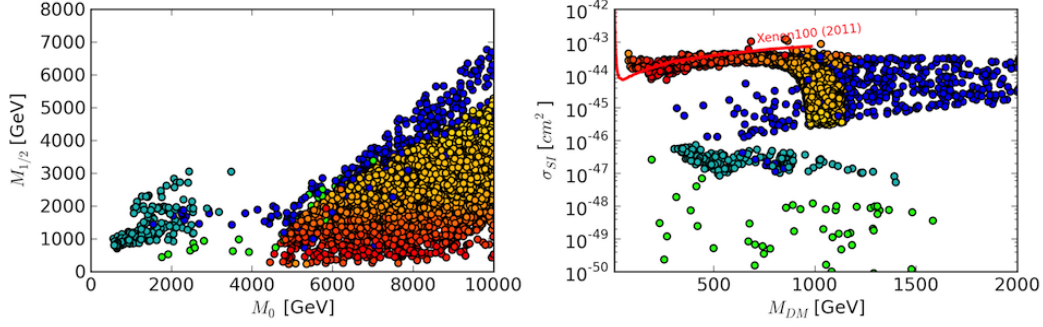


Figure 1: Points in the CMSSM parameter space yielding $M_H = 125 \pm 1$ GeV. Colours represent different dominant DM freeze-out processes. Light blue: slepton co-annihilation; green: stop co-annihilation; red to orange: well-tempered neutralino; yellow: higgsino; dark blue: heavy Higgs resonances. No $(g - 2)_\mu$ constraint is imposed.

distinctive parameter space regions according to the dominant DM annihilation processes [272].

- The light blue points with small m_0 and $M_{1/2}$ represent the slepton co-annihilation region. They feature very large values of $\tan \beta$. Those points represent the best fit value of the CMSSM [277] and have low enough sparticle masses to allow potential SUSY discovery at the LHC. However, their spin-independent direct detection cross section is predicted to be below 10^{-46} cm² and remains unobservable by XENON100. The present XENON100 experimental bound is plotted in the right panel by a solid red line. This is the only parameter region that survives at 3σ level after the $(g - 2)_\mu$ constraint is imposed.
- The green dots represent the stop co-annihilation region. Consequently those points have the lowest possible stop mass and, due to the mass degeneracy with DM, stops can be long lived and seen as stable very slow particles (R -hadrons) at the LHC. The feature of those points is an enormous trilinear coupling and very large mixing. In addition, the gluino mass can be in reach of the LHC. The spin-independent direct detection cross section is, unfortunately, unobservable.
- The dots represented by continuous colour code from red to orange represent the so called well-tempered neutralino, i.e., neutralinos with large bino-higgsino mixing. The colour varies according to the higgsino component from red (predominantly bino) to yellow (pure higgsino). Therefore those points can simultaneously have small DM mass and large DM-nucleon scattering cross sections that can be well tested by XENON100. However, apart from the DM, all other sparticle masses are predicted to be too heavy to be directly produced at the LHC.
- The yellow dots around $M_{DM} \sim 1$ TeV represent the pure higgsino DM that is almost degenerate in mass with the chargino. The sparticle mass spectrum is predicted to be even heavier than in the previous case because the DM scale is fixed to be high. These points represent the most general and most abundant bulk of the $M_H = 125$ GeV Higgs scenario – apart from the light DM and heavy Higgs boson there are no other observable consequences because stops can completely decouple. In our case the 10 TeV bound on stops is imposed only because we did not generate larger values of m_0 .
- The dark blue points represent heavy Higgs resonances. Those points are featured by

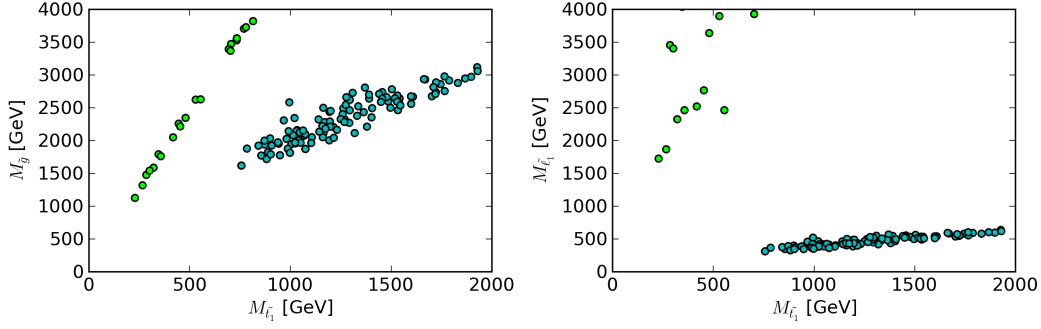


Figure 2: Scatter plots presenting correlations between physical lightest stop and gluino and lightest slepton masses.

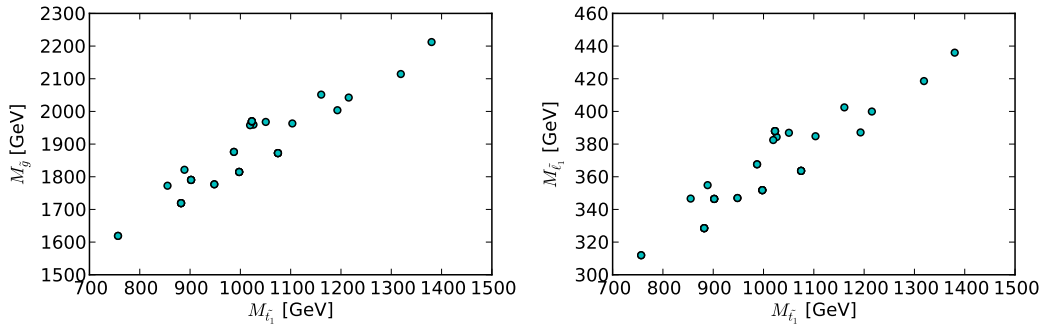


Figure 3: The same as in Fig. 2 after imposing a 3σ constraint on the $(g - 2)_\mu$ prediction.

very large values of $\tan \beta$ and give the heaviest mass spectrum. In essence those points are just smeared out higgsino points due to additional Higgs-mediated processes.

In order to study the testability of those parameter space regions at the LHC we plot in Fig. 2 the physical gluino mass against the lightest stop mass and the lightest slepton mass against the lightest stop mass. Clearly, the slepton and stop co-annihilation regions are the only two regions that are of interest for the LHC phenomenology. According to Ref. [289] particles with those masses may be discovered already at the 7 TeV LHC. Interestingly, due to the stop mass degeneracy with DM the stops can be long-lived. In this case one must search for R -hadrons at the LHC experiments.

So far we have ignored the $(g - 2)_\mu$ constraint. If we impose a hard 3σ cut on the generated parameter space, only the slepton co-annihilation region survives. The result is plotted in Fig. 3 where we repeat the content of Fig. 2 but with the additional $(g - 2)_\mu$ constraint. As expected, the observed deviation in $(g - 2)_\mu$ from the SM prediction is hard to explain in SUSY models with heavy spectrum. Therefore the two measurements, $(g - 2)_\mu$ and $M_H = 125$ GeV, are essentially in conflict in the CMSSM. The conflict is mildest in the slepton co-annihilation case because of large $\tan \beta$ and the lightest sparticle spectrum. Therefore, for the $M_H = 125$ GeV Higgs boson, we predict definite particle masses and correlations between them, shown in Fig. 3, for the LHC. If the CMSSM is realized in Nature and if it contributes significantly to $(g - 2)_\mu$, the sparticle spectrum is essentially fixed and potentially observable at the LHC.

3 DISCUSSION AND CONCLUSIONS

We studied the CMSSM by scanning over its parameter space allowing the sparticle mass parameters to be very large. We required the Higgs boson mass to be in the range 125 ± 1 GeV. The first considered case was without attempting to explain $(g-2)_\mu$ in the context of the CMSSM. We confirmed that for very large A -terms there exists a stop co-annihilation region where all DM, stop and gluino are preferably light. Due to the mass degeneracy between stop and DM the stops can be long lived resulting in non-trivial LHC phenomenology. The second parameter region that is potentially testable at the LHC is the slepton co-annihilation region. For all other cases the $M_H \approx 125$ GeV Higgs boson implies very heavy sparticle masses. The exception is, of course, the DM that can be light due to bino-higgsino mixing even if other sparticles are as heavy as 10 TeV. In this case the CMSSM cannot be tested at the LHC but there still is a chance to see the DM scattering off nuclei in the XENON100. Those results imply that from the point of view of the LHC phenomenology, the CMSSM sparticle spectrum is known and the LHC experiments should perform detailed studies of the stop and slepton co-annihilation spectra. Those, however, are the difficult ones at the LHC because of soft leptons produced in sparticle decays to the DM sparticles.

If, in addition, one attempts to explain also $(g-2)_\mu$ in this framework, there is immediate tension between the high SUSY scale and the large value of the needed $(g-2)_\mu$ contribution. We found that imposing the $(g-2)_\mu$ constraint, only the slepton co-annihilation region survived at 3σ level. In this case the CMSSM has a definite predictions of the sparticle masses and spectrum to be tested at the LHC experiments.

ACKNOWLEDGEMENTS

We thank A. Strumia for several discussions. Part of this work was performed in the Les Houches 2011 summer institute. This work was supported by the ESF grants 8090, 8499, 8943, MTT8, MTT59, MTT60, MJD140, JD164, by the recurrent financing SF0690030s09 project and by the European Union through the European Regional Development Fund.

Contribution 10

Improved vacuum stability in scalar dark matter models

M. Kadastik, K. Kannike, A. Racioppi, M. Raidal

Abstract

If the Higgs boson mass is 125 ± 1 GeV, the standard model cannot be a fundamental theory up to the GUT scale due to the vacuum stability arguments. We show that if the dark matter of the Universe consists of stable scalar particles, the vacuum stability constraints are modified and the theory can be valid up to a high scale. We argue that the present LHC data may favour such a scenario.

1 INTRODUCTION

The scalar potential of the standard model (SM) Higgs boson [290–293] is one of the best studied objects in particle physics. If the Higgs boson mass is $M_H \approx 125$ GeV as indicated by the recent experimental results by ATLAS [143] and CMS [144] experiments, the SM cannot be valid up to the Grand Unification (GUT) or Planck scales [272, 294]. For such a low Higgs boson mass its quartic self-coupling λ runs to negative values at energy scales much below the GUT scale, causing vacuum instability at higher scales Λ . This result is presented in the left panel of Fig. 1 in which the renormalization group equation running of the SM Higgs self-coupling is presented at the two loop level for different values of the Higgs mass. Consequently, the SM alone cannot be valid up to the scales required by gauge coupling unification and proton decays arguments.

On the other hand, any realistic model of new physics beyond the SM must explain the existence of dark matter (DM) in the Universe. By far the simplest extension of the SM is obtained by adding a real [295–297] or complex [298, 299] singlet scalar field to the SM scalar potential. In addition to minimality, such a SM extension is motivated by GUT arguments [299]. In those models the DM and Higgs sectors are related via the Higgs portal and the scalar potentials are in general rather complicated. Due to new self-interactions in the scalar sector, the SM Higgs quartic coupling renormalization is modified, and one might expect that the triviality $\lambda(\Lambda) = 0$ may be achieved for much higher values of Λ .

In addition to the vacuum stability arguments, the scalar DM may also be motivated by the LHC data. In the light of recent XENON100 and LHC results, this possibility has been studied in Refs. [277, 300, 301]. It was argued in Ref. [301] that the LHC data may contain indications for Higgs boson invisible decays consistent with the direct DM searches in XENON100. Thus it is necessary to study the SM-like Higgs boson properties in every possible production and decay channel.

The aim of this note is to point out that, indeed, if the DM of the Universe consists of scalar singlets, the stability of scalar potential of the model may be guaranteed up to the GUT scale even for the Higgs boson mass 125 GeV. Thus, in this case, there is no reason to introduce any intermediate scale in the theory and the known physics can be considered to be fundamental

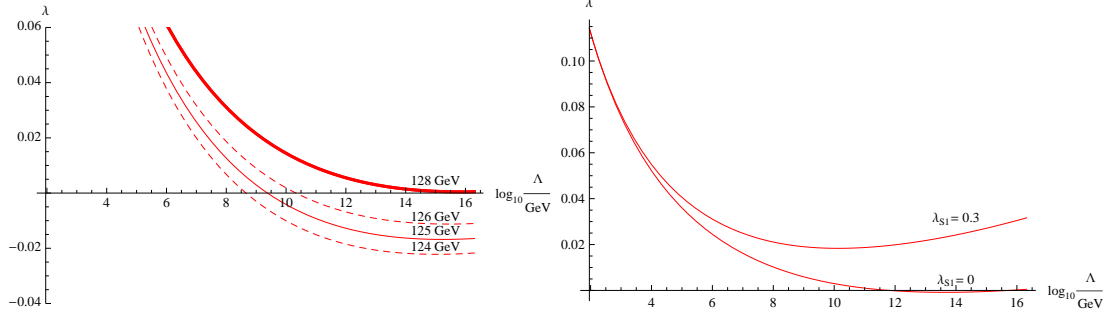


Figure 1: Left: running of the SM Higgs boson self-coupling λ for different Higgs boson masses at the two loop level. Right: running of the Higgs self-coupling in the complex singlet model for two different values of λ_{S1} at one loop level.

until Grand Unification takes over.

2 VACUUM STABILITY IN SCALAR DARK MATTER MODELS

The natural question to ask is that what happens to the vacuum stability in models with extended scalar sector? Here we study the case of complex singlet scalar $S = (S_H + iS_A)/\sqrt{2}$, but the phenomenology in the real singlet case is similar. The vacuum stability of the real singlet model has been previously studied also in [302].

Denoting the SM Higgs boson with H_1 , the most general Lagrangian invariant under the Z_2 transformations $H_1 \rightarrow H_1$, $S \rightarrow -S$ is given by

$$\begin{aligned}
 V = & \mu_1^2 H_1^\dagger H_1 + \lambda_1 (H_1^\dagger H_1)^2 + \mu_S^2 S^\dagger S + \frac{\mu_S'^2}{2} [S^2 + (S^\dagger)^2] + \lambda_S (S^\dagger S)^2 + \frac{\lambda_S'}{2} [S^4 + (S^\dagger)^4] \\
 & + \frac{\lambda_S''}{2} (S^\dagger S) [S^2 + (S^\dagger)^2] + \lambda_{S1} (S^\dagger S) (H_1^\dagger H_1) + \frac{\lambda_{S1}'}{2} (H_1^\dagger H_1) [S^2 + (S^\dagger)^2].
 \end{aligned}
 \tag{1}$$

The vacuum stability conditions for the complex singlet model with a global $U(1)$ are given in [298]. However, those conditions are not applicable here because this model is far too simple compared to the general case (1). For the general model the full vacuum stability conditions are rather complicated and have been addressed previously in Ref. [303]. However, the conditions of [303] turn out to be too restrictive because they are derived by requiring the matrix of quartic couplings to be positive. This is required only if the coefficients of biquadratic terms are negative and, in general, cut out some of the allowed parameter space. The milder conditions arising from pure quartic terms of the potential (1) are

$$\lambda_1 \geq 0, \quad \lambda_S + \lambda_S' \geq |\lambda_S''|.
 \tag{2}$$

For simplicity we consider in addition only the case that the coefficients of the terms biquadratic in real fields (*e.g.* the coefficient of $S_H^2 S_A^2$) are all non-negative, giving

$$\lambda_S - 3\lambda_S' \geq 0, \quad \lambda_{S1} - |\lambda_{S1}'| \geq 0.
 \tag{3}$$

Doing this, we exclude a part of the points that would be allowed by the full vacuum stability conditions. However, this is sufficient for our purposes because our aim is to show that regions of the parameter space exist that lower the SM Higgs boson mass vacuum stability bound.

The one-loop renormalization group equations (RGEs) can be obtained from those in [303] by setting all couplings of the inert doublet to zero. The RGEs show that nonzero λ_{S1} or λ'_{S1} give a positive contribution to the β -function of λ_1 , pushing the scale where $\lambda_1 \equiv \lambda = 0$ higher. For qualitative understanding of the model, we let $\lambda_S = \lambda'_S = \lambda''_S = \lambda'_{S1} = 0$.

In the right panel of Fig. 1 we plot the one loop level running for a 125 GeV Higgs boson quartic coupling for $\lambda_{S1} = 0$ (the SM case) and for $\lambda_{S1} = 0.3$. In the latter case, the minimum bound on the Higgs boson mass from the vacuum stability argument is lowered and the vacuum can be stable up to the GUT or Planck scale. This simple example demonstrates that the 125 GeV Higgs boson excess at the LHC may call for the extended scalar sector that simultaneously solves the vacuum stability and DM problems.

3 CONCLUSIONS

We have considered the implications of a $M_H \approx 125$ GeV Higgs boson for the vacuum stability in scalar DM models. In the SM the 125 GeV Higgs boson implies that the model cannot be consistent with the gauge coupling unification scale nor with the scale required by proton stability. We have shown here that in the case of non-SUSY scalar DM models the vacuum stability bounds are modified due to more complicated scalar potentials. Therefore, unlike the SM, the scalar DM models can be consistent models up to the GUT or Planck scales even if the present LHC excess at $M_H \approx 125$ GeV is confirmed. If this is the case Nature has chosen, the Higgs boson interactions and possibly also its branching fractions at the LHC will be modified due to the coupling to DM.

ACKNOWLEDGEMENTS

Part of this work was performed in the Les Houches 2011 summer institute. This work was supported by the ESF grants 8090, 8499, 8943, MTT8, MTT59, MTT60, MJD140, JD164, by the recurrent financing SF0690030s09 project and by the European Union through the European Regional Development Fund.

Contribution 11

Higgs boson production via new heavy vector-like top decays at the LHC

A. Azatov, O. Bondu, A. Falkowski, M. Felcini, S. Gascon-Shotkin, D. K. Ghosh, G. Moreau, A. Y. Rodríguez-Marrero, S. Sekmen

Abstract

Motivated by the recent severe constraints over a wide mass range from the direct Higgs boson searches at LHC, we first build the minimal model of vector-like quarks where the rate for the gluon fusion mechanism can be greatly suppressed. Within the obtained model, compatible with the present LHC constraints on the direct Higgs search, we demonstrate that the indirect Higgs production, $pp \rightarrow t't'$, $t' \rightarrow th$, allows to discover the Higgs boson and measure several of its possible masses through the decay channels $h \rightarrow \gamma\gamma$, $h \rightarrow WW, ZZ$. We also comment on the recent hint in LHC data from a possible ~ 125 GeV Higgs, in the presence of t' quarks.

1 INTRODUCTION

The primary issue of the present Large Hadron Collider (LHC) is certainly the direct search for the still unobserved cornerstone of the Standard Model (SM), namely the Higgs boson or any signal from alternative Electro-Weak Symmetry Breaking (EWSB) mechanisms. The SM is probably not the ultimate model of nature and it is clear that new channels for the Higgs production, that can arise in extensions of the SM, would have a profound impact on the discovery potential of the Higgs boson at the LHC. An attractive possibility is the Higgs production in decays of additional heavy colored particles as those can be copiously pair produced at the LHC via strong interactions.

Within the well-motivated theories beyond the SM, there are some candidates for such new heavy colored states, extra quarks with vector-like couplings, whose existence is predicted by most of the alternatives to supersymmetry. In this context, to maintain a naturally light Higgs boson, divergent quantum corrections from loops of the top quark are often canceled by top-partner contributions [304–306]. Let us describe important examples here. In the so-called little Higgs scenarios, the vector-like quarks arise as partners of the SM fields being promoted to larger multiplets. In composite Higgs [307–311] and composite top [307–312] models, the vector-like quarks are excited resonances of the bound states constituting the SM particles. In extra-dimensional models with (SM) quarks in the bulk, the vector-like quarks are Kaluza-Klein (KK) excitations of these bulk fields [313] like in the Gauge-Higgs unification mechanism (see e.g. Ref. [314,315]) or in the Randall-Sundrum (RS) scenario [316–318] – where some of those KK excitations, the so-called custodians, can be as light as a few hundred's of GeV [319–324]. Another example is a gauge coupling unification theory where vector-like quarks are embedded into the simplest $SU(5)$ representations [325].

Vector-like quarks with same electric charge as the up-type quarks are often called top-partners (noted t') as these new heavy states mix in general predominantly with the top quark – due to the large top mass and to the related feature that the top quark is in general more intimately connected to ultraviolet physics, like e.g. in composite Higgs models. A t' can also be called a top-partner in the sense that it is contained in the same group representation as the top quark with respect to symmetries, like the approximate global symmetry of the little Higgs models [304–306], the gauge unification symmetry [325] or the custodial symmetry of RS versions with bulk matter [319–324] (explaining the SM fermion mass hierarchies [326–340]).

At this level, one must mention that searches for direct production of vector-like quarks at the LHC have been considered from a model-independent point of view in Ref. [341–345] but also in specific frameworks such as the little Higgs models (versions sufficiently safe from EW precision constraints) [346–350] or the composite Higgs hypothesis [351, 352] and the dual RS context [314, 353–355]. These past searches focus generally on the discovery of the vector-like quarks, rather than using these extra quarks to enhance the discovery and identification potential for other unknown particles such as Higgs scalars.

In relation to Higgs detection, there exist studies utilizing the possible Higgs production through vector-like quark decays, as described in the following. Indeed, it is well known since some time [356, 357] that vector-like quark production could be a copious source of Higgs bosons (Higgs factory).

Relatively light Higgs bosons produced from the decay of top-partners can be highly boosted and good candidates for analyses based on jet substructure. This method has been applied [358] for a ~ 130 GeV Higgs decaying to $b\bar{b}$ at the 14 TeV LHC, in order to identify with good efficiency the jets from Higgs decays. In the simple model considered there, the t' is a singlet under the $SU(2)_L$ gauge group, which determines the t' couplings and its branching fractions (at tree level) for the decays into the Higgs boson and the two EW gauge bosons $t' \rightarrow th$, $t' \rightarrow tZ$, $t' \rightarrow Wb$.

The top-partner can also be singly produced which leads to different final states as compared to the pair production; because of the phase space suppression, the single production becomes competitive with the pair production at a high t' mass, depending upon the considered model (since the involved t' couplings to h , Z^0 , W^\pm are fixed by the t' quantum numbers)¹. The reconstruction of the Higgs boson produced in the t' decay, itself singly produced at the 14 TeV LHC, was studied in Ref. [359] assuming the Higgs mass known (to be 120 GeV) and focusing on the channel $h \rightarrow b\bar{b}$ – with the combinatorial background only. This was performed for a singlet t' in the “Littlest Higgs” model with the asymptotic branching ratio values of the high $m_{t'}$ regime: $B_{t' \rightarrow th} = 25\%$, $B_{t' \rightarrow tZ} = 25\%$, $B_{t' \rightarrow bW} = 50\%$ (from the EW equivalence theorem). Similarly, a vector-like colored b' state produced at the 14 TeV LHC can act as a ‘Higgs factory’ thanks to its decay $b' \rightarrow bh$. It was shown [325] that a Higgs mass reconstruction can be obtained with a limited accuracy, concentrating on the decay $h \rightarrow WW$ ($W \rightarrow l\nu$) for $m_h = 200$ GeV and assuming the $m_{b'}$ value to be deduced from a preliminary analysis based on the more appropriate channel $b' \rightarrow bZ$. Theoretically, the b' was originating from the upper component of a $SU(2)_L$ doublet so there was no channel $b' \rightarrow tW$.

Higgs mass reconstructions via t' and b' decays were also studied for the 14 TeV LHC, based on a light Higgs decaying to $b\bar{b}$ in the basic models with a unique extra t' and/or a unique extra

¹The single production becomes dominant typically around $m_{t'} \sim 700$ GeV as in the scenario with a singlet t' [344] or in little Higgs models [359].

b' [345].

In the present paper, we use the pair production and decay of a vector-like top to develop new searches of the Higgs boson at the LHC and to study other channels for the Higgs mass reconstruction like $h \rightarrow \gamma\gamma$ (diphoton) and $h \rightarrow ZZ$. The original theoretical model considered here, including two top-partners, is constructed to allow interesting interpretations correlating the indirect (via vector-like top decay) and direct Higgs production searches at the LHC, as described in the following. A few characteristic parameter sets – with vector-like top mass in the range between ~ 400 and 800 GeV – are chosen as benchmark points avoiding large t' contributions to the Higgs rates (constrained by present LHC data) and simultaneously allowing for significant branching fraction values ($> 10\%$) of the vector-like top decay to the Higgs boson. Assuming the presence at low-energy scales only of extra vector-like quark multiplets containing some t' , we have elaborated a minimal model allowing to strongly suppress the Higgs production via gluon fusion, as compared to the SM. In this simple but non-trivial model, the $gg \rightarrow h$ cross section suppression factor possibly reaches values below 10^{-1} at hadron colliders; this is to be put in contrast with the t' representations taken usually in the RS scenario [324, 360–363]² and with minimal supersymmetric theories for which such a suppression is not possible to get (see respectively Ref. [324, 360] and Ref. [163]). The chiral case of a fourth quark generation can even only increase considerably the gluon fusion rate.

The minimal t' model suggested here is interesting in the sense that it can easily lead to the following interpretation: for example, a 255 GeV Higgs is excluded in the SM by the present LHC results [367, 368] but can still exist in the above minimal SM extension with t' where the reduced Higgs production cross section can be below the LHC upper limits. In other words, the Higgs boson would really be light but not detectable with the present luminosity/energy, via conventional channels. A channel that could then allow the Higgs discovery would be through the t' pair production and decays, as illustrated in this paper. Another possible hypothesis is that an excess of events, like the recent hint in data explainable by a 125 GeV Higgs [368], would be confirmed soon at the LHC. Then the measured Higgs production cross section times branching ratios could certainly be exactly reproduced by the present t' model, given the parameter freedom in this model and its capability of inducing large Higgs rate corrections of both signs. Then investigating such a new Higgs production channel as the t' decay developed here, would of course be relevant in particular to confirm the Higgs existence. Finally, in the case of a signal from a heavy Higgs, say above 500 GeV³ as we will consider here, the same fit of Higgs data would be instructive as a test of the present t' model and similarly the t' decay should be considered as a complementary channel of Higgs production.

2 THE THEORETICAL MODEL

Let us assume the presence at low-energy scales of a unique additional vector-like quark multiplet including a t' component. Then, irrespective of the representation of this multiplet under the $SU(2)_L$ gauge group (i.e. whether the t' belongs to a singlet, doublet, . . .), the interference between the next heavier top mass eigenstate t_2 [composed of t, t', t'' , with t_1 being the SM

² t' representations (to which SM fields are promoted) with analog rate suppression effects can arise with the $O(3)$ subgroup [323] implementable in the composite Higgs model [175, 364] and RS scenario [365, 366] which can reach strong suppressions, respectively of $\sigma_{gg \rightarrow h}/\sigma_{gg \rightarrow h}^{\text{SM}} \sim 35\%$ and $\sim 10\%$.

³Such a heavy Higgs would be neither SM-like, as disfavored by the EW precision tests, nor belonging to a supersymmetric extension, as forbidden by the Higgs sector structure. However, it could perfectly be e.g. in a RS scenario where its contributions to the oblique T parameter can be compensated by new KK-induced contributions.

top quark] and the t_1 contributions ⁴ to the triangle loop of the gluon-gluon fusion mechanism will be systematically constructive. This is due to the fact that the physical sign of the Yukawa coupling and mass insertion involved in this loop – two chirality flips are necessary – will be systematically identical giving rise to a positive product (for t_1 as well as for t_2). Hence, the cross section of the gluon fusion mechanism may be increased or slightly decreased (because of a possible t Yukawa coupling reduction) relatively to the SM case.

To get the minimal scenario with only additional vector-like quark multiplet including t' components able to strongly suppress gluon fusion, one needs to introduce a first top-partner t' in a $SU(2)_L$ doublet as well as a second top-partner t'' in a singlet. In order to simplify the presentation, we do not consider the doublet including a b' ⁵ that would also be exchanged in the triangle loop. So we end up with the doublet $(q_{5/3}, t')$, $q_{5/3}$ being an exotic quark with electric charge 5/3 and without self-Yukawa coupling (thus with no contribution in the loop). Indeed, with this field content, all the possible generic mass terms and Yukawa couplings appearing in the Lagrangian are,

$$\begin{aligned} \mathcal{L}_{\text{Yuk.}} = & Y \overline{\begin{pmatrix} t \\ b \end{pmatrix}}_L H^\dagger t_R^c + Y' \overline{\begin{pmatrix} q_{5/3} \\ t' \end{pmatrix}}_L H t_R^c + Y'' \overline{\begin{pmatrix} q_{5/3} \\ t' \end{pmatrix}}_{L/R} H t''_{R/L} + \tilde{Y} \overline{\begin{pmatrix} t \\ b \end{pmatrix}}_L H^\dagger t''_R \\ & + Y_b \overline{\begin{pmatrix} t \\ b \end{pmatrix}}_L H b_R^c + m \bar{t}'_L t_R^c + m' \overline{\begin{pmatrix} q_{5/3} \\ t' \end{pmatrix}}_L \begin{pmatrix} q_{5/3} \\ t' \end{pmatrix}_R + m'' \bar{t}'_L t''_R + \text{H.c.} \end{aligned} \quad (1)$$

where H represents the SM Higgs doublet and L/R the fermion chiralities. By construction, the vector-like quarks possess the same quantum numbers for the left-handed and right-handed states. We have not written the Yukawa couplings for the first two quark generations as their mixings with the top-partners t', t'' are negligible compared to the t - t' - t'' mixing and the CKM mixing angles are typically small, so that the first two quark generations are decoupled from b, t, t', t'' . Note that a field redefinition rotating t_R^c and t''_R can allow to eliminate the m term without loss of generality. A last remark is that the Y'' term could be split in two terms with different chiralities and coupling constants. The Lagrangian (1) gives rise, after EWSB, to this top mass matrix:

$$\mathcal{L}_{\text{mass}} = \overline{\begin{pmatrix} t \\ t' \\ t'' \end{pmatrix}}_L \begin{pmatrix} Yv & 0 & \tilde{Y}v \\ Y'v & m' & Y''v \\ m & Y''v & m'' \end{pmatrix} \begin{pmatrix} t^c \\ t' \\ t'' \end{pmatrix}_R + \text{H.c.} \quad (2)$$

with $v \simeq 174$ GeV the SM vacuum expectation value of the Higgs boson. In our notations of Eq.(2), the parameters Y, Y', Y'' and \tilde{Y} contain the whole sign (i.e. the combination of the $SU(2)_L$ contraction signs and Yukawa coupling constant signs). Note that vector-like fermions do not require EWSB to acquire mass. The non-trivial consequence of the present t', t'' charge assignment choice is the presence of Yukawa terms in the block diagonal matrix of Eq.(2) associated to the top-partners ⁶ (such Yukawa matrix elements would be absent in the first case of a unique top-partner). This feature of the mass structure allows for a strong suppressions of the gluon fusion mechanism. In particular, the own top-partner (t', t'') Yukawa coupling (Y'') sign can be chosen independently of the top (t) Yukawa coupling (Y) sign in order to generate a destructive interference between the top and top-partner loops.

⁴The top quark exchange in the loop is the dominant contribution in the SM.

⁵Similar results are expected in such a situation.

⁶Namely the last two lines and columns of this mass matrix.

3 t_2 RATES AND DIRECT CONSTRAINTS

We consider the model described in the previous section and concentrate on the phenomenology of the lighter top eigenstate t_2 ; the t_3 eigenstate production is subdominant given its higher mass. In a second stage, one should add the contributions to the Higgs production from the t_3 decays like $t_3 \rightarrow t_1 h$ or $t_3 \rightarrow t_2 Z$.

In Table 1, we define our benchmark points by the values of the fundamental parameters – including the Higgs mass – and the corresponding m_{t_2}, m_{t_3} values. Those sets of parameters are selected in particular to have large $B_{t_2 \rightarrow t_1 h}$ increasing the studied Higgs signal. Note that in the pure model with a unique doublet $(q_{5/3}, t')$, $B_{t_2 \rightarrow bW}$ is negligible compared to $B_{t_2 \rightarrow t_1 h}$ and $B_{t_2 \rightarrow t_1 Z}$ [345]. For none of the considered benchmark points, the channel $t_2 \rightarrow q_{5/3} W$ is open. The table also provides the theoretical t_2 widths and the $\sigma_{\bar{t}_2 t_2}$ cross sections for the t_2 pair production at LHC computed with the HATHOR program [369] at NNLO. As a comparison, we give in Table 1 the expected SM cross sections [370] for Higgs production via gluon fusion $\sigma_{gg \rightarrow h}^{\text{SM}}$. It is physically important to note that the branching ratios $B_{t_2 \rightarrow t_1 h}$ and $B_{t_2 \rightarrow t_1 Z}$ are non-vanishing in contrast with the case of a fourth generation t' quark so that the observation of such decays (discussed in Section 6) would even prove the vector-like nature of the t' quarks.

The table presents finally the CMS constraints on the observables $\sigma_{\bar{t}_2 t_2} B_{t_2}^2$ derived from the search for pair production of a heavy top-like quark [258, 367, 371] (present bounds from ATLAS are obtained with a lower integrated luminosity, 37 pb^{-1} , and are thus less stringent [368]). It appears that the corresponding theoretical values, predicted in the models considered here, respect those experimental limits for m_{t_2} as low as $\sim 400 \text{ GeV}$ ⁷. Increasing theoretically $B_{t_2 \rightarrow t_1 h}$ goes in the direction of reducing these constraints.

Due to these lower constraints on m_{t_2} typically around 400 GeV, the t_2 pair production suffers from a significant phase space suppression so that the whole rate for a single Higgs production through the t_2 decay is smaller than for the usual gluon fusion mechanism; there is e.g. a factor of ~ 10 for the point A at 14 TeV as shown the Table 1. However, the number of Higgs events coming from the t_2 decay can be significant at high LHC luminosities; this Higgs production channel can thus be interesting and especially in the case where the gluon fusion mechanism is strongly suppressed by the presence of t', t'' states, as occurs for instance with the point B (see all the rates at 14 TeV in the table).

4 CONSTRAINTS FROM DIRECT HIGGS BOSON SEARCHES

Set A - At $m_h = 125 \text{ GeV}$, all the sensitive channels for searching the Higgs boson at hadron colliders are the decays $h \rightarrow \gamma\gamma$, $h \rightarrow WW$ (with $W \rightarrow \ell\nu$), $h \rightarrow ZZ$ (with $Z \rightarrow \ell\bar{\ell}$), $h \rightarrow \tau\bar{\tau}$ and $h \rightarrow b\bar{b}$. The latest bounds on the Higgs boson rates obtained at the LHC read as, $\sigma_{gg \rightarrow h} B_{h \rightarrow \gamma\gamma} / \sigma_{gg \rightarrow h}^{\text{SM}} B_{h \rightarrow \gamma\gamma}^{\text{SM}} < 2$ [367], $\sigma_{gg \rightarrow h} B_{h \rightarrow WW} / \sigma_{gg \rightarrow h}^{\text{SM}} B_{h \rightarrow WW}^{\text{SM}} < 1.3$ [367], $\sigma_{gg \rightarrow h} B_{h \rightarrow ZZ} / \sigma_{gg \rightarrow h}^{\text{SM}} B_{h \rightarrow ZZ}^{\text{SM}} < 2.2$ [367], $\sigma_{gg \rightarrow h} B_{h \rightarrow \tau\tau} / \sigma_{gg \rightarrow h}^{\text{SM}} B_{h \rightarrow \tau\tau}^{\text{SM}} < 3.2$ [367] and $\sigma_{gg \rightarrow h} B_{h \rightarrow b\bar{b}} / \sigma_{gg \rightarrow h}^{\text{SM}} B_{h \rightarrow b\bar{b}}^{\text{SM}} < 5$ [367]. These bounds are compatible with the rates calculated taking into account the $t - t' - t''$ mixing effect on the top quark Yukawa coupling as well as the t_2 and t_3 eigenstate contributions in the triangular loop of the gluon fusion mechanism, for our parameter set A. This parameter set yields indeed:

$$\sigma_{gg \rightarrow h}^t B_{h \rightarrow \gamma\gamma}^t / \sigma_{gg \rightarrow h}^{\text{SM}} B_{h \rightarrow \gamma\gamma}^{\text{SM}} = 1.16 \ ; \ \sigma_{gg \rightarrow h}^t B_{h \rightarrow WW}^t / \sigma_{gg \rightarrow h}^{\text{SM}} B_{h \rightarrow WW}^{\text{SM}} = 1.25 \ [A] \quad (3)$$

$$\sigma_{gg \rightarrow h}^t B_{h \rightarrow ZZ}^t / \sigma_{gg \rightarrow h}^{\text{SM}} B_{h \rightarrow ZZ}^{\text{SM}} = 1.25 \ ; \ \sigma_{gg \rightarrow h}^t B_{h \rightarrow \tau\tau}^t / \sigma_{gg \rightarrow h}^{\text{SM}} B_{h \rightarrow \tau\tau}^{\text{SM}} = 1.25 \ [A] \quad (4)$$

⁷We have also checked that the Tevatron constraints are satisfied.

Parameter Set	A	B	C	D
Y / \bar{Y}	-1.43 / 2	1.15 / 0.4	1.12 / -0.5	1.05 / -0.3
Y' / Y''	1.85 / -1	-1.5 / 1.6	1.1 / 1.65	1.7 / 1.9
$m / m' \text{ (GeV)}$	0 / 370	0 / 770	0 / 810	80 / 1100
$m'' \text{ (GeV)}$	510	980	850	1100
$m_{t_3} \text{ (GeV)}$	722	1181	1125	1454
$m_{t_2} \text{ (GeV)}$	403	626	572	788
$m_h \text{ (GeV)}$	125	255	320	540
$\sigma_{gg \rightarrow h}^{\text{NNLO}} \text{ (pb) @ 7 TeV}$	15.31	3.18	2.25	0.58
$\sigma_{gg \rightarrow h}^{\text{NNLO}} \text{ (pb) @ 14 TeV}$	49.85	13.50	10.59	3.85
$\sigma_{gg \rightarrow h}^{t'}/\sigma_{gg \rightarrow h}^{\text{SM}}$	1.27	0.45	0.40	0.65
$\sigma_{\bar{t}_1 t_1 h}^{\text{NLO}} \text{ (pb) @ 7 TeV}$	0.0194	0.0037	0.0016	$7 \cdot 10^{-4}$
$\sigma_{\bar{t}_1 t_1 h}^{\text{NLO}} \text{ (pb) @ 14 TeV}$	0.138	0.036	0.021	0.015
$\sigma_{\bar{t}_2 t_2}^{\text{NNLO}} \text{ (pb) @ 7 TeV}$	1.361	0.0709	0.136	0.0115
$\sigma_{\bar{t}_2 t_2}^{\text{NNLO}} \text{ (pb) @ 14 TeV}$	13.53	1.164	1.975	0.284
$B_{t_2 \rightarrow t_1 h} \text{ (%)}$	62.6	60.8	13.5	43.0
$B_{t_2 \rightarrow t_1 Z} \text{ (%)}$	28.6	25.0	46.1	40.3
$B_{t_2 \rightarrow bW} \text{ (%)}$	8.8	14.2	40.4	16.6
$\Gamma_{t_2} \text{ (GeV)}$	4.4	19.8	6.5	8.8
$\sigma_{\bar{t}_2 t_2} B_{t_2 \rightarrow bW}^2 \text{ (pb)}$	0.01	0.001	0.022	0.000(3)
LHC bound	< 0.6	×	< 0.597	×
$\sigma_{\bar{t}_2 t_2} B_{t_2 \rightarrow t_1 Z}^2 \text{ (pb)}$	0.11	0.004	0.029	0.002
LHC bound	< 0.45	×	×	×
S / T	0.05 / 0.05	-0.01 / 0.23	-0.01 / 0.30	-0.01 / 0.28

Table 1: Cross sections for the t_2 pair production at the 7 TeV and 14 TeV LHC together with the t_2 widths Γ_{t_2} and branching ratios, for characteristic sets of the parameters [with the induced m_{t_2} , m_{t_3} values]. The LHC upper limits and theoretical predictions for the observables $\sigma_{\bar{t}_2 t_2} B_{t_2 \rightarrow bW}^2$, $\sigma_{\bar{t}_2 t_2} B_{t_2 \rightarrow t_1 Z}^2$ are shown just above the last line (the crosses indicate the absence of experimental limit at the associated m_{t_2} values). In the last line are given the oblique parameters S and T [after subtraction of the SM contributions so that those only include new physics effects]. For the point A, we have used the indicated Y'' value for the t'_R coupling and $Y'' = -0.3$ for the t'_L vertex. Finally, we give the cross section in the $t^{(\prime)}$ model for the $\bar{t}_1 t_1 h$ production which is the subleading reaction able to contribute to the studied signal with tops in the final state (Higgs production in t_2 decays), given our cuts on the selected events. For comparison, we present the cross sections for the main gluon fusion mechanism of Higgs production at LHC in the SM at NNLO, as well as the ratio with the rate in our scenario.

$$\sigma_{gg \rightarrow h}^{t'} B_{h \rightarrow bb}^{t'} / \sigma_{gg \rightarrow h}^{\text{SM}} B_{h \rightarrow bb}^{\text{SM}} = 1.25 [A] \quad (5)$$

The cross section for the Higgs production is enhanced,

$$\sigma_{gg \rightarrow h}^{t'} / \sigma_{gg \rightarrow h}^{\text{SM}} = 1.27 [A],$$

due to the combination of two possible effects: the increase of the t_1 Yukawa coupling and the constructive interferences between the t_1 contribution and the t_2 , t_3 ones. In contrast, the

branching ratio for the decay channel into diphoton is slightly decreased,

$$B_{h \rightarrow \gamma\gamma}^{t'}/B_{h \rightarrow \gamma\gamma}^{\text{SM}} = 0.91 [A].$$

But the resulting product $\sigma_{\text{gg} \rightarrow h}^{t'} B_{h \rightarrow \gamma\gamma}^{t'}$ is increased relatively to the SM case as shown in Eq.(3). Such parameters might reproduce the excesses in the $\gamma\gamma$, ZZ and WW channels observed by the ATLAS [368] and CMS [367]) Collaborations. In particular, it is interesting to note that the present theoretical model allows for either an increase of $\sigma_{\text{gg} \rightarrow h}^{t'}$ compared to the SM, as here, or a decrease as with the following parameter sets.

Sets **B,C** - For these sets of parameters where $m_h = 255$ GeV or 320 GeV, all the Higgs decays have negligible widths relatively to the dominant channels $h \rightarrow ZZ$ and $h \rightarrow WW$, as in the SM case. Hence the branching ratios $B_{h \rightarrow ZZ}$ and $B_{h \rightarrow WW}$ remain unchanged in the present model with vector-like top quarks where only the decay widths for $h \rightarrow gg$, $h \rightarrow \gamma\gamma$ and $h \rightarrow \gamma Z$ are modified. As a consequence, the experimental limits on $\sigma_{\text{gg} \rightarrow h}/\sigma_{\text{gg} \rightarrow h}^{\text{SM}} < 0.50$ (0.40) [for $m_h \simeq 255$ (320) GeV] issued from the LHC combined investigations using the $h \rightarrow ZZ, WW$ channels exclusively [367,368] can be applied directly to our framework where one gets

$$\sigma_{\text{gg} \rightarrow h}^{t'}/\sigma_{\text{gg} \rightarrow h}^{\text{SM}} = 0.45 [B] ; 0.40 [C] \quad (6)$$

which does not conflict with the above LHC limits.

Note that for the point C, $\sigma_{\text{gg} \rightarrow h}^{t'}$ is strongly reduced compared to SM. A factor 1/10 could even be achieved in the present theoretical model but variants of the multiplet choice (non-minimal in term of field content), allowing coupling correction cancellations, should then be used instead to pass the indirect constraints discussed in Section 5

Set **D** - For $m_h = 540$ GeV, the Higgs boson is searched only through its decays into ZZ and WW . The strongest bounds on the Higgs rates from the LHC read as

$\sigma_{\text{gg} \rightarrow h} B_{h \rightarrow ZZ}/\sigma_{\text{gg} \rightarrow h}^{\text{SM}} B_{h \rightarrow ZZ}^{\text{SM}} < 1$ [367] and $\sigma_{\text{gg} \rightarrow h} B_{h \rightarrow WW}/\sigma_{\text{gg} \rightarrow h}^{\text{SM}} B_{h \rightarrow WW}^{\text{SM}} < 1.6$ [367]. These upper limits are clearly in good agreement with the rates calculated in the presence of the t' and t'' states (that modifies $B_{h \rightarrow t\bar{t}}$) for the set D, namely,

$$\sigma_{\text{gg} \rightarrow h}^{t'} B_{h \rightarrow ZZ}^{t'}/\sigma_{\text{gg} \rightarrow h}^{\text{SM}} B_{h \rightarrow ZZ}^{\text{SM}} = 0.69 \quad \sigma_{\text{gg} \rightarrow h}^{t'} B_{h \rightarrow WW}^{t'}/\sigma_{\text{gg} \rightarrow h}^{\text{SM}} B_{h \rightarrow WW}^{\text{SM}} = 0.69 \quad (7)$$

where

$$B_{h \rightarrow ZZ}^{t'}/B_{h \rightarrow ZZ}^{\text{SM}} = 1.06 \quad B_{h \rightarrow WW}^{t'}/B_{h \rightarrow WW}^{\text{SM}} = 1.06 [D].$$

5 INDIRECT CONSTRAINTS AND OBLIQUE PARAMETERS

Given the absence of a precise measurement for the $Zt\bar{t}$ vertex (coupling directly modified by the $t - t' - t''$ mixing), the main indirect constraints to the present model come from the corrections to the gauge boson vacuum polarizations induced by the loops of $q_{5/3}, t', t''$ states. The values of the oblique parameters S, T that we obtain, according to the preliminary calculations of Ref. [372,373], are given in Table 1. They appear to belong to the 1σ regions induced by the long list of EW precision observables measured mainly at the LEP collider [44].

Let us remark that the input parameters of Table 1 (i.e. the theoretical values in the first four lines) have been chosen to fix a panel of characteristic benchmark points for m_{t_2} that pass the indirect constraints as well as the bounds from direct Higgs search described in previous section; however those two types of constraints allow large domains of the parameter space (varying also m_h). The precise setting of the Y coupling reflects mainly the experimental precision on the top quark mass measurement (and not any fine-tuning).

The t' , t'' states could contribute to Flavor Changing Neutral Current (FCNC) reactions which are experimentally well constrained; from the theoretical point of view, these FCNC contributions rely precisely on the whole set of Yukawa coupling constants for the entire quark sector. The treatment of such an high degree of freedom in the parameter space is beyond the scope of the present study.

Finally, given the relative heavyness of the t_2 quark, we have checked that the predicted value for the V_{tb} CKM matrix element is in agreement with the experimental measurement close to unity obtained (without assuming 3×3 unitarity) through the single top quark production cross section at Tevatron [44].

6 HIGGS SIGNAL RECONSTRUCTION IN $t_2\bar{t}_2 \rightarrow th + X$ EVENTS

We have studied the sensitivity, at the 14 TeV LHC, of a search for $pp \rightarrow t_2\bar{t}_2$ production, with one of the t_2 decaying to th , and the other decaying to Wb or tZ or th , resulting into $thWb$, $thtZ$ and $thth$ final states, respectively. For the signal event generation, we have implemented the couplings of the afore described t_2 model in FeynRules [6]⁸ interfaced with MadGRAPH [374] for the *Monte Carlo* generation, PYTHIA [116] for the hadronization part and DELPHES [375] for the fast simulation of the CMS detector response. The main backgrounds were generated with ALPGEN [376] interfaced to PYTHIA and DELPHES, as for the signal events. Physics objects used for the analysis (photons, leptons and jets) were defined emulating the requirements used in real CMS Higgs searches in the 2011 data [367]. Reconstructed jets and leptons (electrons or muons) are required to have a transverse momentum larger than 30 GeV, while for photons a transverse momentum lower cut of 20 GeV is applied. In particular, we followed closely the physics object definition and selection cuts used for the real data 7 TeV Higgs analysis in the diphoton channel [377] and in the four lepton channel [378]. We did not attempt to do a dedicated cut optimization for the 14 TeV signals of interest, in order to be able to extrapolate reliably some measured background rejection factors (in particular for the high cross-section background processes, such as diphoton plus jets and $t\bar{t}$ plus jets) from 7 TeV, where experimental measurements are available, to the 14 TeV case, where we only dispose so far of limited statistics MC samples.

6.1 Search for $th + Wb/tZ/th$ signal in the diphoton plus multijets channel

To study the sensitivity of a search for $thtZ$, $thWb$ and $thth$ final states, when the Higgs is relatively light, as for point A with $m_h = 125$ GeV, we exploit the $h \rightarrow \gamma\gamma$ decay channel. As for a relatively light Higgs in the SM, in spite of the relatively small expected $B(h \rightarrow \gamma\gamma)$ value, this is expected to be a channel with very good sensitivity (high signal-over-background ratio), due to the excellent diphoton mass resolution, that allows to identify the Higgs mass signal over a background that can be precisely measured in the side-bands.

In our analysis, photon identification and isolation requirements are applied that emulate the photon selection used in the CMS search for the SM Higgs boson to diphoton final states [377]. Signals from $th + tZ/Wb/th$, $h \rightarrow \gamma\gamma$, final states are characterized by large number of energetic jets, from top and heavy vector boson decays, in addition to the two photons from the Higgs decay. Thus, we apply also a requirement on the minimum number of jets. The numbers of events expected for the signal and the backgrounds, after diphoton selection

⁸We thank Claude Duhr and Benjamin Fuks for their precious help in this implementation.

and the requirements of more than 6 or 8 jets, are given in Table 2. The background contributions considered for this study are from physics processes where a real photon pair is produced. Background from fake photons is not included. Based on preliminary studies with real data at 7 TeV, it is expected that for the selection requirement proposed here, in particular the large jet multiplicity and the diphoton mass cut, the background from fake photons plus multijets contributes a small fraction of the total background.

Signal (point A)	$\sigma \times B$ (fb)	$N(> 6 \text{ jets})$	$N(> 8 \text{ jets})$	$N(115 \text{ GeV} < m^{\gamma\gamma} < 135 \text{ GeV})$
$thbW, h \rightarrow \gamma\gamma$	3.1	4.0	1.4	1.1
$thtZ, h \rightarrow \gamma\gamma$	10.1	12.5	6.2	5.1
$thth, h \rightarrow \gamma\gamma$	22.1	13.5	7.3	5.8
Background	σ (fb)	$N(> 6 \text{ jets})$	$N(> 8 \text{ jets})$	$N(115 \text{ GeV} < m^{\gamma\gamma} < 135 \text{ GeV})$
$W + \gamma\gamma + \text{jets}$	450	110	20.0	4.0
$t\bar{t} + \gamma\gamma + \text{jets}$	15.5	11.0	8.0	1.2
$t\bar{t}W + \gamma\gamma + \text{jets}$	0.0678	0.05	0.03	0.0020

Table 2: Search for $thbW$, $thtZ$ and $thth$ final states, with $h \rightarrow \gamma\gamma$, in events with two photons plus multijets, at the 14 TeV LHC. The number of produced signal events, per fb^{-1} of integrated luminosity, is given as $\sigma \times B$ (fb), for the signals final states and for benchmark point A (see Table 1), while for the backgrounds of interest, the cross-sections σ are given. The additional columns show the number of expected events, in 20 fb^{-1} at 14 TeV, for the signal final states, compared to the contributions from background processes, after requiring two high transverse momentum, isolated photons, high jet multiplicity and the diphoton invariant mass to be in a 20 GeV window around the generated Higgs mass value of 125 GeV.

In virtue of the good diphoton mass resolution (1-2% for a 110 to 130 GeV Higgs) of the detector, the best discriminating quantity after selection is the reconstructed diphoton mass. The diphoton invariant mass distribution for signal and background events, after the requirement on the number of jets to be larger than six or eight, is shown in Figure 1. The number of events with more than eight jets, with a diphoton mass in the window between 115 GeV and 135 GeV, is also given in Table 2. We estimate that for an integrated luminosity of 20 fb^{-1} , a signal, corresponding to the point A benchmark, is detectable with a significance $S/\sqrt{B} \sim 5$.

6.2 Search for $th + Wb/tZ/th$ signal in the four leptons plus multijets channel

In order to study the sensitivity of a search for $thWb$, $thtZ$ and $thth$ final states, when the Higgs boson is relatively heavy, as expected for the points B, C and D, with $m_h = 225, 320, 540 \text{ GeV}$, respectively, we exploit the decay channel into four charged leptons $h \rightarrow ZZ \rightarrow 4l$. Lepton identification and isolation requirements are applied to emulate the lepton selection used in the CMS search for the SM Higgs boson to four lepton final states [378].

The numbers of events expected after the four lepton requirement, as well as after the additional requirement of a number of jets above 5, are shown for signal and backgrounds in Table 3. The main background is provided by the $t\bar{t}$ +jets process, because of its huge cross-section. The requirement of four high momentum, isolated leptons reduces this background by several orders of magnitude, as shown in Table 3, where a reduction factor due to four lepton requirements is applied, as measured in real data at 7 TeV for the SM Higgs search in the four lepton channel [378].

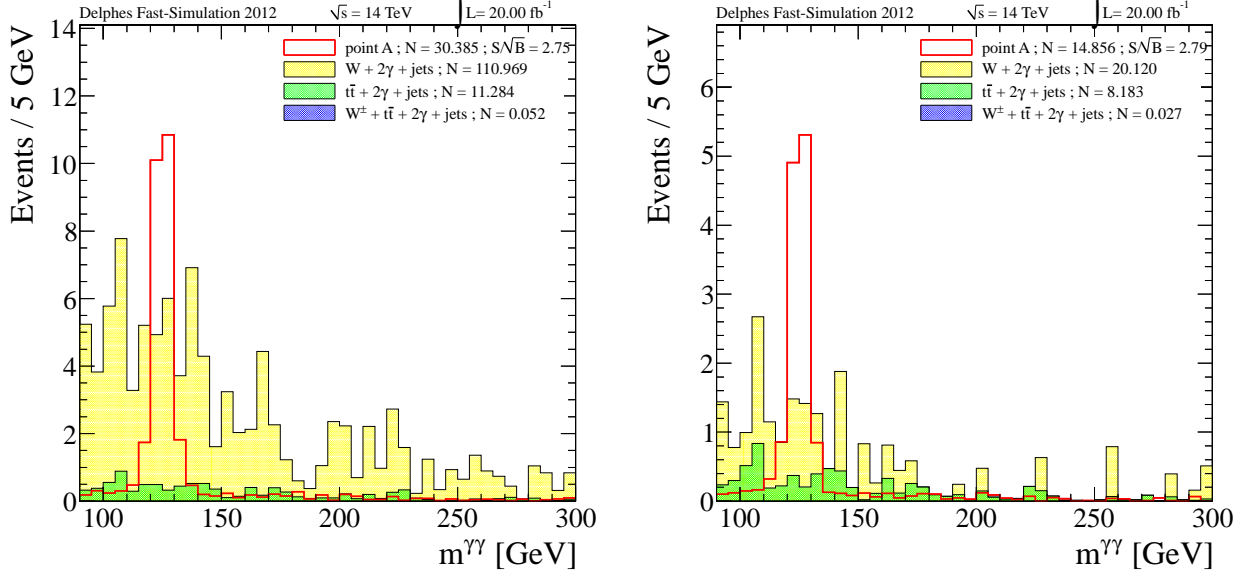


Figure 1: Reconstructed diphoton mass $m^{\gamma\gamma}$ for simulated events at 14 TeV, for the sum of the contributions from $thbW$, $thtZ$ and $thth$, $h \rightarrow \gamma\gamma$, signal final states (point A, see Table 1) compared to the sum of contributions from background processes, after requiring in the simulated events at least two high transverse momentum, isolated photons and more than 6 jets, left panel, or more than 8 jets, right panel. Event numbers are normalized to 20 fb^{-1} of integrated luminosity according to the expected production cross-section times branching fraction values given in Table 2.

Process	$\sigma \times B$ (fb)	$N(4l)$	$N(> 5 \text{ jets})$	$N(m^{4l} > 200 \text{ GeV})$
Signal	$thbW/thtZ/thth$ $h \rightarrow ZZ$	$thbW/thtZ/thth$ $h \rightarrow ZZ$	$thbW/thtZ/thth$ $h \rightarrow ZZ$	$thbW/thtZ/thth$ $h \rightarrow ZZ$
Point B	59.9 / 105 / 256	9.0 / 26.2 / 47.4	4.5 / 15.1 / 29.0	2.9 / 10.6 / 19.2
Point C	66.6 / 76.0 / 22.2	8.7 / 17.5 / 3.9	4.1 / 10.1 / 2.4	2.5 / 6.9 / 1.5
Point D	10.7 / 26.1 / 27.8	1.6 / 7.0 / 5.7	0.8 / 4.1 / 3.5	0.6 / 3.1 / 2.5
Background	$\sigma(\text{fb})$	$N(4l)$	$N(> 5 \text{ jets})$	$N(m^{4l} > 200 \text{ GeV})$
$t\bar{t} + \text{jets}$	$920 \cdot 10^3$	22.2	8.5	2.7
$t\bar{t}W + \text{jets}$	90	<1	<1	<1

Table 3: Search for $thbW$, $thtZ$ and $thth$ final states, with $h \rightarrow ZZ$, in events with four leptons plus multijets, at the 14 TeV LHC. The number of produced events, per fb^{-1} of integrated luminosity, is given as $\sigma \times B$ (fb), for the signals final states, for benchmark points B, C, D (see Table 1), while for the backgrounds of interest, the cross-sections σ are given. The additional columns show the number of expected events, in 20 fb^{-1} at 14 TeV, for the signal final states, compared to the contribution from background processes, after requiring four high transverse momentum, isolated leptons, $N(4l)$, more than five high p_T jets, $N(> 5 \text{ jets})$, and the four lepton mass to be larger than 200 GeV, $N(m^{4l} > 200 \text{ GeV})$.

The distributions of the four lepton invariant mass, m^{4l} , for signal and background events, after the requirement on the number of jets to be larger than five, are shown in Figure 2. The number of events in these distributions are normalized to an integrated luminosity of 20 fb^{-1} using the signal cross sections and final state branching ratios expected for the specific benchmark scenarios (B, C and D), detailed in Table 1. The m^{4l} signal distributions are shown separately for the sum of the normalized contributions from the different final states, $thbW$, $thtZ$, $thth$, as well as for the individual normalized contributions. We also note from the distributions given independently for each final state that all of the three final states can lead to a Higgs discovery, thanks to the good experimental resolution of the $h \rightarrow ZZ \rightarrow 4l$ mass reconstruction. Signal events, with reconstructed mass significantly lower, or higher, than the generated Higgs mass value, are in general events where one lepton from the $h \rightarrow ZZ \rightarrow 4l$ decay does not pass the lepton selection criteria, while another lepton from an accompanying W or Z decays is selected to reconstruct the four lepton mass. The background, mainly from the $t\bar{t}$ + jets process, is mostly concentrated in the m^{4l} region below 200 GeV. Applying a cut $m^{4l} > 200 \text{ GeV}$ removes a large fraction of the background and improves the signal significance, as shown in Table 3. We estimate that, for an integrated luminosity of 20 fb^{-1} , a signal, corresponding to the B and C benchmark scenarios, is detectable with significance $S/\sqrt{B} \gtrsim 5$, after the simple selection cuts described above. About a factor of two larger integrate luminosity, or a more performant analysis, would be needed for a five sigma detection of a signal corresponding to the D scenario, with a t_2 mass of about 800 GeV and a pair production cross section of about 0.3 pb.

7 CONCLUSIONS

8 CONCLUSIONS

We have shown that there exist regions of parameter space in beyond SM scenarios, allowed by present phenomenological and experimental constraints, in particular from the direct Higgs searches, where vector-like top partner production at the LHC may give rise to new Higgs production channels, over a large Higgs mass range, extending from 120 GeV to more than 500 GeV. Indeed the SM Higgs mass exclusion, in the range between 130 and 600 GeV, does not hold in these beyond SM scenarios. We have shown that for some relevant characteristic top-partner and Higgs mass values, the expected production cross sections and decay branching ratios lead to a signal of Higgs production, from the decay of vector-like top-partners, which is detectable at the 14 TeV LHC over a large Higgs mass range (125-540 GeV) using the diphoton and four lepton mass distributions. The Higgs mass peak arising in those distributions can be reconstructed with a good mass resolution ($\sim 1\text{-}2\%$). Further studies [379] are in progress to fully explore the discovery potential of the LHC in these scenarios.

ACKNOWLEDGEMENTS

The authors would like to thank ‘Les Houches’ School for hospitality offered and the organizers of this Workshop (fruitful as always) during which the work contained herein was initiated. D.K.G. acknowledges partial support from the Department of Science and Technology, India under the grant SR/S2/HEP-12/2006.

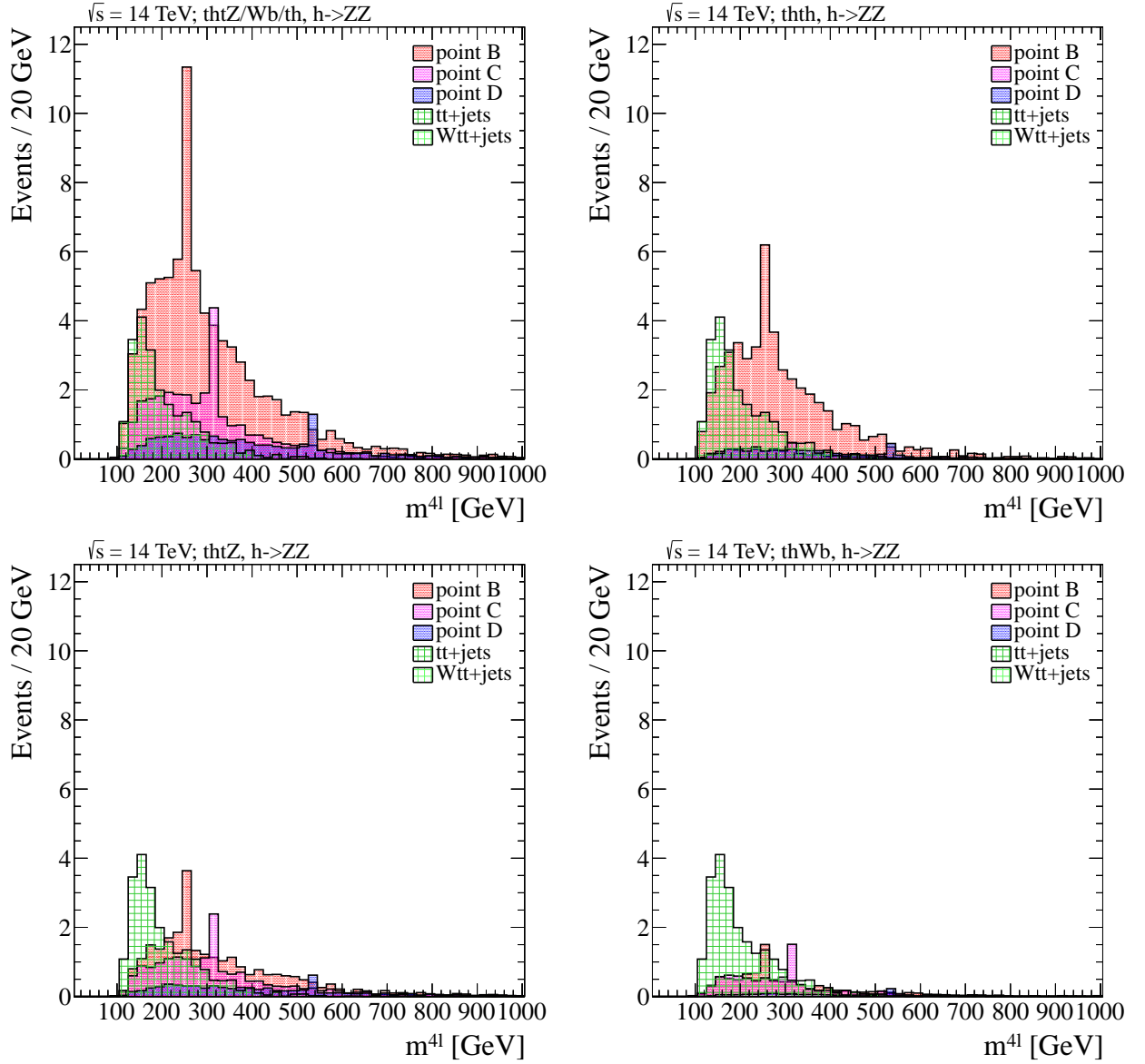


Figure 2: Reconstructed four lepton mass, m^{4l} , for simulated events at 14 TeV, for the sum of the contributions from $thbW$, $thtZ$ and $thth$, $h \rightarrow ZZ$, signal final states (points B, C, D, see Table 1) compared to the sum of the contributions from background processes, after requiring four high transverse momentum, isolated leptons and high jet multiplicity. Event numbers are normalized to 20 fb^{-1} of integrated luminosity according to the expected production cross section times branching fraction values given in the Table 1. The reconstructed four lepton invariant mass distributions, for three different Higgs mass values, $m_h = 255, 320, 540 \text{ GeV}$, are shown summed over the three signal final states (top left right hand side panel) and separately for each signal final state.

Contribution 12

Composite Higgs Models and the $t\bar{t}H$ Channel

Abstract

Despite its suppressed couplings to Standard Model particles, a composite Higgs with mass $m_H = 125$ GeV and a moderate degree of compositeness can be consistent with current Higgs searches, including a sizable enhancement in the $H \rightarrow \gamma\gamma$ channel. Heavy resonances common to many composite Higgs models can mediate new Higgs production mechanisms. In particular, the $t\bar{t}H$ channel can be accessible at the LHC in these models through the exchange of colored vector and fermion resonances. In this case, the $t\bar{t}H$ channel is not a direct measure of the top Yukawa coupling.

1 INTRODUCTION

Composite Higgs models [380, 381] are arguably among the best motivated models of natural electroweak symmetry breaking. Despite the expected presence new strongly coupled resonances, current LHC searches have not significantly constrained the parameter space of composite Higgs models. The main reason is that precision electroweak and flavor constraints already require a moderate degree of compositeness and relatively heavy, $M \geq 2$ TeV, new resonances, beyond the reach of current searches (for a summary see [382] and references there in). Proper tests of the composite nature of the Higgs, based on longitudinal gauge boson and Higgs scattering, will require even more energy or luminosity to have any discriminating power (see for instance [383]). Thus, it makes sense to investigate whether the tremendous effort that is being put on the search for the Higgs can give us information on the composite sector. Indeed, current Higgs searches are beginning to constraint some of the parameter space of the simplest composite Higgs models [364, 384–387]. In this note we argue that the “Higgs effort” the LHC community is going through could give valuable information on other aspects of the composite sector not directly related to the Higgs itself. In particular, new vector and fermion resonances are typically present in these models. New color-octet vector resonances can be produced with a sizable cross section and predominantly decay into a Standard Model (SM) quark and a new fermionic resonance, The latter will decay, with a relatively large branching ratio, into a SM quark and the Higgs. This is a new source of Higgs bosons in composite models that can give information not only on the Higgs itself but also on other composite states, like the color-octet vector and the fermion resonances. Note that this mechanism is intrinsically different to previous studies of new vector-like quark pair production (through their QCD interactions) followed by Higgs decays as discussed elsewhere in these proceedings. In our case, the presence of an intermediate resonance with relatively large couplings and the reduced phase space suppression due to single production allow us to investigate much higher energies and new sectors of the theory.

In this note we consider the minimal composite Higgs model, based on an $SO(5)/SO(4)$ symmetry breaking pattern, with composite fermionic matter transforming on the vector repre-

sensation of $SO(5)$ (MCMH₅ [308, 310, 323]). We take as an example a composite Higgs mass of 125 GeV with a moderate degree of compositeness and focus on the $t\bar{t}H$ channel. Despite the suppressed tree-level Higgs couplings to all SM particles due to the composite nature of the Higgs, there can be enhancements in certain channels with respect to the SM, as currently hinted by LHC data [144, 388]. Many other options in terms of Higgs masses and decay channels are possible even in the minimal composite Higgs model and will be discussed elsewhere [389].

2 The Model

For the sake of concreteness we focus on the minimal $SO(5)/SO(4)$ composite Higgs model based on the 5 representation of $SO(5)$ for the fermion composite states (MCHM₅ [310]). In this model the relevant tree level Higgs couplings to SM particles are given, assuming heavy enough new resonances so that one can neglect the effect of mixing, by (see for instance [364, 383]):

$$R_{hVV} \equiv \frac{g_{hVV}}{g_{hVV}^{\text{SM}}} = \sqrt{1 - \xi}, \quad R_{hff} \equiv \frac{g_{hff}}{g_{hff}^{\text{SM}}} = \frac{1 - 2\xi}{\sqrt{1 - \xi}}, \quad (1)$$

where V and f stand for any electroweak gauge boson and SM fermion respectively. The production cross section receives a suppression proportional to these same factors:

$$\frac{\sigma(gg \rightarrow H)}{\sigma(gg \rightarrow H)_{\text{SM}}} = R_{hff}^2, \quad \frac{\sigma(qq \rightarrow qqH)}{\sigma(qq \rightarrow qqH)_{\text{SM}}}(VBF) = R_{hVV}^2. \quad (2)$$

The different decay widths scale with the corresponding couplings squared except for the $h \rightarrow \gamma\gamma$ channel that reads

$$\Gamma(H \rightarrow \gamma\gamma) = \frac{(R_{hff}I_\gamma + R_{hVV}J_\gamma)^2}{(I_\gamma + J_\gamma)^2} \Gamma^{\text{SM}}(H \rightarrow \gamma\gamma), \quad (3)$$

where

$$I_\gamma = -\frac{8}{3}x_t[1 + (1 - x_t)f(x_t)], \quad J_\gamma = 2 + 3x_W[1 - (2 - x_W)f(x_W)], \quad (4)$$

with $x_t = 4m_t^2/m_h^2$, $x_W = 4m_W^2/m_h^2$ and

$$f(x) = \begin{cases} \arcsin[1/\sqrt{x}]^2, & x \geq 1, \\ -\frac{1}{4} \left[\log \frac{1+\sqrt{1-x}}{1-\sqrt{1-x}} - i\pi \right]^2, & x < 1. \end{cases} \quad (5)$$

We show in Fig. 1 (left panel) the ratio of the Higgs production cross section times branching ratio in several different channels with respect to the corresponding SM one as a function of the degree of compositeness of the Higgs, defined by $\xi = v^2/f^2$ with $v = 246$ GeV and f the decay constant associated to the composite sector. We have separated the production mechanism in gluon fusion and vector boson fusion, as they receive different suppression factors. As we see in the figure, there is a sizeable increase in the $\gamma\gamma$ channel, both in gluon fusion and vector boson fusion. This is due to a larger reduction of the top versus the W contribution in the loop (thus resulting in a smaller cancellation) together with a reduction in the total width.

New vector and fermion resonances are common in composite Higgs models. It has been recently emphasized that single production of new quark resonances, mediated by color octet vector resonances, can be a competitive discovery channel for these models [351, 390–392].

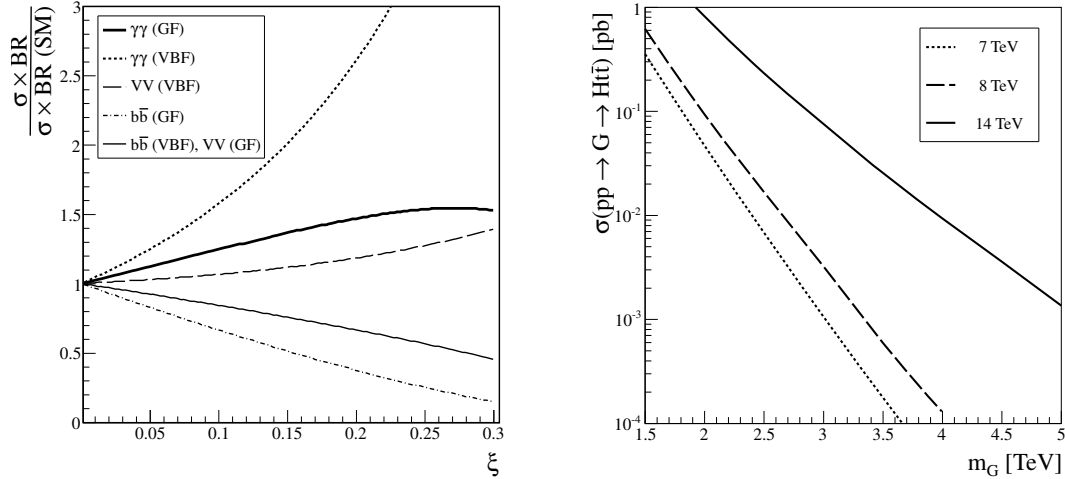


Figure 1: Left panel: ratio of the Higgs production cross section times branching ratio into different channels with respect to the SM as a function of the degree of compositeness ξ (V stands for either W or Z). Right panel: $t\bar{t}H$ production cross section in the benchmark composite model mediated by a color octet vector resonance with decay into a fermionic resonance and a top quark (see text for details).

Only decays into electroweak gauge bosons and a SM quark were considered in these references. However, the heavy quarks will decay with a sizable branching ratio into the composite Higgs and a SM quark. Thus, they provide a novel production mechanism in composite Higgs models that could give further information on the composite sector of the theory. To be specific, in this note we consider the two-site version of the MCHM₅. Full details of the model can be found in [392]. The ingredients relevant for the study in this note are the presence of new massive gluons of mass m_G and new vector-like quarks with a relatively large coupling to the top quark. We choose the masses of the lightest new quarks to be $m_Q = m_G/2$ so that the decay $G \rightarrow Q\bar{Q}$ is kinematically suppressed. The leading decay is then $G \rightarrow Q\bar{t}, t\bar{Q}$. A sizable fraction of the heavy quarks will in turn decay into $Ht, H\bar{t}$, thus resulting in a $t\bar{t}H$ final state. We show in Fig. 1 (right panel) the production cross section times branching fraction in this channel in parameter space as a function of m_G and for the LHC with $\sqrt{s} = 7, 8$ and 14 TeV, respectively.¹ These cross sections are of the order of the SM $t\bar{t}H$ production for $m_G \approx 2 - 2.5$ TeV and become much smaller for higher gluon masses. However we will see in the next section that our new production mechanism has very distinctive kinematics, mainly due to the large mass of the intermediate particles, and the signal can be extracted from the background with a high statistical significance.

3 $t\bar{t}H$ search in composite Higgs models

The process we are interested in consists of single production of the new vector-like quarks mediated by an s-channel exchange of the massive gluon and followed by a decay into a Higgs and a top quark,

$$pp \rightarrow G \rightarrow Q\bar{t}, \bar{Q}t \rightarrow Ht\bar{t}. \quad (6)$$

¹Technically, we have chosen, following the notation in [392], $Y_{*U} = Y_{*D} = g_{*3} = 3$, $\sin \phi_L = 0.6$ and $s_2 = 0.1$ and fermion masses such that $m_{\bar{T}} = m_{T_{5/3}} = m_G/2$. Also, we have fixed the Higgs mass to $m_H = 125$ GeV and its degree of compositeness $\xi = 0.2$.

We consider in this note the $H \rightarrow b\bar{b}$ channel, which has $B(H \rightarrow b\bar{b}) = 0.47$ (the decay into WW^* has also a relatively large branching fraction and will be considered elsewhere [389]). The decays of the Higgs and top quarks result in a very large multiplicity final state that makes, *a priori*, full reconstruction difficult. However we do not need full reconstruction to observe a signal. In fact, it is easy to find a simple set of cuts that reduce the relevant backgrounds to manageable levels. The S_T distribution, defined as the scalar sum of the p_T of the relevant jets, leptons and missing energy, then reduces the remaining background to essentially negligible levels, allowing for a clean extraction of the signal. The initial set of cuts strongly depends on the available energy. In the low energy phase ($\sqrt{s} = 7$ or 8 TeV), the masses that can be tested are not too large and the best strategy is to require a large number of jets and many of them to be tagged as b-jets. In the high energy phase ($\sqrt{s} = 14$ TeV), however, the available energy is enough to produce much heavier resonances. As a result the tops and the Higgs are typically quite boosted and their decay products very collimated. Thus, we ask for a smaller number of (fat) jets but require them to have invariant masses close to the top and the Higgs.

We have simulated the signal and background events with MADGRAPH V4.5.0 [94] and ALPGEN V.2.13 [376], respectively. In both cases the unweighted events have been passed to PYTHIA 6.4 [116] for hadronization and showering and DELPHES V1.9 [375] for detector simulation (we have used a tuned version of the ATLAS card to better agree with published experimental data). The main backgrounds are $t\bar{t}$ and $t\bar{t}b\bar{b}$ (the former has been simulated with up to 4 extra jets properly matched with the parton shower using the MLM method). We have used the CTEQ6L1 PDFs. As we have mentioned, the optimal analyses are different depending on the available center of mass energy. In all cases jets are defined with a cone size $\Delta R = 0.7$, $p_T(j) > 30$ GeV and $|\eta_j| < 5$. Isolated charged leptons (e or μ) are considered when $p_T(l) > 20$ GeV and $|\eta_l| < 2.5$. A b-tagging efficiency of 0.7 has been assumed. In the analysis for the low energy phase we require

- At least 4 jets, of which at least 3 must be tagged as b-jets.
- At least 1 isolated charged lepton.

The analysis of the high energy phase requires

- At least 3 jets, with a minimum of 2 b tags.
- At least 1 isolated charged lepton.
- We then order all the jets according to their invariant mass and require the two jets with the largest invariant masses to be near the top and the Higgs mass, respectively, $|m_{j_1} - m_t| \leq 40$ GeV and $|m_{j_2} - m_H| \leq 40$ GeV.

The cuts above reduce the background to manageable levels. Once the number of background events has been reduced to a reasonable level, we use S_T , defined as the scalar sum of the transverse momenta of the four (three) hardest jets in the low (high) energy analysis, the hardest charged lepton and missing energy in the event, as the discriminating variable. We show in the left panel of Fig. 2 a sample distribution of S_T for the main backgrounds and the signal for $m_G = 3$ GeV at the 14 TeV LHC. In order to estimate the statistical significance of the signal, we introduce the following mass-dependent cut on S_T

- $S_T > 0.9, 1.1, 1.5$ TeV for $m_G = 1.5, 2, 2.5$ TeV (low energy phase),
- $S_T > 1.2, 1.5, 1.7, 2$ TeV for $m_G = 2, 2.5, 3, \geq 3.5$ TeV (high energy phase),

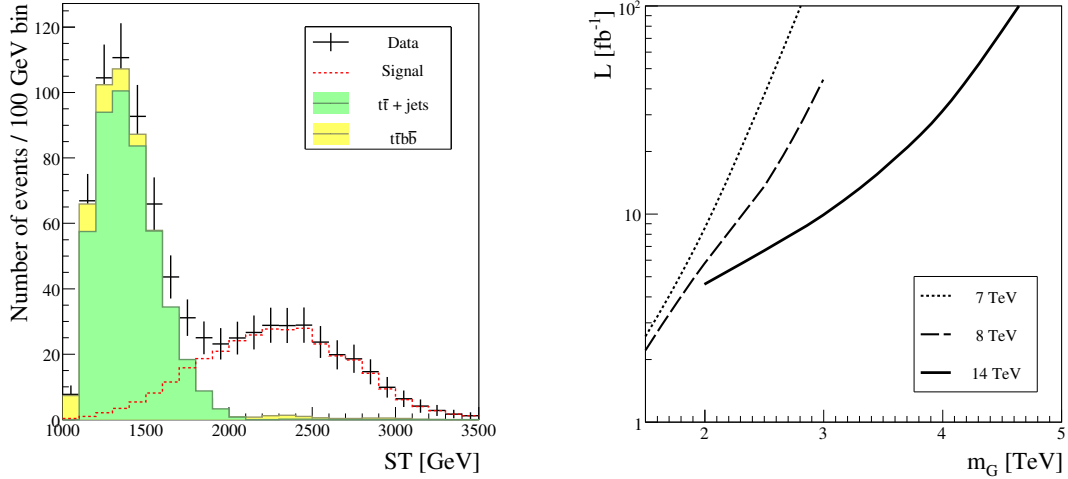


Figure 2: Left panel: S_T distribution for the signal (red dotted) and the $t\bar{t}$ (green) and $t\bar{t}b\bar{b}$ (yellow) backgrounds for $m_G = 3$ TeV and an integrated luminosity of 50 fb^{-1} with $\sqrt{14}$ TeV. Right panel: Luminosity required for a 5σ discovery as a function of m_G for $\sqrt{s} = 7$ TeV (dotted), 8 TeV (dashed) and 14 TeV (solid).

and compute the statistical significance from the formula [393]

$$\mathcal{S}(s, b) = \sqrt{2 \times \left[(s + b) \ln \left(1 + \frac{s}{b} \right) - s \right]}. \quad (7)$$

We show in the right panel of Fig. 2 the luminosity required for a 5σ discovery as a function of m_G for the three energies considered. With the $\sim 5 \text{ fb}^{-1}$ already collected at 7 TeV masses up to $m_G \approx 1.8$ TeV can be probed. This could go up to 2.7 TeV (4.6 TeV) for 20 fb^{-1} at 8 TeV (100 fb^{-1} at 14 TeV).

4 Conclusions

We have seen that a composite Higgs with $m_H = 125$ GeV and a moderate degree of compositeness is compatible with current Higgs searches. In such a model, the Higgs boson can be produced in association with a $t\bar{t}$ pair through the exchange of a heavy gluon with subsequent decay into a new fermion resonance (which decays itself into the Higgs and a SM top) and the top quark. We have shown that simple cuts on the number of jets and b-jets can reduce the background to manageable levels. For the highest masses probed, boosted techniques are very useful. Using then S_T as a discriminating variable allows for a clean extraction of the signal up to masses $m_G \approx 1.8$ TeV, 2.7 TeV and 4.6 TeV for the LHC with $\sqrt{s} = 7, 8$ and 14 TeV, respectively and an integrated luminosity of 5, 20 and 100 fb^{-1} , respectively.

ACKNOWLEDGEMENTS

We would like to thank the Les Houches school for physics for their hospitality during the workshop where some of the work contained herein was performed, as well as the workshop organizers. This work has been partially supported by projects FPA2006-05294, FPA2010-17915, FQM 101, FQM 03048 and FQM 6552 and the FPU programme.

Contribution 13

Top Polarisation in H^-t and Wt production

R. M. Godbole, L. Hartgring, I. Niessen, C. D. White

Abstract

We consider laboratory frame observables obtained from leptonic decay products of top quarks produced in association with a charged Higgs or W boson. These are robust against QCD corrections to top quark decay, and can be used to pin down the parameter space of a charged Higgs boson, or reduce backgrounds in H^-t and (Standard Model) Wt production.

1 INTRODUCTION

The proximity of the top quark mass to the scale of electroweak symmetry breaking makes the top quark sector a potentially useful window through which to look for new physics effects. Particularly useful in this regard is single top production, which in the Standard Model is purely electroweak at leading order. Single top quarks can be produced in association with other particles, such as W bosons or other quarks (in the SM), or more exotic species in new physics scenarios. In general, a singly produced top quark may have a net degree of longitudinal polarisation P_t , in contrast to the case of top quark pair production, which in the SM leaves the top quark *unpolarised* on average ($P_t = 0$). Assuming the top quark decays according to $t \rightarrow Wb \rightarrow ff'b$ (where f is a quark or lepton, and f' the associated antiquark or neutrino), the decay product f is distributed in the top quark rest frame according to

$$\frac{1}{\Gamma_l} \frac{d\Gamma_l}{d \cos \theta_{f,\text{rest}}} = \frac{1}{2} (1 + \kappa_f P_t \cos \theta_{f,\text{rest}}). \quad (1)$$

Here Γ_l is the partial decay width, and the polar angle $\theta_{f,\text{rest}}$ is the angle between the decay product f and the top spin vector in the top quark rest frame. κ_f is the analysing power of the decay product f . If f is a lepton ($f = l$), it is approximately independent of corrections to the top quark *decay*, thus depending solely on the *production* stage of the top quark. In this case, κ_l is approximately one. It follows that by studying leptonic decay products of single top quarks, one may elucidate the net polarisation of the top quark and, in turn, its coupling to BSM (or SM) particles.

Rather than relying on leptonic distributions in the top quark rest frame, it is more practical to consider alternative observables defined in the laboratory (lab) frame, which require reconstruction of just the top quark direction in the lab and not necessarily that of the rest frame. Two such observables are the azimuthal angle ϕ_l between the top quark and its decay lepton (taking the top quark direction and beam axis to define the (x, z) plane), and the polar angle θ_l between the top quark and leptonic directions. These were defined in Ref. [394] in the context of top pair production, and have subsequently been considered in H^-t and Wt production [395, 396].

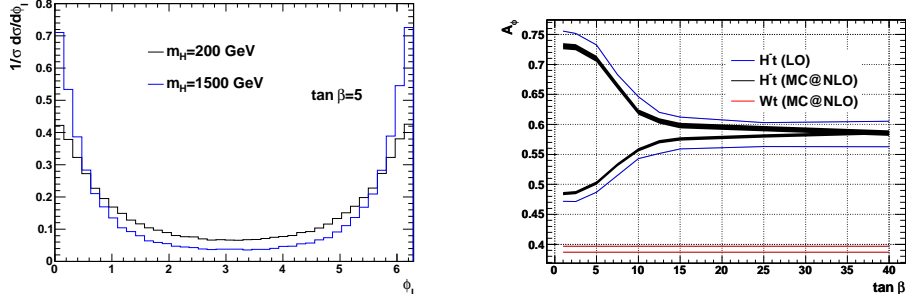


Figure 1: Left: the azimuthal angle ϕ_l of the top quark decay lepton for $\tan\beta = 5$ and extremal charged Higgs mass values; right: the azimuthal asymmetry parameter, for H^-t and Wt production.

2 H^-t PRODUCTION

In the context of a general type II two-Higgs doublet model, we investigated the above angular observables using recently developed MC@NLO software [397]. The polarisation of the top quark depends on the ratio of the vacuum expectation values $\tan\beta$, as well as the charged Higgs boson mass m_{H^-} . Representative results for ϕ_l are shown in Fig. 1. In addition to the distribution itself, one may also consider the asymmetry parameter [394]:

$$A_\phi = \frac{\sigma(\cos\phi_l > 0) - \sigma(\cos\phi_l < 0)}{\sigma(\cos\phi_l > 0) + \sigma(\cos\phi_l < 0)}, \quad (2)$$

which efficiently distils the difference in distributions at different points in parameter space. Results for A_ϕ are also shown in Fig. 1, where MC@NLO results (black) are compared with leading order (LO) results (blue) obtained using MadGraph [96]. Note that there is a pronounced difference in A_ϕ for different points in $(\tan\beta, m_{H^-})$ space, particularly at low Higgs mass values. Furthermore, the MC@NLO curve does not differ significantly from the LO curve, and thus the observable is highly stable with respect to next-to-leading order (NLO) and parton shower effects. The lower band in Fig. 1 constitutes an estimate of the Wt result, using MC@NLO [398]. This is very different to the H^-t result, providing information useful for reducing the Wt background.

Further useful information can be gained from considering the polar angle and a suitable asymmetry parameter is defined in Ref. [396]. This asymmetry is capable of distinguishing different Higgs boson masses at large $\tan\beta$ (where the azimuthal asymmetry cannot). In Ref. [396], we also studied observables related to the energy of the top quark decay products [399], and further useful asymmetry parameters were defined which add complementary information to the angular observables in the boosted top quark limit.

3 Wt PRODUCTION

As well as being a background to H^-t production, Wt production is of interest as a signal in its own right. Top quark pair production is a major background, and one may reduce this background using polarisation information: in pair production the t quark is unpolarised on average, whereas in Wt production it is fully polarised. In Ref. [396] we examined the ϕ_l and θ_l distributions for Wt and $t\bar{t}$ production, for the Wt signal cuts of Ref. [400], using MC@NLO [398]. The corresponding asymmetry parameters are $(A_\phi, A_\theta) = (0.33, 0.02)$ (Wt) and $(0.63, 0.26)$ ($t\bar{t}$). There is thus a pronounced difference, which is potentially useful for distinguishing the two processes in e.g. a multivariate analysis.

CONCLUSIONS

Polarisation information can efficiently be used to distinguish single top quark production processes from their backgrounds, as well as to pin down the parameters of a charged Higgs boson model. Lab frame leptonic observables can be defined, which are robust against NLO and parton shower corrections.

Contribution 14

Probing New Physics with Single Top + X

Devin G. E. Walker, Jiang-Hao Yu and C.-P. Yuan

Abstract

We investigate single top production in association with a variety of Standard Model final states with a focus on the early LHC run. Here X can be jets, large missing transverse momentum and/or electroweak gauge bosons. For this review, we focus on searches for new W' gauge bosons and heavy B' quarks. A general survey of the possible new physics with associated single top production can be found in Ref. [401]. In essence, the channel probes a variety of new physics, is intricately tied to the new physics at the TeV scale and is essential for maximizing the potential of the early LHC for new physics.

1 Introduction

For the first time in history, the TeV scale is being directly probed by the CERN Large Hadron Collider (LHC). Even at this early stage, hints of the Standard Model (SM) higgs boson [144, 402] as well as strong constraints on new physics have been produced. Of particular interest are the constraints on new scalar and gauge bosons (e.g. resonances [403–411]) as well as new exotic fermions [371, 412, 413] which are harbingers of natural new physics scenarios. Some of the most popular scenarios which exhibit this new physics can be found in Refs. [304, 306, 316, 381, 414–425]. In this review, we show how associated single top production (a top quark produced in conjunction with a variety of SM final states) can provide a sensitive probe to heavy B' quarks and W' gauge bosons.

A Motivation from Top Collider Physics: The LHC is a “top factory.” At 7 TeV, 85,000 single top quark events are expected for 1 fb^{-1} of data [426]. Importantly, the production cross section for these background SM events are precisely known at next-to-leading order (NLO) and next-to-leading log (NLL). In addition, processes involving single top (quark) production may be unique in their ability to probe the nature of electroweak symmetry breaking. The top quark mass is of order the electroweak scale thereby suggesting that top quark production may be sensitive to new physics beyond the SM. Unlike other quarks, SM top quarks decay to a W boson and a bottom quark *before* hadronizing. This provides a unique opportunity to probe the underlying electroweak interactions as well as efficiently tag the events. Observation of SM single top production has been experimentally challenging. One of the major reasons is the jet not associated with the top decay is frequently in the forward regions in the detector. It is therefore hard to distinguish these single top events from the dominant QCD backgrounds. The fact that SM single top production has this difficulty is a *strength* when considering single top production from new physics. When new physics is produced that decays to single top + X, the large mass of the new physics often results in the decay products being in the center of the detector.

This review paper is organized as follows: In the next section, we outline the new physics that can be produced from single top + X production at the LHC. As mentioned in the abstract, we restrict our focus to new W' bosons as well as new heavy quarks in this review. Please see Ref. [401] for an analysis of all the new physics listed in the next section. Appendix A includes a brief overview of our reconstruction methodology and any important definitions. Sections 3, 4 and 5 contain our analysis for the new W' s and heavy quarks. Finally we conclude.

2 New Physics Searches with Single Top + X

This review is part of a larger series of papers searching for new physics in the single top + X final state [401]. Here we list the new physics that can be probed.

Single Top Signatures (partonic level)	New Physics Probed
$t + b\text{-jet}/\text{jet}$	W' Gauge Bosons Diquark Resonances Colored Resonances Charged Higgses
$t + Z/W (+ \text{jet})$	Heavy Top Quarks Heavy Bottom Quarks
$t + h + \text{jet}/W$	SM Higgs
$t + h^- + b\text{-jet}$	Charged Higgses
$t + W + \text{jet}$	Charged 5/3 Quarks
$t + \cancel{E}_T + \text{jet}$	Dark Matter Top Fermion Partners (e.g. stops)

The above chart is constructed by considering all possible SM particles on the external legs. Based on the SM symmetries, all possible new physics in the intermediate state(s) are enumerated at tree-level with the simplest tree-level topologies. We require at least one SM top quark in the final state; and, the initial states are light quarks or gluons. For this review, we focus on W' bosons and heavy quarks.

3 Searching for W' Bosons with $t + b\text{-jet}/\text{jet}$

3.1 Theoretical Considerations for W' Bosons

Previous studies of W' bosons decaying to top quarks have focused on the LHC at center of mass energies of 14 TeV [427]. We examine the potential of the early LHC to identify W'

bosons during the early LHC as well as the experimental reach. Many natural models of new physics beyond the SM have relatively light W' bosons. They are needed to cancel quadratic divergences induced by SM W bosons on the higgs potential. However, the tightest exclusion limits come from leptophobic W' bosons which decay to dijets [407, 428]

$$280 < m_{W'} < 1500 \text{ GeV}. \quad (1)$$

To ensure a model independent analysis, we write down the following parametrization

$$\mathcal{L} = \frac{i g_2}{\sqrt{2}} \bar{q}_i \gamma^\mu (f_L P_L + f_R P_R) V_{ij} q'_j W_\mu'^+ + \text{h.c.}, \quad (2)$$

where q and q' are the up and down-type quarks, respectively. Here $i = u, c, t$, $j = d, s, b$, and $g_2 = e/\sin\theta_W$. Also, V_{ij} is the Cabibbo-Kobayashi-Maskawa matrix and $P_{L,R}$ are the chirality projection matrices. For simplicity in the next section, we consider only the case with a purely left-handed current ($f_L = 1$, and $f_R = 0$); our study can be extended easily to other cases.

3.2 Signal and Background Processes for W' Searches

The s - and t -channel signal processes are

$$pp \rightarrow t\bar{b} + \text{h.c.} \quad pp \rightarrow tq \quad \text{or} \quad \rightarrow \bar{t}q. \quad (3)$$

For the t -channel processes on the right, the t and \bar{t} final states are equally possible because the initial b and \bar{b} partons occur with equal probability. For this channel, we only consider top quarks that decay semi-leptonically. The isolated lepton (with a sufficiently large p_T) allows for the event to be effectively tagged. The following SM backgrounds are dominant:

$$pp \rightarrow t + \text{jet}(s) \quad pp \rightarrow W + \text{jets} \quad (4)$$

$$pp \rightarrow \bar{t}t \quad pp \rightarrow WW/Z \quad (5)$$

The SM $pp \rightarrow t + \text{jet}(s)$ background is irreducible. The other SM backgrounds in equations 4 and 5 are important insofar as they can mimic the $t + \text{jet}$ final state.

3.3 Event Simulations for W' Searches

We focus on a 1.5 TeV W' boson with coupling $f_L = 1$. (See equation 2.) We use CTEQ6L parton distribution functions [429] in our event simulations. The renormalization and factorization scales are chosen to be the W' boson mass. The signal and background events are generated with MadGraph5/MadEvent. We impose the following basic p_T cuts

$$p_T^j \geq 25 \text{ GeV} \quad p_T^\ell \geq 25 \text{ GeV}. \quad (6)$$

We also confine our search to the center of the detector

$$|\eta_j| \leq 2.5 \quad |\eta_\ell| \leq 2.5. \quad (7)$$

As mentioned in the introduction for SM single top production, the jet not associated with the top quark decay is often forward in the detector. Restricting our focus to the center of the detector helps to eliminate this background. As mentioned before, we also require the leptons and jets to be well separated. We require the following cone sizes

$$\Delta R_{jj} > 0.4 \quad \Delta R_{j\ell} > 0.4 \quad \Delta R_{\ell\ell} > 0.2. \quad (8)$$

Since we require the top quark to decay semi-leptonically, the resulting neutrino introduces missing transverse momentum (\cancel{E}_T) in the event. To further reduce the SM background, we require

$$\cancel{E}_T > 25 \text{ GeV}. \quad (9)$$

The $t + \text{jet}$ signature has a final state with one isolated charged lepton (electron or muon), two high p_T jets, and large missing transverse momentum (\cancel{E}_T) from the missing neutrino. Large p_T cuts on the leading jet can be used to suppress most of the backgrounds. In the upper panels of Figure 1, we show the p_T distributions for the leading and sub-leading jets for the signal and background. As reminder, we consider the 1.5 TeV W' boson with $f_L = 1$ as the signal; the discriminating power of the p_T cuts is clear in those plots. We require

$$p_T \geq 200 \text{ GeV} \quad (\text{leading jet}), \quad (10)$$

$$p_T \geq 80 \text{ GeV} \quad (\text{subleading jet}). \quad (11)$$

Another useful variable is the scalar sum of the p_T 's of all the particles in the final state. In Appendix A, we define

$$H_T = p_T^{\ell^+} + \cancel{E}_T + \sum_j p_T^j. \quad (12)$$

Here j runs over all of the well-separated jets in the event. We apply the following cut

$$H_T \geq 600 \text{ GeV}. \quad (13)$$

In Figure 1, a slight signal is visible near 1.5 TeV. To further optimize the signal, we apply b-tagging and perform standard sideband analysis. We apply the following invariant mass window cut

$$|m_{l\nu jj} - M_{W'}| < 400 \text{ GeV}. \quad (14)$$

Here $M_{W'}$ center of the resonance peak in the invariant mass distribution in Figure 1. Of course, the ν momentum is determined with the top reconstruction in Appendix A. After all of the cuts, a 1.5 TeV W' boson with a coupling of $f_L = 1$ is clearly visible. For reference, after all of the cuts, the s -channel and t -channel signal cross sections are

$$\sigma(pp \rightarrow W' \rightarrow b l^\pm \nu \bar{b}) = 13.136 \pm 0.0246 \text{ pb}, \quad (15)$$

$$\sigma(pp \rightarrow t(\bar{t}) q \rightarrow b(\bar{b}) l^\pm \nu q) = 8.5404 \pm 0.0218 \text{ fb}. \quad (16)$$

Table 1 gives a breakdown of the effect of the cuts on the signal and background cross sections.

3.4 Discovery Potential and Chiral Properties for W' Boson Searches

The SM backgrounds are suppressed efficiently such that less than 1 background event survives after cuts with an integrated luminosity of 10 fb^{-1} . We now consider a 1 GeV W' gauge bosons with $f_L = 1$. For that amount of luminosity we achieve

$$S/\sqrt{B} \sim 5 \quad (17)$$

where S and B denotes the number of signal and background events, respectively.

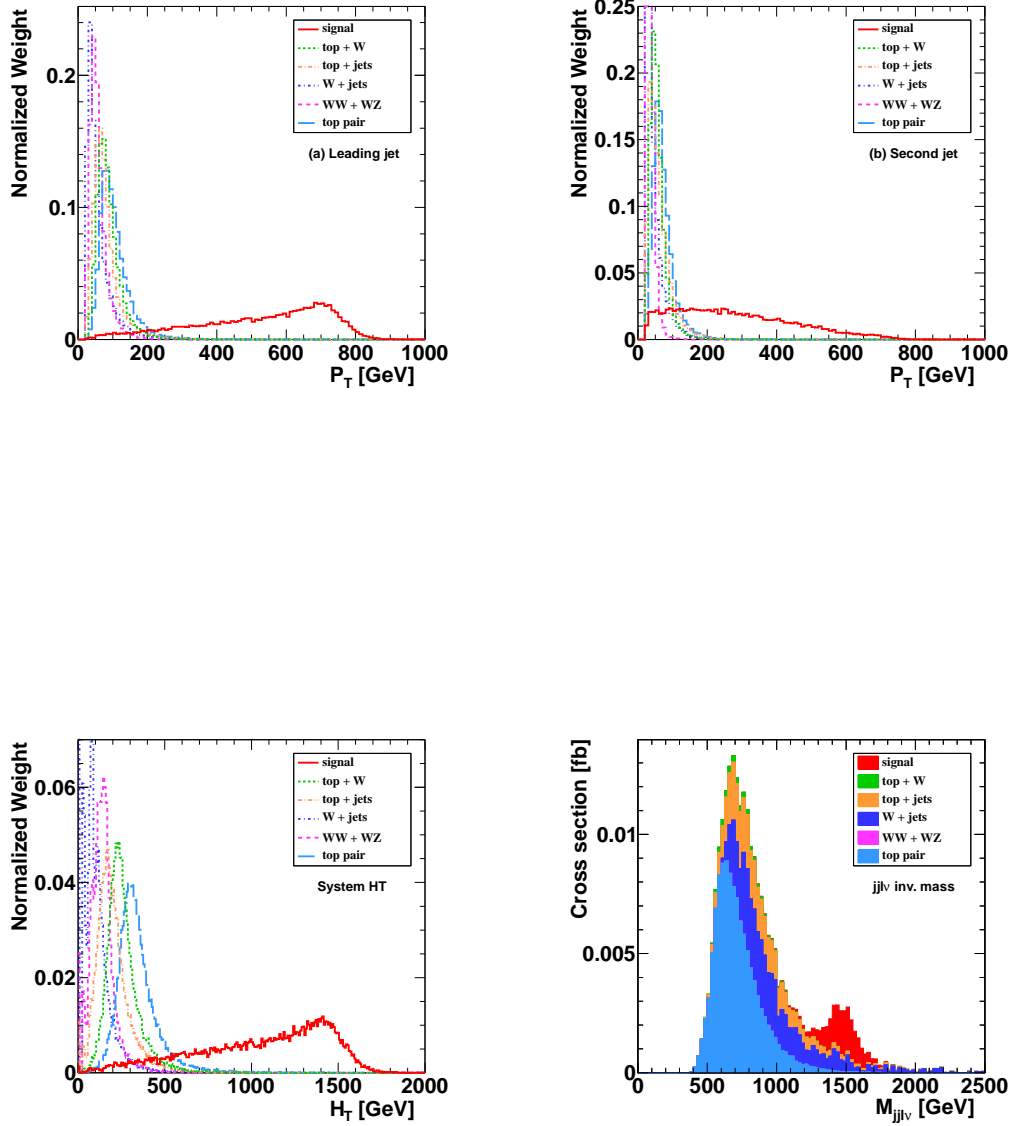


Figure 1: Normalized p_T distributions of the leading jet (upper left panel) and sub-leading jet (upper right panel) for the signal and backgrounds. The signal process features a 1.5 TeV W' boson with the coupling $f_L = 1$. See equation 2 for the definition of f_L . The H_T distributions for signal and backgrounds are also plotted (lower left panel). It is clear an H_T cut can be useful in separating the signal and backgrounds. After the cuts in equations 6-11 and equation 13 are made, the invariant mass distribution is plotted (lower right panel).

$\sigma(\text{fb})$	Signal	$t + W$	$t + \text{jets}$	$t\bar{t}$	WV	$W + \text{jets}$
No cuts	58.96	2861	18877	25840	9888	4018600
Basic cuts (in eq. 6-9)	33.38	833	4049	7207	2265	284516
+ hard p_T cuts (in eq. 10-11)	28.65	11.1	158.5	232.6	3.67	7836.2
+ H_T cut (in eq. 13)	26.45	5.69	59.8	137.6	3.51	3782
+ Tagged b -jet	22.36	3.44	44.8	115.7	0.19	61.98
+ Mass window (in eq. 14)	21.59	0.13	7.80	3.97	0.03	16.02

Table 1: Cross sections for the signal and various background processes without and with the cuts are listed.

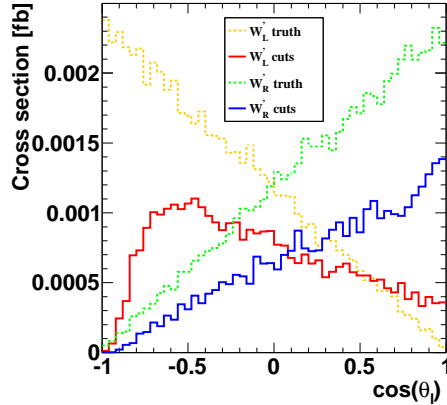


Figure 2: The angular distributions of the final lepton $\cos \theta_l$ for the left-handed W' . See Appendix A for definitions of $\cos \theta_l$.

After the discovery of the W' boson, one would like to know its mass, spin, and couplings. Angular distributions of its decay products can be investigated to definitively determine the spin and chiral structure of the W' boson to the SM fermions. The chirality of the W' coupling to SM fermions is best measured from the polarization of the top quark. Among the top quark decay products, the charged lepton from $t \rightarrow b + l + \nu$ is the best analyzer of the top quark spin. For a left-handed top quark, the charged lepton moves preferentially against the direction of motion of the top quark, while for a right-handed top quark the charged lepton moves along the direction of motion of the top quark. The angular correlation of the lepton is $(1 \pm \cos \theta_l)/2$, with the (+) choice for right-handed and (−) for left-handed top quarks, where θ_l is the angle of the lepton in the rest frame of top quark relative to the top quark direction of motion in the center-of-mass (c.m.) frame of the incoming partons. In Figure 2, we plot $\cos \theta_l$ for $f_L = 1$,

$f_R = 0$ (W'_L) as well as $f_L = 0$ and $f_R = 1$ (W'_R). We expect a flat angular distribution for the SM $t\bar{t}$ background because the top quark and anti-top quark are not polarized. Therefore, the angular distributions of the lepton can be used to discriminate W' models in which the chirality of the W' coupling to SM fermions differs.

4 Searching for Heavy Top and Bottom Quarks with $t + W + \text{jet}$

4.1 Theoretical Considerations for Heavy Quarks

In many models of natural electroweak symmetry breaking, the following tree-level coupling exists

$$B' \rightarrow W t \quad (18)$$

with $\mathcal{O}(1)$ strength. Often the heavy bottom quarks are vector-like because of the minimal impact on precision electroweak bounds. In natural theories, heavy top partners (and the corresponding bottom partners) are *essential* for canceling the quadratic divergences induced by the SM top quark on the higgs potential. Thus, these particles are expected to be relatively light. Recent experimental bounds on heavy tops and bottom quarks are [430]

$$m_{T'} \geq 311 \text{ GeV}, \quad m_{B'} \geq 338 \text{ GeV}. \quad (19)$$

We show this bound can be improved during the early LHC running. In this review, we restrict our focus to B' heavy quarks production with a $t + W$ final state. We parameterize the heavy quark interactions in a manner similar to Ref. [431] in order to keep our analysis model independent¹. After electroweak symmetry breaking, the effective couplings between the electroweak gauge bosons, the third generation SM quarks and the new heavy quarks is

$$\begin{aligned} \mathcal{L} = & \frac{g_2}{\sqrt{2}} W_\mu^+ \left(\bar{t} \gamma^\mu (f_{tB'}^L P_L + f_{tB'}^R P_R) B' \right) + \frac{g_2}{\sqrt{2}} W_\mu^- \left(\bar{b} \gamma^\mu (f_{bT'}^L P_L + f_{bT'}^R P_R) T' \right) \\ & + \frac{g_2}{2 c_W} Z_\mu \left(\bar{t} \gamma^\mu (f_{tT'}^L P_L + f_{tT'}^R P_R) T' + \bar{b} \gamma^\mu (f_{bB'}^L P_L + f_{bB'}^R P_R) B' \right) + h.c. \end{aligned} \quad (20)$$

Here g_2 is the $SU(2)_L$ coupling, c_W is the cosine of the Weinberg angle, $P_{L,R}$ are the usual projection operators and f parametrizes the chirality of the couplings. For the vector-like heavy quarks, the couplings $f_{qQ'}$ in the above Lagrangian can be parametrized in a model independent way as

$$f_{qQ'}^{L,R} \simeq \frac{v}{m_{Q'}} \kappa_{qQ'}^{L,R}, \quad (21)$$

where $\kappa_{qQ'}^{L,R}$ is a dimensionless parameter. For the chiral heavy quarks, the couplings f_{qQ} are equal to

$$f_{qQ}^L = |V_{qQ}^{CKM}|, \quad f_{qQ}^R = 0. \quad (22)$$

In order to generate the heavy bottom quark resonance, we require the following magnetic moment operator

$$\mathcal{O}_1 = \frac{g_s \lambda_i^2}{2M_{B'}} \bar{B}' \sigma^{\mu\nu} G_{\mu\nu} b, \quad (23)$$

¹In Ref. [431], the new heavy quarks couple preferentially to first generation quarks. Thus, the decay of the heavy quarks will involve light quarks instead of the top.

$\sigma(\text{fb})$	Signal	$t + W$	$t + \text{jets}$	$t\bar{t}$	$WV + \text{jets}$	$W + \text{jets}$
No cuts	681.570	2861.00	18877.0	22200.0	10007	2457400
Basic cuts	326.199	833.695	4049.12	5575.53	1721.2	88343.5
+hard cuts	210.469	151.776	257.671	2888.22	288.202	23713.9
+HT cuts (in Eq. 31)	196.531	52.3563	90.6096	1247.64	125.087	12901.4
+Tagging one b -jet	118.559	33.4737	46.2486	580.530	32.5228	284.724
+Mass window cuts in Eq.33	98.4187	12.7315	17.9331	147.630	10.0070	81.3498

Table 2: Cross sections for the signal and various background processes without and with the cuts are listed.

where $G_{\mu\nu} = G^a T^a/2$ is the field strength tensor of the gluon and g_s is the strong coupling constant. By naive dimensional analysis, we take the suppression scale to be twice the excited resonance mass.

4.2 Signal and Background Processes for Heavy Bottom Quarks

As alluded to above, for heavy bottom quarks the signal production processes are

$$pp \rightarrow B' \rightarrow t W^- \quad (24)$$

with the final decays

$$W^\pm \rightarrow l^\pm \nu, \quad t(\bar{t}) \rightarrow b(\bar{b})l^\pm \nu. \quad (25)$$

which is clean for discovery. In addition to the backgrounds listed in equations 4-5, an additional background to be considered is

$$pp \rightarrow t W. \quad (26)$$

The single top SM background in equation 26 is irreducible.

4.3 Event Simulations for Heavy Bottom Quarks ($t + W + \text{jet}$)

The basic selection cuts are all the same as for the W' boson search, up to the requirement

$$\cancel{E}_T > 25 \text{ GeV}. \quad (27)$$

In addition to these basic cuts, we now place additional cuts to optimize the signal.

From Fig. Ref.stopx:bprimekin, it is clear the p_T of leading jet for the signal is much larger than the backgrounds. We require

$$p_T \geq 80 \text{ GeV} \quad (\text{leading jet}) \quad (28)$$

$$p_T \geq 50 \text{ GeV} \quad (\text{subleading jet}). \quad (29)$$

$$p_T \geq 40 \text{ GeV} \quad (\text{additional jet}). \quad (30)$$

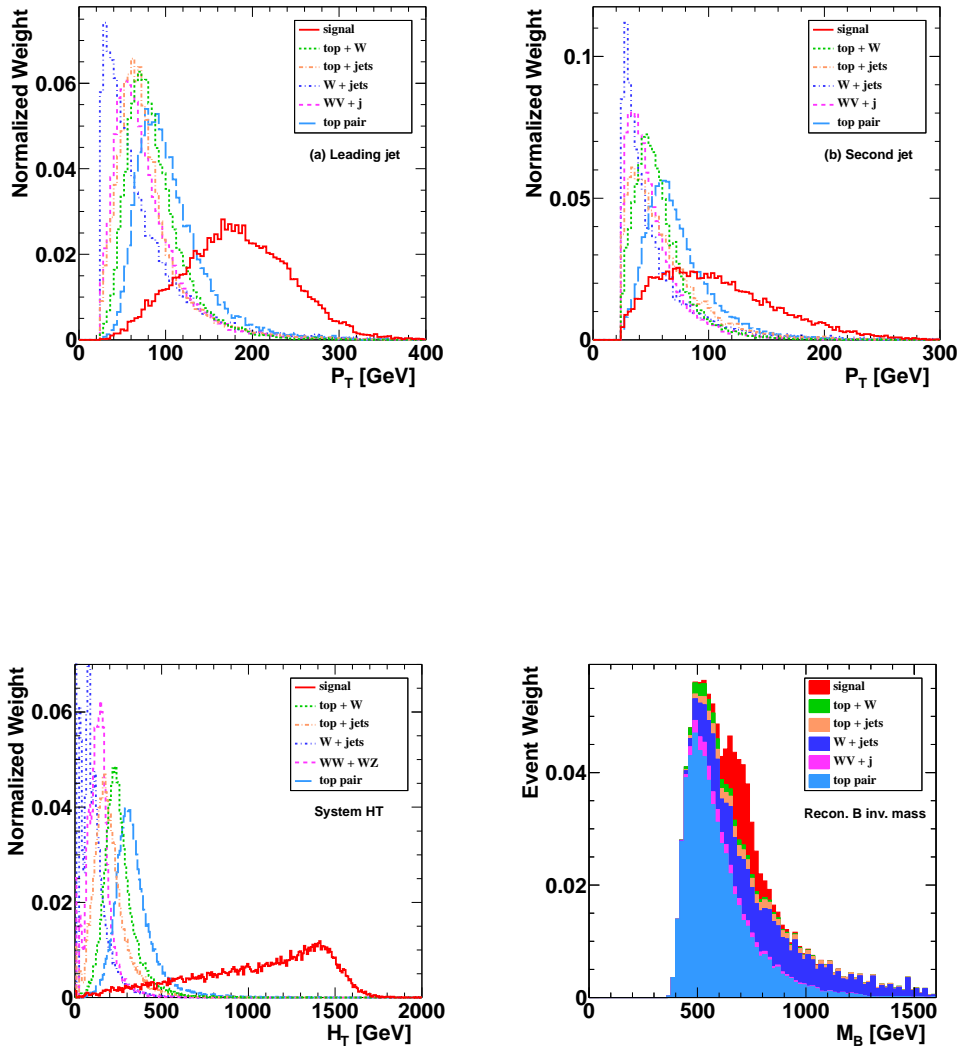


Figure 3: p_T distributions from the leading jet (upper right) and subleading jets (upper left). The H_T distribution is in the lower left panel. It is clear these variables can be used to separate the signal from the background. After the cuts, the reconstructed B' invariant mass distributions for signal and backgrounds is plotted in the lower right panel.

We again define the scalar sum of the p_T 's of all the particles in the final state.

$$H_T = p_T^{\ell^+} + \cancel{E}_T + \sum_j p_T^j. \quad (31)$$

Here j runs over all of the well-separated jets in the event. We apply the following cut

$$H_T \geq 425 \text{ GeV}. \quad (32)$$

We impose the invariant mass window cuts

$$|m_{\ell\nu bjj} - m_{B'}| < 100 \text{ GeV}. \quad (33)$$

After these cuts, we show the B' resonance in Fig. Ref.stopx:bprimekin. For the heavy B' quark with 700 GeV mass, the significance with $1 \text{ fb}^{?1}$ luminosity is

$$S/\sqrt{B} \sim 6. \quad (34)$$

Cross sections for the various background processes without cuts are given in Table 2.

5 Conclusions

In this review, we focused on searches for new W' gauge bosons as well as B' heavy quarks. This is done under the rubric of searches for new physics under single top $+X$. A general survey of the possible new physics with associated single top production can be found in Ref. [401]. We showed TeV W' bosons and B' heavy quarks are easily accessible during the early LHC running.

Acknowledgements

We would like to thank S. Chivukula J. Hewett, T. Rizzo, E. Simmons and B. Shuve for useful discussions. The work of J.-H.Y. and C.-P. Y. is supported in part by the U.S. National Science Foundation under Grant No. PHY-0855561. This work of D.W. is supported in part by a grant from the National Academies of Science and the LHC Theory Initiative.

Appendix

A few basic definitions were used in the analysis in the previous sections are given here. We place some important definitions not included in the above text; if needed, see Ref. [432, 433] for additional background.

A Detector Effects

We often use b-tagging to increase the signal efficiency. A tagging efficiency of 60% is used in our analysis. We take into account a mis-tag rate for a light non-b quark (including the charm quark) to mimic a b jet, with mistag efficiency $\epsilon_{j \rightarrow b} = 0.5\%$

We smear the electron and hadronic energy according to Gaussians given by

$$\frac{\Delta E_j^e}{E_j^e} = \frac{0.05}{\sqrt{E_j/\text{GeV}}} \oplus 0.0055 \quad (\text{A.1})$$

$$\frac{\Delta E_j^h}{E_j^h} = \frac{1}{\sqrt{E_j/\text{GeV}}} \oplus 0.05, \quad (\text{A.2})$$

respectively. The muon momentum is smeared by

$$\frac{\Delta p_T^l}{p_T^l} = 0.36 \frac{p_T^l}{\text{TeV}} \oplus \frac{0.013}{\sqrt{\sin \theta}}. \quad (\text{A.3})$$

where θ is the polar angle of the lepton with respect to the beam direction in the lab frame. These smearing parameters are consistent with both the ATLAS and CMS experiments. Finally, we use FastJet to cluster the final state jets with a cone size $R = 0.4$.

B Top Tagging and Reconstruction

Hadronic Top Reconstruction: Here the top quark decays hadronically to a b-jet and a W bosons which subsequently decays to jets. In order to tag the top simply require the following invariant masses

$$m_W^2 = (p_1 + p_2)^2 \quad m_t^2 = (p_1 + p_2 + p_3)^2. \quad (\text{B.4})$$

to be within the ranges

$$77 < m_W < 83 \text{ GeV} \quad 168 < m_t < 176 \text{ GeV}. \quad (\text{B.5})$$

Semileptonic Top Reconstruction: For simplicity, we consider top decays to electrons or muons only. With only one neutrino in the final state, the missing momentum generates four unknowns. The missing transverse momentum

$$\vec{p}_T^{\text{miss}} = - \sum_i \vec{p}_{T,i} \quad \cancel{E}_T = - \sum_i E_i, \quad (\text{B.6})$$

determines only two of the four components of the missing neutrino momentum. The rest of the components of the momentum can be determined by taking the W boson and top quark mass as an input for on-shell top quark production and decays. To see this explicitly, we first demand that $m_{l\nu}^2 = M_W^2$. The longitudinal momentum of the neutrino is formally expressed as

$$p_L^{(\nu)} = \frac{1}{2 p_T^{(l)2}} \left(A p_L^{(l)} \pm E^{(l)} \sqrt{A^2 - 4 p_T^{(l)2} \cancel{E}_T^2} \right), \quad (\text{B.7})$$

where $A = M_W^2 + 2 \vec{p}_T^{(l)} \cdot \vec{\cancel{E}}_T$. Again $l = e, \mu$. The two-fold degeneracy of the neutrino longitudinal momentum (above) is resolved by considering the top quark mass. Thus, if $A^2 - 4 p_T^{(l)2} \cancel{E}_T^2 \geq 0$, the value of $p_{\nu L}$ that best yields the known top mass via $m_{l\nu b}^2 = m_t^2$ is selected.

Detector effects can reduce the top reconstruction efficiency and, in particular, force the radical in equation B.7 to be negative. In this case, in order to better recover the correct kinematics [432], we instead first reconstruct the top quark directly by demanding $m_{l\nu b}^2 = m_t^2$. The longitudinal momentum of the neutrino is expressed as

$$p_L^{(\nu)} = \frac{A' p_{(bl)L}}{2(E_{(bl)}^2 - p_{(bl)L}^2)} \quad (\text{B.8})$$

$$\pm \frac{1}{2(E_{(bl)}^2 - p_{(bl)L}^2)} \left(p_{(bl)L}^2 A'^2 + (E_{(bl)}^2 - p_{(bl)L}^2) (A'^2 - 4E_{(bl)}^2 \cancel{E}_T^2) \right)^{1/2}$$

where $A' = m_t^2 - M_{(bl)}^2 + 2\vec{p}_{(bl)T} \cdot \vec{E}_F$. Here l runs over e, μ . The two-fold ambiguity is broken by choosing the value that best reconstructs $M_W^2 = m_{l\nu}^2$. Notice because $A' \sim m_t^2$ in the equation above, the value under the radical has a smaller chance of being negative.

C Spin Determination: Lepton Polarization

The charged lepton from top quark decay is maximally correlated with top quark spin. The connection between top quark spin and the charged lepton can be found from the distribution in θ_{hel} , the angle of the lepton in the rest frame of top quark relative to the topquark direction of motion in the overall c.m. frame. This is usually named as ‘‘helicity’’ basis. The angular correlation of the lepton ℓ^+ is given by

$$\frac{1}{\sigma} \frac{d\sigma}{d \cos \theta_{\text{hel}}} = \frac{1 \pm \cos \theta_{\text{hel}}}{2}, \quad (\text{C.9})$$

with the (+) choice for right-handed and (−) for left-handed top quarks; Clearly, the charged lepton from a right-handed top quark prefers to move along the top quark direction . In the top-quark rest frame, 75% (25%) of charged leptons from t_R (t_L) decays follow the top-quark direction.

Contribution 15

Effective axial-vector coupling of the gluon and top-quark charge asymmetry at the LHC

Emidio Gabrielli, Andrea Giammanco, Antonio Racioppi, Martti Raidal

Abstract

We study the top quark charge asymmetry induced by an effective axial-vector coupling of the gluon at the LHC experiments. We showed that rapidity cut-dependent asymmetries are more sensitive to the new physics than the independent ones. We also study the dependence of the asymmetries and variations of the total $t\bar{t}$ cross sections on the invariant mass of the $t\bar{t}$ system and show that it would be necessary to measure those quantities as functions of $m_{t\bar{t}}$ at the LHC. If this is done, in the context of the considered new physics scenario, the 7 TeV LHC has enough sensitivity either to confirm the Tevatron top charge asymmetry anomaly or to rule it out. In the latter case the LHC will be able to put stringent constraint on the new physics scale Λ in this framework.

1 INTRODUCTION

The 3.4σ excess over the standard model (SM) predictions [434–437] in the top-quark charge asymmetry (A_{FB}^t) observed by the CDF collaboration at the Fermilab Tevatron [120], has triggered numerous theoretical and experimental studies of top quark production at hadron colliders. An intriguing property of the measured asymmetry is that it increases with the $t\bar{t}$ invariant mass $m_{t\bar{t}}$. At the same time the measured $t\bar{t}$ production cross section is consistent, within experimental errors, with the SM predictions [438–440] both at Tevatron [441, 442] and at the CERN Large Hadron Collider (LHC) [443, 444]. Motivated by those results, the SM predictions for the $t\bar{t}$ charge asymmetry have been revised [445, 446], showing a moderate 20% increase due to QED and electroweak corrections.

Numerous new physics explanations (see Ref. [447] for a recent summary review) have been proposed to explain the observed anomaly, predicting the existence of new particles whose contributions produce the asymmetry. Those scenarios can be directly tested at the LHC experiments by looking for new particle interactions. In the light of the LHC results several popular explanations to the $t\bar{t}$ charge asymmetry such as the axigluons [448–450], Z' [451] or W' [452] bosons are stringently constrained.

However, effective field theory offers also model-independent tests of the top quark charge asymmetry. Particularly interesting among those is the one due to an effective axial-vector coupling of the gluon [453]. This scenario does predict the correct sign and the correct $m_{t\bar{t}}$ dependence of the Tevatron anomaly and does not necessarily require new light resonances. Therefore tests of this scenario require in particular the measurement of the top quark charge asymmetry dependence on $m_{t\bar{t}}$ at the LHC.

Although the LHC is a pp collider with a symmetric initial state, the $t\bar{t}$ charge asymmetry can be defined and studied at the LHC in $q\bar{q}$ collisions using anti-quarks from the sea [434, 435]. Because the sea quark parton distributions differ from the valence ones, top and anti-top quarks are preferably produced at different rapidities. Therefore, studying top quark charge asymmetries at large rapidities and large invariant masses will enhance the asymmetries both in the SM as well as in scenarios of new physics [445]. At present the ATLAS [454] and CMS [455] experiments have published only their measurements of rapidity cut-independent top quark charge asymmetries. Their results are consistent with the SM predictions. The first results on rapidity and invariant mass-dependent observables for top quark charge asymmetry have been released by the CMS experiment, comparing data with the SM prediction and with our prediction for the considered new physics scenario [456].

The aim of this work is to study rapidity and invariant mass-dependent top quark charge asymmetries at the LHC in the scenario of an effective axial-vector coupling of the gluon. We show that the rapidity and invariant mass-dependent asymmetries are much more appropriate for testing this type of new physics scenarios than the cut-independent ones used by ATLAS [454] and CMS [455] so far. We show that the Tevatron observation of large asymmetry can be either confirmed or ruled out already at the 7 TeV LHC with 10 fb^{-1} data.

2 EFFECTIVE GLUON COUPLINGS IN FIELD THEORY

The most general effective Lagrangian for quark-gluon interactions, containing the lowest dimensional operators, and compatible with gauge-, CP-, and Lorentz-invariance, is [453]

$$\begin{aligned} \mathcal{L} = & -ig_S \left\{ \bar{Q} T^a \left[\gamma^\mu \left(1 + g_V(q^2, M) + \gamma_5 g_A(q^2, M) \right) G_\mu^a \right. \right. \\ & \left. \left. + g_P(q^2, M) q^\mu \gamma_5 G_\mu^a + g_M(q^2, M) \sigma^{\mu\nu} G_{\mu\nu}^a \right] Q \right\}, \end{aligned} \quad (1)$$

where g_S is the strong coupling constant, G_μ^a is the gluon field, T^a are the color matrices, M is some energy scale, q^2 is the invariant momentum-squared carried by the gluon and Q denotes a generic quark field. From now on we will assume that the dominant contribution to the $g_{A,P}(q^2, M)$ form factors arises from new physics (NP) with characteristic scale above the electroweak (EW) scale. In this case the scale M should be identified with the NP scale. Model independently, QCD gauge invariance requires that $2m_Q g_A(q^2, M) = q^2 g_P(q^2, M)$, thus

$$\lim_{q^2 \rightarrow 0} g_{A,V}(q^2, M) = 0 \quad (2)$$

since no $1/q^2$ singularities are present in g_P . As observed before [453], Eq.(2) does not impose any additional constraint on the form factors $g_{A,V}$, which could have different magnitudes at arbitrary q^2 . Therefore, gauge-invariance does not prevent us to have $g_V \ll g_A$ as long as $q^2 \neq 0$. If the origin of the large A_{FB}^t is due to NP that has $(V \pm A)$ currents as in the SM, large g_V and g_A can be generated. However, this scenario is phenomenologically unacceptable [453] because g_V is strongly constrained by the total $q\bar{q} \rightarrow t\bar{t}$ cross section. Thus we will neglect the contribution of the vectorial form factor $g_V(q^2, M)$ in Eq.(1), and consider only NP scenarios that generate g_A with the hierarchy $g_V \ll g_A$. In the limit of $q^2 \ll M^2$, it is useful to parametrize the axial-vector form factor as

$$g_A(q^2, M) = \frac{q^2}{\Lambda^2} F(q^2, \Lambda), \quad (3)$$

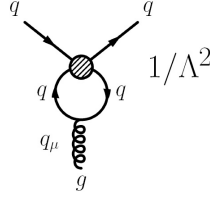


Figure 1: Feynman diagram in the effective low energy theory that generates the effective axial-vector coupling of gluon.

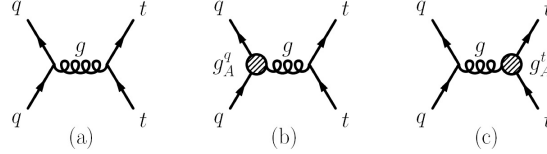


Figure 2: Feynman diagrams (a)-(c) for the $q\bar{q} \rightarrow t\bar{t}$ process, with the contribution of the gluon effective axial-vector couplings $g_A^{q,t}$.

where we absorb the NP coupling α_{NP} and loop factor into the NP scale, $\Lambda^2 = M^2/(4\pi\alpha_{NP})$. Notice the q^2 dependence that enhances the asymmetry at large invariant masses.

Assuming that there are perturbative NP above the EW scale, model independently the effective operators [457]

$$O_{AV}^{1,8} = \frac{1}{\Lambda^2} [\bar{Q} T_{1,8} \gamma^\mu \gamma_5 Q] [\bar{Q} T_{1,8} \gamma^\mu Q], \quad (4)$$

$$O_{PS}^{1,8} = \frac{1}{\Lambda^2} [\bar{Q} T_{1,8} \gamma_5 Q] [\bar{Q} T_{1,8} Q], \quad (5)$$

generate g_A via the one-loop diagrams depicted in Fig. 1. Here $T_1 = 1$ and $T_8 = T^a$, thus both isoscalar and octet operators contribute. Notice that: (i) no g_V is induced due to QCD parity conservation; (ii) the one-loop induced g_A is enhanced by $\log(q^2/\Lambda^2)$; (iii) the operators $O_{AV}^{1,8}$, $O_{PS}^{1,8}$ do not induce flavor changing (FC) processes; however, there could be different quark flavors in the loop in Fig. 1 (extending the operator basis to $Q \rightarrow Q'$, $V \leftrightarrow A$, $P \leftrightarrow S$ is straightforward); (iv) the operators $O_{AV}^{1,8}$, $O_{PS}^{1,8}$ do not interfere with the corresponding QCD induced 4-quark processes. The latter point implies that the stringent LHC constraints [458,459] on 4-quark contact interactions do not apply to our scenario.

Alternatively, large g_A might be generated by new strongly-coupled parity-violating dynamics related to electro-weak symmetry breaking (EWSB) at the 1-2 TeV scale. A plethora of new resonances should occur at the LHC allowing to test this scenario. As we are not able to make predictions in this case, we shall not elaborate on this new physics possibility and simply assume the existence of operators (5).

3 CROSS SECTIONS AT THE LHC

The effective axial-vector coupling of gluon affects the $t\bar{t}$ cross section at the LHC via the parton level processes $q\bar{q} \rightarrow t\bar{t}$ and $gg \rightarrow t\bar{t}$ as depicted in Figs. 2 and 3, respectively. Notice that our scenario modifies not only the subdominant $q\bar{q}$ but also the dominant gg production channel. The effective axial-vector coupling of the top-quark affects only the s-channel (diagram 3(d));

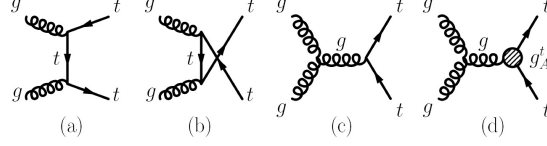


Figure 3: Feynman diagrams (a)-(d) for the $gg \rightarrow t\bar{t}$ process, with the contribution of the gluon effective axial-vector coupling g_A^t .

due to the Ward identity in Eq.(2), the effective axial-vector contribution vanishes in the \hat{t} - and \hat{u} -channels, diagrams 3(a) and 3(b) respectively, because the gluons attached to the axial-vector vertex are on-shell. Therefore detailed measurements of the $t\bar{t}$ cross sections are needed at the LHC to test this scenario.

For $q\bar{q} \rightarrow t\bar{t}$ the differential cross section in the massless light-quarks q limit (summed over all colors) is given by

$$\begin{aligned} \frac{d\sigma^{q\bar{q}}}{d\hat{t}} &= \frac{8\pi\alpha_S^2}{9\hat{s}^4} \left[\left(\hat{t}^2 + (\hat{s} - 2m_t^2)\hat{t} + \frac{\hat{s}^2}{2} + m_t^4 \right) \times \right. \\ &\quad \left. (1 + |g_A^q|^2 + |g_A^t|^2 + |g_A^q|^2|g_A^t|^2) \right. \\ &\quad \left. - 2|g_A^t|^2 m_t^2 \hat{s} (1 + |g_A^q|^2) \right. \\ &\quad \left. + 2\text{Re}[g_A^q] \text{Re}[g_A^t] \hat{s}(\hat{s} + 2\hat{t} - 2m_t^2) \right], \end{aligned} \quad (6)$$

where g_A^q and g_A^t are the corresponding axial-vector form factors for the light-quark q and top-quark, respectively, and $\hat{s}, \hat{t}, \hat{u}$ are the usual Mandelstam variables. After integrating Eq.(6) over the full range of \hat{t} , the total partonic cross section is given by

$$\begin{aligned} \sigma^{q\bar{q}}(\hat{s}) &= \frac{8\pi\alpha_S^2\beta_t}{27\hat{s}} \left\{ \left(1 + 2\frac{m_t^2}{\hat{s}}\right) (1 + |g_A^q|^2) + \right. \\ &\quad \left. \beta_t^2 |g_A^t|^2 (1 + |g_A^q|^2) \right\}, \end{aligned} \quad (7)$$

where $\beta = \sqrt{1 - \rho}$ and $\rho = 4m_t^2/\hat{s}$.

For $gg \rightarrow t\bar{t}$ scattering the differential unpolarized cross section is given by

$$\begin{aligned} \frac{d\sigma^{gg}}{d\hat{t}} &= \frac{\pi\alpha_S^2}{64\hat{s}^2} \left[12M_{ss} + \frac{16}{3} (M_{tt} + M_{uu}) - \frac{2}{3}M_{tu} \right. \\ &\quad \left. + 6(M_{st} + M_{su}) \right], \end{aligned} \quad (8)$$

with

$$\begin{aligned} M_{ss} &= \frac{4}{\hat{s}^2} [(\hat{t} - m_t^2)(\hat{u} - m_t^2) + (\hat{t}\hat{u} - m_t^4) |g_A^t|^2], \\ M_{tt} &= \frac{2}{(\hat{t} - m_t^2)^2} [(\hat{t} - m_t^2)(\hat{u} - m_t^2) - 2m_t^2(\hat{u} + m_t^2)], \\ M_{tu} &= \frac{4m_t^2}{(\hat{t} - m_t^2)(\hat{u} - m_t^2)} (\hat{s} - 4m_t^2), \\ M_{st} &= \frac{4}{\hat{s}(\hat{t} - m_t^2)} [m_t^4 - \hat{t}(\hat{s} + \hat{t})], \end{aligned} \quad (9)$$

and $M_{uu} = M_{tt} \{t \leftrightarrow u\}$, $M_{su} = M_{st} \{t \leftrightarrow u\}$. This expression is $SU(3)_c$ gauge invariant.

After integrating Eq.(8) over the full range of \hat{t} , we obtain for the total partonic cross section

$$\begin{aligned} \hat{\sigma}^{gg}(\hat{s}) &= \frac{\pi\alpha_S^2}{48\hat{s}} \left\{ (16 + \rho(16 + \rho)) \log\left(\frac{1 + \beta}{1 - \beta}\right) \right. \\ &\quad \left. - \beta(28 + 31\rho + 6|g_A|^2(\rho - 1)) \right\}. \end{aligned} \quad (10)$$

Finally, the hadronic cross section $pp \rightarrow t\bar{t}X$ at LHC is obtained by convoluting the partonic cross sections in Eqs. (7),(10) with the corresponding parton distribution functions (PDF) for quarks and gluons, namely

$$\sigma_{pp \rightarrow t\bar{t}X} = \int \left(\sum_q d\mu_q \sigma_{qq}(\hat{s}) + d\mu_g \sigma_{gg}(\hat{s}) \right), \quad (11)$$

where $d\mu_q$ and $d\mu_g$ indicate the differential integrations in $dx_1 dx_2$ convoluted with the quark and gluon PDFs respectively. In the numerical integration of Eq.(11) we have used the CTEQ6L1 parton distribution function (PDF) [429], where we set the PDF scale $\mu = m_t$ with the top quark mass $m_t = 172$ GeV.

4 CHARGE ASYMMETRY AT THE LHC

The most useful top charge asymmetries at the LHC are defined as [445]

- the *cut-independent* charge asymmetry, as measured by ATLAS and CMS,

$$A_C^y = \frac{N(\Delta_y > 0) - N(\Delta_y < 0)}{N(\Delta_y > 0) + N(\Delta_y < 0)}, \quad (12)$$

where $\Delta_y \equiv |y_t| - |y_{\bar{t}}|$;

- the *integrated* pair charge-asymmetry

$$A_C^{\text{cut}}(Y_c) = \frac{N(y_t > y_{\bar{t}}) - N(y_t < y_{\bar{t}})}{N(y_t > y_{\bar{t}}) + N(y_t < y_{\bar{t}})}, \quad (13)$$

as a function of the cut Y_c on mean rapidity, namely $(y_t + y_{\bar{t}})/2 > Y_c$.

All the above observables are defined in the laboratory frame. Due to the symmetry of the initial proton-proton configuration, also $A_C^{\text{cut}}(Y_c)$ will vanish if the full rapidity range is integrated, that is when Y_c approaches its maximum kinematically allowed value.

Top quark pair production by the gluon fusion mechanism, which is dominant at the LHC (representing 70% and 90% of the total cross-section at 7 TeV and 14 TeV c.o.m. energy respectively), is charge symmetric under higher order corrections. However, the contributions of the gluon-gluon collisions can be reduced by imposing a lower cut on the top quark pair invariant mass $m_{t\bar{t}}$. This has the effect of eliminating the regions of lower longitudinal momentum fraction of the colliding partons where the gluon density is much larger than the quark densities. In addition, imposing a lower cut on $m_{t\bar{t}}$ also has the advantage of enhancing the $q\bar{q} \rightarrow t\bar{t}$ contribution to the charge asymmetry, although at the price of reducing the $t\bar{t}$ pair statistics. This

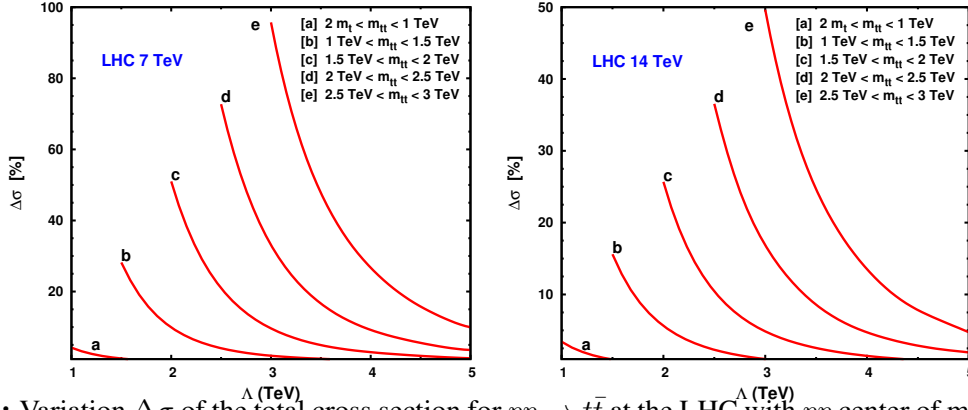


Figure 4: Variation $\Delta\sigma$ of the total cross section for $pp \rightarrow t\bar{t}$ at the LHC with pp center of mass energies $\sqrt{s} = 7$ TeV (left panel) and 14 TeV (right panel) for $m_t = 172$ GeV, as a function of the scale Λ in TeV, for several regions ([a-e]) of $t\bar{t}$ invariant mass $m_{t\bar{t}}$.

requirement has also crucial implications for our scenario, since it increases the contribution of the axial-vector coupling of the gluon to the charge asymmetry. This is due to the fact that the effective coupling g_A grows as $m_{t\bar{t}}^2/\Lambda^2$ at large $m_{t\bar{t}}$ values (but with $m_{t\bar{t}} \leq \Lambda$). We will restrict our analysis to the case of real and universal axial-vector gluon couplings. In particular, we parametrize the axial-vector coupling (for values of $|q^2| < \Lambda^2$) as follows

$$g_A^t = g_A^q = \frac{q^2}{\Lambda^2}. \quad (14)$$

Indeed, in order to explain the Tevatron anomaly on A_{FB}^t , while requiring conservative constraints on the $t\bar{t}$ cross sections at the Tevatron, it was suggested [453] that the most favored scenario is the one where all axial-vector couplings are universal and real, with the NP scale Λ lying in a narrow range $1 \text{ TeV} < \Lambda < 1.3 \text{ TeV}$.

In our numerical analysis we have not included the SM contribution to the charge asymmetry. Indeed, this is almost negligible with respect to the axial-vector gluon contribution for most of the kinematic regions considered here. In particular, we have retained only the g_A contribution in the numerators of the asymmetries neglecting the corresponding SM contribution. However, we have retained the SM effect (at the leading order (LO) in QCD) in the evaluation of the total number of events entering the equation for the charge asymmetry.

Then, following the definition of asymmetry, the exact value of $A_C^{\text{SM+NP}}$, including the SM one (A_C^{SM}), are related to the results of A_C^{NP} presented here by the following equation

$$A_C^{\text{SM+NP}} = A_C^{\text{NP}} + \frac{A_C^{\text{SM}}}{1 + \Delta\sigma}, \quad (15)$$

where $\Delta\sigma$ is the percentage variation of the total cross section (defined as $\Delta\sigma = \sigma^{\text{NP}}/\sigma^{\text{SM}}$), and $\sigma^{\text{NP (SM)}}$ represents the pure NP (SM) contributions to the total cross section evaluated in the same kinematic region of charge asymmetry. The symbol A_C appearing in the figures stands for the pure NP contribution to the charge asymmetry A_C^{NP} as defined above.

The numerical values of $\Delta\sigma$ are plotted in Fig. 4 for the 7 TeV and 14 TeV LHC as function of the new physics scale Λ for several kinematic regions [a-e] of $m_{t\bar{t}}$ as indicated in the Figure. Regarding the choice of ranges of $m_{t\bar{t}}$, we adopted the criterion that the maximum value of $m_{t\bar{t}}$

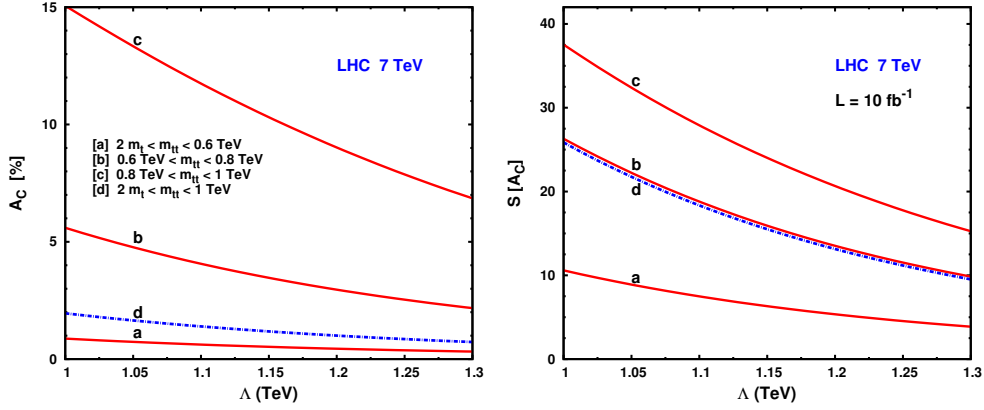


Figure 5: The cut-independent $t\bar{t}$ charge asymmetry A_C in percentage (left plots) and corresponding statistical significance $S[A_C]$ (right plots) at LHC with pp center of mass energy $\sqrt{s} = 7$ TeV and integrated luminosity $L = 10 \text{ fb}^{-1}$, with $m_t = 172$ GeV, as a function of the scale Λ in TeV, for several regions ([a-d]) of $t\bar{t}$ invariant mass $m_{t\bar{t}}$.

satisfies the condition $m_{t\bar{t}}^{\max} \leq \Lambda$ as required by the validity range of the low energy limit in the g_A form factor. The cross sections have been evaluated at leading order (LO) in QCD. The picture that emerges from these results is clear. If we analyse ranges of $m_{t\bar{t}}$ below 1 TeV, curve [a], the expected variation in the total cross section is quite small, below 5% for both the 7 TeV and 14 TeV LHC energies. This is due to the fact that requiring $m_{t\bar{t}}$ to be below 1 TeV, the g_A contribution at low energy is still largely screened by the gluon fusion mechanism, which is the dominant mechanism of top-quark pair production at the LHC. Clearly, by increasing the $m_{t\bar{t}}$ mass range the NP effect could be amplified and larger deviations could be observed in the cross sections, due to the quark-antiquark production mechanism. These results could also be used to set lower bounds on the scale Λ by requiring that no excess in the total cross section is observed with respect to the SM predictions. For instance, by limiting the deviations on total cross section below 20 %, one can see from curve [e] that a lower bound $\Lambda > 4$ TeV could be obtained at LHC 7 TeV. Clearly, by increasing the $m_{t\bar{t}}$ range, the statistical error on the cross section also increases, and a more accurate analysis, which is beyond the purpose of the present work, would be necessary.

Our numerical results for the g_A contributions to the charge asymmetries at the 7 TeV LHC defined in Eqs. (12) and (13) are shown in the left panels of Fig. 5 and Fig. 6, respectively. In order to estimate whether the asymmetries can be measured at the LHC or not, we have used approximate expressions for the statistical significance $S[A_C]$ [448]

$$S[A_C] \simeq A_C \sqrt{L \sigma^{\text{NP+SM}}}, \quad (16)$$

where L stands for the integrated luminosity and $\sigma^{\text{NP+SM}}$ is the total cross section including the SM and NP contributions. In $\sigma^{\text{NP+SM}}$ we have used the LO cross sections multiplied by a rescaling factor K , which is obtained by simply rescaling the total cross section evaluated at LO in QCD to its value corrected to next-to-next-to-leading order (NNLO) in QCD. Those results are presented in the right panels of Fig. 5 and Fig. 6. Notice that the significance in Eq.(16) is a simple theoretical estimation of the true one, since it does not take into account efficiencies, acceptance, resolution, and systematics.

In Fig. 5 we plot the cut-independent $t\bar{t}$ charge asymmetry A_C (left plot) and corresponding significance (right plot) as a function of the scale Λ in the range [1-1.3] TeV. This is the definition adopted by the ATLAS and CMS collaborations to measure the top-quark charge asymmetry at the LHC. The ranges of $m_{t\bar{t}}$ [a-d] appearing in Figs. 5 and 6 are given by

$$\begin{aligned}
[a] &= 2m_t < m_{t\bar{t}} < 0.6 \text{ TeV}, \\
[b] &= 0.6 \text{ TeV} < m_{t\bar{t}} < 0.8 \text{ TeV}, \\
[c] &= 0.8 \text{ TeV} < m_{t\bar{t}} < 1 \text{ TeV}, \\
[d] &= 2m_t < m_{t\bar{t}} < 1 \text{ TeV}.
\end{aligned}
\tag{17}$$

In the following, we will refer to the $m_{t\bar{t}}$ ranges [a-d] as the ones defined in Eq.(17).

As seen from these results, the g_A contribution to A_C is quite large when measured at $m_{t\bar{t}}$ masses close to the value of the scale Λ . In particular, for range [c], A_C could be of order of 15% or 7%, for scales $\Lambda = 1$ TeV or $\Lambda = 1.3$ TeV respectively, while the corresponding significance can reach values of 37 and 15 respectively. On the other hand, when integrated over a large $m_{t\bar{t}}$ range, see for instance the curve relative to range [b], A_C turns out to be quite small (below 2 %) and comparable (although a bit larger) to the SM result [445].

In Table 1 we give some numerical results for the values of the $t\bar{t}$ cut-independent charge asymmetry A_C (in percentage) evaluated at $\Lambda = 1$ TeV and at LHC energies $\sqrt{s} = 7$ TeV and $\sqrt{s} = 8$ TeV, integrated over the following kinematical ranges for $m_{t\bar{t}}$ and Y_{tt} [460]:

$$\begin{aligned}
\Delta_1 &= \{2m_t < m_{t\bar{t}} < 420 \text{ GeV}\}, \\
\Delta_2 &= \{420 \text{ GeV} < m_{t\bar{t}} < 512 \text{ GeV}\}, \\
\Delta_3 &= \{512 \text{ GeV} < m_{t\bar{t}} < 1 \text{ TeV}\}, \\
\Delta_4 &= \{0 < |Y_{tt}| < 0.41\}, \\
\Delta_5 &= \{0.41 < |Y_{tt}| < 0.9\}, \\
\Delta_6 &= \{|Y_{tt}| > 0.9\},
\end{aligned}
\tag{18}$$

where Y_{tt} is defined as the rapidity of the 4-momentum $p_{t\bar{t}} \equiv p_t + p_{\bar{t}}$, where p_t and $p_{\bar{t}}$ are the top- and antitop-quark 4-momenta in the LHC proton-proton center of mass system respectively. For each range Δ_{1-6} in Eq. (18), the other kinematic variables are integrated over the whole allowed kinematical range. In Table 2 we give some numerical results for the values of the significances (see Eq. (16)) of the corresponding cut-independent $t\bar{t}$ charge asymmetries A_C computed in Table 1. Results in Table 2 are evaluated according to our definition of significance as given in Eq. (16), with total cross sections $\sigma^{\text{SM+NP}}$ evaluated at NNLO in QCD, and correspond to an integrated luminosity $L = 10 \text{ fb}^{-1}$. For the case at $\sqrt{s} = 8$ TeV, we have used the same NNLO QCD rescaling factor K as for $\sqrt{s} = 7$ TeV.

In Fig. 6 we show the integrated pair charge asymmetry $A_C^{\text{cut}}(Y_c)$ as defined in Eq.(13) and corresponding significance, as a function of the cut Y_c on the mean rapidity Y defined as $Y = (y_t + y_{\bar{t}})/2$, for the representative value of $\Lambda = 1.3$ TeV. In the case of lower values of Λ , the NP effects are just more pronounced and we will also include the case of $\Lambda = 1$ TeV in our discussion below. As we can see from these results, $A_C^{\text{cut}}(Y_c)$ turns out to be the most sensitive probe of our scenario. In particular, at $\Lambda = 1.3$ TeV, for $m_{t\bar{t}}$ in range [c], the value of $A_C^{\text{cut}}(Y_c)$ can vary, as a function of Y_c , from 8% up to 25% for $\Lambda = 1.3$ TeV and can increase from 15% up to 55% for $\Lambda = 1$ TeV. The value of $A_C^{\text{cut}}(Y_c)$ in range [c] evaluated for $Y_c = 0.3$, where its significance is maximized, is of order of 10% for $\Lambda = 1.3$ TeV and can reach values of 20% for

\sqrt{S}	$A_C^{\%}(\Delta_1)$	$A_C^{\%}(\Delta_2)$	$A_C^{\%}(\Delta_3)$	$A_C^{\%}(\Delta_4)$	$A_C^{\%}(\Delta_5)$	$A_C^{\%}(\Delta_6)$
7 TeV	0.32	0.90	4.9	2.2	1.4	2.1
8 TeV	0.28	0.78	4.3	1.9	1.3	2.0

Table 1: Numerical values of the *cut-independent* $t\bar{t}$ charge asymmetries A_C in percentage, evaluated at $\Lambda = 1$ TeV and for LHC energies $\sqrt{s} = 7$ TeV and $\sqrt{s} = 8$ TeV, integrated in the kinematical ranges Δ_{1-6} given in Eq.(18).

\sqrt{S}	$S_{A_C}(\Delta_1)$	$S_{A_C}(\Delta_2)$	$S_{A_C}(\Delta_3)$	$S_{A_C}(\Delta_4)$	$S_{A_C}(\Delta_5)$	$S_{A_C}(\Delta_6)$
7 TeV	1.5	3.9	21	8.2	5.4	11
8 TeV	1.5	4.1	23	8.6	6.0	13

Table 2: Numerical values of the significance of the *cut-independent* $t\bar{t}$ charge asymmetry A_C , evaluated at $\Lambda = 1$ TeV and for LHC energies $\sqrt{s} = 7$ TeV and $\sqrt{s} = 8$ TeV, corresponding to an integrated luminosity $L = 10 \text{ fb}^{-1}$ and integrated in the kinematical ranges Δ_{1-6} given in Eq.(18).

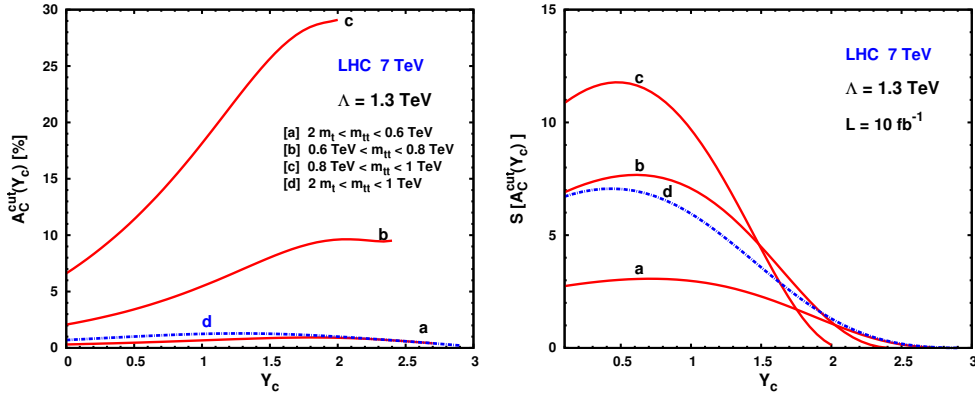


Figure 6: Integrated pair charge asymmetry $A_C^{\text{cut}}(Y_c)$ in percentage (left plots) and corresponding statistical significance $S[A_C^{\text{cut}}(Y_c)]$ (right plots) at LHC with pp center of mass energy $\sqrt{s} = 7$ TeV and integrated luminosity $L = 10 \text{ fb}^{-1}$, with $m_t = 172$ GeV, as a function of the cuts on the mean rapidity $|Y| > Y_c$ (in the lab frame), for several regions ([a-d]) of $t\bar{t}$ invariant mass $m_{t\bar{t}}$. Plots correspond to the scale $\Lambda = 1.3$ TeV.

$\Lambda = 1$ TeV. However, even at $Y_c = 1.5$ the integrated charge asymmetry is still quite large. As shown in Fig. 6, for $\Lambda = 1.3$ TeV, the value of $A_C^{\text{cut}}(1.5)$ is of order 25% and 8% for $m_{t\bar{t}}$ ranges [c] and [b] respectively, with a corresponding significance of order 5 in both cases. For $\Lambda = 1$ TeV, the value of $A_C^{\text{cut}}(1.5)$ can increase up to 50% and 20% if integrated in the ranges [c] and [b] respectively, while the corresponding significances are above 10.

In Fig. 7 we analyze the statistical significance of the cut-independent charge asymmetry A_C versus the scale Λ in the range of $\Lambda=[1.5-4]$ TeV and for several ranges of $m_{t\bar{t}}$ as indicated in the Figure. The left and right plots correspond to LHC center of mass energies of $\sqrt{s} = 7$ TeV and $\sqrt{s} = 14$ TeV respectively. We have used the same convention for the Λ and $m_{t\bar{t}}$ ranges as adopted in Fig. 4. Assuming that no significant deviations from SM predictions on the charge asymmetry A_C will be observed, from results in Fig. 7 one can derive lower bounds on

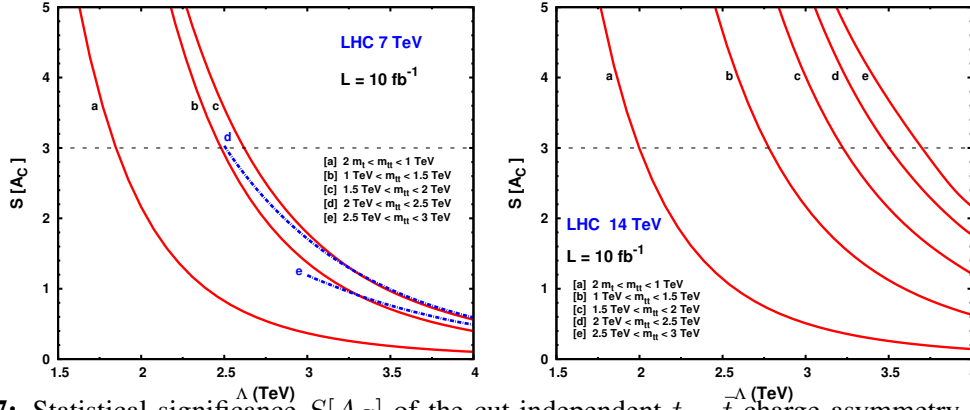


Figure 7: Statistical significance $S[A_C]$ of the cut-independent $t - \bar{t}$ charge asymmetry A_C at LHC with pp center of mass energies $\sqrt{s} = 7$ TeV (left plots) and $\sqrt{s} = 14$ TeV (right plot) with integrated luminosity $L = 10 \text{ fb}^{-1}$, with $m_t = 172$ GeV, as a function of the scale Λ in TeV, for several regions ([a-e]) of $t\bar{t}$ invariant mass $m_{t\bar{t}}$.

the scale Λ . For example, by requiring that $S[A_C] < 3$, we get for $L = 10 \text{ fb}^{-1}$, the following (strongest) lower bounds:

- $\Lambda > 2.6$ TeV, for $m_{t\bar{t}} \in [1.5-2]$ TeV at LHC at 7 TeV;
- $\Lambda > 3.7$ TeV, for $m_{t\bar{t}} \in [2.5-3]$ TeV at LHC at 14 TeV.

As can be seen from the dashed (blue) curves in the left plot of Fig. 7, for LHC at 7 TeV there is no advantage, concerning the lower bounds of Λ , in going to higher bin ranges in $m_{t\bar{t}} > 2$ TeV, due to the loss of statistics.

5 CONCLUSIONS

We have studied the gluon effective axial-vector coupling induced top charge asymmetry at the LHC. We have compared rapidity cut-dependent and independent asymmetries and shown that the former are more sensitive to new physics than the latter. We have also studied the asymmetries and variations of total $t\bar{t}$ cross sections at different invariant masses of the $t\bar{t}$ system and shown that it would be necessary to measure those quantities as functions of $m_{t\bar{t}}$ at the LHC. A first measurement has been performed by the CMS collaboration [456], finding agreement with both the SM and the considered new physics scenario. With more data and a better control of the systematic uncertainties the LHC might either confirm the Tevatron top charge asymmetry anomaly or rule it out in the context of the considered new physics scenario. In the latter case the LHC will be able to put stringent constraint on the new physics scale Lambda.

ACKNOWLEDGEMENTS

We thank T. Chwalek, T. Peiffer, G. Rodrigo, and J. Wagner-Kuhr for several communications. This work was supported by the ESF grants 8090, MTT59, MTT60, JD164, by the recurrent financing SF0690030s09 project and by the European Union through the European Regional Development Fund.

Contribution 16

Searching for sgluons in multitop production at the LHC

Samuel Calvet, Benjamin Fuks, Philippe Gris, Adrien Renaud, Loïc Valéry, Dirk Zerwas

Abstract

In this report, we present the results of our activities addressing the investigation of signatures containing multiple top quarks at the Large Hadron Collider. We use the framework of a simplified effective theory containing color-octet scalar particles decaying to top quarks and light jets and explore final state signatures with either four top quarks or two top quarks and two light jets. We investigate the sensitivity of both a same-sign dilepton plus jets and a single lepton plus jets analysis to the possible presence of new physics events, and we find that signal cross sections down to a few tens of fb can be already probed at the Large Hadron Collider, assuming 10 fb^{-1} of collected data at a center-of-mass energy of 7 TeV.

1 INTRODUCTION

Among all the alternatives proposed to extend the Standard Model of particle physics, supersymmetric theories, and more particularly their minimal version, the so-called Minimal Supersymmetric Standard Model (MSSM) [74, 75], are theoretically and phenomenologically well-motivated. Assuming a symmetry between the fermionic and bosonic degrees of freedom of the theory, they predict fermionic (bosonic) partners for each bosonic (fermionic) Standard Model particle. They feature a solution to the hierarchy problem [461], gauge coupling unification at high energies [462] and contain, as the lightest supersymmetric particle, a candidate to solve the dark matter problem in the universe [463]. However, supersymmetric partners of the Standard Model particles have not been observed yet. Therefore, and in order to remain a viable solution to the hierarchy problem, supersymmetry has to be softly broken, which shifts the masses of the superpartners around the TeV scale.

This explains why searches for the supersymmetric counterparts of the Standard Model particles are among the main experimental topics at the Large Hadron Collider (LHC) experiments at CERN. Direct searches are currently under way and limits on the supersymmetric masses are set to higher and higher scales by the ATLAS and CMS experiments [76, 77]. However, most of the results are derived under the hypothesis of the constrained MSSM, *i.e.*, a framework in which the $\mathcal{O}(100)$ new free parameters of the theory are reduced to four parameters and one sign. Consequently, there exist alternative realizations of supersymmetry with properties different from those expected in the constrained MSSM and thus not covered by the current experimental analyses. Therefore, their investigation at the LHC deserves dedicated studies in order to prepare the interpretation of data within these models. As an example, we have chosen in this work to focus on $N = 1/N = 2$ hybrid supersymmetric theories [464–470] and R -symmetric supersymmetric theories [471–473] which both predict, among others, the

existence of a new color-octet scalar field. In these models, the $SU(3)_c$ vector supermultiplet of the MSSM is supplemented by an additional chiral supermultiplet lying in the adjoint representation of the $SU(3)_c$ gauge group, forming hence a complete gauge supermultiplet of an $N = 2$ supersymmetry. The latter contains a vector degree of freedom which corresponds to the gluon field, two (two-component) fermionic fields mixing to form a Dirac gluino field, in contrast to the Majorana counterpart included in the MSSM, and one color-octet scalar particle commonly dubbed sgluon [474, 475]. Let us note that another type of color-octet scalar particles, called hyperpions, also appear in vectorlike confining theories at the TeV scale [476–481]. While some signatures are similar, the supersymmetric theories can lead to additional final states. In the following we will therefore only consider the supersymmetric case.

Being sensitive to the strong interaction, sgluons (strongly) couple to gluons and quarks and are therefore expected to be copiously pair-produced at the LHC. Then, their observation could be possible through their allowed decays into a pair of light jets, a pair of top quarks, or even an associated pair of a top quark and a light jet. In this work, rather than handling the complete model, which also demands a careful design of a theoretically motivated and not experimentally excluded benchmark scenario, we follow an alternative approach where we construct a simplified model allowing for sgluon pair hadroproduction and decay either into two top quarks and two light jets, or into four top quarks. Assuming a sgluon with a mass lying in the TeV range, together with sensible couplings to quarks and gluons, we analyze the sensitivity of the LHC to the possible observation of sgluon particles within multitop events containing either two top quarks and two additional light jets or four top quarks. Both the single lepton plus jets and same-sign dilepton plus jets channels are investigated.

The outline of this contribution is as follows: In Section 2, we describe the effective theory which we have constructed modeling sgluon pair production and decays at the LHC and define four benchmark scenarios for our phenomenological studies. In Section 3, we present the details of our Monte Carlo simulations and the results of our two phenomenological analyses. Our conclusions are given in Section 4.

2 AN EFFECTIVE THEORY FOR SGLUON PRODUCTION AND DECAY AT THE LHC AND BENCHMARK SCENARIOS

As stated above, sgluons can be pair-produced at the LHC through their couplings to gluons and quarks. The same interactions also allow for sgluon decays, in a flavor conserving fashion or not, to light jets and top quarks. These properties can be embedded into an effective gauge-invariant Lagrangian describing the dynamics of a complex sgluon field σ ,

$$\begin{aligned} \mathcal{L} = \mathcal{L}_{SM} + & \left(\sigma^a \bar{d} T_a \left[a_d P_L + b_d P_R \right] d + \sigma^a \bar{u} T_a \left[a_u P_L + b_u P_R \right] u + a_g d_a^{bc} \sigma^a g_{\mu\nu b} g^{\mu\nu c} + \text{h.c.} \right) \\ & + D_\mu \sigma_a^\dagger D^\mu \sigma^a - m_\sigma \sigma^a \sigma_a^\dagger . \end{aligned} \quad (1)$$

This effective Lagrangian contains the Standard Model Lagrangian \mathcal{L}_{SM} , the sgluon kinetic and mass (m_σ) terms included in the last two terms of the equation above and the sgluon gauge interactions, which are embedded through the $SU(3)_c$ covariant derivative in the adjoint representation,

$$D_\mu \sigma^a = \partial_\mu \sigma^a + g_s f_{bc}^a g_\mu^b \sigma^c , \quad (2)$$

where g_μ^b denotes the gluon field, g_s the strong coupling constant and f_{bc}^a the structure constants of $SU(3)_c$. In complete hybrid or R -symmetric supersymmetric models, additional interactions

Parameter	Scenario I.1	Scenario I.2	Scenario II.2	Scenario II.1
a_g	1.	1.	1.	1.
$(a_u)_{tt}$	0.085	0.085	0	0
$(a_u)_{ct} = (a_u)_{tc}$	0	0	0.04	0.04
$(a_u)_{ut} = (a_u)_{tu}$	0	0	0.04	0.04
m_σ	400 GeV	1000 GeV	400 GeV	1000 GeV
m_t	172 GeV	172 GeV	172 GeV	172 GeV

Table 1: Non-zero input parameters for our four benchmark scenarios. All the other Standard Model parameters follow the conventions of Ref. [107].

of sgluons to quarks and gluons are generated at the one-loop level. The sgluon can hence also singly couple to two, three or four gluons or to a pair of quarks. In our effective theory, this option is allowed through the Lagrangian terms given in the parenthesis of the first line of Eq. (1). In the latter, flavor indices, as well as (anti)fundamental color indices, are understood, and we have introduced the left-handed and right-handed chirality projectors P_L and P_R . In addition, $g_{\mu\nu a}$ stands for the gluon field strength tensor, whilst T_a and d^a_{bc} are the fundamental representation matrices and the symmetric structure constants of $SU(3)$, respectively. The relative coupling strengths are left as free parameters and consist in a set of four complex 3×3 matrices in flavor space a_d, b_d, a_u, b_u and a complex number a_g .

To investigate the main features of sgluon signatures at the LHC, we consider two simplified scenarios I and II, each of them split into two categories (1 and 2) which differ only in the mass assumed for the sgluon. For scenarios I.1 and II.1, the sgluon is assumed to have a mass of 400 GeV, a rather collider-friendly value, while for scenarios I.2 and II.2, it is assumed to be a 1000 GeV particle, yielding a phase-space suppressed but still visible sgluon pair-production cross section at the LHC. The difference between the two sets of scenarios lies in the allowed decay channels for the color-octet scalar particle. For scenarios I.1 and I.2, sgluons are only allowed to decay to a top-antitop pair with a branching ratio equal to unity. In contrast, for scenarios II.1 and II.2, they can decay, with an equal rate, to a top or an antitop quark in association with a light jet originated from an up or charm quark. Let us note that the total branching ratio of sgluon to this tj channel is again assumed equal to unity. Moreover, we are looking for moderately low mass objects. Therefore, kinematically, the parton densities of the proton tell us that gluon fusion mechanism is dominant over the quark-antiquark scattering processes for these masses. The production cross section then depends on the mass of the sgluon and the sgluon-gluon-gluon coupling a_g .

The values of the non-zero parameters of the Lagrangian of Eq. (1) are given, for our four benchmark scenarios, in Table 1, whilst all the Standard Model parameters, with the exception of the top quark mass m_t which is chosen equal to 172 GeV, follow the conventions of Ref. [107]. The numerical values of the non-zero sgluon coupling strengths have been chosen so that the cross sections related to sgluon pair production and decays are visible at the LHC.

3 PHENOMENOLOGICAL INVESTIGATIONS

3.1 Monte Carlo simulations and object definitions

Event simulation is performed for the LHC at $\sqrt{s} = 7$ TeV and for an integrated luminosity of 10 fb^{-1} . Both for signal and background events, the hard scattering process has been de-

Sources of background	Cross sections [pb]
$W \rightarrow l\nu + \text{jets}$	14350
$\gamma^*/Z \rightarrow l\bar{l} + \text{jets}$	1672
$t\bar{t} + \text{jets}$ (semileptonic)	17.1
$t\bar{t} + \text{jets}$ (dileptonic)	3.2
single top (leptonic) + jets [s -channel]	0.49
single top (leptonic) + jets [t -channel]	10.8
single top (semileptonic) + jets [tW -channel]	2.21
single top (dileptonic) + jets [tW -channel]	0.41
$WW + \text{jets} \rightarrow$ at least one lepton	9
$WZ + \text{jets} \rightarrow$ at least one lepton	0.48
$ZZ + \text{jets} \rightarrow$ at least two leptons	2.8
$t\bar{t}W + \text{jets}$	0.03
$t\bar{t}Z + \text{jets}$	0.02
$t\bar{t}WW + \text{jets}$	0.21
$t\bar{t}t\bar{t} + \text{jets}$	$3.7 \cdot 10^{-4}$

Table 2: Cross sections for the different generated sources of background.

scribed with the multipurpose matrix element generator MADGRAPH 5 [96]. Neglecting all quark masses but the top mass, we employ the leading order set of the CTEQ6 parton density fit [429] and identify both the renormalization and factorization scales as the partonic center-of-mass energy. Concerning the simulation of the sgluon signals, we have implemented the Lagrangian of Eq. (1) in the FEYNRULES package [6,78] and used the dedicated UFO-interface to convert the Feynman rules to the UFO format [135], which has been adopted as the standard MADGRAPH model format. Using this framework, our estimates for the (leading order) cross section for sgluon pair production (without decays) are 1.86 pb, 0.82 fb, 1.86 pb and 0.82 fb for our four scenarios I.1, I.2, II.1 and II.2, respectively. The cross sections of the different generated background processes are presented in Table 2.

In order to have a description of the collisions as accurate as possible, we have matched the MADGRAPH event samples with parton showering and hadronization as provided by the PYTHIA program [116, 117]. We have then performed a fast detector simulation with the program DELPHES 1.9 [482], using the publicly available ATLAS detector card.

Jets are reconstructed using the anti- k_t algorithm with a radius parameter set to $R = 0.4$, and only those with a transverse momentum $p_T > 10$ GeV are kept in our analysis. However, jets defined with such a low radius, and particularly those with a low transverse momentum, may suffer from large bias in energy measurement due to the possibly significant fraction of the energy not being reconstructed. We have corrected this effect by an *ad-hoc* calibration based on test samples of dijet events issued from the decay of a Z - or a Z' -boson, the latter having a mass ranging from 200 GeV to 1 TeV. After this calibration, we only retain, at the analysis level, jets with a transverse momentum $p_T > 20$ GeV and a pseudorapidity $|\eta| < 2.5$. In addition, we estimate a b -tagging efficiency of about 60%, together with a charm and light flavor mistagging rate of 10% and 1%, respectively.

Leptons are required to have a transverse momentum $p_T > 20$ GeV. The pseudorapidity of electrons must be less than 2.47 and for muons less than 2.5. Finally, we require isolation

criteria and do not consider in our analysis jets at a relative distance $\Delta R < 0.2$ of an electron and muons at a relative distance $\Delta R < 0.2$ from a jet.

3.2 Event selection

Considering the four tops or two tops plus two light jets signatures described in Section 2, the reconstructed final state can be more or less rich in leptons and jets after the decays of the top quarks. We design two different analyses, the first one asking for a same-sign lepton pair with a moderate number of jets and the second one for exactly one lepton produced in association with a large number of jets. The first analysis is expected to be sensitive to our four scenarios, whilst the second one is especially designed to use the sgluon mass reconstruction to improve the sensitivity for scenarios of type II.

In the following, we define the sensitivity of our analyses as in Ref. [470], *i.e.*, as the statistical error on the background predictions (for a luminosity of 10 fb^{-1}) divided by the efficiency and multiplied by 1.64, similarly to a one-sided Gaussian counting experiment limit. In other words, we estimate the signal cross section which can be excluded at the 95% confidence level in the absence of a new physics observation.

3.2.1 Same-sign dilepton plus jets signature

In order to probe the same-sign dilepton plus jets signature, our event selection criteria consist in rejecting events which do not contain exactly two charged leptons (electrons or muons) with the same electric charge and a transverse momentum $p_T > 20 \text{ GeV}$. We require at least four jets, one or more being tagged as b -jets, with a reconstructed transverse energy of $E_T > 25 \text{ GeV}$. In addition, we impose that the invariant-mass of the lepton pair is above 20 GeV to reject hadronic resonances and we demand a missing transverse energy of at least 40 GeV . It is important to note that requiring same sign leptons allows to reject a significant fraction of the Standard Model background. We then obtain a sensitivity of 110 fb , 61 fb , 380 fb and 209 fb for scenarios I.1, I.2, II.1 and II.2, respectively.

In the case of scenarios of type I, the analysis can be further improved by taking advantage of the larger expected jet multiplicity in the final state due to the decays of the four top quarks. Requiring eight reconstructed jets with a transverse energy $E_T > 25 \text{ GeV}$, two or more of them being b -tagged, we find that the LHC is now sensitive to signal cross sections of 17 fb and 6 fb for the scenarios I.1 and I.2, *i.e.*, for 400 GeV and 1 TeV sgluons, respectively.

The important hadronic activity in the final state suggests a last selection cut on the H_T variable which we define as the scalar sum of the transverse momentum of all the reconstructed leptons and jets, together with the missing transverse energy. Our results for the four scenarios, assuming an optimal cut on the H_T variable, are given in Table 3 together with the value of this cut.

3.2.2 Single lepton plus jets signature

Turning to our second analysis focusing on signatures containing a single lepton produced in association with a large number of jets, we select events containing at least one electron or one muon with a transverse momentum $p_T > 25 \text{ GeV}$ and no other charged lepton with a transverse energy $E_T > 20 \text{ GeV}$. These requirements ensure the orthogonality with the dilepton analysis above. In addition, we demand at least six jets with a reconstructed transverse energy $E_T > 25 \text{ GeV}$, with one or more of them being b -tagged. Since the reconstructed lepton comes from the

Scenario	Sensitivity before H_T cut [fb]	H_T cut [GeV]	Sensitivity after H_T cut [fb]
I.1	17	850	11.8
I.2	6	1750	0.5
II.1	380	650	216
II.2	209	1550	15

Table 3: Sensitivity of our dilepton analysis to a sgluon signal at the LHC assuming the indicated optimal cuts on the H_T variable.

$m_W^{(r)}$	$\sigma_W^{(r)}$	$m_{tW}^{(r)}$	$\sigma_{tW}^{(r)}$	$m_{t\ell}^{(r)}$	$\sigma_{t\ell}^{(r)}$	$\sigma_{\sigma t}^{(r)}$
85.5 GeV	13.2 GeV	90.5 GeV	17.3 GeV	169 GeV	30.8 GeV	0.090

Table 4: Values of the free parameters entering the χ^2 minimization function of Eq. (4).

decay of a W -boson, together with an unobserved neutrino, we drastically reduce the multijet background by requiring missing transverse energy $\cancel{E}_T > 40$ GeV and a moderate W -boson transverse mass $M_T^W > 25$ GeV, the latter being defined as

$$M_T^W = \sqrt{2 p_T^{\text{lepton}} \cancel{E}_T [1 - \cos(\Delta\phi(\text{lepton}, \cancel{E}_T))]} . \quad (3)$$

One obtains a sensitivity to a sgluon signal of 152 fb, 131 fb, 334 fb and 228 fb for scenarios I.1, I.2, II.1 and II.2, respectively.

The single lepton analysis allows to reconstruct the sgluon mass which is used to improve the sensitivity for ditop signal events. Indeed, combinatorics render this task extremely difficult for final states containing four top quarks. Thus, we focus, in the rest of this report, only on the scenarios of type II which have been designed for a signature containing two top quarks and two light jets. We choose to reconstruct the sgluon mass by combining objects so that we minimize a quantity χ^2 defined as

$$\chi^2 = \left[\frac{m_{jj} - m_W^{(r)}}{\sigma_W^{(r)}} \right]^2 + \left[\frac{(m_{jjj} - m_{jj}) - m_{tW}^{(r)}}{\sigma_{tW}^{(r)}} \right]^2 + \left[\frac{m_{l\nu j} - m_{t\ell}^{(r)}}{\sigma_{t\ell}^{(r)}} \right]^2 + \left[\frac{(m_{l\nu j,j} - m_{l\nu j}) - (m_{jjj,j} - m_{jjj})}{\sigma_{\sigma t}^{(r)} [(m_{l\nu j,j} - m_{l\nu j}) + (m_{jjj,j} - m_{jjj})]} \right]^2 . \quad (4)$$

For scenarios of type II, the final state contains one hadronically decaying top quark, one leptonically decaying top quark and two additional light jets. Hence, two of the reconstructed jets are the decay products of a W -boson. We estimate the expected mass of the reconstructed W -boson $m_W^{(r)}$ and the associated uncertainty $\sigma_W^{(r)}$, corresponding to the detector resolution, with the help of the Monte Carlo truth, fitting the reconstructed W -mass with a Gaussian. We find the values given in Table 4. These Gaussian parameters are then used in the χ^2 minimization function above, where among all the possible combinations of jets, we select the one with the invariant mass m_{jj} closest to $m_W^{(r)}$ as indicated by the first term of Eq. (4).

Similarly, using the Monte Carlo truth, one can extract from the events the additional b -jet necessary to reconstruct the hadronic top quark. In order to include this information in the

minimization function, one must however first subtract the W -boson reconstructed mass, the latter being strongly correlated to the reconstructed top mass. The obtained values for the mass difference $m_{tW}^{(r)}$ and the width $\sigma_{tW}^{(r)}$ are again presented in Table 4. These last parameters are used in the second term of the χ^2 function of Eq. (4), where we select the right combination of three jets (b -tagged or not) of invariant mass m_{jjj} yielding a reconstructed hadronically decaying top quark.

The third term of Eq. (4) constrains the reconstruction of the leptonic top quark. Using the information included in the Monte Carlo truth, one derives the parameters $m_{tl}^{(r)}$ and $\sigma_{tl}^{(r)}$, the average mass and the width of the reconstructed (leptonically decaying) top quark. They are obtained in a similar fashion as above and given in Table 4. We include them in the third term of the minimization function, optimizing the selection of the jet (whether it is b -tagged or not) to be matched with the final state lepton and missing energy so that a top quark mass is reconstructed. As above, the difference between the invariant mass m_{lvj} and $m_{tl}^{(r)}$ is minimized. Let us note that the neutrino four-momentum, necessary for the computation of m_{lvj} , is inferred from the reconstructed missing transverse energy and the W -boson mass taken equal to 80.4 GeV [44]¹.

In the last term of Eq. (4), we use the fact that two sgluons are produced, which allows us to require two similar reconstructed masses (without assuming anything on the corresponding numerical value). Combining each of the reconstructed top quarks with an extra jet, one then requires $m_{lvj,j} \approx m_{jjb,j}$. However, in order to decouple this constraint from those related to the reconstruction of the top masses, we subtract the reconstructed top masses m_{jjj} and m_{lvj} from the two reconstructed sgluon masses, similarly to what was done to the second term of Eq. (4). Moreover, in order to remove a too strong dependence on the sgluon mass, which holds especially for heavy sgluons, we add an extra factor, at the denominator, of $(m_{lvj,j} - m_{lvj}) + (m_{jjj,j} - m_{jjj})$ in the fourth term of the minimization function. As for the other terms, the combined width on the sgluon and top mass difference $\sigma_{\sigma t}^{(r)}$ is extracted from a Gaussian fit based on the Monte Carlo truth and given in Table 4.

Finally, to reduce combinatorial issues, we demand that the two leading jets belong to the object combinations reconstructing the mass of the two produced sgluons. The reconstructed mass m_{tj} distribution is presented in Figure 1 (left panel) both for the signal and all possible sources of backgrounds. Signal events for sgluons of 400 GeV and 1 TeV, *i.e.*, scenarios II.1 and II.2, are shown as solid and dashed curves, respectively, whilst the main sources of background coming from $t\bar{t}$ (red), single top (blue) and W plus jets (orange) events are indicated. For the sake of completeness, the other, subleading, possible sources of background are shown as three groups, the first one, $t\bar{t} + X$ (grey) being related to $t\bar{t} + Z$, $t\bar{t} + W$ and $t\bar{t} + WW$ events, the second one to all diboson events (yellow) and the last one to the Standard Model production of four top quarks (turquoise).

Assuming a sgluon test mass M and retaining events for which the reconstructed invariant mass m_{tj} lies within a $[M - 10\%, M + 10\%]$ window around the test mass, the LHC sensitivity to a sgluon signal, shown in Figure 1 (right panel) is found to improve with respect to the global case discussed above. For optimal choices of the test mass, the sensitivity reaches even 278 fb and 48 fb for our scenarios II.1 and II.2, respectively, which has to be compared to the previously found values of 334 fb and 228 fb. Therefore, our analysis is more sensitive to high sgluon mass, provided enough signal events are produced.

¹In this way, a constraint on the W -boson mass is also imposed at the same time.

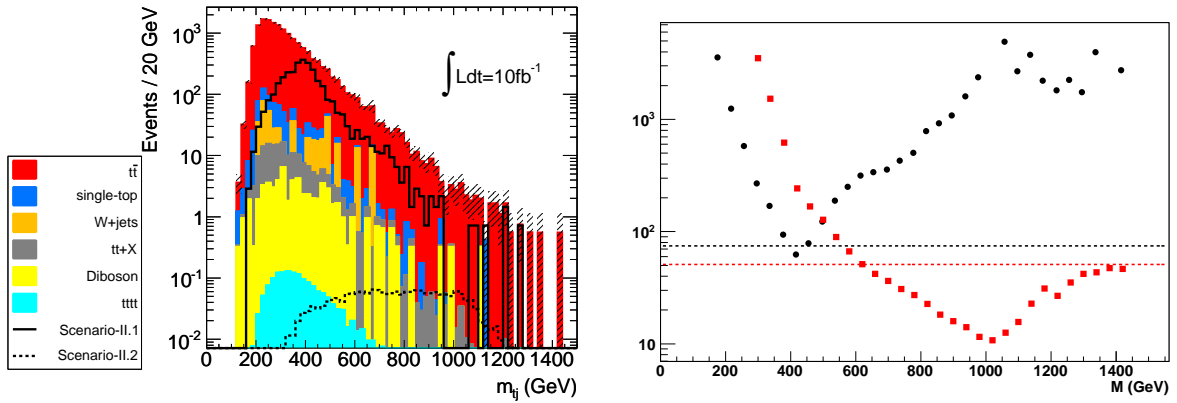


Figure 1: Left: reconstructed top-jet invariant mass m_{tj} , for both signal events corresponding to our scenarios II.1 (solid) and II.2 (dashed) and the different sources of backgrounds (see the description in the text). Right: assuming a test mass M and retaining events for which m_{tj} lies in a $[M - 10\%, M + 10\%]$ window, we present the dependence of the sensitivity of our analysis on M for signal events corresponding to our scenario II.1 (a 400 GeV sgluon, in black) and II.2 (a 1 TeV sgluon, in red). For comparison purposes, the global sensitivities, without using the reconstructed m_{tj} mass, are indicated by dotted lines.

4 CONCLUSIONS

In this paper, we have presented a strategy for searches of new color-octet scalar particles, such as those predicted by hybrid $N = 1/N = 2$ or R -symmetric supersymmetric theories. We have used a simplified effective field theory describing the production and decays of such particles at the LHC and have investigated two different multitop channels, a first one with four tops in the final state and a second one with two top quarks, possibly carrying the same electric charge, produced in association with two light jets.

We have studied the sensitivity of the LHC collider, running at a center-of-mass energy of 7 TeV to such signals, in two dedicated analyses. In one case, we consider same-sign dilepton signatures with a moderate number of jets, whilst in the second case, we only require a single lepton, but ask, in addition, for a larger number of jets. We have shown that cross sections as low as a few tens of fb can be probed, assuming some basic cuts on jet and lepton multiplicity. Moreover, for ditop analyses, we have presented a way to reconstruct the top-jet invariant mass, *i.e.*, the sgluon invariant mass in the case of signal events. We have shown how this observable can be used to improve the sensitivity to signal events for the corresponding analysis, especially for heavier sgluon particles. However, one must note that pile-up of events at the LHC, not considered here, could decrease the sensitivity.

ACKNOWLEDGEMENTS

BF, AR and DZ would like to thank the Les Houches school for physics for their hospitality during the workshop where some of the work contained herein was performed, as well as the workshop organizers. BF acknowledges support from the Theory-LHC France-initiative of the CNRS/IN2P3.

Long-lived Particles

Contribution 17

Metastable charginos and LHC searches

G. Polesello, T. G. Rizzo

Abstract

In the framework of the Minimal Supersymmetric Standard Model, the parameter space yielding long lived charginos is studied. For the case where the charginos decay outside the detector, a limit on the production of metastable charginos in the MSSM is set, on the basis of the results of a recent ATLAS search for long-lived charged particles.

1 INTRODUCTION

The very successful 2010/2011 data-taking at the LHC has allowed the ATLAS and CMS experiments to perform several searches for supersymmetric particles. These searches to date have yielded no discovery, and squark/gluino masses in the TeV range have been excluded for a very constrained set of models based on the assumptions of large mass gaps within sparticles and very simple decay chains.

Several detailed studies are ongoing to assess the coverage of these analyses in the framework of a generic phenomenological Minimal Supersymmetric Model defined in terms of 19 SUSY-breaking parameters (pMSSM) [79]. The aim of these studies is to identify ‘difficult’ models which may have escaped the first round of LHC analysis. The ‘SUSY without prejudice’ study [190, 483] is based on a very extensive scan of the 19-parameters space, featuring the simulation of $\sim 71\text{k}$ model points, and has identified classes of models which escape the available LHC searches based on the requirement of a large imbalance of transverse momentum (E_T^{miss}) in the events. A large class of such models includes situations in which the lightest chargino is approximately degenerate with the neutralino and is long lived, thus appearing as a heavy stable muon-like particle in the detector.

The ATLAS experiment [484] has published a search for long lived heavy particles (LLP) based on the measurement of the momentum and of the velocity β of particles reaching the muon detector [485]. The results of the analysis are interpreted in terms of long-lived sleptons in the framework GMSB SUSY models, and in terms of R-hadrons appearing in models with very heavy quarks and light gluinos.

The purpose of the present study is to reinterpret the results of this analysis as limits on the chargino/neutralino sector of the pMSSM.

2 THE MODEL

In a generic MSSM the partners of the gauge and Higgs bosons of the model, the bino, wino and Higgsinos ($\tilde{B}, \tilde{W}, \tilde{H}_u, \tilde{H}_d$) mix to yield two charginos and four neutralinos. At tree level the chargino and neutralino mixing matrices are determined by four parameters, the mass of the bino M_1 , the mass of the wino M_2 , the common Higgsino mass μ , and $\tan\beta$, the ratio of the

vacuum expectation values of the two Higgs doublets in the model. The broad features of the chargino/neutralino mass spectra are defined by the hierarchy of M_1 , M_2 , and μ . Of special interest for our study is the situation where the hierarchy is such that the Next to Lightest Supersymmetric Particle (NLSP) is the chargino which has a sufficiently small mass splitting with the LSP to render it stable on LHC detector time-scales.

An example of this situation occurs when $M_2 < (M_1, \mu)$. In this case both the lightest chargino ($\tilde{\chi}_1^\pm$) and the lightest neutralino ($\tilde{\chi}_1^0$) are predominantly winos, and both have a mass which is essentially given by M_2 . For sufficiently high $\Delta M(M_1, M_2)$ and $\Delta M(\mu, M_2)$ both $\tilde{\chi}_1^\pm$ and $\tilde{\chi}_1^0$ are pure winos and the mass difference may become smaller than 100 MeV. A similar situation occurs in the opposite limit when $|\mu| < (M_{1,2})$ in which case one obtains an Higgsino LSP with a slightly more massive chargino which is also Higgsino-like. In such cases, if the $\tilde{\chi}_1^\pm$ is NLSP, the only available decay chain for the $\tilde{\chi}_1^\pm$ would be the three-body decay $\tilde{\chi}_1^\pm \rightarrow e\nu\tilde{\chi}_1^0$ which proceeds through the exchange of a virtual W or selectron, and the particle will then appear in the ATLAS detector as a stable charged penetrating particle. For the wino case we studied the mass difference of $\tilde{\chi}_1^\pm$ and $\tilde{\chi}_1^0$ is shown in Fig. 1 as a function of M_2 and μ with the SUSY-HIT program incorporating the loop corrections to the chargino/neutralino masses. The masses of all of the sfermions and of the gluino were put at 3 TeV, the mass of the pseudoscalar Higgs to 1 TeV and the trilinear couplings to zero. The required level of mass degeneracy is achieved for $\Delta M(\mu, M_2)$ in excess of ~ 250 GeV. The dependence on M_1 was also studied, and it was found that for $\Delta M(M_1, M_2)$ in excess of ~ 100 GeV the mass difference is approximately independent of M_1 . Loop corrections are important to determine such a small mass splitting, so this result is valid in the limit of the very high fixed value of the sfermion masses used in this study. However, in an independent study addressing a very broad range of parameters, where these corrections are included using, e.g., the SUSPECT SUSY spectrum generator [79], such small mass splittings still occur with a reasonable frequency [190,483]

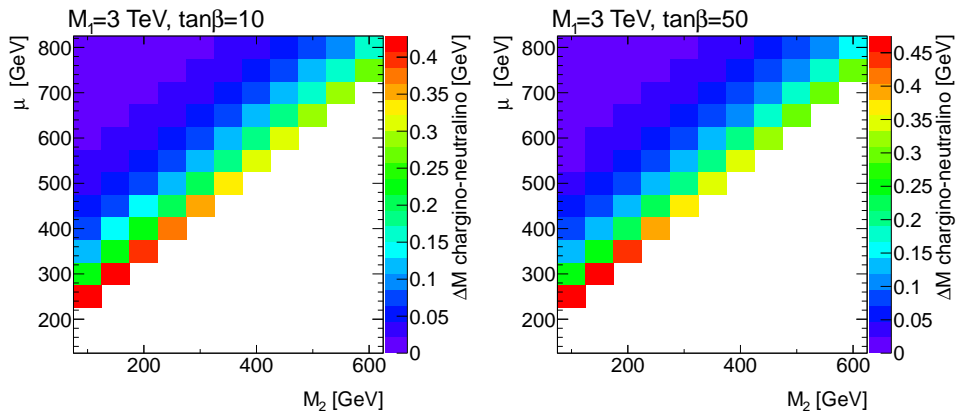


Figure 1: Mass difference $\tilde{\chi}_1^\pm - \tilde{\chi}_1^0$ as a function of M_2 and μ for two values of $\tan\beta$: 10 and 50. M_1 is set at 3 TeV.

3 SIGNAL SIMULATION AND ANALYSIS

In order to explore the wino-like LSP model described in the previous section in more detail, a series of model points were defined based on SUSY-HIT [202] with the following parameters:

$M_1=3$ TeV, $\mu=1$ TeV, $\tan\beta=10$. The M_2 parameter was varied in steps of 20 GeV between 100 and 200 GeV, and in steps of 100 GeV between 200 and 500 GeV. The gluino mass and all the sfermion masses were set to 3 TeV, and the trilinear couplings to zero.

For each point a set of events were generated for the electroweak direct chargino-chargino production with the Herwig++ [486,487] shower Monte Carlo generator. The production cross-section were normalised to the NLO cross-sections calculated with the PROSPINO program [488].¹ From the particle tree in output of the generator the charginos were extracted and passed to a simplified parametrised simulation of the response of the ATLAS detector.

For each chargino the momentum was smeared according to a parametrisation of the momentum resolution of muons in the ATLAS detector as described in [484]. The velocity distribution β was smeared according to the measured distribution for muons as shown in [485]. A simple gaussian smearing does not completely describe the tails of the experimental resolution as shown in the auxiliary plots to [485]. The correct simulation of the complete shape of the distribution is extremely important for the evaluation of the background coming from the tails of the β and momentum measurement of real muons, and no attempt is done to estimate the background, which is taken directly from the ATLAS paper. For signal, where the real β is different from 1, only the correct evaluation of the distribution width is relevant. The real and smeared β distributions for a 110 GeV and a 300 GeV chargino are shown in Fig. 2. From

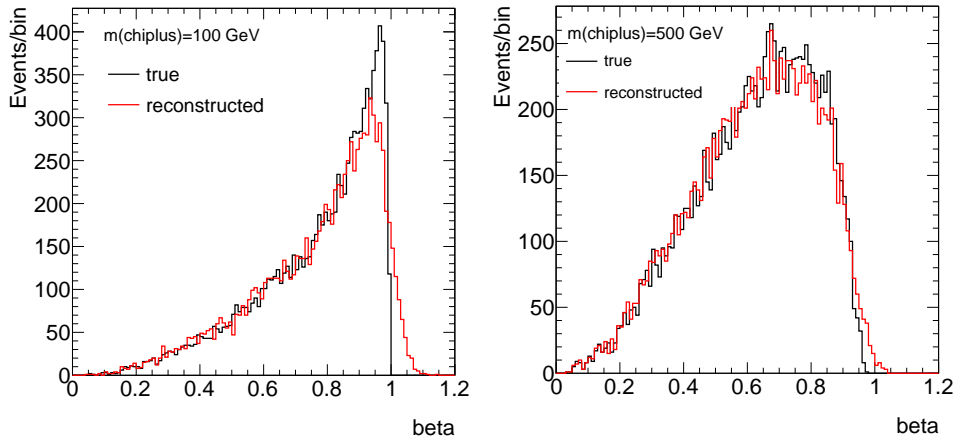


Figure 2: Distribution of the β variable for charginos of respectively 100 (left) and 500 (right) GeV. The black line shows the generated β , the red line the measured one.

the smeared beta and momentum the measured sparticle mass is calculated. The distribution of measured masses for different values of the chargino mass is shown in Fig. 3.

The reconstruction efficiency for LLP candidates is a function of β , as particles with too low a β arrive late in the muon detector and cannot be reconstructed. No measurement is performed above $|\eta| < 2.5$, because of the coverage of the ATLAS tracking detectors. For LLP candidates with $p_T > 20$ GeV and $|\eta| < 2.5$, the efficiency is zero for $\beta < 0.4$, and it reaches a plateau of 0.85 for $\beta \sim 0.65$, determined by the geometrical coverage of the muon detectors. These results were obtained in [485, 489] for GMSB sleptons. We use them for

¹We note that for wino-like charginos, in addition to s -channel γ, Z exchange, a t -channel squark exchange graph is also present which interferes destructively with those in the s -channel. For the Higgsino case, such t -channel exchanges are suppressed due to small Yukawa couplings.

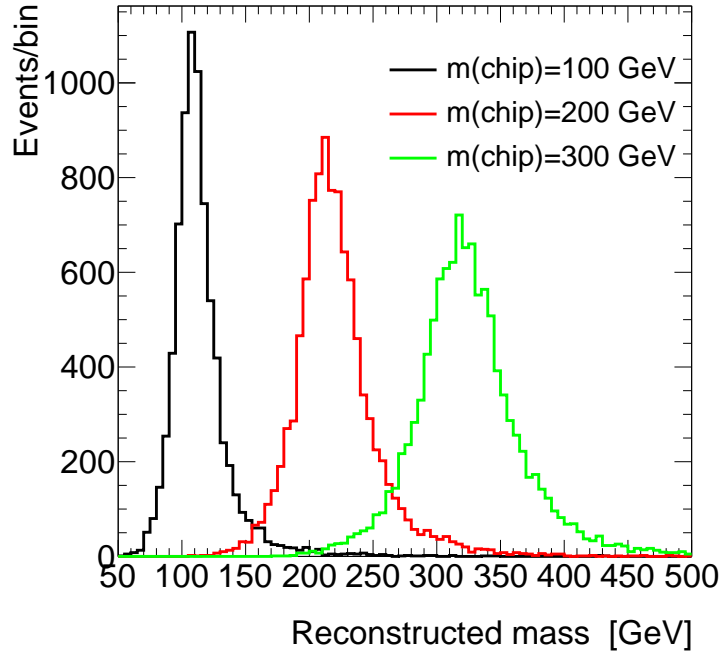


Figure 3: Distribution of the reconstructed values for chargino masses from β and momentum measurements. The distribution is shown for charginos of mass 100, 200 and 300 GeV.

charginos although they might be somewhat different due to different p_T and η distribution for our signal.

For each candidate in the ATLAS analysis a quality cut on the β measurement is applied. The efficiency of this cut can be extracted from Table 3 of [485] and is taken to be 77% independent of the particle mass and β .

Following the ATLAS analysis, we require each event to contain two candidates with $p_T > 20$ GeV within $|\eta| < 2.5$, reconstructed as a muon. Any candidate which combined with a second muon gives a mass within 10 GeV of the Z mass is rejected. We then require that each of the events has at least one candidate passing the following cuts:

- $p_T > 40$ GeV and $|\eta| < 2.5$;
- β quality cuts (in our case the efficiency factor defined above);
- $\beta > 0.95$.

The final step is a cut on the mass of the reconstructed candidate. We show in Table 1 for each of the sample models considered the cut on reconstructed mass, the number of expected events after cuts and the efficiency evaluated with our approximate simulation.

The efficiency increases as a function of the chargino mass, from 30% for a chargino mass of ~ 100 GeV to 40% for a chargino mass of ~ 200 GeV. These efficiencies in [485], vary between 40 and 50% for a comparable range of masses, but for a model yielding different η and momentum distribution for the candidate LLPs.

mass (GeV)	σ_{NLO} (pb)	cut (GeV)	ϵ	Expected signal	Limit expected	Limit measured
107.4	3.29	90	0.29	35.8	11.7	8.8
128.8	1.61	120	0.30	17.6	7.9	5.3
150.2	0.882	130	0.35	11.3	6.2	5.0
171.4	0.518	130	0.37	7.1	6.2	5.0
192.6	0.322	130	0.38	4.5	6.2	5.0
213.7	0.209	130	0.39	3.0	6.2	5.0
318.3	0.0348	130	0.41	0.52	6.2	5.0
421.8	0.0081	130	0.42	0.12	6.2	5.0
524.0	0.00226	130	0.41	0.034	6.2	5.0

Table 1: As a function of the wino-like chargino mass: NLO cross-section, applied cut on the reconstructed candidate mass, analysis efficiency, number of expected signal events in 37 pb^{-1} , expected and measured ATLAS 95% CL upper limit on the number of signal events.

4 Results and outlook

Based on the cross section and efficiency values calculated in the previous section, and on the number of expected events excluded by ATLAS at 95% CL which can be calculated from [485], as reported in Table 1, an approximate limit on the wino-like chargino mass can be evaluated. The final exclusion plot as a function of the chargino mass is given in Fig. 4. Stable

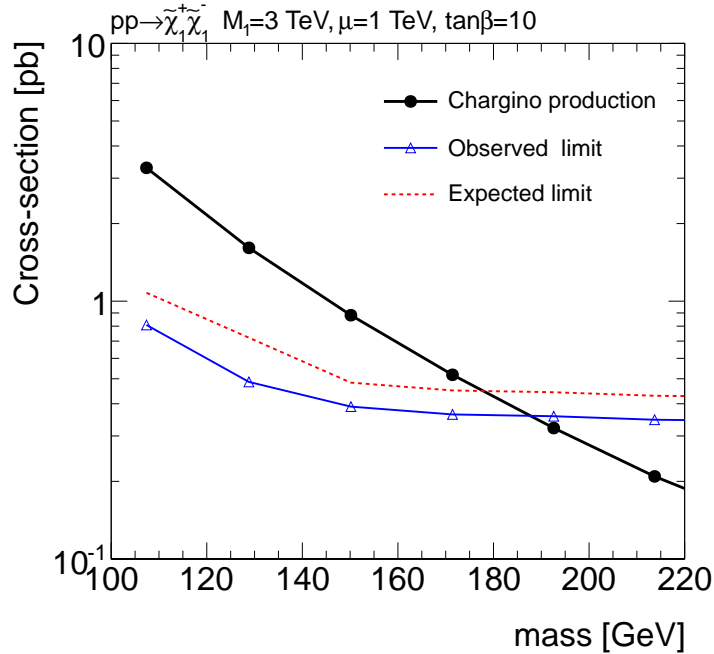


Figure 4: The expected production cross-section for wino-like charginos, and the cross-section upper limit at 95% CL as a function of the chargino mass.

wino-like charginos with masses below approximately 190 GeV are excluded based on the

ATLAS analysis of the 2010 LHC data. (A somewhat weaker result is expected for Higgsino-like charginos which have for the same mass a production cross-section which is approximately a factor 3.5 lower.) From the consideration of the detailed scan of the parameter space discussed in Section 2 this corresponds to excluding M_2 up to ~ 180 GeV for models with the hierarchy $M_2 < (M_1, \mu)$ where M_1 and μ are sufficiently heavier than M_2 .

The LHC experiments have collected in 2011 $\sim 5 \text{ fb}^{-1}$ of data. From the numbers of Table 1 this corresponds to ~ 5 events for a wino-like chargino mass of 520 GeV. Harder cuts on β and reconstructed mass will be needed for the 2011 analysis in order to bring down the SM background to few events. We have checked that for the cuts $\beta > 0.9$ and $\text{mass} > 400$ GeV, the efficiency for the chargino is reduced from 0.41 to 0.38. The 2011 data analysis should therefore be sensitive to masses in the proximity of 500(420) GeV for wino(Higgsino)-like charginos.

5 CONCLUSIONS

The results of an ATLAS search for charged long-lived particles based on the data collected in 2010 at the LHC have been interpreted in the framework of a pMSSM model with degenerate lightest chargino and neutralino. For such models the ATLAS analysis yields a limit of approximately 190 GeV on the wino-like chargino mass. The more than hundredfold increase in statistics in 2011 should allow ATLAS to probe chargino masses in the 400-500 GeV range.

ACKNOWLEDGMENTS

We would like to warmly thank Shikma Bressler who has been very helpful in answering our questions on the ATLAS analysis.

Contribution 18

Displaced vertex signatures at the LHC from B-L heavy neutrinos and MSSM FIMPs.

L. Basso, A. Belyaev, E. Dobson, M. C. Thomas, I. Tomalin, S. M. West, A. J. Williams

Abstract

In the context of two distinct classes of well-motivated BSM models we investigate the detection prospects for collider signatures containing long-lived particles that decay after travelling up to a meter from the interaction point of a collision. The first is a $U(1)_{B-L}$ extension of the SM with a dynamical see-saw mechanism, where the RH neutrino is typically a long-lived particle interacting with the scalar bosons. The second is a version of the MSSM extended by the inclusion of an extra singlet superfield that is feebly coupled to the MSSM.

We show that displaced vertices from the models under study provide a prominent, essentially background-free set of signals, which would allow for the identification of these BSM models even if standard backgrounds, which do not contain displaced vertices, are large. We also comment on the tools used to generate the events including some useful warnings about the details of handling displaced vertices in PYTHIA.

1 INTRODUCTION

Displaced vertices can be common in a number of theories Beyond the Standard Model (BSM). There are many examples, in the literature, of models containing long-lived particles that can potentially lead to displaced vertices at the LHC [113, 355, 490–496].

In this contribution, we study two different classes of models that contain long-lived states that lead to displaced vertices at the LHC. We first consider a minimal $U(1)_{B-L}$ extension of the SM at the TeV scale [113], in which the SM particle content is extended to include one right-handed (RH) neutrino per generation and a further singlet scalar, χ , responsible of the spontaneous symmetry breaking of the extra $U(1)_{B-L}$ group. The interaction between RH neutrinos and the singlet scalar allows for a dynamical implementation of the see-saw mechanism as χ gets a vacuum expectation value (VEV), allowing at the same time for the Higgs bosons to decay into pairs of heavy ($\simeq 100$ GeV) Majorana neutrinos (the heavy partners of the SM-like neutrinos). The mixing of heavy neutrinos with the SM ones enables the decay of the former into a lepton and a SM gauge boson. Being suppressed by the see-saw mechanism, the corresponding decay width is typically very small, thus making the heavy neutrino a long-lived particle. This will give rise to detectable displaced vertices which we study in the context of the Higgs boson decays into multileptons final states via these long-lived neutrinos. We study these signatures for two benchmark scenarios with light Higgs masses relatively small, hence suitable

for the LHC at $\sqrt{s} = 7$ TeV, by simulating Monte Carlo events up to a fast detector simulation employing CalCHEP [1], PYTHIA6 [116] and Delphes [375].

The second BSM model under study is motivated by dark matter models that employ the freeze-in mechanism to generate the dark matter relic abundance [495,496]. These models arise by extending the MSSM with the addition of a singlet superfield, which is feebly coupled to the MSSM states. This extra superfield is assumed to contain the Lightest Supersymmetric Particle (LSP), and consequently the Next to Lightest Supersymmetric Particle (NLSP) will only be able to decay to the LSP via the feeble coupling leading to long-lived NLSPs. We investigate one example of this type of model with a number of benchmark parameter choices. Monte Carlo event simulations for these benchmarks are generated using a combination of MadGraph5 [96], BRIDGE [497] and PYTHIA8 [116, 117].

2 Benchmark models

2.1 Long-lived neutrinos in the B-L model

The first model under study is the so-called “pure” or “minimal” $B-L$ model (see ref. [113,494] for conventions and references) since it has vanishing mixing between the $U(1)_Y$ and the new gauged $U(1)_{B-L}$. This model extends the SM with three right-handed neutrinos (needed for the cancellation of the anomalies related to the new $U(1)$ group) and an additional complex Higgs singlet, responsible for giving mass to the additional Z' gauge boson (see [111, 113] for details). By extending the fermion and the scalar sectors, this model allows for a dynamical generation of the neutrino masses. The scalar sector is now made of two real CP -even scalars, h_1 and h_2 , with $m_{h_1} \leq m_{h_2}$, remnants of the Higgs doublet and singlet fields after electroweak symmetry breaking (EWSB) that mix together:

$$\begin{pmatrix} h_1 \\ h_2 \end{pmatrix} = \begin{pmatrix} \cos \alpha & -\sin \alpha \\ \sin \alpha & \cos \alpha \end{pmatrix} \begin{pmatrix} h \\ h' \end{pmatrix}. \quad (1)$$

The mixing angle $-\frac{\pi}{2} \leq \alpha \leq \frac{\pi}{2}$ can be expressed as $\tan 2\alpha = \frac{\lambda_3 x v}{\lambda_1 v^2 - \lambda_2 x^2}$, where v and x denote the VEV of the doublet and singlet fields, respectively, and $\lambda_{1,2,3}$ are the coefficients of the quartic terms in the scalar potential. Notice that the presence of the new particles (neutrinos and a Z' boson) also alter the properties of the Higgs bosons. Moreover, the scalar mixing angle α is a free parameter of the model, and the light (heavy) Higgs boson couples to the new matter content proportionally to $\sin \alpha$ ($\cos \alpha$), i.e., with the complementary angle with respect to the interactions with the SM content, as in the traditional literature of singlet scalar extended SM.

Neutrino mass eigenstates, obtained after applying the see-saw mechanism, will be called ν_l and ν_h , where the former are the SM-like ones. As the Higgs fields develop a VEV, the relevant Yukawa interactions $\mathcal{L}_Y^\nu = -y_{jk}^\nu \bar{l}_{jL} \nu_{kR} \tilde{H} - y_{jk}^M (\nu_R)_j^c \nu_{kR} \chi + \text{h.c.}$ include the traditional type-I see-saw mass matrix, that can be diagonalised by a rotation about an angle α_ν , such that $\tan 2\alpha_\nu = -\frac{2m_D}{M}$, where $m_D = \frac{y^\nu}{\sqrt{2}} v$ and $M = \sqrt{2} y^M x$. We also require the neutrinos to be degenerate in mass. Thus, $\nu_{L,R}$ can be written as the following linear combination of Majorana mass eigenstates $\nu_{l,h}$:

$$\begin{pmatrix} \nu_L \\ \nu_R \end{pmatrix} = \begin{pmatrix} \cos \alpha_\nu & -\sin \alpha_\nu \\ \sin \alpha_\nu & \cos \alpha_\nu \end{pmatrix} \times \begin{pmatrix} \nu_l \\ \nu_h \end{pmatrix}. \quad (2)$$

With a reasonable choice of Yukawa couplings, the heavy neutrinos can have masses $m_{\nu_h} \sim \mathcal{O}(100)$ GeV $\ll M_{Z'_{B-L}}$. In the following, we describe the features relevant to the

present analysis: the pair production of heavy neutrinos via a light Higgs boson, at the LHC for $\sqrt{s} = 7$ TeV.

Figure 1 shows the production cross sections for the process $pp \rightarrow h_{1(2)} \rightarrow \nu_h \nu_h$, for the case of a light and a heavy Higgs boson, h_1 and h_2 , respectively, as a function of the scalar mixing angle and with suitable heavy neutrino masses. It is clear that large enough cross sections to be relevant at the LHC with $\sqrt{s} = 7$ TeV are possible only when the two Higgs bosons mix strongly, peaking for a value of the mixing angle around $\pi/3$, and for heavy neutrino masses below M_W . The former, in turn, means that all the SM-like processes (production and decay) are suppressed by a factor about $(\cos \pi/3)^2 = 1/4$ as compared to the SM Higgs boson. On the other hand, when decaying into heavy neutrinos, just the production is suppressed (by $(\cos \pi/3) = 1/2$), while $BR(h_1 \rightarrow \nu_h \nu_h)$ can be up to 30%, which is quite a substantial value.

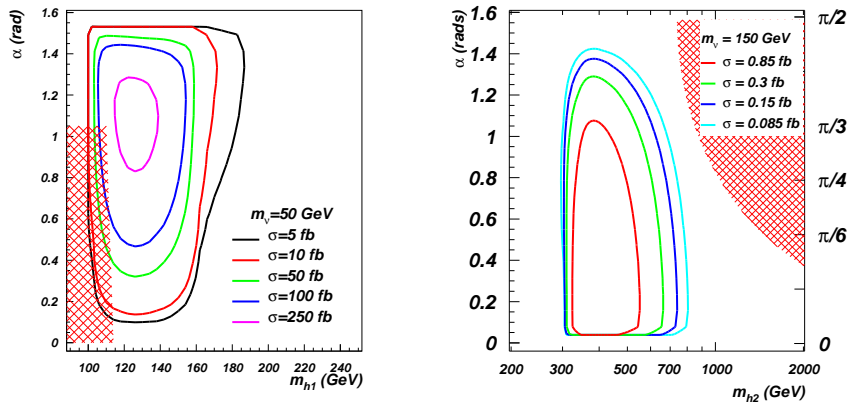


Figure 1: Cross sections for (left) $pp \rightarrow h_1 \rightarrow \nu_h \nu_h$ for $\sqrt{s} = 7$ TeV and for (right) $pp \rightarrow h_2 \rightarrow \nu_h \nu_h$ for $\sqrt{s} = 14$ TeV, as a function of the intermediate Higgs mass and scalar mixing angle [494]. (Cross sections summed over all the neutrino generations.) The areas with red shade are the regions excluded experimentally by LEP (left) and theoretically by Unitarity (right) [498].

The process is interesting because of some peculiar features: first of all, this decay mode is maximised for a range of masses of the Higgs boson that has the lowest overall sensitivity at the LHC for SM processes. It is therefore complementary to standard light Higgs searches at the LHC. Second, each heavy neutrino would decay into a lepton and a SM gauge boson with standard branching ratios [113]: $BR(\nu_h \rightarrow \ell^\pm W^\mp) \sim \frac{2}{3}$, $BR(\nu_h \rightarrow \nu_l Z) \sim \frac{1}{3}$. Including the W and Z boson decays, spectacular multi-lepton decays of the Higgs boson arise. We will focus here on a light Higgs boson. The relevant cross sections are displayed on the left-hand plot in figure 1. In this case, the total cross section is at maximum of 250 fb when all neutrino generations are added up. Naively, it will be totally covered by the background. However, a very efficient way to uncover the signal is to look for displaced vertices, that are a prominent feature of the heavy neutrinos. Figure 2 shows the lifetime of the heavy neutrinos: we clearly see that, over a large portion of the parameter space and depending on the light neutrino mass, the heavy neutrinos are long-lived particles. Hence, the measurement of the mean lifetime of the heavy Majorana neutrinos and of its mass is of crucial importance, allowing for a determination of the absolute mass of the SM-like neutrinos [113]. We selected 2 benchmark points to be covered in the present analysis as summarised in table 1.

Among the possible decay patterns of the heavy neutrinos (see [499]), those that maximise

Sample	M_{h_1}	M_{ν_h}	α	Final state	Proper decay length	σ
$B - L$ Benchmark 1	120 GeV	50 GeV	1.1 rads	all decay modes	43 cm	137.9 fb
$B - L$ Benchmark 2	140 GeV	50 GeV	1.1 rads	all decay modes	43 cm	168.5 fb

Table 1: Description of Monte Carlo samples used in the analysis. The cross sections refer to the sum of the first 2 generations of heavy neutrinos only. The proper decay length is equal to $c \cdot \tau$ where τ is the heavy neutrino life-time.

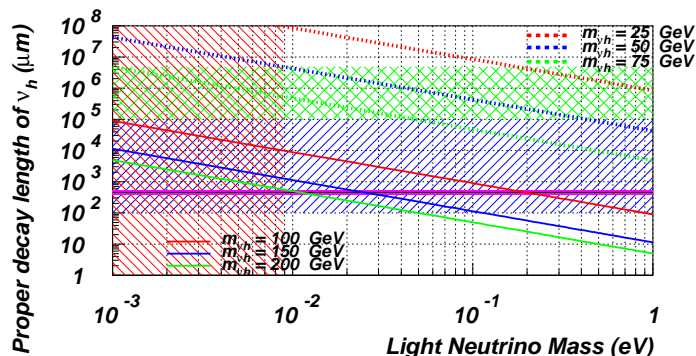


Figure 2: Proper decay length of the heavy neutrinos (in their rest frame) for a choice of their mass and as a function of the light neutrino mass. The purple band presents the proper decay length of the b -quark. The blue (right) band indicates the range of a typical micro-vertex detector, while the green (crossed) band indicates the typical detector dimension. The red shaded are on the left shows the region excluded by neutrino oscillation direct measurements.

the observation chances involve leptonic decays of the heavy neutrinos:

$$pp \rightarrow h_1 \rightarrow \nu_h \nu_h \rightarrow 3\ell 2j \text{ MET}, \quad (3)$$

$$pp \rightarrow h_1 \rightarrow \nu_h \nu_h \rightarrow 4\ell \text{ MET}, \quad (4)$$

the so-called “tri-lepton” and “fully leptonic” decay modes, whose pictorial representations are given in figure 3. A channel without missing energy would also be present (namely, $pp \rightarrow h_1 \rightarrow \nu_h \nu_h \rightarrow 2\ell 4j$), even though this is the channel with the largest cross section, the reconstruction of 4 very soft jets dramatically reduces its efficiency. In the tri-lepton case one heavy neutrino decays into $2\ell + \text{MET}$ and the second one decays into $\ell + 2j$. The fully leptonic decay (when both heavy neutrinos decay into $2\ell + \text{MET}$) is preferred for displaced vertices searches, while the semileptonic decay allows for higher total cross sections and for an efficient kinematic analysis, especially when $m_{\nu_h} > M_W$ [113]. Notice that, without using displaced vertices techniques, the neutrino mass reconstruction would be possible only in the tri-lepton case.

It is worth commenting that other scenarios, not included in the present analysis, might be of interest. First, a very light neutrino, with a mass of around 20 GeV: it would have escaped detection at LEP (because its coupling to the Z boson are heavily see-saw suppressed¹) and it has a very long lifetime, hence resulting at most in a single displaced vertex accompanied

¹For this mass, $BR(Z \rightarrow \nu_i \nu_h) \sim 10^{-11}$ and $BR(Z \rightarrow \nu_h \nu_h) \sim 10^{-20}$.

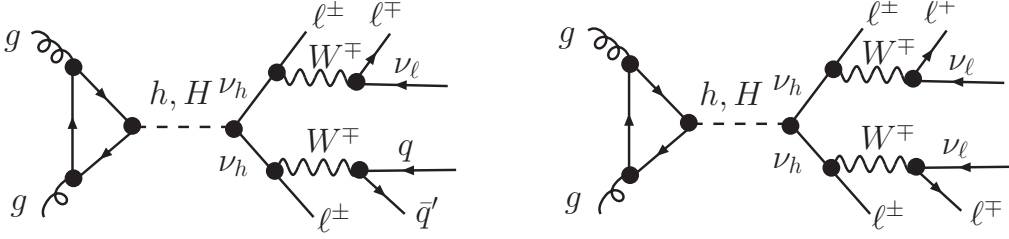


Figure 3: Production and cascade decay for (left-hand) eq. (3) and for (right-hand) eq. (4).

by missing momentum from the non-observed heavy neutrino. The efficiency to observe this signal would decrease in inverse proportion to the lifetime. Second, the decay into pairs of heavy neutrinos could be the only possibility to find the heavy Higgs boson, if weakly mixed with the light partner (therefore feebly coupled also to SM particles, evading the current LHC searches). It is important to stress that the scalar mixing angle α cannot vanish, since the most efficient production mechanisms of the heavy Higgs boson are the typical SM channels at the LHC [494]. Also notice that the couplings to heavy neutrinos are maximised in the weak mixing limit. Given that the cross sections are $\mathcal{O}(1)$ fb, this scenario can be studied at the LHC with full design luminosity even if a SM-like light Higgs boson is found, albeit weakly mixed with the heavy partner.

2.2 Long Lived SUSY states in MSSM models with FIMPs

The second class of models we consider is inspired by dark matter theories that employ the freeze-in mechanism to generate the dark matter relic abundance [495, 496]. This mechanism relies on the dark matter particle never reaching thermal equilibrium with the visible (e.g the SM or MSSM) sector states. In order for this to occur, only very small (we call them feeble) couplings between the hidden sector dark matter states and the visible sector states are allowed. These hidden sector states are referred to as Feebly Interacting Massive Particles (FIMPs).

Let us consider a connection between hidden sector FIMP states and the MSSM in the form of a SUSY particle, Y , that we will take an MSSM neutralino or chargino, decaying to the hidden sector state, X via $Y \rightarrow X + \dots$, where the ellipses represent some SM sector states. Here we assume that both Y and X are odd under R-parity. The relic abundance of X states generated by the freeze-in mechanism reads $\Omega h^2 \sim 10^{24} \Gamma_Y m_X / m_Y^2$ [495], where Γ_Y is the decay rate of Y with X final state. For all particle masses of interest, in order to get $\Omega h^2 \sim 0.1109 \pm 0.0056$ [500], Γ_Y is required to be very small. A consequence of which is that if we produce the particle Y in a detector it will travel a significant distance (greater than a few mm) before decaying. Moreover, the decay width of this state, which could be reconstructed from measurements of a number of such decays, could have a direct link to the relic abundance of dark matter as frozen-in via the decays of Y in the early Universe. Finally, it may also be possible to determine the masses of Y and X using kinematical techniques and therefore test the freeze-in expression for the relic abundance.

Beyond this simple picture, more complicated scenarios are possible and the exact predictions for the decay length and the mass of the X dark matter state can vary [501]. Therefore, we consider a range of parameters and masses to remain as general as possible so that this study can be easily applied to a specific picture of a visible and hidden sector feebly coupled with the the dark matter living in the hidden sector. Going beyond the freeze-in mechanism such a

scenario can occur in a number of different theories, for example in the context of asymmetric dark matter (see e.g. [502, 503]).

Given this motivation, we consider a supersymmetric model with a lightest ordinary supersymmetric particle (LOSP) that has a small decay width to some hidden sector state. This means that in every event in which a pair of supersymmetric particles are produced, there will be two long-lived LOSPs that will decay into hidden sector states. In this analysis, we take a phenomenological approach and optimise the signal by choosing by hand the decay length such that the majority of the decays occur in the tracker thereby allowing for a better reconstruction and a maximisation of the sensitivity of the search. In this way we are looking for the best possible scenario from a detector point of view, which will allow for a better idea of what could be achieved in less ideal scenarios.

We follow the basic set up outlined in both [504] and [501] where a singlet superfield is added to the MSSM and a survey of the potential operators that can be written down is made. We start these analyses and look in more detail at one of these operators. We assume that this extra singlet superfield is even under R-parity and consider only renormalisable operators. Under these assumptions we have chosen to analyse the superpotential Higgs portal operator $\Delta\mathcal{W} = \lambda X H_u H_d$. This choice has been made in order to initiate the study rather than fully cover all possibilities. An immediate extension of this work is to consider all other operators, including the non-renormalisable ones and the case of an R-odd singlet. The consequences of this operator has also been previously studied in [505], where an additional singlet superfield was added to the MSSM in order to solve the “ μ -problem”. The low energy theory studied in [505] has many features in common with the set-up we consider here.

In order for this operator to give rise to a long lived LOSP, the coupling λ has to be small. At order λ this term induces the interactions $\tilde{\chi}_i^- X_f W^+$ and $\tilde{\chi}_i^0 X_f Z$ (and the Hermitian conjugates), where $\tilde{\chi}_i^-$ and $\tilde{\chi}_i^0$ are the MSSM charginos and neutralinos, respectively, and X_f is the fermionic component of the X superfield. We look for final-state muons coming from a displaced vertex as this is a particularly powerful way to search for displaced vertices due to low backgrounds. In each event, we require only one cascade, resulting from the production and decay of a SUSY particle, to yield a displaced muon(s). The SUSY production channel considered is through of chargino pairs. In order for this to be the dominant production channel, we consider a region of parameter space with heavy squarks and gluinos. This choice has been made in order to remove the complication of applying existing limits on squarks and gluinos and also to leave the events as clean as possible.

Some details of the benchmark models we have studied are listed in Table 2. For each benchmark model we generate 100k events using the tools described in section 3. Benchmark 1 (BM1) looks at a possible point in the MSSM parameter space with a neutralino LOSP. The chargino pair production cross section for this point is calculated using both MadGraph5 [96] and CalcHep [1] to be ~ 0.1 pb. The diagrams for the production of a pair of charginos are depicted in Fig. 4. Due to the large masses of the squarks, the t-channel process is sub-dominant compared with the s-channel diagrams. The chargino will decay to a neutralino via a W , and with the large mass difference between the chargino and neutralino in BM1, this W can be produced on shell leading to hard jets or a hard single charged lepton. In our sample we allow the W to decay to all possible final states. The neutralino, as the LOSP, has two possible decay modes, both yielding an X_f in the final state. In our sample we only include events in which the neutralino decays to an X_f and an on-shell Z , with the Z decaying to muons as shown in Fig. 4. The other decay mode is to the light Higgs plus X_f and has a small branching ratio for

Sample	Hard process	Prompt objects	Proper decay length /cm	$M_{\text{FIMP}} / \text{GeV}$	σ / pb
FIMP BM1 Neutralino LOSP	$M_{\tilde{\chi}_1^+} = 235 \text{ GeV}$ $M_{\tilde{\chi}_1^0} = 123 \text{ GeV}$	2 hard Ws	25 50 100 50 50	1 1 1 0.1 25	0.103
FIMP BM2 Neutralino LOSP	Chargino pair prod. $M_{\tilde{\chi}_1^+} = 133 \text{ GeV}$ $M_{\tilde{\chi}_1^0} = 123 \text{ GeV}$	2 soft Ws	25 50 100	1 1 1	1.21
FIMP BM3 Chargino LOSP	Chargino pair prod. $M_{\tilde{\chi}_1^+} = 193 \text{ GeV}$	None	25 50 100	1 1 1	0.677
SM sample 1	$W\mu\nu$	$W\mu\nu$	0		10.46
SM sample 1	$Z\mu\mu$	$Z\mu\mu$	0		1.07
SM sample 2	QCD multijet	QCD multijet	0		1×10^7

Table 2: Description of Monte Carlo samples used in the analysis. The cross sections quoted for the FIMP benchmarks are for the chargino pair production only, see text for more details.

the chosen benchmark points.

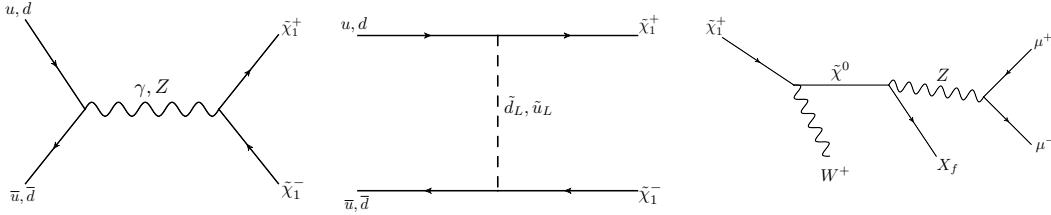


Figure 4: Production for all benchmarks with the cascade decays for BM1 and BM2.

The mass for the X_f state has been chosen to be 1 GeV for the majority of the benchmark scenarios. The reason for this is twofold but ultimately arbitrary. One motivation comes from the fact that we want to produce an on-shell Z in the decay of the neutralino so that we can reconstruct its mass. The other is that in the majority of asymmetric dark matter models the mass needed for the dark matter state is around a 1 GeV. In BM1 we also vary the mass of the X_f state to cover more scenarios and to investigate what effect this has on the kinematics and whether we can use this variation to determine the mass of the hidden sector state and of the LOSP.

As stated above, we only generate Monte Carlo events in which *both* SUSY cascades end with a pair of oppositely charged muons produced in a displaced vertex. We determine what fraction of these will pass cuts imposed on the displaced vertex (and other aspects of the event) in section 5.2. Analyses of real data might require only one rather than two displaced pair of oppositely charged muons. A further analysis would be required in that case to accurately estimate the efficiency. In this analysis, we have simply counted the total number of displaced muon pairs that pass the cuts. As there are two of these displaced muon pairs per event there will be a correlation between the displaced muons produced in the same event but as a first pass this

estimate gives us a good ball park figure with which to work. Given $BR(Z \rightarrow \mu\mu) \sim 0.034$, an estimate, with the chargino pair production cross section of 0.1 pb, of the number of events with at least one displaced pair of oppositely charged muons is $N \sim 8(\sigma/0.1\text{pb})(L/1\text{fb}^{-1})$, where L is the integrated Luminosity, which we have set at a value of 1fb^{-1} .

Benchmark 2 (BM2) contains a lighter chargino and the resulting production cross section is larger, 1.21 pb. Due to the lower chargino mass, the W produced in the decay from the chargino to the neutralino will be soft. Otherwise, BM2 is the same as BM1 and with the increased cross section we expect over 80 events with at least one pair of oppositely charged muons from a displaced vertex.

The lightest chargino can be lighter than the neutralinos if for low $\tan\beta$; $\text{sign}(M_1) \neq \text{sign}(M_2) = \text{sign}(\mu)$, see e.g. [506]. In Benchmark 3 (BM3) the chargino still delivers the dominant SUSY production cross section (as our squarks are still heavy), but it is now the LOSP, long-lived and will decay directly to X_f plus a W . We then consider the decay of the W into a muon plus muon neutrino thereby producing a displaced muon. The obvious difference in this case is that the LOSP has charged track, which produces a kink when it decays to the muon. The number of events expected in this case is much higher due to the larger branching ratio, $BR(W \rightarrow \mu\nu_\mu) \sim 0.11$, as compared to the $Z \rightarrow \mu^+\mu^-$ decay. An estimate for the number of events with at least one displaced muon is close to 150 for 1fb^{-1} .

3 Tools

B-L model Monte Carlo event files have been produced for the present analysis, according to the 2 benchmark points described in Table 1. For each benchmark point, 20k parton level events have been generated in CalcHEP [1], with full 3-body decays of the heavy neutrinos, hence properly taking into account W and Z boson off-shellness. Subsequently, the full samples have been hadronized/parton showered with Pythia v. 6.4.20 and, finally, fast detector simulation has been added by running Delphes v. 1.9 on the samples. Anti- k_T with ‘‘cone size’’ 0.5 has been chosen as jet algorithm to match CMS definitions. We have also modified the standard CMS card to match its isolation criteria.

For the **FIMP model** the Monte Carlo events generated are outlined in Table 2. A MadGraph5 [96] model file was produced using FeynRules [6] based on the existing MSSM model file [78]. The widths and branching ratios of the SUSY particles were calculated using BRIDGE [497] and passed to Pythia8 [116, 117] via the SLHA [15] decay tables. Although BRIDGE is capable of decaying the events in full, it forces all particles in a decay chain to be exactly on-shell (i.e. BRIDGE does not sample widths from the full Breit-Wigner distribution) so we decayed the events using Pythia8 instead. For benchmark 3 the initial scattering is performed in Pythia8 using the MadGraph5 matrix element as a semi-internal process. This was done to counteract a problem with passing events between MadGraph5 and Pythia8 where long-lived states are produced in the initial scattering, see section 3.1 for more details. The subsequent decay chain and showering was performed in Pythia8 using the decay tables obtained from BRIDGE for the chargino and neutralino decays. For comparison, Standard Model samples were also produced and these were generated using only Pythia8.

3.1 Displaced vertices in Pythia

A number of problems had to be overcome to generate displaced vertices correctly using Pythia. The calculation of the decay lifetime τ from the particle width specified in the SLHA header of

the event file does not seem to be performed automatically. As a solution, the lifetime of the long-lived particles can be set by hand during initialisation.

After setting the particle lifetime and decaying the event in *Pythia* we found that all particles have their production coordinates set at the interaction point. Outputting events in the Les Houches Event (LHE) format [507] is not affected, as only the particles lifetime and momentum is recorded, but outputting events to HepMC [508] format or as root trees will generate events with incorrect production vertices. This problem can be overcome by producing the hard process in the LHE format and running the event file through *Pythia* a second time, since, with this method, the production vertices are calculated correctly from the information in the LHE file. However, producing fully showered events including final state radiation (FSR) seems to be problematic with this procedure as displaced particles in the final state that emit a photon are moved back to the interaction point. A solution is to calculate the production vertices for each displaced particle and set them after the full event has been generated by *Pythia*. This was done recursively for all daughter particles from each displaced vertex before writing the event to disk.

A further complication arises in handling event files where the long-lived particle is produced in the initial scattering process. For example, in benchmark 3 for the FIMP model, the charginos are long lived and are produced directly via $pp \rightarrow \tilde{\chi}_1^+ \tilde{\chi}_1^-$. If this event is generated by MadGraph5 and then passed to *Pythia* to decay, it always decays the charginos at the interaction point even if the lifetime has been correctly set. To avoid this for benchmark 3 the scattering process was calculated entirely in *Pythia*.

Finally, in *Pythia6*, the “colour string reconnection” option must be disabled by setting the *Pythia6* option `MSTP(95) = 0`. This is because when deciding which partons to reconnect colour strings to, *Pythia6* does not explicitly check if the partons are at the same spatial coordinate. With colour reconnection enabled, it therefore sometimes reconnects colour strings between prompt partons and partons from the long-lived particle decay.

4 Review of existing measurements of displaced vertex signatures

This section presents the status of existing searches for displaced vertex signatures at hadron colliders.

ATLAS displaced vertex study. In Ref. [509], a search in 33 pb^{-1} of integrated luminosity collected in 2010 with the ATLAS detector for displaced vertices is presented. They study the decay of charged hadrons in association with a high-momentum muon. No signal is observed, and limits are placed on the product of di-squark production cross section and decay-chain branching fraction in a SUGRA scenario in which the lightest neutralino produced in the primary-squark decay undergoes R-parity violating decay into a muon and two quarks. The upper limits at 95% C.L. on the production cross section times branching fraction are at the level 0.5-100 pb for high-mass particles with lifetimes and velocities such that they decay at radial distances between 4 mm and 180 mm from the pp interaction point.

CMS displaced vertex study. In Ref. [510], a search in 1.1 fb^{-1} of integrated luminosity collected in 2011 with the CMS detector for displaced vertices is presented. The search is for Higgs bosons decaying to two long-lived, massive, neutral particles. The analysis searches for these long-lived particles via their decay to dileptons (both electron and muon) within the volume of the CMS tracker. No significant excess was observed above the Standard Model background and upper limits were placed typically in the range $0.003 - 0.03 \text{ pb}$, for X bosons

whose lifetime is such that their mean transverse decay length is less than 1 m.

CDF displaced vertex study. In Ref. [511], the results of a search for new particles with long lifetime that decay to a Z boson were presented in 163 pb^{-1} of data recorded with the CDF detector. Dimuons with invariant mass near the Z peak are vertexed and the decay length distribution studied. No evidence of a long-lived component was found, and cross section limits were presented on a fourth generation quark model. For a long-lived particle of mass 150 GeV, limits were set at 95% C.L. in the range $3 - 50 \text{ pb}$ for a decay length between 1 mm and 1 m.

D0 displaced vertex study. In Ref. [512], a search for a neutral particle, pair produced in $p\bar{p}$ collisions at a centre-of-mass energy $\sqrt{s} = 1.96 \text{ TeV}$, which decays into two muons and lives long enough to travel at least 5 cm before decaying, was presented. The analysis used 380 pb^{-1} of data recorded with the D0 detector. No candidates were observed, and limits were set on the pair-production cross section times branching fraction into dimuons+X for such particles. For a mass of 10 GeV and lifetime of $4 \times 10^{11} \text{ s}$, values greater than 0.14 pb were excluded at 95% C.L.

5 Experimental signatures

This section presents the kinematic and other properties of the two theoretical models presented in Sections 2.1 and 2.2. It also proposes an experimental analysis strategy, which exploits these properties to distinguish the signals from SM backgrounds at the LHC. Furthermore, in the hypothesis that a significant signal were to be seen, it considers how one might confirm that it is indeed due to one of these models, and explores how one might measure the model parameters.

The FIMP model of Section 2.2 predicts long-lived particles decaying to dileptons plus missing energy. This is also one of the possible decay modes of the long-lived particles of the $B - L$ model of Sect. 2.1. The analysis strategies for the two models will thus be very similar, with the methods used for the FIMP model tending to be a subset of those used for the $B - L$ model. In the two sub-sections that follow, results will be presented first for the $B - L$ model, and then for the FIMP model, emphasizing for the latter just the differences with respect to the former.

5.1 Phenomenology of Long-Lived Heavy Neutrino Decays in the B-L Model

This sub-section examines the properties of the two benchmarks described in Section 2.1, in which the light Higgs boson decays to a pair of long-lived, heavy neutrinos ν_h . We focus on the two most accessible experimentally ν_h decay modes, namely $\nu_h \rightarrow \ell^+ \ell'^- \nu$ and $\nu_h \rightarrow q\bar{q}' \ell^\pm$. Approximately 17% of ν_h decay to the $\ell^+ \ell'^- \nu$ mode, via both intermediate channels $\nu_h \rightarrow \ell^\pm W^\mp$ and $\nu_h \rightarrow Z \nu_\ell$. Approximately 45% of ν_h decay to the $q\bar{q}' \ell^\pm$ mode. (Here ℓ or ℓ' indicate the sum of electron or muon modes.) The studies were done by simulating the events with CalcHep/Pythia and simulating the detector response using Delphes, configured to model the CMS detector, as described in section 3. Delphes was configured to assume that electrons, muons and jets can be reconstructed down to p_T of 2, 4 and 20 GeV respectively. No efficiency loss was simulated arising from the triggers, since it is assumed that new triggers would need to be developed for this channel. It should be noted that Delphes does not record spatial coordinates, and so does not simulate loss of efficiency caused by the difficulty in reconstructing displaced tracks. All histograms shown in this section are normalised to one generated signal event. The statistical information shown in the histograms always corresponds to the 140 GeV Higgs mass.

The CMS displaced lepton search (Section 4) indicates that searching for a pair of oppositely charged leptons that are consistent with originating from a displaced vertex is a powerful way of searching for this kind of signal, reducing the background to very low levels. The leptons facilitate triggering. Thus the best way to search for heavy neutrinos should be via the $\ell^+\ell^-\nu$ mode. If necessary, the background events could be reduced further by searching for the $e^\pm\mu^\mp\nu$ mode or alternatively by requiring the presence of an additional displaced lepton from the second heavy neutrino. Figure 5a shows the p_T of the leptons from the heavy neutrino decay. Because of the low Higgs mass, these are relatively soft. In their publication (Section 4), CMS used triggers with lepton p_T thresholds of 23 GeV (33 GeV) for the dimuon (dielectron) channels, respectively. Unless these trigger thresholds can be reduced, (e.g. by requiring the presence of three leptons at trigger level), the trigger efficiency for heavy neutrinos would be poor (e.g. for the 120 GeV mass Higgs case, only 23% (7%) of reconstructed leptons have $p_T > 23$ (33) GeV). The generated transverse decay length distribution of the ν_h is approximately exponential in shape, with a mean of 25 (32) cm for the 120 (140) GeV Higgs mass. Since CMS has some efficiency to reconstruct tracks from long-lived exotics with transverse decay lengths of up to 50 cm (see Section 4), at least some of ν_h decay products would be found.

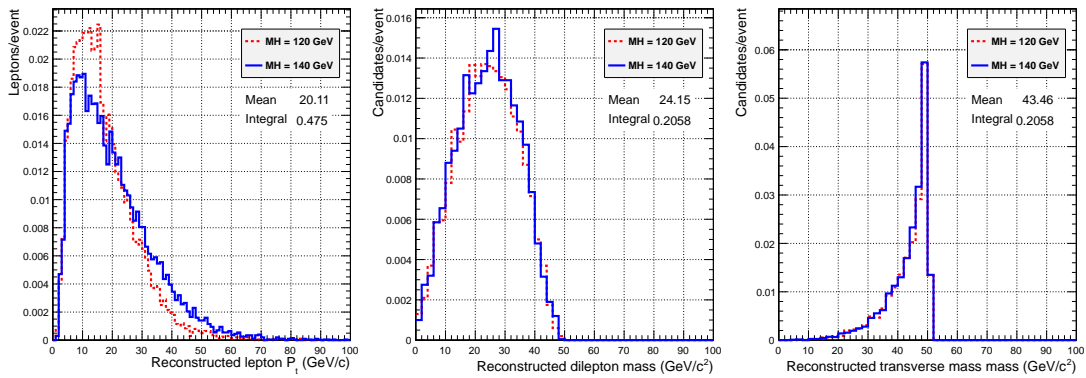


Figure 5: For the $\ell^+\ell^-\nu$ mode: the left-hand figure shows the p_T of the reconstructed leptons from the heavy neutrino decay; the middle figure shows the reconstructed dilepton mass spectrum; and the right-hand figure the reconstructed ν_h mass, as determined using the more sophisticated method described in the text.

If an excess of displaced dileptons is seen, one would wish to confirm if it were caused by heavy neutrinos and to measure the model parameters. Figure 5b shows the reconstructed invariant mass of the dileptons from the exotic decay. The end-point of this distribution can be used to estimate the heavy neutrino mass. Figure 5c shows a more sophisticated and accurate method to estimate the heavy neutrino mass. In this case, it is assumed that the heavy neutrino flight direction can be precisely determined from the vector between the reconstructed primary vertex and the displaced vertex. Defining the momentum component of the dilepton system perpendicular to the heavy neutrino flight direction as $\vec{p}_T^{\text{flight}}(\ell\ell)$, momentum conservation dictates that the corresponding quantity for the unobserved neutrino must be $\vec{p}_T^{\text{flight}}(\nu) = -\vec{p}_T^{\text{flight}}(\ell\ell)$. The transverse energy of the dilepton system with respect to the flight direction is then $E_T^{\text{flight}}(\ell\ell) = \sqrt{M(\ell\ell)^2 + p_T^{\text{flight}}(\ell\ell)^2}$ whilst that of the light neutrino (since it is massless with a very good degree of approximation) is $E_T^{\text{flight}}(\nu) = p_T^{\text{flight}}(\nu)$. Hence the transverse mass

of the heavy neutrino decay products, where ‘transverse’ is defined as meaning perpendicular to the flight direction, is $M_T^{\text{flight}} = \sqrt{[E_T^{\text{flight}}(\ell\ell) + E_T^{\text{flight}}(\nu)]^2 - [\vec{p}_T^{\text{flight}}(\ell\ell) + \vec{p}_T^{\text{flight}}(\nu)]^2} = E_T^{\text{flight}}(\ell\ell) + E_T^{\text{flight}}(\nu)$. This is analogous to the transverse mass commonly used in hadronic colliders to reconstruct the mass of a resonance that decays to a neutrino plus visible decay products. It differs in that here, it is the component of the light neutrino momentum parallel to the flight direction that is unknown, whereas conventionally it is the component along the beam-axis that is unknown. As shown in Figure 5c, the quantity M_T^{flight} is always less than the heavy neutrino mass (aside from resolution effects), but has far more entries near the end-point of the spectrum than the simpler method, thus allowing for a more precise measurement. It ought to be noted that the end-point technique works here only because the heavy neutrino is lighter than the SM gauge bosons, therefore decaying via effective 3-body decays. Instead the more refined transverse mass reconstruction works regardless of the heavy neutrino mass.

The displaced lepton vertex position would provide an approximate measurement of the heavy neutrino lifetime, although this would be complicated by the presence of the light neutrino amongst the heavy neutrino decay products, which would prevent a precise determination of its momentum. From the statistical information in Figure 5c, it can be seen that 0.21 dilepton candidates/event are reconstructed (for the 140 GeV Higgs mass), indicating only a small efficiency loss with respect to the $2 \times 0.17 = 0.34$ generated. We emphasize here that the combined measurement of the heavy neutrino lifetime and mass would enable to infer the related light neutrino mass [113].

In events containing a displaced dilepton vertex, one could search for a second heavy neutrino decaying through the $\nu_h \rightarrow q\bar{q}'\ell^-$ channel. This could be done by searching for a third displaced lepton and investigating if it formed a displaced vertex with a number of reconstructed charged hadrons. (ATLAS successfully found displaced vertices containing a lepton + hadrons in their analysis of Section 4.) Doing so would allow one to measure the relative branching ratio of the two heavy neutrino decay modes. As an additional step, one could then search for a pair of jets, arising from the $q\bar{q}'$ pair from the heavy neutrino decay, whose directions would be compatible with these hadrons. Figures 6a and 6b show the p_T of the reconstructed lepton and jets from the heavy neutrino in this channel. The soft jet spectrum represents a major challenge. Even assuming that one can reconstruct jets down to p_T of 20 GeV, which is optimistic, particularly in the presence of pile-up, the efficiency to reconstruct these jets is poor. However, if one succeeds, one can then estimate the heavy neutrino mass by plotting the reconstructed lepton + dijet invariant mass, as shown in Figure 6c. (It should also be noted that in the cases in which the $q\bar{q}'$ pair is reconstructed, simulation indicates that $\approx 80\%$ of the time they are reconstructed as two separate jets, as opposed to a single merged jet. One can thus require the presence of two reconstructed jets from the displaced vertex. Doing so improves the mass resolution.) From the statistical information in this histogram, it can be seen that 0.046 lepton + dijet candidates/event are reconstructed (for the 140 GeV Higgs mass), compared with the $2 \times 0.45 = 0.90$ generated $\nu_h \rightarrow q\bar{q}'\ell^\pm$ decays per event. The poor efficiency is due to the difficulty in reconstructing such soft jets.

To measure the Higgs boson mass, one could use either the tri-lepton final state (as in eq. (3)) or the four-lepton final state (as in eq. (4)). In both cases, the end-point of the spectrum would allow one to infer the Higgs mass. Figures 7a and 7b show the Higgs mass reconstructed from its visible decay products in these two channels. Furthermore, as can be seen from the statistical information in the histograms, the efficiency to reconstruct both heavy neutrinos in an event is at the percent level. As before, more sophisticated techniques can be employed to

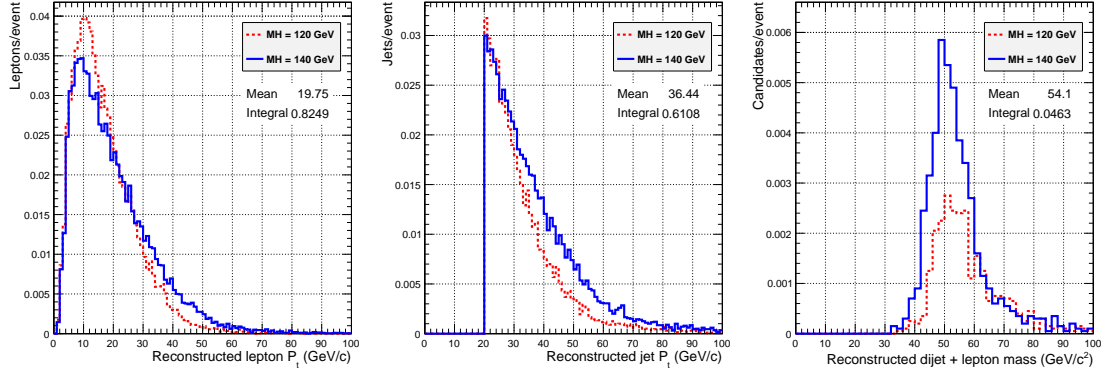


Figure 6: For the $q\bar{q}'\ell^\pm$ mode: the left-hand figure shows the p_T of the reconstructed lepton and the central figure shows the p_T of the reconstructed jets from the heavy neutrino decay. The right-hand figure shows the reconstructed invariant mass of the lepton plus dijet from the heavy neutrino decay.

reconstruct the Higgs mass, exploiting the reconstructed flight directions of the heavy neutrinos, the known heavy neutrino mass (assumed its mass has already been measured using the techniques described above) and the measured missing momentum transverse to the beam-axis $p_T(\text{miss})$. In the tri-lepton final state, one can exploit the missing transverse momentum to construct the transverse mass of the Higgs decay products (with respect to the beam axis) $M_T = \sqrt{[E_T(\text{vis}) + p_T(\text{miss})]^2 - [\vec{p}_T(\text{vis}) + \vec{p}_T(\text{miss})]^2}$, where $E_T(\text{vis}) = \sqrt{M(\text{vis})^2 + p_T(\text{vis})^2}$ and vis represents the visible Higgs decay products. This quantity M_T is plotted in Figure 7c. Were it not for the finite jet and missing energy resolutions, it would always be less than the Higgs mass, and its end-point could be used to estimate the latter.

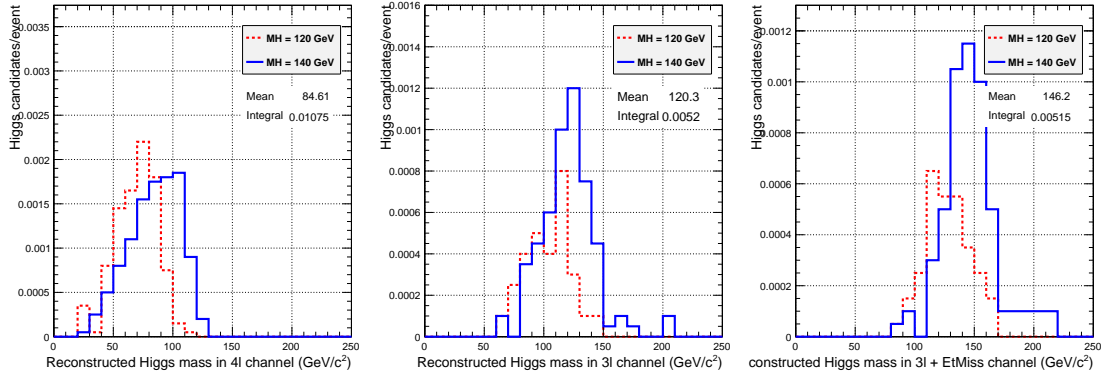


Figure 7: The reconstructed Higgs mass from the visible decay products in the 4-lepton (left) and tri-lepton channels (central), and from the visible decay products and missing transverse momentum in the tri-lepton channel (right).

5.2 Phenomenology of FIMP model

This section describes the properties of the benchmarks described in Section 2.2. The event samples were made according to the procedure discussed in Section 3. All benchmarks consid-

ered predict a long-lived particle decaying into a fermionic dark matter particle in addition to a W or Z boson. In this analysis we consider the subsequent decay of the boson in the muon decay channel.

Figure 8 shows the transverse momentum and angular separation (if applicable) of the muons originating from the heavy boson decay in all three benchmarks. The corresponding distribution for the SM Drell-Yan background is also shown for comparison. The kinematic constraints imposed by existing detector searches are marked on the plot. In the interests of maximising acceptance, the optimal lepton p_T requirement should be as low as possible. A single or di-muon trigger is envisaged to record the events studied here and, due to the muon vertex displacement, the trigger is expected not to rely on inner detector tracking information. As already described, trigger prescaling, needed due to the high luminosity of the LHC, means that the trigger threshold is likely to be at the lowest $\simeq 20$ GeV and may well be higher. However, the muons originating from these models are more energetic than in the $B - L$ model and thus a higher yield of events is envisaged. Some cut on the angular separation between the muons – either transverse or otherwise – would be necessary to avoid background contamination from cosmic rays. The looser this cut is, the more sensitivity the analysis will have to these models. The D0, and to a lesser extent the CMS, analyses will have reduced sensitivity to the FIMP model as their requirements on angular separation are sufficiently tight that they would remove many candidates.

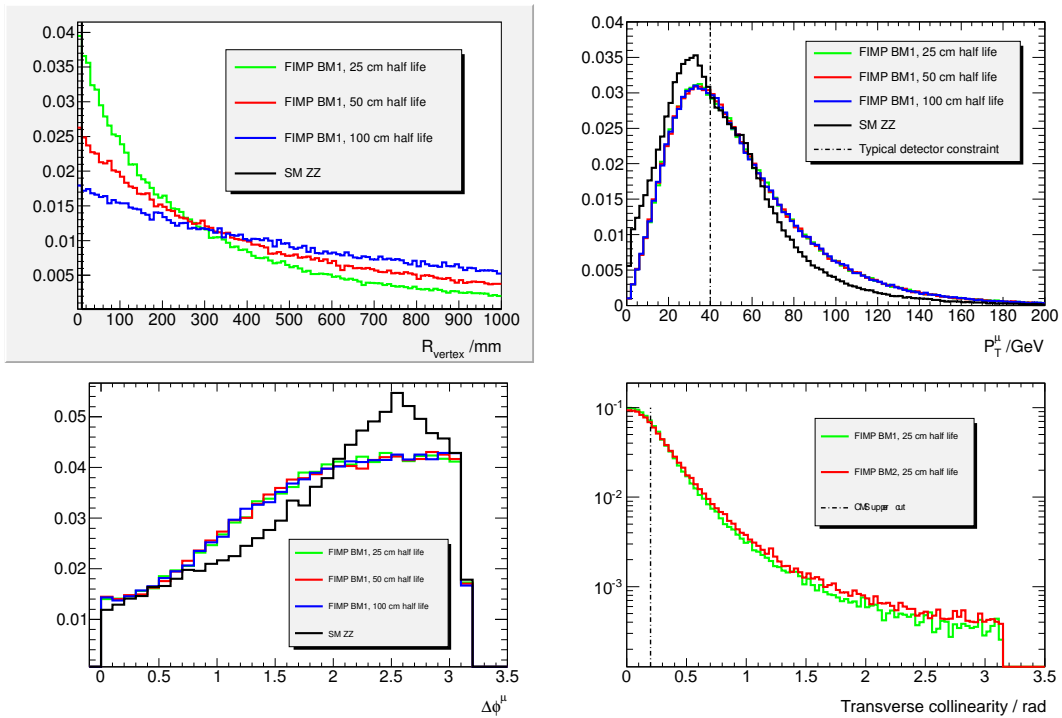


Figure 8: Radial displacement (top left), transverse muon momenta (top right), transverse angular muon separation (bottom left) and transverse collinearity (bottom right) of displaced Z decay. Standard Model Drell-Yan kinematics from a prompt Z decay are also shown for comparison. Existing cuts on these variables in displaced vertex searches are shown on the plot.

Searching for a muon pair displaced from the interaction point is a powerful way of discriminating these models from Standard Model background signatures. Figure 8 shows the

typical R displacement predicted by the FIMP models when the mean lifetime is set at 25, 50 and 100 cm in BM1. As in the previous model, a measured R displacement represents the lifetime of the chargino lifetime and thus its coupling to the FIMP. For any displaced particle, the most likely point of decay is $(0, 0, 0)$ and then an exponential decay from that point is observed, its mean lifetime governed by the decay length of the particle. It can be seen in the CMS and ATLAS studies that the efficiency for reconstructing these vertices also drops sharply as the displacement is increased.

The displaced vertex represents a decay into a Z boson and a fermionic dark matter particle which will be observed as missing transverse energy in the detector. Unlike the $B - L$ model, the model considered here does not allow for two leptons of different flavour to originate from the same vertex and thus we only consider decays to two, oppositely charged muons. The invariant mass of muon pairs, observed at a radial displacement R , will follow the same distribution as the invariant mass in Standard Model Z decays. A cut around the Z mass peak of the vertex could prove powerful in the proposed analysis, as there are no Standard Model physics backgrounds in which a high mass displaced $\mu\mu$ vertex would be seen in the detector.

The transverse collinearity angle between the reconstructed momentum vector of the Z boson and the vector from the primary to the secondary vertex – the neutralino direction of flight – is also shown in figure 8. It is seen that the most likely direction of the Z is collinear to the neutralino although there is a significant portion of events in which this is not the case. The collinearity cut imposed in the CMS analysis – an upper limit of 0.2 radians – would be likely to remove a significant number of FIMP decays, should they be present, from their selected events.

The presence of missing transverse energy in the event is also considered. Figure 9 shows the total missing transverse energy from both the neutrinos and the FIMPs and from only the FIMPs in the event, respectively. All benchmarks are shown (with 25 cm mean life) as well as SM $W \rightarrow \mu\nu$ events. Only BM3, due to the additional contribution from the displaced W decay, predicts larger missing transverse energy than the SM W sample. This implies that the transverse missing energy contribution provided by a 1 GeV FIMP is comparable to that from the neutrino in a $W \rightarrow \mu\nu$ decay, and for this reason a cut on transverse missing energy may not be a powerful discriminant for these models.

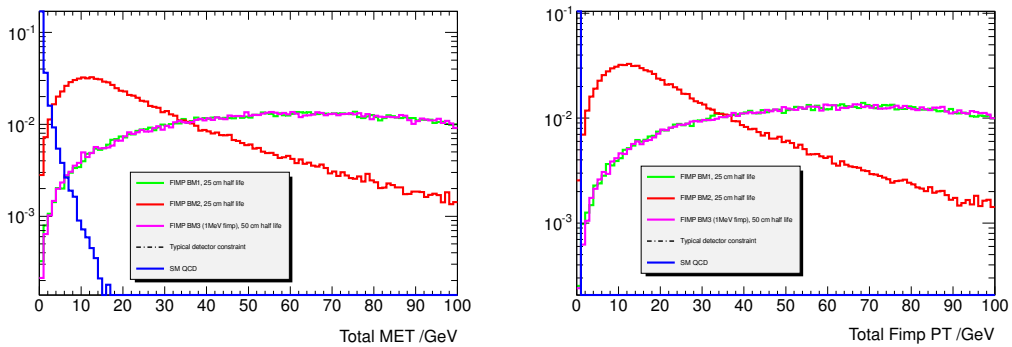


Figure 9: Missing transverse energy from combination of neutrinos and FIMPS (left), and from FIMPS only (right) in all 3 benchmarks. The distribution expected from Standard Model $W\mu\nu$ is shown for comparison.

5.3 Sensitivity of current displaced vertex searches to models

Among the current searches for displaced vertex signatures at hadron colliders, the CMS search has the most sensitivity to the model under consideration. The D0 analysis would have limited sensitivity to the model due to the cut on the angular separation between the muons, and the limits set by the CDF analysis (limited by the luminosity available) do not reach the cross sections for the range of FIMP models considered. The ATLAS search is not relevant for the FIMP model as the event selection is on a different final state topology (muon+hadrons).

To estimate the potential sensitivity of a CMS-like search for FIMP decays, a similar event selection is run – at truth level – for the benchmarks. The requirement applied is two energetic (transverse momenta > 25 GeV) and fiducial ($|\eta| < 2.4$) muons associated with the same vertex. A veto is applied to muons that are back-to-back (transverse angular separation < 2.8). The transverse collinearity cut employed by the CMS analysis, which would remove many FIMP events, is not applied. The expected yields per fb of data for each benchmark is summarised in table 3, having taken into account the branching ratio, $\Gamma(\mu)$, for having at least one of the legs decaying muonically. No physics background was seen to pass the proposed event selection, and it is assumed that there is zero machine or detector background given the high mass of the displaced vertex.

There will be additional losses to the number of events seen to pass the fiducial selection at truth level, due to imperfect detector reconstruction of the event. As has been discussed, the largest losses will be in triggering and reconstruction of the displaced vertex. A functional form of efficiency – although it must be noted this is very detector dependent – to reconstruct a muon as a function of radial displacement was assumed from studying the publicly-available CMS efficiency plots. The form was taken as linear fall off from unity at zero displacement to zero at 40 cm displacement. As would be expected, the longer the life-time of the particle is, the more events are lost due to imperfect efficiency modelling in the detector. The results here suggest that certain models (BM2) may very well already be ruled out by existing displaced vertex searches, but others (BM1) may not yet be visible with the current detector limitations and integrated luminosity available.

The p_T cut used on the leptons in the CMS analysis significantly reduces its efficiency in a search for low mass Higgs bosons – CMS quotes limits only for Higgs masses > 200 GeV. Their publication does not therefore rule out the benchmarks presented in Section 2.1. One should note that the heavy neutrinos in the $B - L$ model have only a 2.9% branching ratio to $\mu\mu\nu$ (when summed up over the three generations). And that the probability of both of these muons being reconstructed with transverse momenta exceeding the cut used by CMS and of the dimuon system being collinear with the exotica flight direction to within 0.2 radians (also required by CMS) is only 2.7%. If one attempted to reinterpret the CMS publication in terms of limits on the $B - L$ cross section, the result would be a limit of approximately $0.01\text{pb}/(0.029 \times 0.027) = 10$ pb. This is well above the theoretically expected cross section.

Selection	$N_{BM1} \times \Gamma(\mu)$	$N_{BM2} \times \Gamma(\mu)$	$N_{BM3} \times \Gamma(\mu)$	$N_{SM} \times \Gamma(\mu)$
W	1	0	0	$\simeq 5000000$
Z	0.05	0	0	$\simeq 100000$
Displaced Vertex	4	42	0.01	$\simeq 0$

Table 3: Expected yield of FIMP events for 1 fb^{-1} of luminosity passing Standard Model and CMS-style displaced vertex selections at truth level.

Due to the cascade decays inherent in the FIMP models, such events can be quite noisy with many hard leptons and jets produced at the interaction point. Standard W and Z event topology selections were applied to the samples. It was found that the expected contribution from the models considered here would be well below the current fractional uncertainty on measured W and Z cross sections [513]. This suggests that if these events were produced at the LHC, they would not be detected in ATLAS or CMS SM analyses if event yields or basic kinematics alone are considered.

The strategies developed in Section 5.1 for determining the mass of long-lived particles would require some modification of the FIMP analysis. The method illustrated in Figure 5b of measuring the endpoint of the dilepton mass spectrum would only work if the Z boson is off mass-shell, since otherwise, the dilepton invariant mass would simply be equal to the Z boson mass. Thus this method is only applicable if the mass difference between the gaugino and the FIMP is less than the Z mass. The more sophisticated method illustrated in Figure 5c, which uses the measured long-lived particle flight direction as a constraint, does not suffer from this limitation. However, it does assume that the invisible particle is massless, so could only be employed for the FIMP analysis if the FIMP has a much lower mass than the long-lived particle.

6 Conclusions

We have investigated two classes of models, which are quite different from the theoretical point of view. Both models predict long-lived particles – heavy Majorana neutrinos (from Higgs boson decay) in the case of $B - L$ model and charginos/neutralinos in the case of an MSSM model extended by a singlet superfield that is feebly coupled to the standard MSSM states (FIMP model). The decay of these long-lived particles provide spectacular displaced, multi-lepton (or lepton + jet) signatures, which are virtually background-free.

For selected benchmark points of the $B - L$ and FIMP models, we performed an analysis showing that experimental observation of these displaced vertices at the LHC should be possible. We also demonstrated how one could reconstruct the masses of the long-lived particles, profiting from the reconstructed vertex positions to constrain the long-lived particle flight direction. Similar analysis techniques could be applied to other BSM models featuring long-lived particles. In the case of the $B - L$ model, the measurement of the mean lifetime and mass of the Majorana neutrinos could be important ingredients, allowing one to deduce the absolute mass of SM-like neutrinos [113]. We showed that published searches from the Tevatron and the LHC experiments have poor sensitivity to these models.

ACKNOWLEDGEMENTS

L.B and A.B. thank the NExT Institute and Royal Society for partial financial support. L.B. has also been partially supported by the Deutsche Forschungsgemeinschaft through the Research Training Group GRK 1102 *Physics of Hadron Accelerators*. SMW and AJW thank the Higher Education Funding Council for England and the Science and Technology Facilities Council for financial support under the SEPNet Initiative and the IPPP for financial support.

Dark Matter

Contribution 19

Impact of semi-annihilations on dark matter phenomenology – an example of Z_N symmetric scalar dark matter

G. Bélanger, K. Kannike, A. Pukhov, M. Raidal

Abstract

We study the impact of semi-annihilations $\chi\chi \leftrightarrow \chi X$, where χ is dark matter and X is any standard model particle, on dark matter phenomenology. We formulate scalar dark matter models with minimal field content that predict non-trivial dark matter phenomenology for different discrete Abelian symmetries Z_N , $N > 2$, and contain semi-annihilation processes. We implement such an example model in micrOMEGAS and show that semi-annihilations modify the phenomenology of this type of models.

1 INTRODUCTION

The origin of dark matter of the Universe is not known. In popular models with new particles beyond the standard model particle content, such as the minimal supersymmetric standard model, an additional discrete Z_2 symmetry is introduced [514]. As a result, the lightest new Z_2 -odd particle, χ , is stable and is a good candidate for dark matter. The phenomenology of this type of models is studied extensively.

The discrete symmetry that stabilises dark matter must be the discrete remnant of a broken gauge group [515], because global discrete symmetries are broken by gravity. The most natural way for the discrete symmetry to arise is from breaking of a $U(1)_X$ embedded in a larger gauge group, e.g. $SO(10)$ [516]. The latter contains gauged $B - L$ as a part of the symmetry, and the existence of dark matter can be related to the neutrino masses, leptogenesis and, in a broader context, to the existence of leptonic and baryonic matter [299, 303, 517].

Obviously, the discrete remnant of $U(1)_X$ need not to be Z_2 – in general it can be any Z_N Abelian symmetry. The possibility that dark matter may exist due to Z_N , $N > 2$, is a known [354, 518–525] but much less studied scenario¹. Model independently, it has been pointed out in Ref. [525] that in Z_N models the dark matter annihilation processes contain new topologies with different number of dark matter particles in the initial and final states – called semi-annihilations –, for example $\chi\chi \leftrightarrow \chi X$, where X can be any standard model particle. It has been argued that those processes may significantly change the predictions for generation of dark matter relic abundance in thermal freeze-out. However, no detailed studies have been performed that compare dark matter phenomenology of different Z_N models. This is difficult also because presently the publicly available tools for computing dark matter relic abundance do not include the possibility of imposing Z_N discrete symmetry instead of Z_2 .

¹Phenomenology of Z_3 -symmetric dark matter in supersymmetric models has been studied in Refs. [518, 520] and in extra dimensional models in Refs. [354, 519].

The aim of this work is to formulate the minimal scalar dark matter model that predicts different non-trivial scalar potentials for different Z_N symmetries and to study their phenomenology. In particular we are interested in quantifying the possible effects of semi-annihilation processes $\chi\chi \leftrightarrow \chi X$ on generating the dark matter relic abundance. In order to perform quantitatively precise analyses we implement minimal Z_3 symmetric scalar dark matter models that contain one singlet and one extra doublet in micrOMEGAs [206, 526]. Using this tool we show that, indeed, the semi-annihilations affect the dark matter phenomenology and should be taken into account in a quantitatively precise way in studies of any particular model.

2 Z_N LAGRANGIANS

2.1 Z_N symmetry

Under an Abelian Z_N symmetry, where N is a positive integer, addition of charges is modulo N . Thus the possible values of Z_N charges can be taken to be $0, 1, \dots, N - 1$ without loss of generality. A field ϕ with Z_N charge X transforms under a Z_N transformation as $\phi \rightarrow \omega^X \phi$, where $\omega^N = 1$, that is $\omega = \exp(i2\pi/N)$.

A Z_N symmetry can arise as a discrete gauge symmetry from breaking a $U(1)_X$ gauge group with a scalar whose X -charge is N [515, 517].

For larger values of N the conditions the Z_N symmetry imposes on the Lagrangian approximates a $U(1)$ symmetry for two reasons. First, assuming renormalizability, the number of possible Lagrangian terms is limited and will be exhausted for some small finite N , though they may come up in different combinations for different values of N . Second, if the Z_N symmetry arises from some $U(1)_X$, the X -charges of particles cannot be arbitrarily large, because that would make the model nonperturbative – if N is larger than the largest charge in the model, the restrictions on the Lagrangian are the same as in the unbroken $U(1)$.

We shall see below that for the large number of possible assignments of Z_N charges to the fields, the number of possible distinct potentials is much smaller.

2.2 Field content of the minimal model

In order to study how different discrete Z_N symmetries impact dark matter phenomenology the example model must contain more than one type of dark matter candidates. The minimal dark matter model that possesses such properties contains, in addition to the standard model fermions and the standard model Higgs boson H_1 , one extra scalar doublet H_2 and one extra complex scalar singlet S [299]. In the case of Z_2 symmetry, as proposed in [299], those new fields can be identified with the well known inert doublet H_2 [527–530] and the complex singlet S [295–298, 302]. The phenomenology of those models is well studied. However, when they are put together, qualitatively new features concerning dark matter phenomenology, electroweak symmetry breaking and collider phenomenology occur [299, 303, 531–533]. The field content of the minimal scalar Z_N model is summarized in Table 1.

Table 1: Scalar field content of the low energy theory with the components of the standard model Higgs H_1 in the Feynman gauge. The value of the Higgs VEV is $v = 246$ GeV.

Field	$SU(3)$	$SU(2)_L$	T^3	$Y/2$	$Q = T^3 + Y/2$
$H_1 = \begin{pmatrix} G^+ \\ \frac{v+h+iG^0}{\sqrt{2}} \end{pmatrix}$	1	2	$\begin{pmatrix} \frac{1}{2} \\ -\frac{1}{2} \end{pmatrix}$	$\frac{1}{2}$	$\begin{pmatrix} 1 \\ 0 \end{pmatrix}$
$H_2 = \begin{pmatrix} H^+ \\ \frac{H^0+iA^0}{\sqrt{2}} \end{pmatrix}$	1	2	$\begin{pmatrix} \frac{1}{2} \\ -\frac{1}{2} \end{pmatrix}$	$\frac{1}{2}$	$\begin{pmatrix} 1 \\ 0 \end{pmatrix}$
$S = \frac{S_H+iS_A}{\sqrt{2}}$	1	1	0	0	0

2.3 Constraints on charge assignments

The assignments of Z_N charges have to satisfy

$$\begin{aligned}
X_S &> 0, \\
X_1 &\neq X_2, \\
-X_\ell + X_1 + X_e &= 0 \pmod{N}, \\
-X_q + X_1 + X_d &= 0 \pmod{N}, \\
-X_q - X_1 + X_u &= 0 \pmod{N}.
\end{aligned} \tag{1}$$

The first and second conditions arise from avoiding the $|H_1|^2 S$ term and from avoiding Yukawa terms for H_2 , respectively, and the rest from requiring Yukawa terms for H_1 .

The choice of Z_N charges for standard model fermions, the standard model Higgs H_1 , the inert doublet H_2 and the complex singlet S must be such that there are no Yukawa terms for H_2 and no mixing between H_1 and H_2 : only annihilation and semiannihilation terms for H_2 and S are allowed.

All possible scalar potentials contain a common piece because the terms where each field is in pair with its Hermitian conjugate are allowed under any Z_N and charge assignment. We denote it by V_c , where the ‘c’ stands for ‘common’:

$$\begin{aligned}
V_c &= \mu_1^2 |H_1|^2 + \lambda_1 |H_1|^4 + \mu_2^2 |H_2|^2 + \lambda_2 |H_2|^4 + \mu_S^2 |S|^2 + \lambda_S |S|^4 \\
&+ \lambda_{S1} |S|^2 |H_1|^2 + \lambda_{S2} |S|^2 |H_2|^2 + \lambda_3 |H_1|^2 |H_2|^2 + \lambda_4 (H_1^\dagger H_2)(H_2^\dagger H_1).
\end{aligned} \tag{2}$$

2.4 The Z_2 scalar potential

There are 256 ways to assign 0, 1 to the standard model and dark sector fields. Of these, 8 satisfy Eq. (1); among them, there are 2 different assignments to the dark sector fields, both

giving rise to the unique scalar potential

$$\begin{aligned}
V = & V_c + \frac{\mu'_S}{2}(S^2 + S^{\dagger 2}) + \frac{\lambda_5}{2} \left[(H_1^\dagger H_2)^2 + (H_2^\dagger H_1)^2 \right] \\
& + \frac{\mu_{SH}}{2}(S^\dagger H_1^\dagger H_2 + S H_2^\dagger H_1) + \frac{\mu'_{SH}}{2}(S H_1^\dagger H_2 + S^\dagger H_2^\dagger H_1) \\
& + \frac{\lambda'_S}{2}(S^4 + S^{\dagger 4}) + \frac{\lambda''_S}{2}|S|^2(S^2 + S^{\dagger 2}) \\
& + \lambda_{S1}|S|^2|H_1|^2 + \lambda_{S2}|S|^2|H_2|^2 \\
& + \frac{\lambda'_{S1}}{2}|H_1|^2(S^2 + S^{\dagger 2}) + \frac{\lambda'_{S2}}{2}|H_2|^2(S^2 + S^{\dagger 2}).
\end{aligned} \tag{3}$$

2.5 Z_3 scalar potentials

There are 6561 ways to assign 0, 1, 2 to the fields. Of these, 108 satisfy Eq. (1); among them, there are 12 different assignments to the dark sector fields, giving rise to 2 different scalar potentials. The example potential we choose to work with is

$$\begin{aligned}
V_{Z_3} = & V_c + \frac{\mu''_S}{2}(S^3 + S^{\dagger 3}) + \frac{\lambda_{S12}}{2}(S^2 H_1^\dagger H_2 + S^{\dagger 2} H_2^\dagger H_1) \\
& + \frac{\mu_{SH}}{2}(S H_2^\dagger H_1 + S^\dagger H_1^\dagger H_2),
\end{aligned} \tag{4}$$

which induces the semi-annihilation processes we are interested in. The second one is obtained from Eq. (4) by changing $S \rightarrow S^\dagger$ (with $\mu_{SH} \rightarrow \mu'_{SH}$ and $\lambda_{S12} \rightarrow \lambda_{S21}$).

2.6 Z_4 scalar potentials

There are 65536 ways to assign 0, 1, 2, 3 to the fields. Of these, 576 satisfy Eq. (1); among them, there are 36 different assignments to the dark sector fields, giving rise to 5 different scalar potentials. Among those the only potential that contains semi-annihilation terms is

$$\begin{aligned}
V_{Z_4}^1 = & V_c + \frac{\lambda'_S}{2}(S^4 + S^{\dagger 4}) + \frac{\lambda_5}{2} \left[(H_1^\dagger H_2)^2 + (H_2^\dagger H_1)^2 \right] \\
& + \frac{\lambda_{S12}}{2}(S^2 H_1^\dagger H_2 + S^{\dagger 2} H_2^\dagger H_1) + \frac{\lambda_{S21}}{2}(S^2 H_2^\dagger H_1 + S^{\dagger 2} H_1^\dagger H_2).
\end{aligned} \tag{5}$$

The other four scalar potentials can be formally obtained from the Z_2 -invariant potential Eq. (3) by setting all the new terms added to V_c to zero, with the exception of the 1) λ'_S , μ_{SH} , 2) λ'_S , μ'_{SH} , 3) μ'_S , λ'_S , λ''_S , λ'_{S1} , λ'_{S2} , 4) μ'_S , λ'_S , λ''_S , λ'_{S1} , λ'_{S2} , μ_{SH} , μ'_{SH} terms.

3 RELIC DENSITY IN CASE OF THE Z_3 SYMMETRY

3.1 Evolution equations

Consider the Z_3 -symmetric theory. The imposed Z_3 symmetry implies, as usual, just one dark matter candidate. This is because the Z_3 charges 1 and -1 correspond to particle and anti-particle. The new feature is that processes of the type $\chi\chi \rightarrow \chi X$, where X is any standard model particle, also contribute to dark matter annihilation. The equation for the number density reads

$$\frac{dn}{dt} = -v\sigma_{\chi\chi \rightarrow XX} (n^2 - n_{\text{eq}}^2) - \frac{1}{2}v\sigma_{\chi\chi \rightarrow \chi X} (n^2 - n n_{\text{eq}}) - 3Hn. \tag{6}$$

We define

$$\sigma_v = v\sigma_{\chi\chi \rightarrow \chi\chi} + \frac{1}{2}v\sigma_{\chi\chi \rightarrow \chi X}v \quad \text{and} \quad \alpha = \frac{1/2\sigma_{\chi\chi \rightarrow \chi X}}{\sigma_v}, \quad (7)$$

which means that $0 \leq \alpha \leq 1$. In terms of the abundance, $Y = n/s$, where s is the entropy density, we obtain

$$\frac{dY}{dt} = -s\sigma_v (Y^2 - \alpha Y Y_{\text{eq}} - (1 - \alpha)Y_{\text{eq}}^2) \quad (8)$$

or

$$\frac{dY}{ds} = \frac{\sigma_v}{H} (Y^2 - \alpha Y Y_{\text{eq}} - (1 - \alpha)Y_{\text{eq}}^2). \quad (9)$$

To solve this equation we follow the usual procedure [526]. Writing $Y = Y_{\text{eq}} + \Delta Y$ we find the starting point for the numerical solution of this equation using the Runge-Kutta method using

$$\frac{dY_{\text{eq}}}{ds} = \frac{\sigma_v}{H} Y \Delta Y (2 - \alpha), \quad (10)$$

where $\Delta Y \ll Y$. This is similar to the standard case except that ΔY increases by a factor $1/(1 - \alpha/2)$. Furthermore, when solving numerically the evolution equation, the decoupling condition $Y^2 \gg Y_{\text{eq}}^2$ is modified to

$$Y^2 \gg \alpha Y Y_{\text{eq}} + (1 - \alpha)Y_{\text{eq}}^2. \quad (11)$$

This implies that freeze-out starts at an earlier time and lasts until a later time as compared with the standard case. This modified evolution equation is implemented in micrOMEGAs [206, 208].

3.2 Numerical results with micrOMEGAs

Using the scalar potential defined in Eq. (4) we have implemented in micrOMEGAs the scalar model with a Z_3 symmetry. The scalar sector is composed of one additional complex scalar doublet and one complex singlet. The neutral component of the doublet mixes with the singlet, the lightest component \tilde{h}_1 is therefore the dark matter candidate, while the heavy component \tilde{h}_2 can decay into $\tilde{h}_1 h$, where h is the standard model like Higgs boson. The Z_3 charge of $\tilde{h}_1, \tilde{h}_2, \tilde{h}^+$ is 1.

We then compute the dark matter relic density as well as the elastic scattering cross section on nuclei. Here we average over dark matter and anti-dark matter cross section assuming that they have the same density. The main contribution here comes from the Z -exchange diagram because there is a $\tilde{h}_1 \tilde{h}_1^* Z$ coupling². Furthermore one can easily show that the scattering amplitudes are not the same for protons and neutrons. Since the current experimental bounds on $\sigma_{\chi n}^{\text{SI}}$ are extracted from experimental results assuming that the couplings to protons (f_p) and neutrons (f_n) are equal, we define the normalized cross section on a point-like nucleus [237]:

$$\sigma_{\tilde{h}_1 N}^{\text{SI}} = \frac{\mu_{\psi 1}^2}{\pi} \frac{[Z f_p + (A - Z) f_n]^2}{A^2}. \quad (12)$$

This quantity can directly be compared with the limit on $\sigma_{\chi n}^{\text{SI}}$.

²In the inert doublet model with a Z_2 symmetry [527, 529], a λ_5 term splits the complex doublet into a scalar and a pseudoscalar, when the mass splitting is small such coupling leads to inelastic scattering.

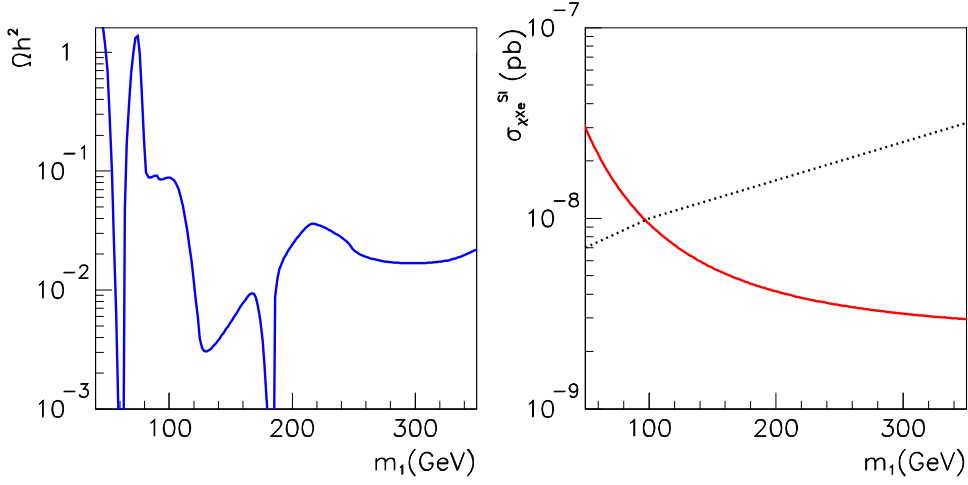


Figure 1: Ωh^2 as a function of the dark matter mass (left panel) and $\sigma_{\tilde{h}_1 X e}^{\text{SI}}$. The experimental limit from XENON100 [196] is also displayed (dashed line.)

To illustrate the behavior of the relic density of dark matter, we choose the parameters $\lambda_2 = 0.73, \lambda_3 = 0.16, \lambda_4 = 0.45, \lambda_S = 0.93, \lambda_{S1} = 0.06, \lambda_{S2} = 0.03, \lambda_{S21} = 0.69, \mu_S'' = 427.5$ GeV. Furthermore we fix the mass of the Higgs sector to be $M_h = 125$ GeV, $M_{h_2} = 371.2$ GeV and let $M_{\tilde{h}_1}$ vary. We also assume that \tilde{h}_1 is almost singlet taking $\sin \theta_h = 0.9995$.

The variation of Ωh^2 with the dark matter mass is displayed in Fig. 1. When the dark matter mass is around 50 GeV the main annihilation channel is through Z -exchange, note that this, however, leads to a very large direct detection rate. As $m_1 = m_{\tilde{h}_1}$ increases above $m_Z/2$, the relic density increases dramatically. At this point α is very small since the process $\tilde{h}_1 \tilde{h}_1 \rightarrow \tilde{h}_1^* Z$ is kinematically forbidden. After the threshold for W pair production, the relic density starts to drop, the process $\tilde{h}_1 \tilde{h}_1 \rightarrow \tilde{h}_1^* Z$ soon becomes kinematically accessible and α increases rapidly. The contribution of this channel rises rapidly leading to a drop of Ωh^2 to values below the preferred region extracted from WMAP measurements [284]. For yet larger dark matter masses the annihilation process $\tilde{h}_1 \tilde{h}_1 \rightarrow h_2^* \rightarrow \tilde{h}_1^* h$ occurs near the h_2 resonance, this is the second drop in Ωh^2 displayed in Fig. 1. As the dark matter mass increases further, several processes involving one non-standard particle in the final state can take place (notably $W^+ H^-, h \tilde{h}_1^*, h \tilde{h}_2^*, Z \tilde{h}_2^*$); such processes completely dominate and $\alpha \approx 1$.

The value of the SI cross section for the same parameters is displayed in Fig. 1 right panel. The region where $\Omega h^2 \approx 0.1$ just satisfies the Xenon100 bound [196]. Note that to achieve that it was necessary to have an almost pure singlet dark matter. Heavier dark matter satisfy easily the direct detection bounds, although their abundance is too low to explain all of the dark matter.

4 CONCLUSIONS

We have formulated scalar dark matter models with the minimal particle content in which dark matter stability is due to the discrete Z_N symmetry, $N > 2$. Already the minimal models containing one extra scalar singlet and doublet possess non-trivial dark matter phenomenology. In particular, the annihilation processes with new topologies like $\chi\chi \rightarrow \chi X$, where χ is the dark matter and X is any standard model particle, change the dark matter freeze-out process and must be taken into account when calculating the dark matter relic abundance. We have performed an example study of semi-annihilations in the Z_3 symmetric scalar dark matter model by implementing the model to micrOMEGAs and studying the impact of semi-annihilations to the relic abundance and on the predictions of dark matter direct detection. We conclude that in this type of models semi-annihilations may significantly affect the phenomenology and must be taken into account in numerical analyses quantitatively exactly.

ACKNOWLEDGEMENTS

Part of this work was performed in the Les Houches 2011 summer institute. K.K. and M.R. were supported by the ESF grants 8090, 8499, 8943, MTT8, MTT59, MTT60, MJD140, by the recurrent financing SF0690030s09 project and by the European Union through the European Regional Development Fund. A.P. was supported by the Russian foundation for Basic Research, grant RFBR-10-02-01443-a. The work of A.P. and G.B. was supported in part by the GDRI-ACPP of CNRS.

From Results to Interpretation

Contribution 20

Searches for New Physics: Les Houches Recommendations for the Presentation of LHC Results

*S. Kraml, B.C. Allanach, M. Mangano, H.B. Prosper, S. Sekmen (editors),
C. Balazs, A. Barr, P. Bechtle, G. Belanger, A. Belyaev, K. Benslama, M. Campanelli, K. Cranmer, A. De Roeck, M.J. Dolan, J.R. Ellis, M. Felcini, B. Fuks, D. Guadagnoli, J.F. Gunion, S. Heinemeyer, J. Hewett, A. Ismail, M. Kadastik, M. Krämer, J. Lykken, F. Mahmoudi, S.P. Martin, T. Rizzo, T. Robens, M. Tytgat, A. Weiler*

Abstract

We present a set of recommendations for the presentation of LHC results on searches for new physics, which are aimed at providing a more efficient flow of scientific information between the experimental collaborations and the rest of the high energy physics community, and at facilitating the interpretation of the results in a wide class of models. Implementing these recommendations would aid the full exploitation of the physics potential of the LHC.

1 INTRODUCTION

The LHC has very successfully begun to explore the TeV energy scale, and will be the energy frontier machine for the foreseeable future. Everyone who has had a hand in bringing this scientific and technological marvel to fruition deserves considerable credit and our thanks: the physicists and engineers who conceived, designed, and built it; those who operate the machine and its experiments; those who produce experimental results; those who try to understand them, and the public and its representatives whose generous support has enabled all this to happen.

The LHC was designed as a machine of discovery. There are high hopes that groundbreaking discoveries will indeed occur and shed light on electroweak symmetry breaking (be it via the Higgs mechanism or some other new dynamics) and new physics beyond the Standard Model (SM) of electroweak and strong interactions. It is of highest priority to our community to exploit fully the physics potential of the LHC. One aspect of this exploitation is the interpretation of LHC results in the contexts of different models of new physics. This is crucial if we are to unravel the correct new physics model, determine its parameters, and move beyond the SM.

The ATLAS and CMS collaborations are providing detailed experimental results [534, 535] of searches in many different channels. They are also providing interpretations in terms of popular models, such as the CMSSM¹, or in terms of Simplified Models². These results

¹Constrained Minimal Supersymmetric Standard Model, see e.g. [536].

²Simplified Models are designed as an effective-Lagrangian description of a small number of accessible new particles. This approach has a long heritage; for a recent paper advocating it see e.g. [537].

are being used to test as large a variety of beyond-the-SM (BSM) scenarios as possible. For example, the searches for supersymmetry (SUSY), including [199, 200, 233, 538–540], were interpreted in a number of different SUSY-breaking schemes, see e.g. [235, 277, 279, 281, 541, 542], as well as in the weak-scale “phenomenological” MSSM [191, 192]. The sensitivity to light stops was investigated in [543–545], while implications of compressed SUSY spectra were analyzed in [546]. Interpretations were also made for non-SUSY models, for instance for the minimal universal extra dimension (UED) model in [547]. Similar non-collaboration efforts to interpret Higgs search results [144, 402] in a large variety of BSM scenarios are also underway. These examples illustrate the community’s interest in the LHC experimental results—interest that will surely grow as results become more comprehensive and readily available.

A systematic way of presenting LHC results will also greatly facilitate the comparison and combination of analyses within and across the LHC collaborations, as well as the assessment of the physics potential of future facilities. Furthermore, agreement on a set of recommendations and their implementation would be a further step towards a more comprehensive approach to the storage, persistence and future use of LHC results.

In this contribution, we therefore propose a set of recommendations for the presentation of LHC results aimed at maximizing its scientific return. Many of the experimental publications already implement several of the basic recommendations we make. But, as we shall see, our recommendations go substantially beyond current practice. Our wish is to work towards an agreement on a common standard for the presentation of results. The goal is to help the community make the most of an extraordinary scientific opportunity.

2 EXECUTIVE SUMMARY

We here summarize our recommendations, which we present in four broad categories: analysis description, detector modeling, analysis dissemination and analysis design. Moreover, we include some recommendations regarding the interpretation of the results. Where appropriate, we split our recommendations into options:

- (a) “crucial” (mandatory) recommendations, defined as actions that we believe should be undertaken, following revision motivated by feedback from the experiments, and
- (b), (c) “desirable steps”, i.e. actions that would help, but whose implementation is recognized as either being controversial, and thus needing more debate, or requiring major efforts and a longer timescale.

Recommendations without such sub-division are understood as “crucial”. An extensive discussion of these recommendations will be published as an independent document.

1. (a) Provide a clear, explicit description of the analysis in publications. In particular, the most crucial information such as basic object definitions and event selection should be clearly displayed in the publications, preferably in tabular form, and kinematic variables utilised should be unambiguously defined. Further information necessary to reproduce the analysis should be provided, as soon as it becomes available for release, on a suitable common platform.
- (b) The community should identify, develop and adopt a common platform to store analysis databases, collecting object definitions, cuts, and all other information, including well-encapsulated functions, necessary to reproduce or use the results of the

analyses, and as required by other recommendations.

2. (a) Provide histograms or functional forms of efficiency maps wherever possible in the auxiliary information, along with precise definitions of the efficiencies, and preferably provide them in standard electronic forms that can easily be interfaced with simulation or analysis software.
(b) The community should take responsibility for providing, validating and maintaining a simplified simulation code for public use, reproducing the basic response of the LHC detectors. The validation and tuning of this tool should be based on comparisons with actual performance plots, and/or other inputs, made available by the experiments along the lines of Recommendation 2a. Limits of validity should be investigated and clearly documented.
3. (a) Provide all crucial numbers regarding the results of the analysis, preferably in tabulated form in the publication itself. Further relevant information, like fit functions or distributions, should be provided as auxiliary material.
Addendum:
For multi-bin results, provide an ensemble of sets of the numbers B , δB , \mathcal{L} , $\delta\mathcal{L}$, Q , k , etc in the auxiliary information. These would be created by sampling from the various experiment-specific systematic effects, such as the jet energy scale, jet energy resolution, etc. Results should be quoted without inclusion of systematic/theoretical uncertainties external to the experiment.
(b) When feasible, provide a mathematical description of the final likelihood function in which experimental data and parameters are clearly distinguished, either in the publication or the auxiliary information. Limits of validity should always be clearly specified.
(c) Additionally provide a digitized implementation of the likelihood that is consistent with the mathematical description.
4. In the interpretation of experimental results, preferably provide the final likelihood function (following Recommendations 3b/3c). When this is not possible or desirable, provide a grid of confidence levels over the parameter space. The expected constraints should be given in addition to the observed ones, and whatever sensitivity measure is applied must be precisely defined. Modeling of the acceptance needs to be precisely described.
5. For Higgs searches, provide all relevant information on a channel-by-channel basis for both production and decay processes.
6. When relevant, design analyses and signal regions that are based on disjoint sets of events.

3 CONCLUSIONS

This document presents a set of recommendations for the presentation of LHC results on searches for new physics, which are aimed at providing a more efficient flow of scientific information

and at facilitating the interpretation of the results in wide classes of models. It originated from discussions at this Les Houches “Physics at TeV Colliders 2011” workshop and was thoroughly discussed and refined, with valuable input from representatives of the ATLAS and CMS collaborations, in a dedicated miniworkshop organized by the LHC Physics Centre at CERN [548]. The target of these recommendations are physicists both within and outside the LHC experiments, interested in the best exploitation of the BSM search analyses.

The added value for the experiments, and the whole HEP community, in extending the scope of the information made available about the experimental results, is a faster and more precise feedback on the implications of these results for a broad range of theoretical scenarios. Correlations and consistency checks among the findings of different experiments, at the LHC and elsewhere, will be facilitated, and will provide crucial input in the choice of the best research directions in both the near and far future, at the LHC and elsewhere. Improving the way the results of the LHC searches are documented and stored furthermore provides a forum to explore alternative approaches to long-term data archiving.

The tools needed to provide extended experimental information will require some dedicated efforts in terms of resources and manpower, to be supported by both the experimental and the theory communities. Practical solutions towards the development of these tools and the implementation of the proposed recommendations will be addressed in dedicated Workshops and working groups.

ACKNOWLEDGEMENTS

We are grateful to the ATLAS and CMS search group conveners for helpful and supportive advice. We are also grateful to the ATLAS and CMS physics coordinators, in particular Richard Hawking and Greg Landsberg, for very constructive discussions on these recommendations. BCA would like to thank other members of the Cambridge SUSY Working Group for helpful suggestions.

This work has been partially supported by IN2P3, the Royal Society, STFC, and the ARC Centre of Excellence for Particle Physics at the Terascale. The work of JE is supported in part by the London Centre for Terauniverse Studies (LCTS), using funding from the European Research Council via the Advanced Investigator Grant 267352. JFG is supported by US DOE grant DE-FG03-91ER40674. HBP is supported in part by US DOE grant DE-FG02-97ER41022..

Contribution 21

High Energy Physics Model Database – HEPMDB: Towards decoding of the underlying theory at the LHC.

Maksym Bondarenko, Alexander Belyaev, Lorenzo Basso, Edward Boos, Vyacheslav Bunichev, R. Sekhar Chivukula, Neil D. Christensen, Simon Cox, Albert De Roeck, Stefano Moretti, Alexander Pukhov, Sezen Sekmen, Andrei Semenov, Elizabeth H. Simmons, Claire Shepherd-Themistocleous, Christian Speckner

Abstract

We present here the first stage of development of the High Energy Physics Model Data-Base (HEPMDB) which is a convenient centralized storage environment for HEP models, and can accommodate, via web interface to the HPC cluster, the validation of models, evaluation of LHC predictions and event generation-simulation chain. The ultimate goal of HEPMDB is to perform an effective LHC data interpretation isolating the most successful theory for explaining LHC observations.

1 The idea behind HEPMDB

The year 2010 has marked the start of real data taking at the CERN Large Hadron Collider (LHC). The central task of the LHC is to find signals from new physics and to reveal the underlying dynamics of Nature responsible for such signals. This is a highly non-trivial problem since many promising models could and do lead to similar signatures. For the next decades research in High Energy Physics (HEP) will be concentrated on interpreting the data from the LHC. We propose to create a High Energy Physics Model Data-Base (HEPMDB) which will be an unparalleled tool to isolate the most successful theory in explaining LHC observations. This project is aimed at boosting the activity of HEP groups around the world and will play an important role in the LHC data interpretation.

The first phase of the HEPMDB prototype is accessible at <https://hepmdb.soton.ac.uk>. The HEPMDB was created as a result of ideas discussed in the context of the “Dictionary of LHC signatures” activity [549], at the FeynRules workshop [550] and at the “Mini-Workshop on Dynamical Symmetry Breaking models and tools” [551]. Following the “Dictionary of LHC signatures” activities it was agreed that the identification of the underlying theory from LHC signals can only be sensibly realised via a flexible database which collects models and their specific signatures.

The HEPMDB is aimed to:

1. Collect HEP models for various multipurpose Matrix Element (ME) generators like CalcHEP [1], CompHEP [90,91], FeynArts [552,553], MadGraph/MadEvent [93,96,134,135], AMEGIC ++/COMIX within SHERPA [118,119]. and WHIZARD [98]. Under “HEP models” we denote the set of particles, Feynman rules and parameters written in the format specific for a given package.

2. Collect model sources which can be used to generate HEP models for various ME generators using FeynRules [6] or LanHEP [9], which automate the process of generating Feynman Rules, particle spectra, etc.. Under “model source” we denote the model (lagrangian etc.) written in the form of input for FeynRules or LanHEP. For the moment, FeynRules interfaces to CompHEP, CalcHEP, FeynArts, GoSam [133], MadGraph/MadEvent, SHERPA and WHIZARD [108] are available. LanHEP works with CalcHEP, CompHEP, FeynArts and GoSam. Also, the latest LanHEP v.3.15 has an option (under test) of outputting the model in UFO format [135] which provides a way to interface it with MadGraph/MadEvent.
3. Allow users to upload their models onto a server in order to perform evaluation of HEP processes and event generation for their own models using the full power of the High Performance Computing (HPC) cluster standing behind the HEPMDB itself. The HPC cluster at Southampton University, IRIDIS3 is the state-of-the-art fastest university-owned HPC resource in the UK, with 1008 8-core compute nodes (Intel Nehalem 2.26 GHz), at least 24GB of memory per node, all connected with fast infiniband network for parallel communication. This is one of the very powerful features of the HEPMDB: it provides a web interface to various ME generators which can then also be run directly on the HPC cluster. This way, users can perform calculations for any model from the HEPMDB (including their own models which they can upload), avoiding problems related to installing the actual software, which can sometimes be quite cumbersome.
4. Cross check and validate models for different ME generators. We should note that similar functionality is also provided by the FeynRules web validation framework [554] which is also presented in these proceedings. However, the FeynRules web validation is mainly geared towards comparing FeynRules models and can use its knowledge of the model format to provide a highly automatized test procedure for those, while the HEPMDB works in a more generic way and will provide access to more model formats at the price of slightly less automatization. Also, one should stress that uploads and evaluations at the HEPMDB are available to *all users*. This is an important new feature of the HEPMDB as compared to the FeynRules website.
5. Collect predictions and specific features of various models in the form of a (sub)database of signatures and perform comparisons of various model predictions with experimental data. There are a lot of different aspects related to this problem, details of which are outside the scope of the current short contribution. We would like to mention though, that this task includes a comprehensive development of a database of signatures as well as development of the format of presentation of these signatures. This format will be consistent with the format which will be used by the experimentalists for the presentation of the LHC data, discussed at the workshop in the context of the “Les Houches Recommendations for the Presentation of LHC Results” activity.
6. Trace the history of model modifications (in case modifications take place), and makes available all versions of the models. Through this application, we stress the importance of reproducibility of the results coming from the HEPMDB or from a particular model downloaded from the HEPMDB.

We would like to stress that the HEPMDB is an important project which has no analogy at the moment. It is different from projects which sound quite similar but in fact serve a different purpose. For example, the “Database of Numerical HEP scattering cross sections”

(<http://durpdg.dur.ac.uk/HEPDATA/REAC>) collects various particle scattering process cross-sections which are connected to experimental searches of different reactions. On the other hand the "Signatures of New Physics at the LHC" web-site (<http://www.lhcnewphysics.org/>) collects various BSM signatures, classifies them and the related papers. The part of the HEPMDB related to signatures definitely has a lot in common with "Signatures of New Physics at the LHC" but the global aim of the HEPMDB is generically different. The HEPMDB is aimed to provide an important connection between theory (in the form of theoretical models which users can upload), phenomenology (in the form of cross sections and distributions which users can evaluate at the HEPMDB) and experiment (in the form of collections of model-specific signatures and simulated events which can be used by experimental collaborations).

2 The current status of the HEPMDB

The HEPMDB project main page is presented in Fig. 21.1(a). At the moment the HEPMDB allows the user to perform the following operations.

1. Find and download an existing HEP model from the database. The search engine checks patterns in the following fields: Model, Authors, References, Abstract, Signatures and Information (see Fig. 21.1(b)).
2. Upload a new model (upon user registration). The model can be uploaded in the format of any ME generator. Also, a user can upload the model *source* in FeynRules or LanHEP formats. An example of the model entries as well as the model history is given in Fig. 21.1(c).
3. Perform the evaluation of cross sections for user-defined processes for the chosen model from the HEPMDB and produce a corresponding LHE file with generated parton-level events. This file becomes available for download once the process is finished. Currently, the HEPMDB allows the user to perform these calculations (using the aforementioned HPC) for CalcHEP and WHIZARD models only. An example of such an evaluation is given in Fig. 21.1(d).
4. Update or add features and respective signatures specific to each model. These features and signatures can be used in the future to distinguish the model from others and connect it to the LHC signatures.
5. Keep track of model changes, providing reproducibility of the results obtained with previous versions of the models uploaded to the HEPMDB.

3 HEPMDB: conclusions and future prospects

The present stage of the HEPMDB is a first step towards realizing a systematic comparison of various model predictions with experimental data and decrypting of the underlying theory.

The following improvements and additions will take place in the HEPMDB in the coming months.

1. The LanHEP and FeynRules packages will be added to provide event generation from model sources.
2. The MadGraph/MadEvent and CompHEP packages will be added.

3. A systematic model validation process will be started and the respective pages will be added.
4. The possibility to study events beyond parton level will be carefully considered, up to detector simulation. One concrete possibility would be the chain
LHE events \rightarrow HEPMC events \rightarrow FASTSIM events (ROOT format). For the last step, Delphes [375] seems a promising candidate.
5. The structure of the database of signatures will be extended to deal with correlated signatures (i.e. whereby multiple signatures, or lack thereof, must be accounted for simultaneously).
6. The possibility to produce plots for various kinematic distributions will be added.

On the longer time scale (of the order of one year) we plan to install the MicrOMEGAs package for evaluation of the dark matter relic density as well as to provide a possibility for scans of various model parameter spaces. During this stage, a development of the format for model predictions consistent with the format for presentation of the LHC data by experimentalists is planned. The question about including automatic tools for NLO evaluations is under discussion and will be developed further at the later stages of the HEPMDB development.

To conclude, we hope that starting from the present stage, the HEPMDB development will be boosted further via involvement of the HEP community. The HEPMDB is already a convenient centralized storage environment for HEP models, and can accommodate, via web interface to the HPC cluster, validation of models, evaluation of LHC predictions and event generation and simulation. We think that in the near future the HEPMDB will also become a powerful tool for isolation of the most successful theory in explaining the LHC data.

ACKNOWLEDGEMENTS

AB and MB acknowledge financial support of HEPMDB at its initial stage by the University of Southampton and IPPP Institute. AB, LB and SM thank the NExT Institute and SEPnet for partial financial support. AB also does so with the Royal Society. CS and (partially) LB have been supported by the Deutsche Forschungsgemeinschaft through the Research Training Group GRK 1102 *Physics of Hadron Accelerators*. NC was partially supported by the United States National Science Foundation under grant NSF-PHY-0705682 and partially by the PITTsburgh Particle Physics, Astrophysics and Cosmology Center (PITT PACC).

HEPMDB
High Energy Physics Models DataBase

Home Tools Signatures Contact Us

Search in HEPMDB Show All Models

About HEPMDB

HEPMDB is created to facilitate the connection between High Energy theory and experiment, to store and validate theoretical models, to develop dictionary of the model signatures aimed to identify the fundamental theory responsible for signals expected at the LHC. HEPMDB is also designed for collecting different signatures for its models as well as respective experimental efficiencies. Using this information HEPMDB will be able to compare its BSM model predictions with LHC data which and would allow to discriminate an underlying theory. The database is in the development stage and your input in the 'Forum' section is highly appreciated. Database collects Particle Physics Models. These models are supposed to be public and represent themselves a set of Feynman Rules which can be in form of input for any of Matrix Element generators such as CalcHEP, CompHEP, FeynArts, Madgraph, SHERPA, WHIZARD. HEPMDB has an entrance for Model authors -- 'Authors' -- where Authors can test and validate their models. To become an 'Author', you should register in a 'Register' section. 'Authors' are welcomed to also upload LanHEP or FeynRules source of their models.

Validation

Test and model validation will be available in the nearest future and would include the computing of theoretical predictions for your model on our site via submitting jobs into the High Performance Computing Cluster (HPCC) at University site. It will also allow to run Feynman Rules generators -- LanHEP and FeynRules through the HPCC. You will learn news about this option in 'Forum' section. HEPMDB also collects signatures of Particle Physics Models, for which we suggest to use keywords which 'Authors' supposed to assign to their models. The database of signatures is in the permanent development and is available in the 'Signatures' section. Information and links on relevant packages, e.g. Matrix Element generators or Feynman Rules generator is located in the section 'Tools'.

News

New database is available
2011-06-07 20:21:27
A new database is available to download from our system. It is possible to validate this model on our system as well.
[More >](#)

IBM
2011-03-29 01:05:39
We now have confirmation from IBM that all the Indis 3 nodes will be arriving on the 26th September.
[More >](#)

Indis 3
2011-03-29 01:05:11
The current Indis 3 is our third generation cluster and is one of the largest computational facilities in the UK.
[More >](#)

UNIVERSITY OF Southampton

Durham University

(a)

HEPMDB
High Energy Physics Models DataBase

Home Tools Signatures Contact Us

Search in HEPMDB Show All Models

Search Models :: Results for [nMSSM]

- nMSSM**
from CalcHEP group
nMSSM models based on NMSSTools_2.3.1 spectrum calculator for CalcHEP package are presented. See details about NMSSTools in <http://www.th.u-psud.fr/NMDECAV/nmsstools.html> We present two ...
- NMSSM with Flavor violation**
Florian Staub
The Next-to-minimal standard model with the most general flavor structure in the quarks/squark as well as lepton/slepton sector. Model files produced by SARAH 3.0.20 Supports SLHA+ functional...
- NMSSM without Flavor violation**
Florian Staub
The NMSSM without any flavor violation in the quark/squark as well as lepton/slepton sector Model files produced by SARAH 3.0.20...
- nMSSM**
Florian Staub
The near-to-minimal supersymmetric standard including the most general flavor structure in the quark/squark and lepton/slepton sector. Model files created with SARAH 3.0.21 Supports SLHA+ funct...

(b)

HEPMDB
High Energy Physics Models DataBase

Home Tools Signatures Contact Us

Search in HEPMDB Show All Models

Model : NMSSM with Flavor violation

Authors
Florian Staub

Added By
Florian Staub

References
arXiv:0910.1785
arXiv:0909.2863

Abstract
The Next-to-minimal standard model with the most general flavor structure in the quarks/squark as well as lepton/slepton sector.

Information
The Next-to-minimal standard model with the most general flavor structure in the quarks/squark as well as lepton/slepton sector. Model files produced by SARAH 3.0.20 Supports SLHA+ functionality to read spectrum files produced with the NMSSM extension of SPheno created by SARAH.

Tools
CalcHEP [model]

Model History
2011-10-17 19:57:46
2011-10-17 19:54:02

[Download Model File](#) [Validate Model on HPCC](#)

(c)

CalcHEP Validation

Job #19461-----Friday 30th of October 2011 09:14:55 PM-----

CalcHEP Numerical details

Done!

Process	sigm (fb)	PID	Time (hr)	# events
u, d -> g	1.3036e+00	30279	0.00	157257
u, d -> g	1.1896e+00	30278	0.00	137157
d, s -> g	4.2576e-01	30281	0.00	21721
d, s -> g	4.2567e-01	30285	0.00	21721
g, c -> g	7.3054e+00	30282	0.00	871481
Total	1.0225e+01			12871287

Decay	width (GeV)	PID	Time (hr)	# events
WtoLW		30297	0.00	
WtoLL		30297	0.00	
Total	1.0229e+01		0.01	

Download the file [2011-10-30-single.lhe](#)

Message

```

201111 17:14:55 Job 19461 was finished
201111 17:14:56 Job 19398 was finished
201111 17:14:26 You successfully submitted a job on HPCCs: #19392. You will be notified by email when the job is finished.
201111 17:14:05 Error: You can run this batch using 'Run Full Batch File' menu only.
201111 17:14:08 Model # 3 was calculated by CalcHEP.
201111 17:14:17 You successfully submitted a job on HPCCs: #14193. You will be notified by email when the job is finished.
201111 17:10:40 Load calcHEP parameters
201111 17:10:19 Model # 2 was calculated by CalcHEP.
201111 17:09:57 Load calcHEP parameters
201111 17:09:48 You successfully submitted a job on HPCCs: #19461. You will be notified by email when the job is finished.
  
```

UNIVERSITY OF Southampton

Durham University

(d)

Figure 1: HEPMDB - (a) main page, (b) example of the search pattern and results, (c) model details, (d) ME evaluation.

Bibliography

- [1] A. Pukhov arXiv:hep-ph/0412191 [hep-ph].
- [2] P. Gondolo, J. Edsjo, P. Ullio, L. Bergstrom, M. Schelke, et al. *New Astron.Rev.* **49** (2005) 149–151.
- [3] T. E. Jeltema and S. Profumo *JCAP* **0811** (2008) 003, arXiv:0808.2641 [astro-ph].
- [4] S. Profumo and T. Jeltema, *DMMW - A tool for multi-wavelength dark matter searches.*, 2011.
- [5] L. Maccione, C. Evoli, D. Gaggero, G. Di Bernardo, and D. Grasso, *DRAGON: A public code to compute the propagation of high-energy Cosmic Rays in the Galaxy.*, 2011.
- [6] N. D. Christensen and C. Duhr *Comput.Phys.Commun.* **180** (2009) 1614–1641, arXiv:0806.4194 [hep-ph].
- [7] A. Strong, I. Moskalenko, T. Porter, G. Johannesson, E. Orlando, et al. arXiv:0907.0559 [astro-ph.HE].
- [8] F. E. Paige, S. D. Protopopescu, H. Baer, and X. Tata arXiv:hep-ph/0312045 [hep-ph].
- [9] A. Semenov *Comput.Phys.Commun.* **180** (2009) 431–454, arXiv:0805.0555 [hep-ph].
- [10] G. Belanger, F. Boudjema, A. Pukhov, and A. Semenov arXiv:1005.4133 [hep-ph].
- [11] M. Cirelli, G. Corcella, A. Hektor, G. Hutsi, M. Kadastik, et al. *JCAP* **1103** (2011) 051, arXiv:1012.4515 [hep-ph].
- [12] A. Arbey and F. Mahmoudi *Comput.Phys.Commun.* **182** (2011) 1582–1583.
- [13] E. Boos, M. Dobbs, W. Giele, I. Hinchliffe, J. Huston, et al. arXiv:hep-ph/0109068 [hep-ph].
- [14] M. R. Whalley, D. Bourilkov, and R. C. Group arXiv:hep-ph/0508110. <http://hepforge.cedar.ac.uk/lhapdf/>.
- [15] P. Z. Skands, B. Allanach, H. Baer, C. Balazs, G. Belanger, et al. *JHEP* **0407** (2004) 036, arXiv:hep-ph/0311123 [hep-ph].
- [16] B. Allanach, C. Balazs, G. Belanger, M. Bernhardt, F. Boudjema, et al. *Comput.Phys.Commun.* **180** (2009) 8–25, arXiv:0801.0045 [hep-ph].
- [17] F. Mahmoudi, S. Heinemeyer, A. Arbey, A. Bharucha, T. Goto, et al. *Comput.Phys.Commun.* **183** (2012) 285–298, arXiv:1008.0762 [hep-ph].
- [18] H. Goldberg *Phys.Rev.Lett.* **50** (1983) 1419.
- [19] L. M. Krauss *Nucl.Phys.* **B227** (1983) 556. Revised version.
- [20] M. Srednicki, R. Watkins, and K. A. Olive *Nucl.Phys.* **B310** (1988) 693.
- [21] P. Gondolo and G. Gelmini *Nucl.Phys.* **B360** (1991) 145–179.
- [22] J. Edsjo and P. Gondolo *Phys.Rev.* **D56** (1997) 1879–1894, arXiv:hep-ph/9704361 [hep-ph].
- [23] A. Arbey and F. Mahmoudi *Phys.Lett.* **B669** (2008) 46–51, arXiv:0803.0741 [hep-ph].
- [24] A. Arbey and F. Mahmoudi *JHEP* **1005** (2010) 051, arXiv:0906.0368 [hep-ph].
- [25] A. Arbey and F. Mahmoudi *Comput.Phys.Commun.* **181** (2010) 1277–1292, arXiv:0906.0369 [hep-ph].
- [26] A. Arbey arXiv:1106.1363 [astro-ph.CO].

- [27] G. Blanger, F. Boudjema, A. Pukhov, and A. Semenov *Comput. Phys. Commun.* **180**(5) (2009) 747–767.
- [28] V. Ginzburg, V. Dogiel, V. Berezhinsky, S. Bulanov, and V. Ptuskin, *Astrophysics of cosmic rays*. North Holland, 1990.
- [29] S. Gillessen, F. Eisenhauer, S. Trippe, T. Alexander, R. Genzel, et al. *Astrophys.J.* **692** (2009) 1075–1109, arXiv:0810.4674 [astro-ph].
- [30] A. W. Strong, I. V. Moskalenko, and V. S. Ptuskin *Ann. Rev. Nucl. Part. Sci.* **57** (2007) 285–327, arXiv:astro-ph/0701517.
- [31] T. Bringmann, M. Doro, and M. Fornasa *JCAP* **0901** (2009) 016, arXiv:0809.2269 [astro-ph].
- [32] J. Lavalle, J. Pochon, P. Salati, and R. Taillet *Astron. Astrophys.* **462** (2007) 827–848, arXiv:astro-ph/0603796.
- [33] P. Brun, G. Bertone, J. Lavalle, P. Salati, and R. Taillet *Phys. Rev.* **D76** (2007) 083506, arXiv:0704.2543 [astro-ph].
- [34] J. Lavalle, Q. Yuan, D. Maurin, and X. J. Bi *Astron. Astrophys.* **479** (2008) 427–452, arXiv:0709.3634 [astro-ph].
- [35] J. F. Navarro, C. S. Frenk, and S. D. White *Astrophys.J.* **462** (1996) 563–575, arXiv:astro-ph/9508025 [astro-ph].
- [36] A. Kravtsov, A. Klypin, J. Bullock, and J. Primack *Astrophys.J.* **502** (1998) 48.
- [37] L. Bergstrom, P. Ullio, and J. H. Buckley *Astropart. Phys.* **9** (1998) 137.
- [38] J. Einasto *Trudy Inst. Astrofiz. Alma-Ata* **51** (1965) 87.
- [39] B. Moore, T. Quinn, F. Governato, J. Stadel, and G. Lake *Mon. Not. Roy. Astron. Soc.* **310** (1999) 1147.
- [40] A. Burkert *Astrophys.J.* **25** (1995) 447.
- [41] J. Alwall, E. Boos, L. Dudko, M. Gigg, M. Herquet, et al. arXiv:0712.3311 [hep-ph].
- [42] J. Butterworth, F. Maltoni, F. Moortgat, P. Richardson, S. Schumann, et al. arXiv:1003.1643 [hep-ph].
- [43] A. J. Buras arXiv:hep-ph/9806471 [hep-ph]. To appear in 'Probing the Standard Model of Particle Interactions', F. David and R. Gupta, eds., 1998, Elsevier Science B.V.
- [44] Particle Data Group Collaboration, K. Nakamura et al. *J.Phys.G* **G37** (2010) 075021.
- [45] S. Weinberg *Phys.Rev.Lett.* **43** (1979) 1566–1570.
- [46] E. Ma *Phys.Rev.Lett.* **81** (1998) 1171–1174, arXiv:hep-ph/9805219 [hep-ph].
- [47] P. Minkowski *Phys. Lett.* **B67** (1977) 421.
- [48] M. Gell-Mann, P. Ramond, and R. Slansky *Conf.Proc.* **C790927** (1979) 315–321. To be published in *Supergravity*, P. van Nieuwenhuizen & D.Z. Freedman (eds.), North Holland Publ. Co., 1979.
- [49] T. Yanagida *Conf.Proc.* **C7902131** (1979) 95.
- [50] S.L. Glashow, in *Quarks and Leptons*, eds. M.Lèvy et al. (Plenum, New York 1980), p. 707.
- [51] R. N. Mohapatra and G. Senjanovic *Phys.Rev.Lett.* **44** (1980) 912.
- [52] J. Schechter and J. Valle *Phys.Rev.* **D22** (1980) 2227.
- [53] T. Cheng and L.-F. Li *Phys.Rev.* **D22** (1980) 2860.

- [54] R. Foot, H. Lew, X. He, and G. C. Joshi *Z.Phys.* **C44** (1989) 441.
- [55] E. K. Akhmedov, M. Lindner, E. Schnapka, and J. Valle *Phys.Rev.* **D53** (1996) 2752–2780, [arXiv:hep-ph/9509255](https://arxiv.org/abs/hep-ph/9509255) [hep-ph].
- [56] R. Mohapatra and J. Valle *Phys.Rev.* **D34** (1986) 1642.
- [57] A. Rossi *Phys.Rev.* **D66** (2002) 075003, [arXiv:hep-ph/0207006](https://arxiv.org/abs/hep-ph/0207006) [hep-ph].
- [58] B. Allanach, C. Balazs, G. Belanger, F. Boudjema, D. Choudhury, et al. In *Les Houches Physics at TeV Colliders 2005 BSM Working Group Summary Report* hep-ph 0602198.
- [59] B. C. Allanach, C. Grojean, P. Z. Skands, E. Accomando, G. Azuelos, et al. [arXiv:hep-ph/0602198](https://arxiv.org/abs/hep-ph/0602198) [hep-ph].
- [60] M. Malinsky, J. Romao, and J. Valle *Phys.Rev.Lett.* **95** (2005) 161801, [arXiv:hep-ph/0506296](https://arxiv.org/abs/hep-ph/0506296) [hep-ph].
- [61] M. Hirsch, M. Malinsky, W. Porod, L. Reichert, and F. Staub [arXiv:1110.3037](https://arxiv.org/abs/1110.3037) [hep-ph].
- [62] V. De Romeri, M. Hirsch, and M. Malinsky *Phys.Rev.* **D84** (2011) 053012, [arXiv:1107.3412](https://arxiv.org/abs/1107.3412) [hep-ph].
- [63] S. Khalil and A. Masiero *Phys.Lett.* **B665** (2008) 374–377, [arXiv:0710.3525](https://arxiv.org/abs/0710.3525) [hep-ph].
- [64] P. Fileviez Perez and S. Spinner *Phys.Rev.* **D83** (2011) 035004, [arXiv:1005.4930](https://arxiv.org/abs/1005.4930) [hep-ph].
- [65] B. O’Leary, W. Porod, and F. Staub [arXiv:1112.4600](https://arxiv.org/abs/1112.4600) [hep-ph].
- [66] A. Elsayed, S. Khalil, and S. Moretti [arXiv:1106.2130](https://arxiv.org/abs/1106.2130) [hep-ph].
- [67] R. Slansky *Phys.Rept.* **79** (1981) 1–128.
- [68] B. Holdom *Phys.Lett.* **B166** (1986) 196.
- [69] K. Babu, C. F. Kolda, and J. March-Russell *Phys.Rev.* **D57** (1998) 6788–6792, [arXiv:hep-ph/9710441](https://arxiv.org/abs/hep-ph/9710441) [hep-ph].
- [70] F. del Aguila, G. Coughlan, and M. Quiros *Nucl.Phys.* **B307** (1988) 633.
- [71] F. del Aguila, J. Gonzalez, and M. Quiros *Nucl.Phys.* **B307** (1988) 571.
- [72] R. Fonseca, M. Malinsky, W. Porod, and F. Staub *Nucl.Phys.* **B854** (2012) 28–53, [arXiv:1107.2670](https://arxiv.org/abs/1107.2670) [hep-ph].
- [73] F. Braam and J. Reuter [arXiv:1107.2806](https://arxiv.org/abs/1107.2806) [hep-ph].
- [74] H. P. Nilles *Phys. Rept.* **110** (1984) 1–162.
- [75] H. E. Haber and G. L. Kane *Phys. Rept.* **117** (1985) 75–263.
- [76] <https://twiki.cern.ch/twiki/bin/view/AtlasPublic/SupersymmetryPublicResults> .
- [77] <https://twiki.cern.ch/twiki/bin/view/CMSPublic/PhysicsResultsSUS> .
- [78] C. Duhr and B. Fuks *Comput. Phys. Commun.* **182** (2011) 2404–2426, [arXiv:1102.4191](https://arxiv.org/abs/1102.4191) [hep-ph].
- [79] A. Djouadi, J.-L. Kneur, and G. Moultaka *Comput.Phys.Commun.* **176** (2007) 426–455, [arXiv:hep-ph/0211331](https://arxiv.org/abs/hep-ph/0211331) [hep-ph].
- [80] J. Wess and J. Bagger, *Supersymmetry and Supergravity*. Princeton University Press, second ed., 1992.
- [81] B. Fuks and M. Rausch de Traubenberg, *Supersymétrie - exercices avec solutions*. Editions Ellipses Marketing, 2011.
- [82] J. P. Derendinger and C. A. Savoy *Nucl. Phys.* **B237** (1984) 307.

- [83] N. K. Falck *Z. Phys.* **C30** (1986) 247.
- [84] S. P. Martin and M. T. Vaughn *Phys.Rev.* **D50** (1994) 2282, arXiv:hep-ph/9311340 [hep-ph].
- [85] Y. Yamada *Phys.Lett.* **B316** (1993) 109–111, arXiv:hep-ph/9307217 [hep-ph].
- [86] Y. Yamada *Phys.Rev.Lett.* **72** (1994) 25–27, arXiv:hep-ph/9308304 [hep-ph].
- [87] Y. Yamada *Phys.Rev.* **D50** (1994) 3537–3545, arXiv:hep-ph/9401241 [hep-ph].
- [88] I. Jack, D. Jones, S. P. Martin, M. T. Vaughn, and Y. Yamada *Phys.Rev.* **D50** (1994) 5481–5483, arXiv:hep-ph/9407291 [hep-ph].
- [89] U. Ellwanger, C. Hugonie, and A. M. Teixeira *Phys. Rept.* **496** (2010) 1, arXiv:0910.1785 [hep-ph].
- [90] A. Pukhov et al. arXiv: [hep-ph/9908288].
- [91] CompHEP Collaboration, E. Boos et al. *Nucl. Instrum. Meth.* **A534** (2004) 250–259, arXiv:hep-ph/0403113.
- [92] T. Stelzer and W. F. Long *Comput. Phys. Commun.* **81** (1994) 357–371, arXiv:hep-ph/9401258.
- [93] F. Maltoni and T. Stelzer *JHEP* **02** (2003) 027, arXiv:hep-ph/0208156.
- [94] J. Alwall et al. *JHEP* **09** (2007) 028, arXiv:0706.2334 [hep-ph].
- [95] J. Alwall et al. *AIP Conf. Proc.* **1078** (2009) 84–89, arXiv:0809.2410 [hep-ph].
- [96] J. Alwall, M. Herquet, F. Maltoni, O. Mattelaer, and T. Stelzer *JHEP* **1106** (2011) 128, arXiv:1106.0522 [hep-ph].
- [97] M. Moretti, T. Ohl, and J. Reuter arXiv:hep-ph/0102195.
- [98] W. Kilian, T. Ohl, and J. Reuter arXiv:0708.4233 [hep-ph].
- [99] P. Langacker *Rev. Mod. Phys.* **81** (2009) 1199–1228, arXiv:hep-ph/0801.1345.
- [100] J. Erler, P. Langacker, S. Munir, and E. R. Pena *JHEP* **08** (2009) 017, arXiv:hep-ph/0906.2435.
- [101] R. Blumenhagen, M. Cvetič, P. Langacker, and G. Shiu *Ann.Rev.Nucl.Part.Sci.* **55** (2005) 71–139, arXiv:hep-th/0502005 [hep-th].
- [102] T. G. Rizzo arXiv:hep-ph/9612440.
- [103] M. Cvetič and P. Langacker arXiv:hep-ph/9707451.
- [104] T. Appelquist, B. A. Dobrescu, and A. R. Hopper *Phys. Rev.* **D68** (2003) 035012, arXiv:hep-ph/0212073.
- [105] M. S. Carena, A. Daleo, B. A. Dobrescu, and T. M. P. Tait *Phys. Rev.* **D70** (2004) 093009, arXiv:hep-ph/0408098.
- [106] E. Accomando, A. Belyaev, L. Fedeli, S. F. King, and C. Shepherd-Themistocleous *Phys.Rev.* **D83** (2011) 075012, arXiv:1010.6058 [hep-ph].
- [107] N. D. Christensen, P. de Aquino, C. Degrande, C. Duhr, B. Fuks, et al. *Eur.Phys.J.* **C71** (2011) 1541, arXiv:0906.2474 [hep-ph].
- [108] N. D. Christensen, C. Duhr, B. Fuks, J. Reuter, and C. Speckner arXiv:1010.3251 [hep-ph].
- [109] E. Salvioni, G. Villadoro, and F. Zwirner *JHEP* **0911** (2009) 068, arXiv:0909.1320 [hep-ph].
- [110] L. Basso, S. Moretti, and G. M. Pruna *JHEP* **1108** (2011) 122, arXiv:1106.4762 [hep-ph].

- [111] L. Basso, S. Moretti, and G. M. Pruna Phys. Rev. **D82** (2010) 055018, arXiv:1004.3039 [hep-ph].
- [112] D. Thain, T. Tannenbaum, and M. Livny Concurrency - Practice and Experience **17** (2005) no. 2-4, 323–356.
- [113] L. Basso, A. Belyaev, S. Moretti, and C. H. Shepherd-Themistocleous Phys. Rev. **D80** (2009) 055030, arXiv:hep-ph/0812.4313.
- [114] G. Corcella et al. JHEP **01** (2001) 010, arXiv:hep-ph/0011363.
- [115] S. Gieseke, D. Grellscheid, K. Hamilton, A. Papaefstathiou, S. Platzer, et al. arXiv:1102.1672 [hep-ph].
- [116] T. Sjostrand, S. Mrenna, and P. Z. Skands JHEP **0605** (2006) 026, arXiv:hep-ph/0603175 [hep-ph].
- [117] T. Sjostrand, S. Mrenna, and P. Z. Skands Comput.Phys.Commun. **178** (2008) 852–867, arXiv:0710.3820 [hep-ph].
- [118] T. Gleisberg et al. JHEP **02** (2004) 056, arXiv:hep-ph/0311263.
- [119] T. Gleisberg et al. JHEP **02** (2009) 007, arXiv:0811.4622 [hep-ph].
- [120] CDF Collaboration, T. Aaltonen et al. Phys.Rev. **D83** (2011) 112003, arXiv:1101.0034 [hep-ex].
- [121] D0 Collaboration, V. Abazov et al. Phys.Rev.Lett. **100** (2008) 142002, arXiv:0712.0851 [hep-ex].
- [122] F. del Aguila, J. de Blas, and M. Perez-Victoria JHEP **1009** (2010) 033, arXiv:1005.3998 [hep-ph].
- [123] J. Aguilar-Saavedra and M. Perez-Victoria JHEP **1105** (2011) 034, arXiv:1103.2765 [hep-ph].
- [124] A. Semenov Comput. Phys. Commun. **115** (1998) 124–139.
- [125] A. V. Semenov arXiv:hep-ph/0208011.
- [126] A. Semenov arXiv:1005.1909 [hep-ph].
- [127] T. Hahn and M. Perez-Victoria Comput. Phys. Commun. **118** (1999) 153–165, arXiv:hep-ph/9807565.
- [128] J. A. M. Vermaseren arXiv:math-ph/0010025.
- [129] D. Fliegner, A. Retey, and J. A. M. Vermaseren arXiv:hep-ph/9906426.
- [130] D. Fliegner, A. Retey, and J. A. M. Vermaseren arXiv:hep-ph/0007221.
- [131] M. Tentyukov et al. arXiv:cs/0407066.
- [132] M. Tentyukov and J. A. M. Vermaseren arXiv:hep-ph/0702279.
- [133] G. Cullen, N. Greiner, G. Heinrich, G. Luisoni, P. Mastrolia, G. Ossola, T. Reiter, and F. Tramontano (2011), arXiv:1111.2034 [hep-ph].
- [134] P. de Aquino, W. Link, F. Maltoni, O. Mattelaer, and T. Stelzer arXiv:1108.2041 [hep-ph].
- [135] C. Degrande, C. Duhr, B. Fuks, D. Grellscheid, O. Mattelaer, et al. arXiv:1108.2040 [hep-ph].
- [136] <http://feynrules.phys.ucl.ac.be> .
- [137] <https://hepmdb.soton.ac.uk> .
- [138] M. Bahr, S. Gieseke, M. Gigg, D. Grellscheid, K. Hamilton, et al. Eur.Phys.J. **C58** (2008) 639–707, arXiv:0803.0883 [hep-ph].

- [139] F. Staub arXiv: [hep-ph/0806.0538] [hep-ph].
- [140] B. Fuks et al. Feynrules contribution to Les Houches 2011 .
- [141] B. Allanach, M. Battaglia, G. Blair, M. S. Carena, A. De Roeck, et al. Eur.Phys.J. **C25** (2002) 113–123, arXiv:hep-ph/0202233 [hep-ph].
- [142] J. A. Aguilar-Saavedra, A. Ali, B. C. Allanach, R. L. Arnowitt, H. A. Baer, et al. Eur.Phys.J. **C46** (2006) 43–60, arXiv:hep-ph/0511344 [hep-ph].
- [143] ATLAS Collaboration, *Combination of Higgs Boson Searches with up to 4.9 fb^{-1} of pp Collisions Data Taken at a center-of-mass energy of 7 TeV with the ATLAS Experiment at the LHC*, Dec, 2011. ATLAS-CONF-2011-163.
- [144] CMS Collaboration, S. Chatrchyan et al. arXiv:1202.1488 [hep-ex].
- [145] S. Kraml et al., eds., *Workshop on CP Studies and Non-Standard Higgs Physics*. CERN-2006-009, hep-ph/0608079.
- [146] A. Djouadi Phys.Rept. **459** (2008) 1–241, arXiv:hep-ph/0503173 [hep-ph].
- [147] M. Drees, R. Godbole, and P. Roy World Scientific (2005) .
- [148] H. Baer and X. Tata Univ. Press, Cambridge, UK (2006) .
- [149] G. Bélanger, F. Boudjema, F. Donato, R. Godbole, and S. Rosier-Lees Nucl.Phys. **B581** (2000) 3–33, arXiv:hep-ph/0002039 [hep-ph].
- [150] N. Arkani-Hamed, L. J. Hall, H. Murayama, D. Tucker-Smith, and N. Weiner Phys. Rev. **D64** (2001) 115011, arXiv:hep-ph/0006312.
- [151] G. Bélanger, F. Boudjema, A. Cottrant, R. Godbole, and A. Semenov Phys.Lett. **B519** (2001) 93–102, arXiv:hep-ph/0106275 [hep-ph].
- [152] A. Bottino, F. Donato, N. Fornengo, and S. Scopel Phys.Rev. **D69** (2004) 037302, arXiv:hep-ph/0307303 [hep-ph].
- [153] Y. Mambrini arXiv:1112.0011 [hep-ph].
- [154] K. Ghosh, B. Mukhopadhyaya, and U. Sarkar Phys.Rev. **D84** (2011) 015017, arXiv:1105.5837 [hep-ph].
- [155] S. Andreas, C. Arina, T. Hambye, F.-S. Ling, and M. H. Tytgat Phys.Rev. **D82** (2010) 043522, arXiv:1003.2595 [hep-ph].
- [156] R. Dermisek and J. F. Gunion Phys.Rev.Lett. **95** (2005) 041801, arXiv:hep-ph/0502105 [hep-ph].
- [157] S. Chang, R. Dermisek, J. F. Gunion, and N. Weiner Ann.Rev.Nucl.Part.Sci. **58** (2008) 75–98, arXiv:0801.4554 [hep-ph].
- [158] U. Ellwanger, C. Hugonie, and A. M. Teixeira Phys.Rept. **496** (2010) 1–77, arXiv:0910.1785 [hep-ph].
- [159] J. van der Bij and S. Dilcher Phys.Lett. **B638** (2006) 234–238, arXiv:hep-ph/0605008 [hep-ph].
- [160] O. J. Eboli and D. Zeppenfeld Phys.Lett. **B495** (2000) 147–154, arXiv:hep-ph/0009158 [hep-ph].
- [161] H. Davoudiasl, T. Han, and H. E. Logan Phys.Rev. **D71** (2005) 115007, arXiv:hep-ph/0412269 [hep-ph].
- [162] R. Godbole, M. Guchait, K. Mazumdar, S. Moretti, and D. Roy Phys.Lett. **B571** (2003) 184–192, arXiv:hep-ph/0304137 [hep-ph].
- [163] A. Djouadi Phys.Lett. **B435** (1998) 101–108, arXiv:hep-ph/9806315 [hep-ph].

- [164] G. Bélanger, F. Boudjema, and K. Sridhar Nucl.Phys. **B568** (2000) 3–39, arXiv:hep-ph/9904348 [hep-ph].
- [165] M. S. Carena, S. Heinemeyer, C. Wagner, and G. Weiglein Eur.Phys.J. **C26** (2003) 601–607, arXiv:hep-ph/0202167 [hep-ph].
- [166] R. Kinnunen, S. Lehti, A. Nikitenko, and P. Salmi J.Phys.G **G31** (2005) 71–88, arXiv:hep-ph/0503067 [hep-ph].
- [167] R. Dermisek and I. Low Phys.Rev. **D77** (2008) 035012, arXiv:hep-ph/0701235 [HEP-PH].
- [168] I. Low and S. Shalgar JHEP **0904** (2009) 091, arXiv:0901.0266 [hep-ph].
- [169] A. Djouadi, V. Driesen, W. Hollik, and J. I. Illana Eur.Phys.J. **C1** (1998) 149–162, arXiv:hep-ph/9612362 [hep-ph].
- [170] U. Ellwanger Phys.Lett. **B698** (2011) 293–296, arXiv:1012.1201 [hep-ph].
- [171] O. Lebedev, H. M. Lee, and Y. Mambrini arXiv:1111.4482 [hep-ph].
- [172] M. Carena, E. Ponton, and J. Zurita Phys.Rev. **D82** (2010) 055025, arXiv:1005.4887 [hep-ph].
- [173] M. Carena, E. Ponton, and J. Zurita arXiv:1111.2049 [hep-ph].
- [174] F. Boudjema and G. La Rochelle arXiv:1112.1434 [hep-ph].
- [175] A. Falkowski Phys.Rev. **D77** (2008) 055018, arXiv:0711.0828 [hep-ph].
- [176] I. Low, R. Rattazzi, and A. Vichi JHEP **1004** (2010) 126, arXiv:0907.5413 [hep-ph].
- [177] A. Arbey, M. Battaglia, A. Djouadi, F. Mahmoudi, and J. Quevillon arXiv:1112.3028 [hep-ph].
- [178] H. Baer, V. Barger, and A. Mustafayev arXiv:1112.3017 [hep-ph].
- [179] L. J. Hall, D. Pinner, and J. T. Ruderman arXiv:1112.2703 [hep-ph].
- [180] G. Guo, B. Ren, and X.-G. He arXiv:1112.3188 [hep-ph].
- [181] S. Heinemeyer, O. Stal, and G. Weiglein arXiv:1112.3026 [hep-ph].
- [182] P. Draper, P. Meade, M. Reece, and D. Shih arXiv:1112.3068 [hep-ph].
- [183] P. Ferreira, R. Santos, M. Sher, and J. P. Silva arXiv:1112.3277 [hep-ph].
- [184] M. Carena, S. Gori, N. R. Shah, and C. E. Wagner arXiv:1112.3336 [hep-ph].
- [185] U. Ellwanger arXiv:1112.3548 [hep-ph].
- [186] G. Burdman, C. Haluch, and R. Matheus arXiv:1112.3961 [hep-ph].
- [187] J. F. Gunion, Y. Jiang, and S. Kraml arXiv:1201.0982 [hep-ph].
- [188] S. King, M. Muhlleitner, and R. Nevzorov arXiv:1201.2671 [hep-ph].
- [189] A. Djouadi, O. Lebedev, Y. Mambrini, and J. Quevillon arXiv:1112.3299 [hep-ph].
- [190] J. A. Conley, J. S. Gainer, J. L. Hewett, M. P. Le, and T. G. Rizzo Physical Review D (2011), arXiv:1103.1697 [hep-ph].
- [191] S. Sekmen, S. Kraml, J. Lykken, F. Moortgat, S. Padhi, et al. arXiv:1109.5119 [hep-ph].
- [192] A. Arbey, M. Battaglia, and F. Mahmoudi Eur.Phys.J. **C72** (2012) 1847, arXiv:1110.3726 [hep-ph].
- [193] A. Arbey, M. Battaglia, and F. Mahmoudi arXiv:1112.3032 [hep-ph].
- [194] A. Akeroyd, F. Mahmoudi, and D. Santos JHEP **1112** (2011) 088, arXiv:arXiv:1108.3018 [hep-ph].

- [195] CMS and LHCb Collaborations (2011), LHCb-CONF-2011-047, CMS PAS BPH-11-019.
- [196] XENON100 Collaboration Collaboration, E. Aprile et al. Phys.Rev.Lett. **107** (2011) 131302, arXiv:1104.2549 [astro-ph.CO].
- [197] G. Jungman, M. Kamionkowski, and K. Griest Phys. Rept. **267** (1996) 195–373, arXiv:hep-ph/9506380.
- [198] CMS Collaboration arXiv:arXiv:1109.2352 [hep-ex].
- [199] CMS Collaboration. CMS-PAS-SUS-11-010.
- [200] CMS Collaboration. CMS-PAS-SUS-11-011.
- [201] A. Djouadi, J. Kalinowski, and M. Spira Comput.Phys.Comm. **108** (1998) 56–74, arXiv:hep-ph/9704448 [hep-ph].
- [202] A. Djouadi, M. Muhlleitner, and M. Spira Acta Phys.Polon. **B38** (2007) 635–644, arXiv:hep-ph/0609292 [hep-ph].
- [203] D. Albornoz Vásquez, G. Bélanger, and C. Boehm Phys. Rev. D **84**, **095015** (2011), arXiv:1108.1338 [hep-ph].
- [204] D. Albornoz Vasquez, G. Belanger, R. Godbole, and A. Pukhov arXiv:1112.2200 [hep-ph].
- [205] D. Albornoz Vásquez, G. Bélanger, C. Boehm, A. Pukhov, and J. Silk Phys.Rev. **D82** (2010) 115027, arXiv:1009.4380 [hep-ph].
- [206] G. Belanger, F. Boudjema, A. Pukhov, and A. Semenov Comput.Phys.Comm. **176** (2007) 367–382, arXiv:hep-ph/0607059 [hep-ph].
- [207] G. Bélanger, F. Boudjema, A. Pukhov, and A. Semenov Comput. Phys. Commun. **180** (2009) 747–767, arXiv:0803.2360 [hep-ph].
- [208] G. Belanger, F. Boudjema, P. Brun, A. Pukhov, S. Rosier-Lees, et al. Comput.Phys.Comm. **182** (2011) 842–856, arXiv:1004.1092 [hep-ph].
- [209] P. Bechtle, O. Brein, S. Heinemeyer, G. Weiglein, and K. E. Williams Comput.Phys.Comm. **181** (2010) 138–167, arXiv:0811.4169 [hep-ph].
- [210] P. Bechtle, O. Brein, S. Heinemeyer, G. Weiglein, and K. E. Williams Comput.Phys.Comm. **182** (2011) 2605–2631, arXiv:1102.1898 [hep-ph].
- [211] CMS Collaboration, S. Chatrchyan et al. Phys.Rev.Lett. **106** (2011) 231801, arXiv:1104.1619 [hep-ex].
- [212] CMS Collaboration, S. Chatrchyan et al. CMS-PAS-HIG-11-011.
- [213] A. Brignole, J. A. Casas, J. R. Espinosa, and I. Navarro Nucl. Phys. **B666** (2003) 105–143, arXiv:hep-ph/0301121.
- [214] M. Dine, N. Seiberg, and S. Thomas Phys. Rev. **D76** (2007) 095004, arXiv:arXiv:0707.0005 [hep-ph] [hep-ph].
- [215] I. Antoniadis, E. Dudas, and D. Ghilencea JHEP **0803** (2008) 045, arXiv:arXiv:0708.0383 [hep-ph] [hep-th].
- [216] I. Antoniadis, E. Dudas, D. Ghilencea, and P. Tziveloglou Nucl.Phys. **B808** (2009) 155–184, arXiv:arXiv:0806.3778 [hep-ph] [hep-ph].
- [217] I. Antoniadis, E. Dudas, D. Ghilencea, and P. Tziveloglou Nucl.Phys. **B831** (2010) 133–161, arXiv:arXiv:0910.1100 [hep-ph] [hep-ph].
- [218] M. Carena, K. Kong, E. Ponton, and J. Zurita Phys.Rev. **D81** (2010) 015001, arXiv:arXiv:0909.5434 [hep-ph] [hep-ph].

- [219] P. Batra and E. Ponton Phys.Rev. **D79** (2009) 035001, arXiv:arXiv:0809.3453 [hep-ph] [hep-ph].
- [220] K. Blum, C. Delaunay, and Y. Hochberg Phys.Rev. **D80** (2009) 075004, arXiv:arXiv:0905.1701 [hep-ph] [hep-ph].
- [221] S. Cassel, D. Ghilencea, and G. Ross Nucl.Phys. **B825** (2010) 203–221, arXiv:arXiv:0903.1115 [hep-ph] [hep-ph].
- [222] J. Casas, J. Espinosa, and I. Hidalgo JHEP **0401** (2004) 008, arXiv:hep-ph/0310137 [hep-ph].
- [223] K. Cheung, S. Y. Choi, and J. Song Phys.Lett. **B677** (2009) 54–58, arXiv:arXiv:0903.3175 [hep-ph] [hep-ph].
- [224] M. Berg, J. Edsjo, P. Gondolo, E. Lundstrom, and S. Sjors JCAP **0908** (2009) 035, arXiv:arXiv:0906.0583 [hep-ph] [hep-ph].
- [225] N. Bernal and A. Goudelis JCAP **1003** (2010) 007, arXiv:arXiv:0912.3905 [hep-ph] [hep-ph].
- [226] S. Cassel and D. Ghilencea arXiv:arXiv:1103.4793 [hep-ph] [hep-ph].
- [227] N. Bernal, K. Blum, Y. Nir, and M. Losada JHEP **0908** (2009) 053, arXiv:arXiv:0906.4696 [hep-ph] [hep-ph].
- [228] K. Blum and Y. Nir Phys.Rev. **D78** (2008) 035005, arXiv:arXiv:0805.0097 [hep-ph] [hep-ph].
- [229] K. Blum, C. Delaunay, M. Losada, Y. Nir, and S. Tulin JHEP **1005** (2010) 101, arXiv:arXiv:1003.2447 [hep-ph] [hep-ph].
- [230] N. Bernal, M. Losada, and F. Mahmoudi JHEP **1107** (2011) 074, arXiv:arXiv:1104.5395 [hep-ph] [hep-ph].
- [231] W. Altmannshofer, M. Carena, S. Gori, and A. de la Puente Phys.Rev. **D84** (2011) 095027, arXiv:arXiv:1107.3814 [hep-ph] [hep-ph].
- [232] U. Ellwanger and C. Hugonie Comput.Phys.Commun. **175** (2006) 290–303, arXiv:hep-ph/0508022 [hep-ph].
- [233] ATLAS Collaboration, G. Aad et al. arXiv:1109.6572 [hep-ex].
- [234] A. Buckley, J. Butterworth, L. Lonnblad, H. Hoeth, J. Monk, et al. arXiv:1003.0694 [hep-ph].
- [235] D. Grellscheid, J. Jaeckel, V. V. Khoze, P. Richardson, and C. Wymant arXiv:1111.3365 [hep-ph].
- [236] F. Borzumati and Y. Nomura Phys.Rev. **D64** (2001) 053005, arXiv:hep-ph/0007018 [hep-ph].
- [237] G. Bélanger, M. Kakizaki, E. Park, S. Kraml, and A. Pukhov JCAP **1011** (2010) 017, arXiv:1008.0580 [hep-ph].
- [238] G. Bélanger, S. Kraml, and A. Lessa JHEP **1107** (2011) 083, arXiv:1105.4878 [hep-ph].
- [239] Z. Thomas, D. Tucker-Smith, and N. Weiner Phys. Rev. **D77** (2008) 115015, arXiv:0712.4146 [hep-ph].
- [240] J. Kopp, T. Schwetz, and J. Zupan JCAP **1002** (2010) 014, arXiv:0912.4264 [hep-ph].
- [241] T. Schwetz and J. Zupan JCAP **1108** (2011) 008, arXiv:1106.6241 [hep-ph].
- [242] CMS Collaboration. CMS-PAS-SUS-11-008.

- [243] ALEPH, DELPHI, L3 and OPAL Collaboration, LEP Higgs Working for Higgs boson searches arXiv:hep-ex/0107032.
- [244] L3 Collaboration, P. Achard et al. Phys. Lett. **B609** (2005) 35–48, arXiv:hep-ex/0501033.
- [245] V. Barger, P. Langacker, H.-S. Lee, and G. Shaughnessy Phys.Rev. **D73** (2006) 115010, arXiv:hep-ph/0603247 [hep-ph].
- [246] G. Bélanger, J. Da Silva, and A. Pukhov JCAP **1112** (2011) 014, arXiv:1110.2414 [hep-ph].
- [247] G. Krocker arXiv:1112.0868 [hep-ex].
- [248] G. Bélanger, M. Kakizaki, and A. Pukhov JCAP **2011** (2011) no. 02, 009, hep-ph/1012.2577. <http://stacks.iop.org/1475-7516/2011/i=02/a=009>.
- [249] H.-C. Cheng, K. T. Matchev, and M. Schmaltz Phys. Rev. **D66** (2002) 036005, arXiv:hep-ph/0204342.
- [250] I. Gogoladze and C. Macesanu Phys. Rev. **D74** (2006) 093012, arXiv:hep-ph/0605207.
- [251] K. Nishiwaki, K.-y. Oda, N. Okuda, and R. Watanabe [hep-ph/1108.1764].
- [252] LEP Working Group for Higgs boson searches Collaboration, R. Barate et al. Phys. Lett. **B565** (2003) 61–75, arXiv:hep-ex/0306033.
- [253] M. Baak, M. Goebel, J. Haller, A. Hoecker, D. Ludwig, et al. arXiv:1107.0975 [hep-ph].
- [254] M. Bobrowski, A. Lenz, J. Riedl, and J. Rohrwild Phys. Rev. **D79** (2009) 113006, arXiv:0902.4883 [hep-ph].
- [255] M. S. Chanowitz Phys. Rev. **D79** (2009) 113008, arXiv:0904.3570 [hep-ph].
- [256] D0 Collaboration, V. M. Abazov et al. Phys.Rev. **D84** (2011) 112001, arXiv:1108.3091 [hep-ex].
- [257] P. Q. Hung Phys. Rev. Lett. **80** (1998) 3000–3003, arXiv:hep-ph/9712338.
- [258] CMS Collaboration, S. Chatrchyan et al. CMS-PAS-EXO-11-051.
- [259] CMS Collaboration. CMS PAS EXO-11-036.
- [260] ATLAS Collaboration. ATLAS-CONF-2011-135.
- [261] W.-S. Hou Chin. J. Phys. **47** (2009) 134, arXiv:0803.1234 [hep-ph].
- [262] S. Ham, S. Oh, and D. Son Phys.Rev. **D71** (2005) 015001, arXiv:hep-ph/0411012 [hep-ph].
- [263] R. Fok and G. D. Kribs Phys. Rev. **D78** (2008) 075023, arXiv:0803.4207 [hep-ph].
- [264] K. Riesselmann and S. Willenbrock Phys.Rev. **D55** (1997) 311–321, arXiv:hep-ph/9608280 [hep-ph].
- [265] N. Cabibbo, L. Maiani, G. Parisi, and R. Petronzio Nucl.Phys. **B158** (1979) 295–305.
- [266] G. Altarelli and G. Isidori Phys.Lett. **B337** (1994) 141–144.
- [267] J. A. Casas, J. R. Espinosa, and M. Quiros Phys. Lett. **B382** (1996) 374–382, arXiv:hep-ph/9603227.
- [268] T. Hambye and K. Riesselmann Phys.Rev. **D55** (1997) 7255–7262, arXiv:hep-ph/9610272 [hep-ph].
- [269] A. Wingerter Phys.Rev. **D84** (2011) 095012, arXiv:1109.5140 [hep-ph].
- [270] ALEPH Collaboration arXiv:1012.2367 [hep-ex].

- [271] M. S. Chanowitz, M. Furman, and I. Hinchliffe Nucl.Phys. **B153** (1979) 402.
- [272] M. Kadastik, K. Kannike, A. Racioppi, and M. Raidal arXiv:1112.3647 [hep-ph].
- [273] O. Buchmueller, R. Cavanaugh, A. De Roeck, M. Dolan, J. Ellis, et al. arXiv:1112.3564 [hep-ph].
- [274] S. Akula, B. Altunkaynak, D. Feldman, P. Nath, and G. Peim arXiv:1112.3645 [hep-ph].
- [275] C. Strege, G. Bertone, D. Cerdeno, M. Fornasa, R. de Austri, et al. arXiv:1112.4192 [hep-ph].
- [276] J. Cao, Z. Heng, D. Li, and J. M. Yang arXiv:1112.4391 [hep-ph].
- [277] M. Farina, M. Kadastik, D. Pappadopulo, J. Pata, M. Raidal, et al. Nucl.Phys. **B853** (2011) 607–624, arXiv:1104.3572 [hep-ph].
- [278] O. Buchmueller, R. Cavanaugh, D. Colling, A. De Roeck, M. Dolan, et al. Eur.Phys.J. **C71** (2011) 1722, arXiv:1106.2529 [hep-ph].
- [279] O. Buchmueller, R. Cavanaugh, A. De Roeck, M. Dolan, J. Ellis, et al. arXiv:1110.3568 [hep-ph].
- [280] G. Bertone, D. Cerdeno, M. Fornasa, R. de Austri, C. Strege, et al. JCAP **1201** (2012) 015, arXiv:1107.1715 [hep-ph].
- [281] A. Fowlie, A. Kalinowski, M. Kazana, L. Roszkowski, and Y. Tsai arXiv:1111.6098 [hep-ph].
- [282] S. Bethke Eur.Phys.J. **C64** (2009) 689–703, arXiv:0908.1135 [hep-ph].
- [283] Tevatron Electroweak Working Group, for the CDF and D0 Collaborations Collaboration, M. Lancaster arXiv:1107.5255 [hep-ex].
- [284] D. Larson, J. Dunkley, G. Hinshaw, E. Komatsu, M. Nolta, et al. Astrophys.J.Suppl. **192** (2011) 16, arXiv:1001.4635 [astro-ph.CO].
- [285] M. Davier, A. Hoecker, B. Malaescu, and Z. Zhang Eur.Phys.J. **C71** (2011) 1515, arXiv:1010.4180 [hep-ph].
- [286] M. Misiak, H. Asatrian, K. Bieri, M. Czakon, A. Czarnecki, et al. Phys.Rev.Lett. **98** (2007) 022002, arXiv:hep-ph/0609232 [hep-ph].
- [287] LHCb-ANA-2011-039.
- [288] O. Buchmueller, R. Cavanaugh, A. De Roeck, J. Ellis, H. Flacher, et al. Eur.Phys.J. **C64** (2009) 391–415, arXiv:0907.5568 [hep-ph].
- [289] H. Baer, V. Barger, A. Lessa, and X. Tata arXiv:1112.3044 [hep-ph].
- [290] F. Englert and R. Brout Phys.Rev.Lett. **13** (1964) 321–323.
- [291] P. W. Higgs Phys. Lett. **12** (1964) 132–133.
- [292] P. W. Higgs Phys.Rev.Lett. **13** (1964) 508–509.
- [293] G. Guralnik, C. Hagen, and T. Kibble Phys.Rev.Lett. **13** (1964) 585–587.
- [294] J. Elias-Miro, J. R. Espinosa, G. F. Giudice, G. Isidori, A. Riotto, et al. arXiv:1112.3022 [hep-ph].
- [295] J. McDonald Phys. Rev. **D50** (1994) 3637–3649, arXiv:hep-ph/0702143.
- [296] C. P. Burgess, M. Pospelov, and T. ter Veldhuis Nucl. Phys. **B619** (2001) 709–728, arXiv:hep-ph/0011335.
- [297] V. Barger, P. Langacker, M. McCaskey, M. J. Ramsey-Musolf, and G. Shaughnessy Phys. Rev. **D77** (2008) 035005, arXiv:0706.4311 [hep-ph].

- [298] V. Barger, P. Langacker, M. McCaskey, M. Ramsey-Musolf, and G. Shaughnessy *Phys. Rev.* **D79** (2009) 015018, arXiv:0811.0393 [hep-ph].
- [299] M. Kadastik, K. Kannike, and M. Raidal *Phys.Rev.* **D81** (2010) 015002, arXiv:0903.2475 [hep-ph].
- [300] Y. Mambrini *Phys.Rev.* **D84** (2011) 115017, arXiv:1108.0671 [hep-ph].
- [301] M. Raidal and A. Strumia *Phys.Rev.* **D84** (2011) 077701, arXiv:1108.4903 [hep-ph].
- [302] M. Gonderinger, Y. Li, H. Patel, and M. J. Ramsey-Musolf *JHEP* **1001** (2010) 053, arXiv:0910.3167 [hep-ph].
- [303] M. Kadastik, K. Kannike, and M. Raidal *Phys.Rev.* **D80** (2009) 085020, arXiv:0907.1894 [hep-ph].
- [304] N. Arkani-Hamed, A. G. Cohen, and H. Georgi *Phys. Lett.* **B513** (2001) 232–240, arXiv:hep-ph/0105239.
- [305] N. Arkani-Hamed et al. *JHEP* **08** (2002) 021, arXiv:hep-ph/0206020.
- [306] N. Arkani-Hamed, A. Cohen, E. Katz, and A. Nelson *JHEP* **0207** (2002) 034, arXiv:hep-ph/0206021 [hep-ph].
- [307] R. Contino, Y. Nomura, and A. Pomarol *Nucl.Phys.* **B671** (2003) 148–174, arXiv:hep-ph/0306259 [hep-ph].
- [308] K. Agashe, R. Contino, and A. Pomarol *Nucl.Phys.* **B719** (2005) 165–187, arXiv:hep-ph/0412089 [hep-ph].
- [309] K. Agashe and R. Contino *Nucl.Phys.* **B742** (2006) 59–85, arXiv:hep-ph/0510164 [hep-ph].
- [310] R. Contino, L. Da Rold, and A. Pomarol *Phys.Rev.* **D75** (2007) 055014, arXiv:hep-ph/0612048 [hep-ph].
- [311] G. Burdman and L. Da Rold *JHEP* **0712** (2007) 086, arXiv:0710.0623 [hep-ph].
- [312] C. T. Hill *Phys.Lett.* **B266** (1991) 419–424.
- [313] H.-C. Cheng, B. A. Dobrescu, and C. T. Hill *Nucl.Phys.* **B589** (2000) 249–268, arXiv:hep-ph/9912343 [hep-ph].
- [314] M. S. Carena, E. Ponton, J. Santiago, and C. E. Wagner *Nucl.Phys.* **B759** (2006) 202–227, arXiv:hep-ph/0607106 [hep-ph].
- [315] M. S. Carena, E. Ponton, J. Santiago, and C. Wagner *Phys.Rev.* **D76** (2007) 035006, arXiv:hep-ph/0701055 [hep-ph].
- [316] L. Randall and R. Sundrum *Phys.Rev.Lett.* **83** (1999) 3370–3373, arXiv:hep-ph/9905221 [hep-ph].
- [317] M. Gogberashvili *Int.J.Mod.Phys.* **D11** (2002) 1635–1638, arXiv:hep-ph/9812296 [hep-ph].
- [318] T. Gherghetta and A. Pomarol *Nucl.Phys.* **B586** (2000) 141–162, arXiv:hep-ph/0003129 [hep-ph].
- [319] K. Agashe, A. Delgado, M. J. May, and R. Sundrum *JHEP* **0308** (2003) 050, arXiv:hep-ph/0308036 [hep-ph].
- [320] C. Bouchart and G. Moreau *Nucl.Phys.* **B810** (2009) 66–96, arXiv:0807.4461 [hep-ph].
- [321] A. Djouadi, G. Moreau, and F. Richard *Nucl.Phys.* **B773** (2007) 43–64, arXiv:hep-ph/0610173 [hep-ph].

- [322] A. Djouadi, G. Moreau, and R. K. Singh Nucl.Phys. **B797** (2008) 1–26, arXiv:0706.4191 [hep-ph].
- [323] K. Agashe, R. Contino, L. Da Rold, and A. Pomarol Phys.Lett. **B641** (2006) 62–66, arXiv:hep-ph/0605341 [hep-ph].
- [324] C. Bouchart and G. Moreau Phys.Rev. **D80** (2009) 095022, arXiv:0909.4812 [hep-ph].
- [325] C. Kilic, K. Kopp, and T. Okui Phys.Rev. **D83** (2011) 015006, arXiv:1008.2763 [hep-ph].
- [326] S. J. Huber and Q. Shafi Phys.Lett. **B498** (2001) 256–262, arXiv:hep-ph/0010195 [hep-ph].
- [327] S. J. Huber and Q. Shafi Phys.Lett. **B512** (2001) 365–372, arXiv:hep-ph/0104293 [hep-ph].
- [328] S. J. Huber and Q. Shafi Phys.Lett. **B544** (2002) 295–306, arXiv:hep-ph/0205327 [hep-ph].
- [329] S. J. Huber and Q. Shafi Phys.Lett. **B583** (2004) 293–303, arXiv:hep-ph/0309252 [hep-ph].
- [330] S. Chang, C. Kim, and M. Yamaguchi Phys.Rev. **D73** (2006) 033002, arXiv:hep-ph/0511099 [hep-ph].
- [331] G. Moreau and J. Silva-Marcos JHEP **0603** (2006) 090, arXiv:hep-ph/0602155 [hep-ph].
- [332] G. Moreau and J. Silva-Marcos JHEP **0601** (2006) 048, arXiv:hep-ph/0507145 [hep-ph].
- [333] K. Agashe, G. Perez, and A. Soni Phys.Rev. **D71** (2005) 016002, arXiv:hep-ph/0408134 [hep-ph].
- [334] K. Agashe, G. Perez, and A. Soni Phys.Rev.Lett. **93** (2004) 201804, arXiv:hep-ph/0406101 [hep-ph].
- [335] K. Agashe, G. Perez, and A. Soni Phys.Rev. **D75** (2007) 015002, arXiv:hep-ph/0606293 [hep-ph].
- [336] K. Agashe, A. E. Blechman, and F. Petriello Phys.Rev. **D74** (2006) 053011, arXiv:hep-ph/0606021 [hep-ph].
- [337] Y. Grossman and M. Neubert Phys.Lett. **B474** (2000) 361–371, arXiv:hep-ph/9912408 [hep-ph].
- [338] T. Appelquist, B. A. Dobrescu, E. Ponton, and H.-U. Yee Phys.Rev. **D65** (2002) 105019, arXiv:hep-ph/0201131 [hep-ph].
- [339] T. Gherghetta Phys.Rev.Lett. **92** (2004) 161601, arXiv:hep-ph/0312392 [hep-ph].
- [340] G. Moreau Eur.Phys.J. **C40** (2005) 539–554, arXiv:hep-ph/0407177 [hep-ph].
- [341] G. Cacciapaglia, A. Deandrea, D. Harada, and Y. Okada JHEP **1011** (2010) 159, arXiv:1007.2933 [hep-ph].
- [342] G. Cacciapaglia, A. Deandrea, L. Panizzi, N. Gaur, D. Harada, et al. arXiv:1108.6329 [hep-ph].
- [343] S. Gopalakrishna, T. Mandal, S. Mitra, and R. Tibrewala Phys.Rev. **D84** (2011) 055001, arXiv:1107.4306 [hep-ph].
- [344] J. Aguilar-Saavedra Phys.Lett. **B625** (2005) 234–244, arXiv:hep-ph/0506187 [hep-ph].

- [345] J. Aguilar-Saavedra JHEP **0911** (2009) 030, arXiv:0907.3155 [hep-ph].
- [346] G. Burdman, M. Perelstein, and A. Pierce Phys.Rev.Lett. **90** (2003) 241802, arXiv:hep-ph/0212228 [hep-ph].
- [347] T. Han, H. E. Logan, B. McElrath, and L.-T. Wang Phys.Rev. **D67** (2003) 095004, arXiv:hep-ph/0301040 [hep-ph].
- [348] M. Perelstein, M. E. Peskin, and A. Pierce Phys.Rev. **D69** (2004) 075002, arXiv:hep-ph/0310039 [hep-ph].
- [349] H.-C. Cheng, I. Low, and L.-T. Wang Phys.Rev. **D74** (2006) 055001, arXiv:hep-ph/0510225 [hep-ph].
- [350] G. Cacciapaglia, S. Choudhury, A. Deandrea, N. Gaur, and M. Klasen JHEP **1003** (2010) 059, arXiv:0911.4630 [hep-ph].
- [351] N. Vignaroli arXiv:1107.4558 [hep-ph].
- [352] R. Contino and G. Servant JHEP **0806** (2008) 026, arXiv:0801.1679 [hep-ph].
- [353] C. Dennis, M. Karagoz, G. Servant, and J. Tseng arXiv:hep-ph/0701158 [hep-ph].
- [354] K. Agashe and G. Servant JCAP **0502** (2005) 002, arXiv:hep-ph/0411254 [hep-ph].
- [355] New Physics Working Group Collaboration, G. Brooijmans et al. arXiv:1005.1229 [hep-ph].
- [356] F. del Aguila, L. Ametller, G. L. Kane, and J. Vidal Nucl. Phys. **B334** (1990) 1.
- [357] F. del Aguila, G. L. Kane, and M. Quiros Phys. Rev. Lett. **63** (1989) 942.
- [358] G. D. Kribs, A. Martin, and T. S. Roy arXiv:1012.2866 [hep-ph].
- [359] G. Azuelos, K. Benslama, D. Costanzo, G. Couture, J. Garcia, et al. Eur.Phys.J. **C39S2** (2005) 13–24, arXiv:hep-ph/0402037 [hep-ph].
- [360] A. Djouadi and G. Moreau Phys.Lett. **B660** (2008) 67–71, arXiv:0707.3800 [hep-ph].
- [361] A. Djouadi, G. Moreau, F. Richard, and R. K. Singh Phys.Rev. **D82** (2010) 071702, arXiv:0906.0604 [hep-ph].
- [362] A. Djouadi, G. Moreau, and F. Richard Phys.Lett. **B701** (2011) 458–464, arXiv:1105.3158 [hep-ph].
- [363] A. Azatov, M. Toharia, and L. Zhu Phys.Rev. **D82** (2010) 056004, arXiv:1006.5939 [hep-ph].
- [364] J. Espinosa, C. Grojean, and M. Muhlleitner JHEP **1005** (2010) 065, arXiv:1003.3251 [hep-ph].
- [365] F. Ledroit, G. Moreau, and J. Morel JHEP **0709** (2007) 071, arXiv:hep-ph/0703262 [HEP-PH].
- [366] S. Casagrande, F. Goertz, U. Haisch, M. Neubert, and T. Pfoh JHEP **1009** (2010) 014, arXiv:1005.4315 [hep-ph].
- [367] CERN Council Presentation, December 2011:
<http://indico.cern.ch/conferenceDisplay.py?confId=164890>, and, CMS web page: <https://twiki.cern.ch/twiki/bin/view/CMSPublic/PhysicsResults>..
- [368] CERN Council Presentation, December 2011:
<http://indico.cern.ch/conferenceDisplay.py?confId=164890>, and, ATLAS web page: <https://twiki.cern.ch/twiki/bin/view/AtlasPublic>..

- [369] M. Aliev, H. Lacker, U. Langenfeld, S. Moch, P. Uwer, et al. *Comput.Phys.Commun.* **182** (2011) 1034–1046, arXiv:1007.1327 [hep-ph].
- [370] LHC Higgs Cross Section Working Group Collaboration, S. Dittmaier et al. arXiv:1101.0593 [hep-ph].
- [371] CMS Collaboration, S. Chatrchyan et al. *Phys.Rev.Lett.* **107** (2011) 271802, arXiv:1109.4985 [hep-ex].
- [372] R. Barbieri, L. J. Hall, Y. Nomura, and V. S. Rychkov *Phys.Rev.* **D75** (2007) 035007, arXiv:hep-ph/0607332 [hep-ph].
- [373] L. Lavoura and J. P. Silva *Phys.Rev.* **D47** (1993) 2046–2057.
- [374] M. Herquet and F. Maltoni *Nucl.Phys.Proc.Suppl.* **179-180** (2008) 211–217.
- [375] S. Ovyn, X. Rouby, and V. Lemaître arXiv:0903.2225 [hep-ph].
- [376] M. L. Mangano, M. Moretti, F. Piccinini, R. Pittau, and A. D. Polosa *JHEP* **07** (2003) 001, arXiv:hep-ph/0206293.
- [377] CMS Collaboration, S. Chatrchyan et al. CMS-PAS-HIG-11-030.
- [378] CMS Collaboration, S. Chatrchyan et al. CMS-PAS-HIG-11-025.
- [379] A. Azatov, O. Bondu, A. Falkowski, M. Felcini, S. Gascon-Shotkin, et al. arXiv:in preparation [hep-ph].
- [380] D. B. Kaplan and H. Georgi *Phys.Lett.* **B136** (1984) 183.
- [381] D. B. Kaplan, H. Georgi, and S. Dimopoulos *Phys.Lett.* **B136** (1984) 187.
- [382] J. Santiago PoS **ICHEP2010** (2010) 557, arXiv:1103.4114 [hep-ph].
- [383] R. Contino, C. Grojean, M. Moretti, F. Piccinini, and R. Rattazzi *JHEP* **1005** (2010) 089, arXiv:1002.1011 [hep-ph].
- [384] A. Azatov, R. Contino, and J. Galloway arXiv:1202.3415 [hep-ph].
- [385] J. Espinosa, C. Grojean, and M. Muhlleitner arXiv:1202.1286 [hep-ph].
- [386] D. Carmi, A. Falkowski, E. Kuflik, and T. Volansky arXiv:1202.3144 [hep-ph].
- [387] J. Espinosa, C. Grojean, M. Muhlleitner, and M. Trott arXiv:1202.3697 [hep-ph].
- [388] ATLAS Collaboration, G. Aad et al. arXiv:1202.1408 [hep-ex].
- [389] A. Carmona, M. Chala, and J. Santiago in preparation.
- [390] R. Barcelo, A. Carmona, M. Masip, and J. Santiago *Phys.Lett.* **B707** (2012) 88–91, arXiv:1106.4054 [hep-ph].
- [391] R. Barcelo, A. Carmona, M. Chala, M. Masip, and J. Santiago *Nucl.Phys.* **B857** (2012) 172–184, arXiv:1110.5914 [hep-ph].
- [392] C. Bini, R. Contino, and N. Vignaroli *JHEP* **1201** (2012) 157, arXiv:1110.6058 [hep-ph].
- [393] CMS Collaboration, G. Bayatian et al. CERN-LHCC-2006-001, CMS-TDR-008-1.
- [394] R. M. Godbole, K. Rao, S. D. Rindani, and R. K. Singh *JHEP* **11** (2010) 144, arXiv:1010.1458 [hep-ph].
- [395] K. Huitu, S. Kumar Rai, K. Rao, S. D. Rindani, and P. Sharma *JHEP* **04** (2011) 026, arXiv:1012.0527 [hep-ph].
- [396] R. M. Godbole, L. Hartgring, I. Niessen, and C. D. White *JHEP* **1201** (2012) 011, arXiv:1111.0759 [hep-ph].
- [397] C. Weydert et al. *Eur. Phys. J.* **C67** (2010) 617–636, arXiv:0912.3430 [hep-ph].
- [398] S. Frixione, E. Laenen, P. Motylinski, B. R. Webber, and C. D. White *JHEP* **07** (2008)

- 029, arXiv:0805.3067 [hep-ph].
- [399] J. Shelton Phys. Rev. **D79** (2009) 014032, arXiv:0811.0569 [hep-ph].
- [400] C. D. White, S. Frixione, E. Laenen, and F. Maltoni JHEP **11** (2009) 074, arXiv:0908.0631 [hep-ph].
- [401] D. Walker, C.-P. Yuan, and J.-H. Yu to appear .
- [402] ATLAS Collaboration arXiv:1202.1408 [hep-ex].
- [403] ATLAS Collaboration, G. Aad et al. arXiv:1201.1091 [hep-ex].
- [404] ATLAS Collaboration, G. Aad et al. Phys.Rev.Lett. **107** (2011) 272002, arXiv:1108.1582 [hep-ex].
- [405] ATLAS Collaboration, G. Aad et al. Phys.Lett. **B705** (2011) 28–46, arXiv:1108.1316 [hep-ex].
- [406] ATLAS Collaboration, G. Aad et al. Phys. Lett. B **708** (2012) 37–54, arXiv:1108.6311 [hep-ex].
- [407] CMS Collaboration, S. Chatrchyan et al. Phys.Lett. **B704** (2011) 123–142, arXiv:1107.4771 [hep-ex].
- [408] ATLAS Collaboration, G. Aad et al. arXiv:1112.2194 [hep-ex].
- [409] CMS Collaboration, S. Chatrchyan et al. arXiv:1112.0688 [hep-ex].
- [410] ATLAS Collaboration, G. Aad et al. arXiv:1112.4462 [hep-ex].
- [411] ATLAS Collaboration, G. Aad et al. arXiv:1112.4828 [hep-ex].
- [412] ATLAS Collaboration, G. Aad et al. arXiv:1112.5755 [hep-ex].
- [413] ATLAS Collaboration, G. Aad et al. arXiv:1112.3580 [hep-ex].
- [414] S. Dimopoulos and H. Georgi Nucl.Phys. **B193** (1981) 150.
- [415] S. Weinberg Phys.Rev. **D13** (1976) 974–996.
- [416] L. Susskind Phys.Rev. **D20** (1979) 2619–2625.
- [417] C. T. Hill Phys.Rev. **D24** (1981) 691.
- [418] C. T. Hill Phys.Lett. **B266** (1991) 419–424.
- [419] R. Chivukula, B. A. Dobrescu, H. Georgi, and C. T. Hill Phys.Rev. **D59** (1999) 075003, arXiv:hep-ph/9809470 [hep-ph].
- [420] C. T. Hill and E. H. Simmons Phys.Rept. **381** (2003) 235–402, arXiv:hep-ph/0203079 [hep-ph].
- [421] N. Arkani-Hamed, S. Dimopoulos, and G. Dvali Phys.Lett. **B429** (1998) 263–272, arXiv:hep-ph/9803315 [hep-ph].
- [422] J. L. Hewett and T. G. Rizzo Phys.Rept. **183** (1989) 193.
- [423] R. Chivukula, E. H. Simmons, H.-J. He, M. Kurachi, and M. Tanabashi Phys.Rev. **D72** (2005) 015008, arXiv:hep-ph/0504114 [hep-ph].
- [424] R. Chivukula, B. Coleppa, S. Di Chiara, E. H. Simmons, H.-J. He, et al. Phys.Rev. **D74** (2006) 075011, arXiv:hep-ph/0607124 [hep-ph].
- [425] R. Sekhar Chivukula, N. D. Christensen, B. Coleppa, and E. H. Simmons Phys.Rev. **D80** (2009) 035011, arXiv:0906.5567 [hep-ph].
- [426] ATLAS Collaboration ATLAS-CONF-2011-101, CERN, Geneva, Jul, 2011.
- [427] S. Gopalakrishna, T. Han, I. Lewis, Z.-g. Si, and Y.-F. Zhou Phys.Rev. **D82** (2010) 115020, arXiv:1008.3508 [hep-ph].
- [428] CDF Collaboration, T. Aaltonen et al. Phys.Rev. **D79** (2009) 112002,

- arXiv:0812.4036 [hep-ex].
- [429] J. Pumplin et al. JHEP **0207** (2002) 012, arXiv:hep-ph/0201195 [hep-ph].
- [430] CMS Collaboration, S. Chatrchyan et al. Phys.Lett. **B701** (2011) 204–223, arXiv:1102.4746 [hep-ex].
- [431] A. Atre, G. Azuelos, M. Carena, T. Han, E. Ozcan, et al. JHEP **1108** (2011) 080, arXiv:1102.1987 [hep-ph].
- [432] V. Barger, T. Han, and D. G. Walker Phys.Rev.Lett. **100** (2008) 031801, arXiv:hep-ph/0612016 [hep-ph].
- [433] T. Han arXiv:hep-ph/0508097 [hep-ph].
- [434] J. H. Kuhn and G. Rodrigo Phys.Rev.Lett. **81** (1998) 49–52, arXiv:hep-ph/9802268 [hep-ph].
- [435] J. H. Kuhn and G. Rodrigo Phys.Rev. **D59** (1999) 054017, arXiv:hep-ph/9807420 [hep-ph].
- [436] M. Bowen, S. Ellis, and D. Rainwater Phys.Rev. **D73** (2006) 014008, arXiv:hep-ph/0509267 [hep-ph].
- [437] O. Antunano, J. H. Kuhn, and G. Rodrigo Phys.Rev. **D77** (2008) 014003, arXiv:0709.1652 [hep-ph].
- [438] V. Ahrens, M. Neubert, B. D. Pecjak, A. Ferroglia, and L. L. Yang Phys.Lett. **B703** (2011) 135–141, arXiv:1105.5824 [hep-ph].
- [439] M. Cacciari, S. Frixione, M. L. Mangano, P. Nason, and G. Ridolfi JHEP **0809** (2008) 127, arXiv:0804.2800 [hep-ph].
- [440] S. Moch and P. Uwer Phys.Rev. **D78** (2008) 034003, arXiv:0804.1476 [hep-ph].
- [441] CDF Collaboration, T. Aaltonen et al. Phys.Rev. **D82** (2010) 052002, arXiv:1002.2919 [hep-ex].
- [442] D0 Collaboration, V. Abazov et al. Phys.Lett. **B679** (2009) 177–185, arXiv:0901.2137 [hep-ex].
- [443] ATLAS-CONF-2011-140, CERN, Geneva, 2011.
- [444] CMS-PAS-TOP-11-007, CERN, Geneva, 2011.
- [445] J. H. Kuhn and G. Rodrigo arXiv:1109.6830 [hep-ph].
- [446] W. Hollik and D. Pagani Phys.Rev. **D84** (2011) 093003, arXiv:1107.2606 [hep-ph].
- [447] S. Westhoff arXiv:1108.3341 [hep-ph].
- [448] P. Ferrario and G. Rodrigo Phys.Rev. **D78** (2008) 094018, arXiv:0809.3354 [hep-ph].
- [449] P. Ferrario and G. Rodrigo Phys.Rev. **D80** (2009) 051701, arXiv:0906.5541 [hep-ph].
- [450] G. Rodrigo and P. Ferrario Nuovo Cim. **C33** (2010) 04, arXiv:1007.4328 [hep-ph].
- [451] S. Jung, H. Murayama, A. Pierce, and J. D. Wells Phys.Rev. **D81** (2010) 015004, arXiv:0907.4112 [hep-ph].
- [452] K. Cheung, W.-Y. Keung, and T.-C. Yuan Phys.Lett. **B682** (2009) 287–290, arXiv:0908.2589 [hep-ph].
- [453] E. Gabrielli and M. Raidal Phys.Rev. **D84** (2011) 054017, arXiv:1106.4553 [hep-ph].
- [454] ATLAS-CONF-2011-106, CERN, Geneva, 2011.

- [455] CMS-PAS-TOP-11-014, CERN, Geneva, 2011.
- [456] CMS-PAS-TOP-11-030, CERN, Geneva, 2011.
- [457] C. Delaunay, O. Gedalia, Y. Hochberg, G. Perez, and Y. Soreq *JHEP* **1108** (2011) 031, [arXiv:1103.2297 \[hep-ph\]](#).
- [458] CMS Collaboration, V. Khachatryan et al. *Phys.Rev.Lett.* **106** (2011) 201804, [arXiv:1102.2020 \[hep-ex\]](#).
- [459] ATLAS Collaboration, G. Aad et al. *New J.Phys.* **13** (2011) 053044, [arXiv:1103.3864 \[hep-ex\]](#).
- [460] Private communications with the CMS collaboration members T. Chwalek, A. Giammanco, T. Peiffer, and J. Wagner-Kuhr. (2011) .
- [461] E. Witten *Nucl.Phys.* **B188** (1981) 513.
- [462] S. Dimopoulos, S. Raby, and F. Wilczek *Phys.Rev.* **D24** (1981) 1681–1683.
- [463] J. R. Ellis, J. Hagelin, D. V. Nanopoulos, K. A. Olive, and M. Srednicki *Nucl.Phys.* **B238** (1984) 453–476.
- [464] P. Fayet *Nucl.Phys.* **B113** (1976) 135.
- [465] L. Alvarez-Gaume and S. Hassan *Fortsch.Phys.* **45** (1997) 159–236, [arXiv:hep-th/9701069 \[hep-th\]](#).
- [466] S. Choi, M. Drees, A. Freitas, and P. Zerwas *Phys.Rev.* **D78** (2008) 095007, [arXiv:0808.2410 \[hep-ph\]](#).
- [467] S. Choi, M. Drees, J. Kalinowski, J. Kim, E. Popena, et al. *Phys.Lett.* **B672** (2009) 246–252, [arXiv:0812.3586 \[hep-ph\]](#).
- [468] S. Choi, D. Choudhury, A. Freitas, J. Kalinowski, J. Kim, et al. *JHEP* **1008** (2010) 025, [arXiv:1005.0818 \[hep-ph\]](#).
- [469] S. Choi, D. Choudhury, A. Freitas, J. Kalinowski, and P. Zerwas *Phys.Lett.* **B697** (2011) 215–221, [arXiv:1012.2688 \[hep-ph\]](#).
- [470] S. Schumann, A. Renaud, and D. Zerwas [arXiv:1108.2957 \[hep-ph\]](#).
- [471] A. Salam and J. Strathdee *Nucl.Phys.* **B87** (1975) 85.
- [472] P. Fayet *Nucl.Phys.* **B90** (1975) 104–124.
- [473] G. D. Kribs, E. Poppitz, and N. Weiner *Phys.Rev.* **D78** (2008) 055010, [arXiv:0712.2039 \[hep-ph\]](#).
- [474] T. Plehn and T. M. Tait *J.Phys.G* **G36** (2009) 075001, [arXiv:0810.3919 \[hep-ph\]](#).
- [475] S. Choi, M. Drees, J. Kalinowski, J. Kim, E. Popena, et al. *Acta Phys.Polon.* **B40** (2009) 1947–1956, [arXiv:0902.4706 \[hep-ph\]](#).
- [476] C. Kilic, T. Okui, and R. Sundrum *JHEP* **0807** (2008) 038, [arXiv:0802.2568 \[hep-ph\]](#).
- [477] C. Kilic, S. Schumann, and M. Son *JHEP* **0904** (2009) 128, [arXiv:0810.5542 \[hep-ph\]](#).
- [478] C. Kilic, T. Okui, and R. Sundrum *JHEP* **1002** (2010) 018, [arXiv:0906.0577 \[hep-ph\]](#).
- [479] C. Kilic and T. Okui *JHEP* **1004** (2010) 128, [arXiv:1001.4526 \[hep-ph\]](#).
- [480] D. A. Dicus, C. Kao, S. Nandi, and J. Sayre *Phys.Rev.* **D83** (2011) 091702, [arXiv:1012.5694 \[hep-ph\]](#).
- [481] J. Sayre, D. A. Dicus, C. Kao, and S. Nandi *Phys.Rev.* **D84** (2011) 015011,

- arXiv:1105.3219 [hep-ph].
- [482] S. Ovin, X. Rouby, and V. Lemaitre arXiv:0903.2225 [hep-ph].
- [483] J. A. Conley, J. S. Gainer, J. L. Hewett, M. P. Le, and T. G. Rizzo Eur.Phys.J. **C71** (2011) 1697, arXiv:1009.2539 [hep-ph].
- [484] ATLAS Collaboration, G. Aad et al. JINST **3** (2008) S08003.
- [485] ATLAS Collaboration, G. Aad et al. Phys.Lett. **B703** (2011) 428–446, arXiv:1106.4495 [hep-ex].
- [486] S. Gieseke, D. Grellscheid, K. Hamilton, A. Ribon, P. Richardson, et al. arXiv:hep-ph/0609306 [hep-ph].
- [487] M. Gigg and P. Richardson Eur.Phys.J. **C51** (2007) 989–1008, arXiv:hep-ph/0703199 [HEP-PH].
- [488] W. Beenakker, R. Hopker, and M. Spira arXiv:hep-ph/9611232.
- [489] S. Tarem, S. Bressler, H. Nomoto, and A. Di Mattia Eur.Phys.J. **C62** (2009) 281–292.
- [490] P. Langacker, R. W. Robinett, and J. L. Rosner Phys.Rev. **D30** (1984) 1470.
- [491] M. J. Strassler and K. M. Zurek Phys.Lett. **B651** (2007) 374–379, arXiv:hep-ph/0604261 [hep-ph].
- [492] M. J. Strassler and K. M. Zurek Phys.Lett. **B661** (2008) 263–267, arXiv:hep-ph/0605193 [hep-ph].
- [493] N. Arkani-Hamed and S. Dimopoulos JHEP **0506** (2005) 073, arXiv:hep-th/0405159 [hep-th].
- [494] L. Basso, S. Moretti, and G. M. Pruna Phys. Rev. **D83** (2010) 055014, arXiv:1011.2612 [hep-ph].
- [495] L. J. Hall, K. Jedamzik, J. March-Russell, and S. M. West JHEP **1003** (2010) 080, arXiv:0911.1120 [hep-ph].
- [496] L. J. Hall, J. March-Russell, and S. M. West arXiv:1010.0245 [hep-ph].
- [497] P. Meade and M. Reece arXiv:hep-ph/0703031 [hep-ph].
- [498] L. Basso, A. Belyaev, S. Moretti, and G. M. Pruna Phys. Rev. **D81** (2010) 095018, arXiv:1002.1939 [hep-ph].
- [499] L. Basso arXiv:1106.4462 [hep-ph].
- [500] WMAP Collaboration Collaboration, E. Komatsu et al. Astrophys.J.Suppl. **192** (2011) 18, arXiv:1001.4538 [astro-ph.CO].
- [501] C. Cheung, G. Elor, L. J. Hall, and P. Kumar JHEP **1103** (2011) 085, arXiv:1010.0024 [hep-ph].
- [502] D. Hooper, J. March-Russell, and S. M. West Phys.Lett. **B605** (2005) 228–236, arXiv:hep-ph/0410114 [hep-ph].
- [503] D. E. Kaplan, M. A. Luty, and K. M. Zurek Phys.Rev. **D79** (2009) 115016, arXiv:0901.4117 [hep-ph].
- [504] S. Chang and M. A. Luty arXiv:0906.5013 [hep-ph].
- [505] S. P. Martin Phys.Rev. **D62** (2000) 095008, arXiv:hep-ph/0005116 [hep-ph].
- [506] G. D. Kribs, A. Martin, and T. S. Roy JHEP **0901** (2009) 023, arXiv:0807.4936 [hep-ph].
- [507] J. Alwall, A. Ballestrero, P. Bartalini, S. Belov, E. Boos, et al. Comput.Phys.Commun. **176** (2007) 300–304, arXiv:hep-ph/0609017 [hep-ph].

- [508] M. Dobbs and J. B. Hansen *Comput.Phys.Commun.* **134** (2001) 41–46.
- [509] ATLAS Collaboration, G. Aad et al. [arXiv:1109.2242](https://arxiv.org/abs/1109.2242) [hep-ex].
- [510] CMS Collaboration CMS-PAS-EXO-11-004.
- [511] CDF Collaboration, A. L. Scott *Int.J.Mod.Phys.* **A20** (2005) 3263–3266, [arXiv:hep-ex/0410019](https://arxiv.org/abs/hep-ex/0410019) [hep-ex].
- [512] D0 Collaboration, V. Abazov et al. *Phys.Rev.Lett.* **97** (2006) 161802, [arXiv:hep-ex/0607028](https://arxiv.org/abs/hep-ex/0607028) [hep-ex].
- [513] ATLAS Collaboration, G. Aad et al. [arXiv:1109.5141](https://arxiv.org/abs/1109.5141) [hep-ex].
- [514] G. R. Farrar and P. Fayet *Phys.Lett.* **B76** (1978) 575–579.
- [515] L. M. Krauss and F. Wilczek *Phys.Rev.Lett.* **62** (1989) 1221.
- [516] H. Fritzsch and P. Minkowski *Annals Phys.* **93** (1975) 193–266.
- [517] S. P. Martin *Phys.Rev.* **D46** (1992) 2769–2772, [arXiv:hep-ph/9207218](https://arxiv.org/abs/hep-ph/9207218) [hep-ph].
- [518] L. E. Ibanez and G. G. Ross *Phys.Lett.* **B260** (1991) 291–295.
- [519] K. Agashe and G. Servant *Phys.Rev.Lett.* **93** (2004) 231805, [arXiv:hep-ph/0403143](https://arxiv.org/abs/hep-ph/0403143) [hep-ph].
- [520] H. K. Dreiner, C. Luhn, and M. Thormeier *Phys.Rev.* **D73** (2006) 075007, [arXiv:hep-ph/0512163](https://arxiv.org/abs/hep-ph/0512163) [hep-ph].
- [521] E. Ma *Phys.Lett.* **B662** (2008) 49–52, [arXiv:0708.3371](https://arxiv.org/abs/0708.3371) [hep-ph].
- [522] K. Agashe, D. Kim, M. Toharia, and D. G. Walker *Phys.Rev.* **D82** (2010) 015007, [arXiv:1003.0899](https://arxiv.org/abs/1003.0899) [hep-ph].
- [523] K. Agashe, D. Kim, D. G. Walker, and L. Zhu *Phys.Rev.* **D84** (2011) 055020, [arXiv:1012.4460](https://arxiv.org/abs/1012.4460) [hep-ph].
- [524] B. Batell *Phys.Rev.* **D83** (2011) 035006, [arXiv:1007.0045](https://arxiv.org/abs/1007.0045) [hep-ph].
- [525] F. D’Eramo and J. Thaler *JHEP* **1006** (2010) 109, [arXiv:1003.5912](https://arxiv.org/abs/1003.5912) [hep-ph].
- [526] G. Belanger, F. Boudjema, A. Pukhov, and A. Semenov *Comput.Phys.Commun.* **174** (2006) 577–604, [arXiv:hep-ph/0405253](https://arxiv.org/abs/hep-ph/0405253) [hep-ph].
- [527] N. G. Deshpande and E. Ma *Phys.Rev.* **D18** (1978) 2574.
- [528] E. Ma *Phys.Rev.* **D73** (2006) 077301, [arXiv:hep-ph/0601225](https://arxiv.org/abs/hep-ph/0601225) [hep-ph].
- [529] R. Barbieri, L. J. Hall, and V. S. Rychkov *Phys.Rev.* **D74** (2006) 015007, [arXiv:hep-ph/0603188](https://arxiv.org/abs/hep-ph/0603188) [hep-ph].
- [530] L. Lopez Honorez, E. Nezri, J. F. Oliver, and M. H. Tytgat *JCAP* **0702** (2007) 028, [arXiv:hep-ph/0612275](https://arxiv.org/abs/hep-ph/0612275) [hep-ph].
- [531] M. Kadastik, K. Kannike, A. Racioppi, and M. Raidal *Phys.Rev.Lett.* **104** (2010) 201301, [arXiv:0912.2729](https://arxiv.org/abs/0912.2729) [hep-ph].
- [532] M. Kadastik, K. Kannike, A. Racioppi, and M. Raidal *Phys.Lett.* **B694** (2010) 242–245, [arXiv:0912.3797](https://arxiv.org/abs/0912.3797) [hep-ph].
- [533] K. Huitu, K. Kannike, A. Racioppi, and M. Raidal *JHEP* **1101** (2011) 010, [arXiv:1005.4409](https://arxiv.org/abs/1005.4409) [hep-ph].
- [534] <https://twiki.cern.ch/twiki/bin/view/AtlasPublic>.
- [535] <https://twiki.cern.ch/twiki/bin/view/CMSPublic/PhysicsResults>.
- [536] S. AbdusSalam, B. Allanach, H. Dreiner, J. Ellis, U. Ellwanger, et al. *Eur.Phys.J.* **C71** (2011) 1835, [arXiv:1109.3859](https://arxiv.org/abs/1109.3859) [hep-ph].
- [537] D. Alves, N. Arkani-Hamed, S. Arora, Y. Bai, M. Baumgart, et al. [arXiv:1105.2838](https://arxiv.org/abs/1105.2838)

- [hep-ph].
- [538] CMS Collaboration Collaboration, S. Chatrchyan et al. *Phys.Rev.Lett.* **107** (2011) 221804, arXiv:1109.2352 [hep-ex].
- [539] ATLAS Collaboration Collaboration, G. Aad et al. *Phys. Lett.* **B709** (2012) 137–157, arXiv:1110.6189 [hep-ex].
- [540] ATLAS Collaboration, G. Aad et al. *Phys.Rev.* **D85** (2012) 012006, arXiv:1109.6606 [hep-ex].
- [541] B. Allanach, T. Khoo, and K. Sakurai arXiv:1110.1119 [hep-ph].
- [542] Y. Kats, P. Meade, M. Reece, and D. Shih arXiv:1110.6444 [hep-ph].
- [543] M. Papucci, J. T. Ruderman, and A. Weiler arXiv:1110.6926 [hep-ph].
- [544] X.-J. Bi, Q.-S. Yan, and P.-F. Yin arXiv:1111.2250 [hep-ph].
- [545] N. Desai and B. Mukhopadhyaya arXiv:1111.2830 [hep-ph].
- [546] T. J. LeCompte and S. P. Martin arXiv:1111.6897 [hep-ph].
- [547] S. Chang, K. Y. Lee, and J. Song arXiv:1112.1483 [hep-ph].
- [548] Workshop on “Searches for New Physics: Les Houches Recommendations for the Presentation of LHC Results”, CERN, 13 Feb 2012, <https://indico.cern.ch/conferenceDisplay.py?confId=173341>.
- [549] A. Belyaev et al. *Pramana* **72** (2009) 229–238, arXiv:0806.2838 [hep-ph].
- [550] *FeynRules 2010 Workshop on automatization for BSM physics*, <http://indico.in2p3.fr/conferenceDisplay.py?confId=2487>, Mont Saint Odile, April, 2010.
- [551] *Mini-Workshop on Dynamical Symmetry Breaking models and tools*, <http://indico.cern.ch/conferenceDisplay.py?confId=100099>, Southampton, July, 2010.
- [552] J. Kublbeck, H. Eck, and R. Mertig *Nucl. Phys. Proc. Suppl.* **29A** (1992) 204–208.
- [553] T. Hahn *Comput. Phys. Commun.* **140** (2001) 418–431, arXiv:hep-ph/0012260.
- [554] FeynRules website, <https://feynrules.irmp.ucl.ac.be/>.